SSSTJ VOL.10 NO.2 July 2023
ISSN 2351-0889

SSSTJ

Suan Sunandha Science and Technology Journal
Volume 10, Number 2,July 2023

Suan Sunandha Science and Technology Journal
©2023 Faculty of Science and Technology, Suan Sunandha Rajabhat University

General Information

The Suan Sunandha Science and Technology Journal (SSSTJ) is a double-blind peer reviewed scientific journal published twice a year (January and July) by the Faculty of Science and Technology, Suan Sunandha Rajabhat University. Submissions of manuscripts should be sent to the Editor of the SSSTJ by online system: https://li02.tci-thaijo.org/index.php/ssstj The manuscript will be taken that all contributing authors attest that manuscripts and material submitted to the SSSTJ are original and have not been published or submitted elsewhere and the authors concede to the open-access distribution of the manuscript, including all contents contained therein.

Aim and scope:

Suan Sunandha Science and Technology Journal (SSSTJ) is an international academic journal that gains foothold at Suan Sunandha Rajabhat University, Thailand and opens to scientific communications in Southeast Asia, Asia and worldwide. It aims to contribute significant articles in science and technology researches. Published papers are focused on state of the art science and technology. Committee of the journal and association will review submitted papers. The authors may include researchers, managers, operators, students, teachers and developers.

Followingareasareconsideredforpublication:

1.Biology
2.Biotechnology
3.EnvironmentalScienceandTechnology
4.FoodScienceandTechnology
5.Microbiology
6.Applied Science
7.Computer Science and Information Technology
8.Other related fields

Available online at https://li02.tci-thaijo.org/index.php/ssstj

Suan Sunandha Science and Technology Journal
©2023 Faculty of Science and Technology, Suan Sunandha Rajabhat University

Editorial Team

Executive Editor

Chaisri Tharasawatpipat, Suan Sunandha Rajabhat University, Thailand

Editor-in -Chief

Narong Sangwaranatee, Suan Sunandha Rajabhat University, Thailand

Associate Editor

Sirilak Namwong, Suan Sunandha Rajabhat University, Thailand

Boon-ek Yingyongnarongkul, Ramkhamheang University, Thailand

Sumitra Nuanmeesri, Suan Sunandha Rajabhat University, Thailand

Nisakorn Sangwaranatee, Suan Sunandha Rajabhat University, Thailand

Narun Luewarasirikul, Suan Sunandha Rajabhat University, Thailand

Thanida Chuacharoen, Suan Sunandha Rajabhat University, Thailand

Noppadon Chamchoi, Suan Sunandha Rajabhat University, Thailand

Bagher Javadi, Suan Sunandha Rajabhat University, Thailand

Editorial Board

Hongjoo Kim, Kyungpook, National University, South Korea

Mitra Djamal, Institut Teknologi Bandung, Indonesia

Jakrapong Kaewkhao, Nakhon Pathom Rajabhat University, Thailand

Naratip Vittayakorn, King Mongkut's Institute of Technology Ladkrabang, Thailand

Rattikorn Yimnirun, Vidyasirimedhi Institute of Science and Technology, Thailand

Ying I. Tsai, Chia-Nan University of Pharmacy and Science, Taiwan

Benjaphorn Prapagdee, Mahidol University, Thailand

Nguyen Hieu Trung, Can Tho University,Viet Nam

Nongluksna Sriubolmas, Chulalongkorn University, Thailand

Thanh Son Dao, Hochiminh City University of Technology, Vietnam

©2023 Faculty of Science and Technology, Suan Sunandha Rajabhat University

Saengchan Senapin, Thailand National Center for Genetic Engineering and Biotechnology, Thailand

Sittiruk Roytrakul, Thailand National Center for Genetic Engineering and Biotechnology, Thailand

Soo Rin Kim, Kyungpook National University, Korea

Stephen Raymond Morley, Leicester Royal Infirmary, United Kingdom

Vorapot Kanokantapong, Chulalongkorn University, Thailand

Yaowapa Lorjaroenphon, Kasetsart University, Thailand

Managing Department

Panisara Nitutorn, Suan Sunandha Rajabhat University, Thailand

Naruedom Chewpraditkul, Suan Sunandha Rajabhat University, Thailand

Available online at https://li02.tci-thaijo.org/index.php/ssstj

Suan Sunandha Science and Technology Journal
©2023 Faculty of Science and Technology, Suan Sunandha Rajabhat University

SSSTJ Authors Guide

Types of paper:

The journal publishes research articles and academic articles. Full length articles are typically 4 - 10 manuscript pages (including tables, figures, equations and formulas). The articles may cover a variety of topics which are related to science or technology. Articles must use previously published works to support the discussion of a particular subject or topic.

Plagiarism:

Submission of an manuscript implies that the work described has not been published previously (except in the form of an abstract or as part of a published lecture or academic thesis), that it is not under consideration for publication elsewhere, that its publication is approved by all authors and tacitly or explicitly by the responsible authorities where the work was carried out, and that, if accepted, it will not be published elsewhere in the same form, in English or in any other language, without the written consent of the copyright-holder.

Articles and any other material published in the SSSTJ the opinions of the author(s) and should not be construed to reflect the opinions of the editor(s) or the publisher. Manuscripts that do not meet the general criteria or standards for publication in the SSSTJ will be immediately returned to the authors, without detailed review. At their discretion, editors may request from the corresponding author a statement describing specific original contributions made by each co-author.

Manuscript submission:

For submission of all manuscripts, follow the instructions of the online submission system. Hard copy submissions cannot be accepted. Before submission, prepare and keep ready all information on the manuscript (title, full name and affiliation of all authors, corresponding author email, abstract, name of all files to be submitted).The author submitting the manuscript will be corresponding author. Manuscripts are accepted only in American English. All submitted articles should report original, previously unpublished research results, experimental or theoretical, and will be peer-reviewed.

Role of the funding agency:

You are requested to identify who provided financial support for conducting the research and/or preparation of the article and to briefly describe the role of the sponsor(s), if any, in study design; in the collection, analysis and interpretation of data; in the writing of the report; and in the decision to submit the article for publication. If the funding source(s) had no such involvement then this should be stated.

Suan Sunandha Science and Technology Journal
©2023 Faculty of Science and Technology, Suan Sunandha Rajabhat University

Journal access:

Open access:

- Articles are freely available to both subscribers and the wider public.
- Articles are made available to subscribers at https://li02.tci-thaijo.org/index.php/ssstj

Regardless of how you choose to publish your article, the journal will apply the same peer review criteria and acceptance standards.

Peer review:

All published journal papers are refereed by the international competent researchers and scientists. Therefore, a full double - blind international refereeing process is used in which 1) Papers are sent to reviewers for their peer review process. 2) The reviewers' recommendations determine whether a paper will be accepted / accepted subject to change / subject to resubmission with significant changes / rejected. For papers which require changes, the same reviewers will be used to ensure that the quality of the revised paper is acceptable. All papers are refereed, and the Editor-in-Chief reserves the right to refuse any typescript, whether on invitation or otherwise, and to make suggestions and/or modifications before publication.

Additional information:

Manuscripts must be submitted by the senior author, who must accept responsibility on behalf of all authors for all ethical requirements. The author submitting the manuscript will be listed as the corresponding author in the published version of each accepted manuscript. There are no submission fees or page charges.

Revised manuscripts should be returned including revision notes. The revision notes should address the issues raised in the referee report and clearly state per page (indicate paragraph and line) which changes have been made. Additional materials may be requested at the discretion of the editor. Authors requested to revise their submission to SSSTJ will be given 4 weeks in which to submit the revised submission. Revised submissions received after 4 weeks from the time at which the revision was requested will be considered as new submissions.

References:

There are no strict requirements on reference formatting at submission. But the authors are expected to follow the American Psychological Association (APA 6th edition) style. Where applicable, author(s) name(s), journal title/book title, chapter title/article title, year of publication, volume number/book chapter and the pagination must be present. Use of DOI is highly encouraged.

Article structure:

Subdivision - numbered sections

Divide your article into clearly defined and numbered sections. Subsections should be numbered 1.1, 1.2, etc. (the abstract is not included in section numbering). Use this numbering also for internal cross-referencing:

©2023 Faculty of Science and Technology, Suan Sunandha Rajabhat University

do not just refer to 'the text'. Any subsection may be given a brief heading. Each heading should appear on its own separate line.

Article formatting:

Full-length articles published in the SSSTJ should include a title, the author's name, the author's address, the corresponding author email, Abstract, Introduction, Materials and Methods, Results and Discussion, Acknowledgements and References.

- **Font:** Times New Roman (headings 11pt and normal text 10pt)
- **Title:** Concise and informative. This should briefly summarize the scope of the article. Avoid abbreviations and formulas where possible. The title should be centered at the top of the page. e.g., Notes on the Biology of *Varanus semiremix*
- **Authors name and affiliation:** The full names referenced by numerical superscripts with affiliation and addresses of all authors, and the full address of the corresponding author. The name of the corresponding author along with phone, fax and e-mail information. e.g.

  Author's Name
  Author's affiliation
  Author's address
  Corresponding author email
- **Corresponding author:** Clearly indicate who will handle correspondence at all stages of refereeing and publication, also post-publication. Ensure that the e-mail address is given and that contact details are kept up to date by the corresponding author.
- **Abstract:** The abstract should contain brief information on purpose, methods, results and conclusion (without subheadings). It indicates significant data, and point out major findings and conclusions. Provide 200 – 250 words in length.
- **Keywords:** 3 – 6 keywords should be listed.
- **Introduction**: The introduction should provide sufficient background knowledge and information to allow the reader to understand and evaluate the value of the study. It must also supply a rationale for the study. Cite references to provide the most salient background rather than an exhaustive review of the topic.
- **Materials and Methods:** Specific details about materials, instrumentation and experimental protocols should be given here. This section should contain sufficient details so that others are able to reproduce the experiment(s). The source of special equipment or chemicals should also be given with the name and location of manufacturers, e.g. (Merck, Germany) or (Sigma, USA). Techniques previously published or standardized can be simplified by literature citations. The statistical procedures used should be explained. Primary headings for this section are in bold, indented, with numbering. The text is run from a new line under the heading with an indentation.
- **Results and Discussions:** The results should be presented with clarity and precision. The discussions should provide an interpretation of the data and relate them to existing knowledge.

©2023 Faculty of Science and Technology, Suan Sunandha Rajabhat University

Emphasis should be given to important new findings and new hypotheses should be described clearly. This section may be subdivided and headed as in the Materials and Methods section. At the end of this section, the authors should state the conclusion in a few sentences.

- **Conclusion:** The main conclusions of the study may be presented in a short conclusion section, which may stand alone or form a subsection of a Results and Discussions section.
- **Acknowledgment:** The acknowledgments should be stated in separate section at the end of the article before the references.
- **References:** Please make sure that every reference cited in the text is also present in the reference list and vice versa.
- **Appendices (optional):** If there is more than one appendix, they should be identified as A, B, etc. Formulae and equations in appendices should be given separate numbering: Eq. (A.1), Eq. (A.2), etc.; in a subsequent appendix, Eq. (B.1) and so on. Similarly for tables and figures: Table A.1; Figure A.1, etc.

- **Tables and Figures:**

  Tables: Please submit tables as editable text and not as image. Tables must be embedded into text. Headings should be in bold letters, and aligned in the text left. Vertical lines are not used. A table should not exceed one page when printed. Use lower case letters in superscripts a, b, c ... for special remarks.

  Figure legends: It should be typed in numerical order. Begin each legend with a title and include sufficient description so that the figure is understandable without reading the text of the manuscript.

  Figures: Each figure must be embedded into text. It should be prepared using applications capable of generating high resolution TIFF, JPEG, PNG.

  - Color or grayscale photographs: minimum of 300 dpi
  - Bitmapped line drawings: minimum of 1000 dpi
  - Combination bitmapped line (color or grayscale photographs: minimum of 500 dpi)
  - Headings should be in bold letters, and aligned in the text Centre

Checklist before submission:

The following list will be useful during the final checking of an article prior to sending it to the journal for review.

Ensure that the following contents are present:

One author has been designated as the corresponding author with contact details:

- E-mail address
- Affiliation
- Full postal address
- Corresponding author email

All necessary files have been uploaded, and contain:

- Keywords
- All figure captions

Suan Sunandha Science and Technology Journal
©2023 Faculty of Science and Technology, Suan Sunandha Rajabhat University

- All tables (including title, description)
- Manuscript has been 'spell-checked' (Spellchecker tool of MS word) and 'grammar-checked'.
- All references mentioned in the reference list are cited in the text, and vice versa.

Additional information: For additional information regarding format, content, submissions, or authoring guidelines, please contact the editor (e-mail: ssstj.contact@gmail.com).

SSSTJ has both online and printing versions.
ISSN 2351-0889
e-ISSN 2539-5742 (Online)
Published by: Faculty of Science and Technology, Suan Sunandha Rajabhat University

SUAN SUNANDHA SCIENCE AND TECHNOLOGY JOURNAL

Suan Sunandha Rajabhat University, Faculty of Science and Technology
1 U-thong Nok Road, Dusit, Bangkok 10300 THAILAND

CONTENTS

July 2023, Volume 10, No.2

Available online at https://li02.tci-thaijo.org/index.php/ssstj

Suan Sunandha Science and Technology Journal
©2023 Faculty of Science and Technology, Suan Sunandha Rajabhat University

Influence of Tinuvin 292 on Chlorinated Rubber Varnish/ Coating Properties under UV Radiation

Nguyen Trung Thanh*

Department of Chemical Technology, Institute of Technology
Hanoi, Vietnam
***Corresponding author e-mail: nguyentrungthanhk42@gmail.com**

Received: *27 December 2022* / **Revised**: *13 February 2023* / **Accepted**: *28 February 2023*

Abstract

This article presents the effect of Tinuvin 292 (a light stabilizer based on liquid hindered amine) on properties of chlorinated rubber varnish/coating under 100 UV-thermo-humidity complex cycles. The properties included relative hardness, adhesion, flexural strength, impact resistance, and gloss loss. The results showed that 2.5 weight percent (wt%) of Tinuvin 292 had much improved physical properties of varnish coating such as relative hardness, adhesion, flexural strength, impact resistance, and gloss loss. Fourier-transform infrared spectroscopy (FT-IR), Thermogravimetric analysis (TGA), and Field Emission Scanning Electron Microscopy (FESEM) were used to evaluate the changes of aged coatings in comparison to the initial ones. FT-IR spectrums also showed that intensities of CH_2 and C=O (ester) groups changed strongly or slightly depending on the appearance of Tinuvin 292. SEM images indicated that the surface of aged coating with Tinuvin 292 was smoother than coating without Tinuvin 292. TGA also expressed that thermal oxidation stability of chlorinated rubber varnish/ coating had been enhanced with 2.5 wt% of Tinuvin 292.

Keywords: Chlorinated rubber paint, Aged coating, Polymer, Tinuvin 292

1. Introduction

Carbon black, graphene oxide (GO), titanium oxide (TiO_2), zinc oxide (ZnO) have been added in compositions of coatings materials (Crescenzo, Zendri, Pons, Lospez, & Marco, 2014; Das, Pandey, Mohanty, & Nayak, 2017; Kızılkonca & Erim, 2019) to protect paint or varnish coatings from aging under UV light. However, the anti-UV additives agglomeration made them difficult to be well dispersed in liquid paints as well as losing their transparency (Cogulet, Blanchet, & Landry, 2019; Kahrizsangi, Neshati, Shariatpanahi, & Akbarinezhad, 2015; Nguyen et al., 2017; Pintus, Wei, & Schreiner, 2016). Chlorinated rubber paint is made from chlorinated rubber resin of 60-68% chlorine group and characterized by fast dry, inflammable coating. Chlorinated rubber coatings have been widely used in shipbuilding, water conservancy, petrochemical industry and it also performs as a good anti-corrosion coating (Ahmed, Emira, & Tawfik, 2013; Olabisi & Adewale, 2015; Sakhri, Perrin, Aragon, Lamouric, & Benaboura, 2010; Talbert, 2007). To improve performance and promote the development of weather resistance properties, chlorinated rubber paints have been modified with coal tar pitch, thermoplastic acrylic resins (Ismail & Harun, 2016; Liu, Xiong, Lv, & Zuo, 2009; Morsi, Emira, El-Sawy, Mohsen, & Khorshed, 2019). Bano and colleagues (Bano, Khan, & Kazmi, 2013) investigated the chlorinated rubber coating in which coatings were exposed at some places such as seaside, industrial and urban areas. Accelerated testing was performed with a salt spraying chamber. Visual examination results of blistering, rusting and SEM micrographs indicated that there was a little degradation of the coating surface at natural exposure testing sites or accelerated testing. The carbonyl compounds formation was observed by FTIR spectroscopy. Lang and colleagues (Lang et al., 2019) had tested a commercially available chlorinated rubber-based iron oxide red paint for 9 months, results showed that coating did not perform well, which could not resist the colonization of major fouling organisms. Also, Sakhri and colleagues (Sakhri et al., 2010) studied on effect of zinc phosphate and polyaniline pigments on chlorinated rubber paints to prevent corrosion on mild steel. The anticorrosion performance of coatings with presence of polyaniline emeraldine salt or zinc phosphate were

Suan Sunandha Science and Technology Journal
©2023 Faculty of Science and Technology, Suan Sunandha Rajabhat University

compared by using salt spray in 3.5% NaCl solution immersion. The results showed that protection of polyaniline was better in comparison with zinc phosphate. The time to have the first rust spot in 3.5% NaCl solution of coating with 1.5 wt% polyaniline reached 960 hours, which was about six times higher than coating without polyaniline.

Tinuvin 292 is a liquid hindered amine light stabilizer that is a pure mixture of Bis (1, 2, 2, 6, 6-pentamethyl-4-piperidyl) sebacate and Methyl 1, 2, 2, 6, 6-pentamethyl-4-piperidyl sebacate. Tinuvin 292 has been used in coatings materials to extend lifetime and protect them from UV rays (Selli, Duman, & Yagyemez, 2021; Shenoy & Marathe, 2007).

As mentioned before, many works have been done on chlorinated rubber paint for enhancing its properties but hardly any papers published on improving degradation of this varnish. In this article chlorinated rubber-based varnish coating was investigated on the effect of Tinuvin 292 to its degradation under UV-thermo-humidity condition. Changing in coating's surfaces, physical properties, gloss and resistance in thermal oxidation of coatings were also investigated.

2. Materials and Methods

2.1 Chemicals

Binders: (1) Chlorinated rubber resin, Pergut 20 (Germany) with its specifications as Viscosity at 23°C, 20% in xylene 16-24 mPa.s; Appearance: White or pale-yellow loose and soft powders; Chlorine content (Cl) > 64; Ash content □ 0.3%; Water content □ 0.5%. (2) Acrylic resin, Degalan 709 (Germany) with its specifications as Solid content: 40%; Flash point: 23°C; Glass transition temperature of 49°C.

Solvents: Xylene, acetone, butyl acetate: Industrial products (China).

Anti-UV additive: Tinuvin 292 was a product of Kremer Pigmente GmbH & Co. KG (Germany).

2.2 Vanish preparation

Raw materials were prepared as in Table 1. Chlorinated rubber resin and acrylic resin were dissolved in xylene, then acetone, butyl acetate was added. Varnish mixture was stirred well in about 10 minutes at the speed of 100 rounds per minute. Filtering - canning: a 100 hole/mm^2 mesh was used to remove impurities in the varnish, then switch to canning.

Table 1. Composition of varnish.

No.	Components	Content (wt%)
1	Chlorinated rubber resin	40
2	Acrylic resin	5
3	Xylene	30
4	Acetone	12-14
5	Butyl acetate	10.5
6	Tinuvin 292	0-2.5

2.3 Sample preparation

Physical properties measurement

Samples were prepared on steel panels (in accordance with ISO 1514:2016). Varnish coatings were painted on the 15x 10x 0.2 cm cleaned steel panels by a sprayer with pressure of 4 kg/cm^2. The steel panels were abraded with 400-grade abrasive papers and cleaned with distilled water and ethanol and then dried before covering.

These coatings were prepared and kept for 7 days at temperature of (25±2) °C and humidity of (50±5) % before testing. A minitest 600 Erichsen digital meter was used to measure the dried coating thickness.

2.4 Analysis methods

UV-thermo-humidity complex stability was tested according to ASTM D4587-11 under the UV light of UVB-313 fluorescent lamps in chamber Atlas UVCON UC-327-2. The aging cycle included 8 hours of UV light at 60°C and 4 hours at 50°C in dark water condensation. Chemical changes of coatings were analyzed by Fourier-transform infrared spectroscopy (FT-IR), FT-IR spectrometer Nicolet 8700. Morphology of coating surfaces were determined by SEM images, which were recorded by FESEM Hitachi S4800 machine. Relative hardness, Impact resistance, Flexural strength, and adhesion of coating were determined in accordance with ISO 1522:2006, ISO 6272-1:2011, ISO 1519:2011 and ISO 2409:2013, respectively. Gloss of coating was determined in accordance with ISO 2813:2014 at an angle of 60 degrees.

Thermal oxidation resistance was carried out in air condition by Thermogravimetric analysis (TGA) on NETZSCH TG 209F1 LIBRA machine with temperature raising rate of 10°C/minute from room temperature to 600°C.

3. Results and Discussion

3.1 Effect of Tinuvin 292 content on

Suan Sunandha Science and Technology Journal
©2023 Faculty of Science and Technology, Suan Sunandha Rajabhat University

properties tested coating under UV-thermo-humidity complex condition

Effect of Tinuvin 292 content on physical properties and gloss of aged coatings:

Samples with thickness of 30-40 µm were formulated with Tinuvin 292 contents of 0; 1.0; 2.0; 2.5 and 3.0 named as S0, S1, S2, S3 and S4, respectively were tested with 100 cycles UV-thermo-humidity complex. Results were shown in Table 2 and Table 3.

Table 2. Gloss and physical properties of initial coating.

Samples	Gloss at 60°	Physical properties of coating			
		Adhesion (Points)	Flexural strength (mm)	Impact resistance (kg.cm)	Relative hardness
S0	81	1	2	200	0.59
S1	81	1	2	200	0.59
S2	81	1	2	200	0.59
S3	80	1	2	200	0.59
S4	80	1	2	200	0.59

Table 3. Gloss and physical properties of aged coating.

Samples	Gloss at 60°	Physical properties of coating			
		Adhesion (Points)	Flexural strength (mm)	Impact resistance (kg.cm)	Relative hardness
S0	43	5	6	80	0.71
S1	49	4	5	140	0.68
S2	61	2	3	180	0.64
S3	76	1	2	200	0.60
S4	77	1	2	200	0.60

Table 2 showed that physical properties and gloss of coating were not affected by investigated Tivunin 292 contents. Table 3 showed that after 100 cycles of UV-thermo-humidity complex testing, content of Tivunin 292 increased, adhesion, flexural strength, impact resistance, gloss loss of coatings reduced or changed less. After testing, impact resistance of S0 (sample without Tinuvin 292) decreased sharply, from 200 kg.cm to 80 kg.cm and relative hardness increased from 0.59 to 0.71 or flexural strength increased to 6 mm from 2 mm. It can conclude that coating became more brittle and lost its adhesion. Meanwhile, in S3 (sample with 2.5 wt% of Tinuvin 292) or S4 (sample with 3 wt% of Tinuvin 292) the adhesion, flexural strength, impact resistance and gloss loss of coating changed slightly. results also showed that in Tinuvin 292 content more than 2.5 wt%, the relative hardness did not increase. This can be explained that Tinuvin 292 had worked as an anti-UV additive which prevented polymer chains from breaking down and cutting, so polymer aging by UV rays was limited (Kotnarowska, 2018; Selli et al., 2021; Shenoy & Marathe, 2007). Hence, with Tinuvin 292, physical properties and gloss of coating would be improved in comparison to those of coating without Tinuvin 292 after 100 cycles of UV-thermo-humidity complex testing (Nikafshar et al., 2017; Rus, Kemp, & Clark, 2008). Results also showed that Tinuvin 292 with content of 2.5 wt% and above, did not change the properties of coating after 100 UV-thermo-humidity complex cycles testing. It showed that S3 was the most suitable sample and therefore was chosen for further study.

3.2 Fourier-transform infrared spectroscopy (FT-IR) analysis

Generally, degradation of polymers may not be seen with their appearances but by chemical changes of their functional groups. In this research, FT-IR spectroscopy was used to determine chemical changes of coatings' functional groups before and after aging with 100 cycles of UV-thermo-humidity complex. S0 and S3 were chosen for testing. Results were shown in Figure 1 and Table 4.

Suan Sunandha Science and Technology Journal
©2023 Faculty of Science and Technology, Suan Sunandha Rajabhat University

Table 4. Selected measured IR bands of coating.

No.	Typical spectrum	Wavenumbers (cm^{-1})
1	νCH, stretch	3430
		3390
		3362
		3360
2	$\nu_{as}(CH_2=)$, asymmetry in vinyl group	2958
		2956
3	$\nu_{as}(CH_2=)$, asymmetry in carbon chain	2929
		2928
		2859
4		1725
	ν (CO) of fat acid	1721
		1720
5	ν (C=C) in vinyl group	1600
		1599
		1597
		1596
6	νC–O stretch, vibrations	1125
		1120
		1119
7	δ(CH), oscillation deformation of CH in aromatic ring	743
		742

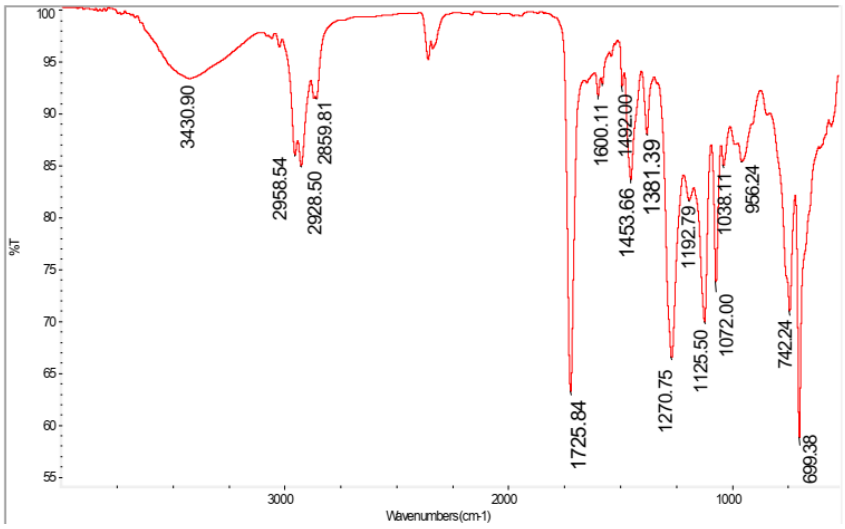

(a)

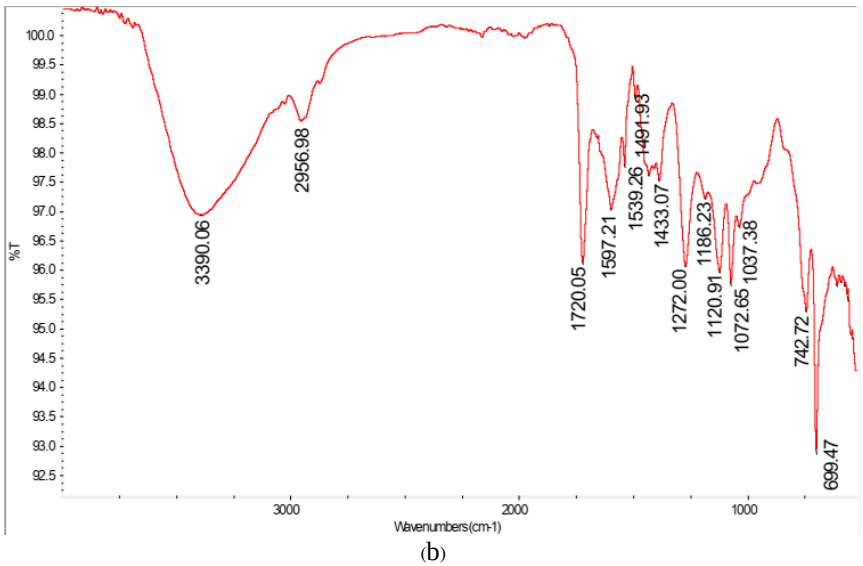

(b)

Suan Sunandha Science and Technology Journal
©2023 Faculty of Science and Technology, Suan Sunandha Rajabhat University

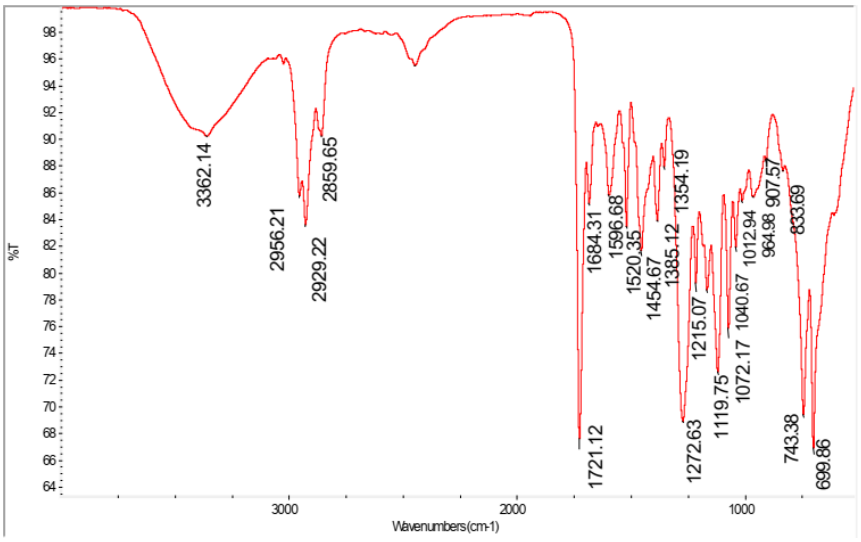

(c)

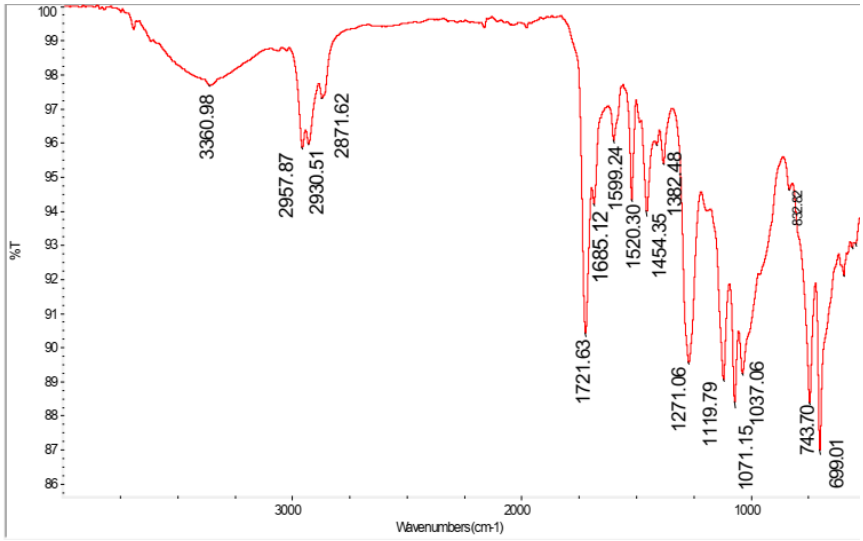

(d)

Figure 1. IR of initial S0 (a), aged S0 (b), initial S3 (c) and aged S3 (d).

Figures 1a and 1b showed (Moore, 2017) that peak intensity of CH_2 (2958) was strongly decreased, peaks 2928 and 2859 in Figure 1a could not be seen in Figure 1b. This might be explained that polymer molecular chains had been broken leading to the shorter molecular length. At that time, ester group intensities peaks (1725 of C=O or 1125 of C-O) fell off and ester bond was destructed to formulate new bonds of ketones as optical oxidation or C=O and C-O groups were stretched and shaked (Nikafshar et al., 2017). As shown in Figures 1c and 1d, there was little difference between initial and aged samples' intensities. These figures showed that intensities of CH_2 (2956, 2929, 2859) or ester groups (1721 of C=O and 1119 of C-O) of Tinuvin 292 aged coating was also stretched but vibrations or intensities of these peaks decreased insignificantly in comparison to the initial coating. The changes in intensities of ester groups or methylene after UV-thermo-humidity complex cycles testing was the same with reported by Thanh (2022a) or for 168 h for exposure to fluorescent UV radiation, heat, and water simulating weathering effects by Kızılkonca and Erim (2019).

Besides that, degradation of polymers under UV rays condition may occur due to chain cutting or disproportionate macroradicals and bivalent bonds terminated (Kotnarowska, 2018; Nikafshar et al., 2017; Rus et al., 2008). Coating with Tinuvin 292 in the (S3) condition had very little difference with initial and aged samples, macroradicals occurred to the Tinuvin 292 conjugated devalent bonds. Tinuvin

Suan Sunandha Science and Technology Journal
©2023 Faculty of Science and Technology, Suan Sunandha Rajabhat University

292 played as an UV rays absorbent which led to reduce the varnish coating degradation (Kozak, 2015; Moore, 2017; Rus et al., 2008; Thanh, 2022b; Yu, Li, Zhong, & Xu, 2004).

3.3 Morphology varnish coatings' surface

To investigate the effects of UV-thermo-humidity complex on coatings' surface, S0 and S3 were carried out with 100 UV-thermo-humidity complex cycles. Results were shown in Figure 2.

Figure 2 showed that after testing 100 UV-thermo-humidity complex cycles, the surface of the S3 sample was almost unchanged, there were no cracks, blisters or peeling on it. Meanwhile, in comparison with the initial coating surface, the aged surface of S0 was rougher and pinholes were observed on the sample surface. It can be explained that the oxidation process occurred and the surface of the sample destroyed by UV rays to generate micro-cavities and micro-holes on it (Queant, Blanchet, Landry, & Schorr, 2018; Yu et al., 2004). The pinholes also happened on the coating's surface of acrylic without TiO_2, ZnO under 800-hour aging in a UV/condensation weathering chamber (Nguyen et al., 2017). Those results showed that 2.5 wt% of Tinuvin 292 could protect chlorinated rubber varnish coating for UV-thermo-humidity complex 100 cycles.

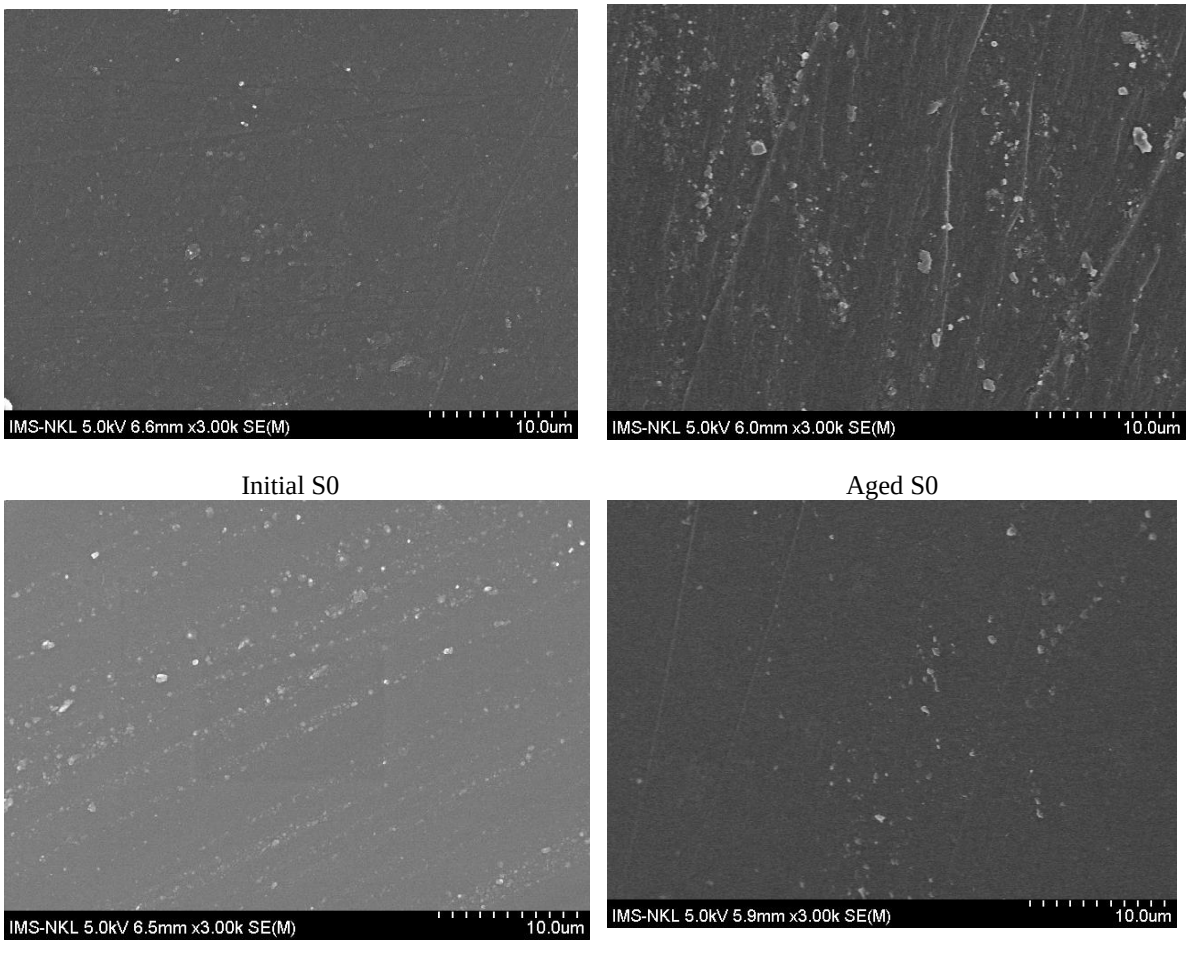

Initial S0 Aged S0

Initial S3 Aged S3

Figure 2. SEM of initial and aged coatings' surfaces.

3.4 Thermal oxidation stability of varnish coating with and without Tinuvin 292

Thermogravimetric analysis (TGA) was used to study effects of Tinuvin 292 on coatings' thermal oxidation stability. S0 and S3 of before and after testing were conducted on TGA. Results were shown in Figure 3 and Table 5.

Table 5 and Figure 3 showed the different curve slopes of different samples. Weight loss of

Suan Sunandha Science and Technology Journal
©2023 Faculty of Science and Technology, Suan Sunandha Rajabhat University

samples was also different at different temperatures. Results showed that Tinuvin 292 had significantly improved thermostability of coating, too. TGA curve slope of aged S0 was the highest (Kotnarowska, 2018; Queant et al., 2018; Talbert, 2007; Thanh, 2020). It might be explained that under 200ºC, decomposition mainly took place to low molecular matters or remaining solvents in coatings. at this period the decomposition volume was of 2-4% At this temperature, decomposition volume was a bout 2-6% of epoxy cured with toluene diisocyanate (Thanh, 2022b). Up to 400ºC, the decomposition happened with low molecular substances or residual functional groups in polymer branches. The decomposition of initial S0 and initial S3 was the same. Meanwhile, aged S0 was decomposed higher than aged S3 and strongest of all. This can be explained that after aging, polymer chains S0 had been broken sharply and S3 had lower decomposition than S0 because Tinuvin 292 had worked as an anti-oxidation agent to protect polymer chains from breaking (Hu, Li, Gao, & Zhao, 2009; Moore, 2017; Yu et al., 2004). Besides, polymer chemical bonds had been protected from breaking with Tinuvin 292 and reducing incisions in polymer chains which would prevent oxygen permeation into coating. Thus thermal oxidation stability of coating had been enhanced. at 500ºC and above organic components had been combusted or broken down, meanwhile, non-degradable parts of samples were equivalent, so the decomposition of samples was not much different at that temperature (Queant et al., 2018; Thanh, 2022b; Yousif & Haddad, 2013).

Table 5. Effect of Tinuvin 292 on thermal oxidation stability of coatings.

Samples	Weight loss (%)		
	300ºC	400ºC	500ºC
Initial S0	53.24	65.17	96.33
Aged S0	59.68	69.85	98.4
Initial S3	49.85	66.73	95.10
Aged S3	54.15	67.95	97.99

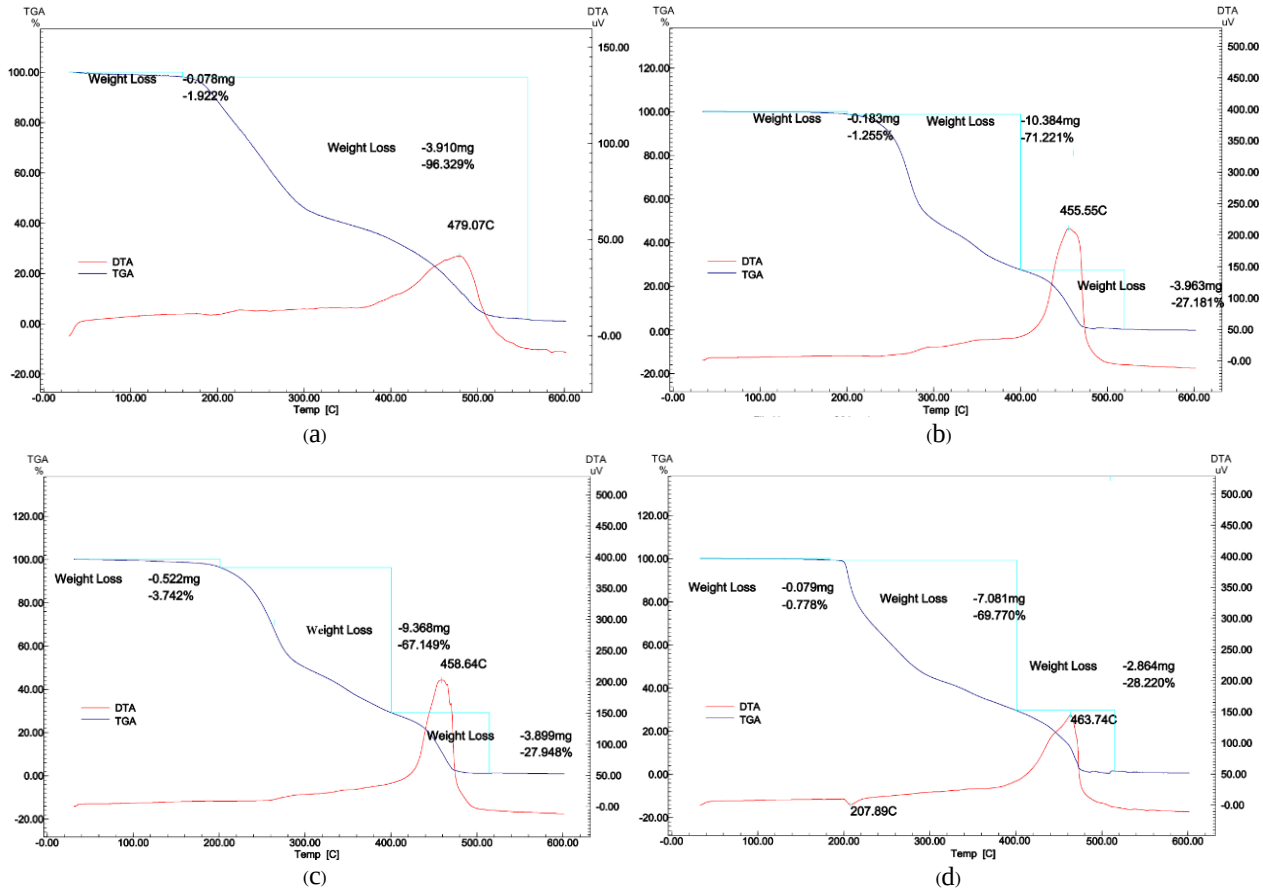

Suan Sunandha Science and Technology Journal
©2023 Faculty of Science and Technology, Suan Sunandha Rajabhat University

Figure 3. TGA of initial S0 (a), aged S0 (b), initial S3 (c) and aged S3 (d).

4. Conclusions

In the range of 3 wt%, Tinuvin 292 content caused increasing the adhesion, flexural strength, impact resistance, relative hardness, gloss loss of chlorinated rubber varnish coating that would protect better under 100 UV-thermo-humidity complex cycles testing condition. The suitable content of Tinuvin 292 for chlorinated rubber coating is 2.5 wt%. Chlorinated rubber varnish coating with 2.5 wt% of Tinuvin 292 could suffer from 100 UV-thermo-humidity complex cycles without cracks, blisters or surface changing. Tinuvin 292 has improved thermal oxidation resistance of varnish coating. at 300ºC, decomposition of aged sample with and without Tinuvin 292 were 54.15 and 59.68, respectively.

Conflict of Interest

The authors declare that there is no conflict of interest regarding the publication of this article.

References

Ahmed, N. M., Emira, H. S., & Tawfik, H. M. (2013). Anticorrosive efficiency of ion-exchanged bentonites in chlorinated rubber paints. *Pigment & Resin Technology*, *42*(3), 186-194. doi:10.1108/03699421311317352

Bano, H., Khan, M. I., & Kazmi, S. A. (2013). SEM-EDX and FTIR studies of chlorinated rubber coating. *Journal of the Chemical Society of Pakistan*, *35*(1), 95-108.

Cogulet, A., Blanchet, P., & Landry, V. (2019). Evaluation of the impacts of four weathering methods on two acrylic paints: Showcasing distinctions and particularities. *Coatings*, *9*(2), 121. doi:10.3390/coatings9020121

Crescenzo, M. M. D., Zendri, E., Pons, M. S., Lospez, L. F., & Marco, D. J. Y. (2014). The use of waterborne paints in contemporary murals: Comparing the stability of vinyl, acrylic and styrene-acrylic formulations to outdoor weathering conditions. *Polymer Degradation and Stability*, *107*, 285-293. doi:10.1016/j.polymdegradstab.2013.12.034

Das, S., Pandey, P., Mohanty, S., & Nayak, S. K. (2017). Investigation into the influence of UV aging on green polyurethane/nanosilica composite coatings based on transesterified castor oil and palm oil isocyanate. *Journal of Inorganic and Organometallic Polymers and Materials*, *27*(3), 641-657. doi:10.1007/s10904-017-0506-z

Hu, J., Li, X., Gao, J., & Zhao, Q. (2009). Ageing behavior of acrylic polyurethane varnish coating in artificial weathering environments. *Progress in Organic Coatings*, *65*(4), 504-509. doi:10.1016/j.porgcoat.2009.05.002

Ismail, I., & Harun, M. K. (2016). Cathodic disbonding of industrial chlorinated rubber-based primer used in rubber/metal composites: An electrochemical impedance spectroscopy analysis. *Rubber Chemistry and Technology*, *89*(4), 712-723. doi:10.5254/rct.16.83793

Kahrizsangi, A. G., Neshati, J., Shariatpanahi, H., & Akbarinezhad, E. (2015). Improving the UV degradation resistance of epoxy coatings using modified carbon black nanoparticles. *Progress in Organic Coatings*, *85*, 199-207. doi:10.1016/j.porgcoat.2015.04.011

Kızılkonca, E., & Erim, F. B. (2019). Development of anti-aging and anticorrosive nanoceria dispersed alkyd coating for decorative and industrial purposes. *Coatings*, *9*(10), 610. doi:10.3390/coatings9100610

Kotnarowska, D. (2018). Influence of ageing with UV radiation on physicochemical properties of acrylic-polyurethane coatings. *Journal of Surface Engineered Materials and Advanced Technology*, *8(4)*, 95-109.

Kozak, A. (2015). Multi-criteria assessment of an acrylic coating exposed to natural and artificial weathering. *Procedia Engineering*, *108*, 664-672. doi:10.1016/j.proeng.2015.06.197

Lang, Y., Sun, Y., Yu, M., Ji, Y., Wang, L., & Zhang, Z. (2019). Differential colonization dynamics of marine biofilm-forming eukaryotic microbes on different protective coating materials. *Polymers*, *11*(1), 161. doi:10.3390/polym11010161

Liu, X., Xiong, J., Lv, Y., & Zuo, Y. (2009). Study on corrosion electrochemical behavior of several different coating systems by EIS. *Progress in Organic Coatings*, *64*(4), 497-503. doi:10.1016/j.porgcoat.2008.08.012

Moore, E. (2017). *Fourier transform infrared spectroscopy (FTIR): Methods, analysis, and*

Suan Sunandha Science and Technology Journal
©2023 Faculty of Science and Technology, Suan Sunandha Rajabhat University

research insights. New York: Nova Science Publishers.

Morsi, S. M. M., Emira, H. S., El-Sawy, S. M., Mohsen, R. M., & Khorshed, L. A. (2019). Synthesis and characterization of kaolinite/polyaniline nanocomposites and investigating their anticorrosive performance in chlorinated rubber/alkyd coatings. *Polymer Composites*, *40*(7), 2777-2789. doi:10.1002/pc.25086

Nguyen, T. V., Dao, P. H., Duong, K. L., Duong, Q. H., Vu, Q. T., Nguyen, A. H., ... Le, T. L. (2017). Effect of R-TiO_2 and ZnO nanoparticles on the UV-shielding efficiency of water-borne acrylic coating. *Progress in Organic Coatings*, *110*, 114-121. doi:10.1016/j.porgcoat.2017.02.017

Nikafshar, S., Zabihi, O., Ahmadi, M., Mirmohseni, A., Taseidifar, M., & Naebe, M. (2017). The effects of UV light on the chemical and mechanical properties of a transparent epoxy-diamine system in the presence of an organic UV absorber. *Materials*, *10*(2), 180. doi:10.3390/ma10020180

Olabisi, O., & Adewale, K. (2015). *Handbook of thermoplastics* (2nd ed.). Boca Raton, FL: CRC Press.

Pintus, V., Wei, S., & Schreiner, M. (2016). Accelerated UV ageing studies of acrylic, alkyd, and polyvinyl acetate paints: Influence of inorganic pigments. *Microchemical Journal*, *124*, 949-961. doi:10.1016/j.microc.2015.07.009

Queant, C., Blanchet, P., Landry, V., & Schorr, D. (2018). Comparison of two encapsulation systems of UV stabilizers on the UV protection efficiency of wood clear coats. *Journal of Polymer Engineering*, *39*(1), 94-103. doi:10.1515/polyeng-2018-0026

Rus, A. Z. M., Kemp, T. J., & Clark, A. J. (2008). Degradation studies of polyurethanes based on vegetable oils. Part 1. Photodegradation, *Progress in Reaction Kinetics and Mechanism*, *33*(4), 363-391. doi:10.3184/146867808X377140

Sakhri, A., Perrin, F. X., Aragon, E., Lamouric, S., & Benaboura, A. (2010). Chlorinated rubber paints for corrosion prevention of mild steel: A comparison between zinc phosphate and polyaniline pigments. *Corrosion Science*, *52*(3), 901-909. doi:10.1016/j.corsci.2009.11.010

Selli, N. T., Duman, F., & Yagyemez, T. (2021). Evaluation of antislip properties of ceramic-polymer composite coating on ceramic tiles. *The International Journal of Materials and Engineering Technology*, *4*(1), 79-90.

Shenoy, M. A., & Marathe, Y. D. (2007). Studies on synergistic effect of UV absorbers and hindered amine light stabilisers. *Pigment & Resin Technology*, *36*(2), 83-89. doi:10.1108/03699420710733510

Talbert, R. (2007). *Paint technology handbook*. Boca Raton, FL: CRC Press.

Thanh, N. T. (2020). The effects of TDI on selected properties of ester epoxy alkyd varnish. *VNU Journal of Science: Natural Sciences and Technology*, *36*(4), 1-8. doi:10.25073/2588-1140/vnunst.4933

Thanh, N. T. (2022a). Effect of graphene oxide on UV-thermo-humidity degradation of environmentally friendly alkyd composite coating. *Malaysian Journal on Composites Science and Manufacturing*, *9*(1), 1-10. doi:10.37934/mjcsm.9.1.110

Thanh, N. T. (2022b). Study on effects of isocyanate on some properties of epoxy varnish. V*ietnam Journal of Chemistry*, *60*(1), 15-20. doi:10.1002/vjch.202100030

Yousif, E., & Haddad, R. (2013). Photodegradation and photostabilization of polymers, especially polystyrene: Review. *SpringerPlus*, *2*, 398. doi:10.1186/2193-1801-2-398

Yu, H., Li, S., Zhong, J., & Xu, K. (2004). Studies of thermooxidative degradation process of chlorinated natural rubber from latex. *Thermochimica Acta*, *410*(1-2), 119-124. doi:10.1016/S0040-6031(03)00402-7

Available online at https://li02.tci-thaijo.org/index.php/ssstj

SSSTJ

Suan Sunandha Science and Technology Journal
©2023 Faculty of Science and Technology, Suan Sunandha Rajabhat University

Impact of Exposure Status on the Diversity and Successional Pattern of Cadaverous Arthropods on Slaughtered Juvenile Pig (*Sus scrofa* Linn.) Carcasses in Wukari, Nigeria

Chukwu Alexander Timothy, Emmanuel Okrikata*, Jummai Amos Tidi

Department of Biological Sciences, Federal University Wukari, P.M.B. 1020, Katsina-Ala Road, Wukari, Taraba State, Nigeria
***Corresponding author e-mail:** eokrikata@gmail.com

Received: *12 October 2022* / **Revised:** *30 January 2023* / **Accepted:** *30 March 2023*

Abstract

Knowledge of successional colonization of cadaver is important in medico-legal studies especially with regards to postmortem interval (PMI) estimation. Paucity of data especially as it relates to juveniles has limited the appropriate application of this knowledge for the benefit of man. To bridge this knowledge gap, juvenile human cadaver was modeled using 2 slaughtered juvenile pigs – *Sus scrofa* Linn. (≈ 10 kg mean weight) at the study site. One pig was exposed to sunlight while the other shaded under a tree. Both pigs were protected from scavengers and allowed through the decay stages and sampling for adult arthropods continued till the dry-remain stage of decomposition. Data collected were used to compute frequency of occurrence and relative abundance. Paleontological Statistical Tool ($Past_3$) was used to compute diversity indices. Of the 2032 arthropods of 20 species, across 17 families retrieved, the exposed carcass attracted 44.1% comprising 16 species within 15 families while the shaded carcass attracted 14 species within 12 families. Over 50% species similarity on the contrasting carcasses was observed. Calliphoridae, Muscidae, Dermestidae, Histeridae and Formicidae made-up the dominant families sampled. While *Musca domestica* L. (Muscidae) and *Anochetus* sp. (Formicidae) were exclusively dominant for the shaded carcass, *Crematogaster* sp. (Formicidae) was exclusively dominant for the exposed carcass. Both carcasses completed decomposition in 14 days but exhibited a shorter advanced-decay stage for the shaded carcass and shorter dry remain stage for the exposed carcass. We thus conclude that, there was little distinction in the diversity and succession pattern of the arthropods colonizing both carcasses (shaded and exposed).

Keywords: Cadaverous arthropods, Decomposition, Juvenile insects, Succession

1. Introduction

Arthropods play inestimable roles in nature. One of which is the decomposition of carcasses which aids natural recycling of organic matter (Alboshabaa & Al-Musawy, 2016; Timothy, Okrikata, & Tidi, 2022). Decomposition of carrion is reported to occur in five distinct stages which are fresh, bloated, early decay, advanced decay and the dry remain stages, each of which attracts a specific array of arthropods (Timothy et al., 2022). The knowledge of this successional pattern by which arthropods, insects in particular, invade a carrion is referred to as Forensic Entomology. It is instrumental in determining the minimum post mortem interval (PMI_{min}) of a cadaver, hence strategic in medico-legal investigations (Ojianwuna, Odibo, Akpan, & Egwaoje, 2019).

With accessibility and favorable weather conditions, insects are first to arrive on dead bodies (Byrd & Tomberlin, 2019). Larval development of dipterans on a carrion can be used to estimate the PMI_{min} of a carrion with great accuracy within the first 72 hours or more, while the successional pattern of invading arthropod species is engaged, particularly, at the advanced stages of decomposition (Griffiths, Krosch, & Wright, 2020; Maisonhaute & Forbes, 2021; Timothy et al., 2022). Byrd and Tomberlin (2019) showed that, successional studies of invading cadaverous entomofauna is important in providing valuable information with regards habitat of the corpse, surrounding circumstances of death among others, which can aid police investigation and justice services.

Due to the anatomical, physiological and decompositional similarities of pigs with humans, pigs are the best used animal models for studying the successional pattern of necrophagous arthropods associated with human cadavers (Keshavarzi, Zaimy, Yusuf, Shahriarinamadi, & Parkhideh, 2019; Matuszewski et al., 2020). Although factors such as geographic location, temperature, humidity, exposure to sunlight, size of

Suan Sunandha Science and Technology Journal
©2023 Faculty of Science and Technology, Suan Sunandha Rajabhat University

carrion as well as manner of death among others have been identified to influence species diversity and richness on a carrion (Sonker, Rawat, & Singh, 2018), "the size" factor has largely been undermined in Nigeria and most developing countries as hardly has any forensic entomofaunal study modeled for juvenile human cadaver been conducted; despite the menace of juvenile homicide experienced in Africa, and Nigeria in particular. This investigation is thus designed to fill this knowledge gap by assessing the impact of exposure status on the abundance, diversity and successional pattern cadaverous arthropods attracted to slaughtered juvenile pig carrion in the study area.

2. Materials and Methods

2.1 Study site

The study was carried out in the Research Garden of Biological Sciences Department, Federal University Wukari, Taraba State, Nigeria within the months of March and April, 2022. Wukari Local Government Area is a semi-urban environment in the Southern guinea savanna zone which has a land area of 4,308 square kilometers, an altitude of 187m above sea level, an average annual rainfall of 1205 mm, average temperature of 26.8ºC and lies between latitude 7.89N and longitude 9.77E (Timothy & Emmanuel, 2020).

2.2 Specimen acquisition and preparation

Two male pig (*Sus scrofa* Linn.) specimens (average weight: 10 kg; approximate age: 4 months) were bought from a piggery in Wukari town and were killed by slaughtering. The pigs were kept at 25 m distance apart with one specimen placed under a tree shade while the other was left exposed to sunlight throughout the research period. Each specimen was placed on a metal mesh and covered with a metal cage which only permitted access by arthropods (Figure 1).

2.3 Animal research ethics

At the time of the study, there was no ethical committee in relation to animal use in research in the University. However, all the principles of 3Rs (Replacement, Reduction and Refinement) of the Guidance on the Operation of the Animals (Scientific Procedures) Act 1986 were strictly followed.

Figure 1. Juvenile pig carcasses: **A.** Fresh exposed carcass, **B.** Fresh shaded carcass, **C.** Shaded advanced decay stage of carcass.

2.4 Sampling protocol

The day the specimens were slaughtered was recorded as Day 0 while sampling commenced from Day 1 to the dry remain stage of the carrion (between 1400 hrs - 1800 hrs daily) following the procedure described by Grassberger and Frank (2004). Only adult arthropods were sampled. Aerial insects were sampled using two standard sweeps of the sweep net while ground insects were sampled by manual searching and picking (Griffiths et al., 2020; Tembe & Mukaratirwa, 2021; Timothy et al., 2022). A pitfall trap which was ¾ filled with soapy water was also kept within 1m distance around the carrion for sampling mostly nocturnal and other ground arthropods and was serviced daily. Care was taken to sample arthropods using the same sampling intensity, to ensure that sampling intensity does not become a confounding factor. Daily information collected from visual observation and photographs from the carrion and its surroundings include: odour and intensity, physical changes of the carrion and the presence of arthropods during each stage of the carrion (Tembe & Mukaratirwa, 2021). All sampled insects were

Suan Sunandha Science and Technology Journal
©2023 Faculty of Science and Technology, Suan Sunandha Rajabhat University

collected in collecting bottles containing 70% alcohol and were transported to the Biological Sciences Laboratory of Federal University Wukari for morphological identification and sorting while sample specimens were sent to the insect museum of Institute of Agricultural Research (IAR) in Ahmadu Bello University Zaria, Nigeria, for confirmatory identification.

2.5 Data analysis

Pooled data of species abundance collected using the different sampling techniques was used to compute frequency of occurrence (FO) as well as the relative abundance (RA) vis-à-vis exposure status and decomposition stages. Taxa with FO ≥ 25% and RA ≥ 1% were regarded as dominant species and were categorized into feeding guilds while those with FO < 25% and/or RA < 1% were regarded as rare species as described by Emmanuel, Emmanuel Oludele and Monday Unwabunne (2019). Diversity indices such as Shannon-Weiner diversity indices (H), Margalef's species richness (R) and Buzas and Gibson's Evenness (E) for the different stages of decomposition were computed using the Paleantological Statistical Tool – $Past_3$ (Hammer, Harper, & Ryan, 2001). Similarity of arthropods in the contrasting environment was computed using Jaccard's similarity model:

$$Jaccard\ index = X \cap Y / X \cup Y \times 100$$

Where:
X∩Y = Number in both sets,
X∪Y = Number in either set.

3. Results

3.1 Stages of decomposition and associated arthropods

Although both carcasses completed the decomposition process in 14 days as seen in Table 1, there was a longer advanced decay stage experienced in carcass exposed to sunlight (4 - 9 days) in contrast with its shaded counterpart (4 - 6 days). However, the shaded carcass took longer (7 days) to complete the dry-remain stage (from 7^{th} - 14^{th} day) as compared to the exposed carcass whose dry-remain stage lasted for 4 days (from 10^{th} - 14^{th} day). Each stage of decomposition attracted different species composition vis-à-vis exposure status, even though some dipterans, coleopterans and hymenopterans were sampled all through the stages of decomposition as observed in Table 1 where; *Chrysomya chloropyga* Wied. (Diptera: Calliphoridae) and *Anochetus* sp. (Hymenoptera: Formicidae) colonized the shaded carcass from the fresh to dry remain stage while for the exposed carcass; *Hister monitor* Lewis (Coleoptera: Histeridae), *Dermestes maculatus* Deg. (Coleoptera: Dermestidae) and *C. chloropyga* (Diptera: Calliphoridae) occurred all through the decomposition stages. Apart from Histeridae, Dermestidae and Tenebrionidae which occurred at either the fresh or bloated stage of either or both carcasses, other coleopteran families such as Curculionidae, Staphylinidae, Cleridae and Scarabaeidae occurred either at late advanced-decay stage and/or dry-remain stage of either or both carcasses.

For Diptera; Calliphoridae and Muscidae had up to 80% colonization of the decomposition stages for both carcasses while other families such as Syrphidae and Asilidae were sampled either at the advanced-decay stage or dry-remain stages of either or both carcasses as seen in Table 1. *Stenocoris southwoodi* Ahmad (Hemiptera - Alydidae) was sampled at the advanced-decay and dry-remain stages of the exposed carcass while the hymenoptera (constituted by the formicid family) occurred at different stages of decomposition of both carcasses. In addition, Termitidae (Isoptera) and Gryllidae (Orthoptera) were sampled at the dry remaining stages of the exposed and shaded carcass, respectively (Table 1).

3.2 Abundance and frequency of occurrence of arthropods associated with slaughtered juvenile pig carcasses

A total of 2,032 arthropods consisting of 20 identified arthropod species across 17 Families from 7 Orders were sampled from both carcasses, with the exposed carcasses attracting 44.1% (896) of the total arthropods retrieved. As shown in Table 2, 16 identified insect species across 15 families from 6 orders were sampled from the exposed carcass while 14 species across 12 families from 5 orders were sampled from the shaded carcass. *Crematogaster* sp. (Formicidae – Hymenoptera) had the highest relative abundance (RA) (45.76%) for the exposed carcass while *Ommatius* sp. (Asilidae – Diptera), *Anomala resplendens* Fahr. (Scarabaeidae – Coleoptera), *Korynetes analis* Klug. (Cleridae – Coleoptera) and *Philonthus* sp. (Staphylinidae – Coleoptera) had the least RA (0.11%). For the shaded carcass, *Anochetus* sp. (Formicidae – Hymenoptera) had the highest relative abundance (47.45%) while *Endustomus senegalensis* Cast. (Tenebrionidae – Coleoptera) had the RA (0.09%).

Result for frequency of occurrence (FO) of species across the decomposition stages as also shown in Table 2 indicates that although *Crematogaster* sp. had the highest RA value, *D. maculatus* (Dermestidae – Coleoptera) with RA value of 7.81% had the highest FO value (100%) for the exposed carcass, with *Ommatius* sp.,

Suan Sunandha Science and Technology Journal
©2023 Faculty of Science and Technology, Suan Sunandha Rajabhat University

A. resplendens, *K. analis* and *Philonthus* sp. having the least FO values (7.14%). For the shaded carcass, *Anochetus* sp. had 100% FO value while *E. senegalensis* had the least value (7.14%).

Table 1. Arthropodal presence on slaughtered juvenile pig carcasses at different stages of decomposition.

Order	Family	Genus/Species	Shaded carcass					Exposed carcass				
			FSH (0-1d)	BLT (2d)	Ac. Decay (3d)	Ad. Decay (4-6d)	Dry (7-14d)	FSH (0-1d)	BLT (2d)	Ac. Decay (3d)	Ad. Decay (4-9d)	Dry (10-14d)
Arachnida	Araenae	***	-	-	X	X	-	-	-	-	X	-
Coleoptera	Histeridae	*Hister monitor* Lewis		X	X	X	X	X	X	X	X	X
	Dermestidae	*Dermestes maculatus* Deg.	-	X	X	X	X	X	X	X	X	X
	Tenebrionidae	*Zophosis* sp.	-	X	X	X	X	-	X	X	X	X
	Cleridae	*Korynetes analis* Klug	-	-	-	-	-	-	-	-	X	-
	Staphylinidae	*Philonthus* sp.	-	-	-	-	-	-	-	-	X	-
	Curculionidae	*Sclerocardius* sp.	-	-	-	-	X	-	-	-	X	X
	Scarabaeidae	*Anomala resplendens* Fahr.	-	-	-	-	X	-	-	-	X	-
	Tenebrionidae	*Endustomus senegalensis* Cast.	-	-	-	-	X	-	-	-	-	-
Diptera	Calliphoridae	*Chrysomya chloropyga* Wied.	X	X	X	X	X	X	X	X	X	X
	Syrphidae	*Mesembrius* sp.	-	-	-	-	-	-	-	-	X	-
	Muscidae	*Musca domestica* L.	-	X	X	X	X	X	X	X	X	-
	Asilidae	*Ommatius* sp.	-	-	-	-	X	-	-	-	X	-
Hemiptera	Alydidae	*Stenocoris southwoodi* Ahmad	-	-	-	-	-	-	-	-	X	X
Hymenoptera	Formicidae	*Camponotus perrisii* For.	-	X	-	-	X	X	X	-	-	-
	Formicidae	*Camponotus maculatus* Fab.	-	X	X	X	-	-	-	-	-	-
	Formicidae	*Crematogaster* sp.	-	-	-	-	-	X	X	X	X	X
	Formicidae	*Anochetus* sp.	X	X	X	X	X	-	-	-	-	-
	Formicidae	*Pheidole* sp.	-	-	X	X	X	-	-	-	X	X
Isoptera	Termitidae	*Macroterma* sp.	-	-	-	-	-	-	-	-	-	X
Orthoptera	Gryllidae	*Gymnogryllus lucens* Walk.	-	-	-	-	X	-	-	-	-	-

FSH = Fresh stage, BLT = Bloated stage, Ac. Decay = Active decay stage, Ad. Decay = Advanced decay stage, d = day/days, (-) = Absent, (X) = Present, (***) = unidentified Araneaen species and are herein treated as a single population/taxon.

Table 2. Abundance and frequency of occurrence of arthropods associated with slaughtered juvenile pig carcass.

Order	Family	Genus/Species	Shaded carcass			Exposed Carcass		
			Abundance	RA (%)	FO (%)	Abundance	RA (%)	FO (%)
Arachnida	Araenae	***	3	0.26	21.43	1	0.11	7.14
Coleoptera	Histeridae	*Hister monitor* Lewis	119	10.47	78.57	109	12.17	71.43
	Dermestidae	*Dermestes maculatus* Deg.	59	5.19	92.86	70	7.81	100
	Tenebrionidae	*Zophosis* sp.	19	1.67	57.14	91	10.16	85.71
	Cleridae	*Korynetes analis* Klug	-	-	-	1	0.11	7.14
	Staphylinidae	*Philonthus* sp.	-	-	-	1	0.11	7.14
	Curculionidae	*Sclerocardius* sp.	10	0.88	35.71	5	0.56	28.57
	Scarabaeidae	*Anomala resplendens* Fahr.	2	0.18	14.29	1	0.11	7.14
	Tenebrionidae	*Endustomus senegalensis* Cast.	1	0.09	7.14	-	-	-
Diptera	Calliphoridae	*Chrysomya chloropyga* Wied.	236	20.77	78.57	145	16.20	64.29
	Syrphidae	*Mesembrius* sp.	-	-	-	3	0.33	14.29
	Muscidae	*Musca domestica* L.	19	1.67	35.71	7	0.80	28.57
	Asilidae	*Ommatius* sp.	4	0.35	14.29	1	0.11	7.14
Hemiptera	Alydidae	*Stenocoris southwoodi* Ahmad	-	-	-	3	0.33	21.43

Suan Sunandha Science and Technology Journal
©2023 Faculty of Science and Technology, Suan Sunandha Rajabhat University

Hymenoptera	Formicidae	*Camponotus perrisii* For.	6	0.53	14.29	2	0.22	14.29
	Formicidae	*Camponotus maculatus* Fab.	17	1.50	28.57	-	-	-
	Formicidae	*Anochetus* sp.	539	47.45	100	-	-	-
	Formicidae	*Crematogaster* sp.	-	-	-	410	45.76	92.89
	Formicidae	*Pheidole* sp.	101	8.90	42.86	27	3.01	35.71
Isoptera	Termitidae	*Macroterma* sp.	-	-	-	19	2.12	7.14
Orthoptera	Gryllidae	*Gymnogryllus lucens* Walk.	1	0.09	7.14	-	-	-
TOTAL			**1136**	**100**		**896**	**100**	

RA = Relative abundance, FO = Frequency of Occurrence, (***) = unidentified Araenaen species and are herein treated as a single population/taxon.

Table 3. Abundance, diversity (H), evenness (E) and richness (R) of dominant cadaverous arthropod orders associated with slaughtered juvenile pig carcasses at different stages of decomposition.

	Shaded carcass			**Exposed carcass**		
Stages/Order	**Coleoptera**	**Diptera**	**Hymenoptera**	**Coleoptera**	**Diptera**	**Hymenoptera**
Fresh	0	11	15	5	16	1
Bloated	17	73	197	43	53	32
Active Decay	26	47	151	40	38	15
Advanced Decay	97	59	59	151	47	252
Dry Remain	70	69	241	39	2	139
Total	210	259	663	278	156	439
Shannon (H)	1.185	1.49	1.366	1.247	1.362	1.003
Evenness (E)	0.818	0.888	0.784	0.696	0.781	0.545
Richness (R)	0.561	0.72	0.616	0.711	0.792	0.657

Table 4. Jaccard's similarity index for all sampled and dominant species collected from slaughtered Juvenile pig carcasses exposed/shaded from sunlight.

Description	**All sampled species**	**Dominant species**
/Exposed ∩ Shaded/	11	5
/Exposed U Shaded/	21	9
Jaccard similarity (%)	52.4	55.6

/Exposed ∩ Shaded/ = similar species shared by both carcasses.

/Exposed U Shaded/ = total number of sampled species.

3.3 Abundance, diversity, evenness and richness of dominant insect orders associated with slaughtered juvenile pig carcasses exposed or shaded from sunlight

Three insect Orders; Coleoptera, Diptera and Hymenoptera constituted the dominant species sampled from both carcasses. The abundance for the respective orders of insects were 278, 156 and 439 on carcass exposed to sunlight while the corresponding values on shaded carcass were 210, 259 and 663 (Table 3). Results of diversity indices as shown in Table 3 shows that Dipterans sampled from both carcasses has the highest values of Shannon diversity (H = 1.362 and 1.49), evenness (E = 0.781 and 0.888) and Richness (R = 0.792 and 0.72) for the exposed and shaded carcasses, respectively. Overall, diversity of insects on shaded carcass were > those on exposed carcass. The evenness index generally followed the same trend. Species richness was however generally higher on exposed carcass (Table 3).

3.4 Species similarity

Jaccard's similarity index shows high similarity in arthropod species diversity retrieved from the shaded and exposed carcass as the similarity index were > 50% irrespective of species being considered (all species sampled or dominant species) (Table 4).

3.5 Feeding guild of dominant Insects colonizing slaughtered juvenile pig carcasses

Tables 5 and 6 show the dominant insect species colonizing the exposed and shaded carcasses and their feeding guilds, respectively. As shown in Table 5, the exposed carcass had 6 dominant insect species from 3 orders (Coleoptera - 3, Diptera - 1 and Hymenoptera - 2) colonizing the carcass. Two of the insects are necrophagous (*D. maculatus* and *C. chloropyga*), one primarily

Suan Sunandha Science and Technology Journal
©2023 Faculty of Science and Technology, Suan Sunandha Rajabhat University

predaceous (*Zophosis* sp.), another one (*Hister monitor*) both predaceous and saprophagous while the other two which are Hymenopterans were omnivorous in nature as they were found to be primarily predaceous and phytophagous.

Table 5. Feeding guild of dominant insects associated with slaughtered juvenile pig carcass exposed to sunlight.

Order	Family	Genus/Species	Feeding guild
Coleoptera	Histeridae	*Hister monitor*	Predaceous/Saprophagous
	Dermestidae	*D. maculatus*	Necrophagous
	Tenebrionidae	*Zophosis* sp.	Predacious
Diptera	Calliphoridae	*C. chloropyga*	Necrophagous
Hymenoptera	Formicidae	*Crematogaster* sp.	Predaceous/Phytophagous
	Formicidae	*Pheidole* sp.	Predaceous/Phytophagous

The shaded carcass had 8 dominant insects across 3 orders (Coleoptera - 3, Diptera - 2 and Hymenoptera - 3) colonizing it as shown in Table 6. Of the dominant species, two (*D. maculatus* and *C. chloropyga*) are necrophagous, one (*H. monitor*) is both predaceous and saprophagous, and another (*Musca domestica* L.) is saprophagous, coprophagous and necrophagous. The three hymenopteran species (*Anochetus* sp., *C. maculatus* and *Pheidole* sp.) are, however, primarily predaceous and phytophagous.

Table 6. Feeding guild of dominant insects associated with slaughtered juvenile pig carcass shaded from sunlight.

Order	Family	Genus/Species	Feeding guild
Coleoptera	Histeridae	*H. monitor*	Predaceous/Saprophagous
	Dermestidae	*D. maculatus*	Necrophagous
	Tenebrionidae	*Zophosis* sp.	Predacious
Diptera	Calliphoridae	*C. chloropyga*	Necrophagous
	Muscidae	*M. domestica*	Saprophagous/Coprophagous/Necrophagous
Hymenoptera	Formicidae	*C. maculatus*	Predaceous/Phytophagous
	Formicidae	*Anochetus* sp.	Predaceous/Phytophagous
	Formicidae	*Pheidole* sp.	Predaceous/Phytophagous

3.6 Physical characteristics of decomposition of exposed and shaded slaughtered juvenile pig carcasses.

Table 7 shows that the fresh, bloated and active-decay stages occurred within 3 days with each stage taking place in a successive day. The advanced-decay stage lasted the longest (6 days) while the dry remain stage lasted for 5 days before gradual disintegration of the dry skin into soil particles was observed. In contrast, that of the shaded carcass as shown in Table 8 indicates that the fresh, bloated and active-decay stages also lasted one day each while the advanced-decay and dry remain stages took 3 and 8 days respectively before a gradual disintegration of the dry skin into soil particles.

Table 7. Physical characteristics of slaughtered juvenile pig carcass exposed to sunlight at the decomposition stages.

Stages of decomposition	Period (days)	Sampling time	Physical changes	Odor presence and intensity	Dominant species
Fresh (day 0 - 1)	1	2.00 pm - 6.00 pm	Soft torsos and flexible limbs	None	*H. monitor and C. chloropyga*
Bloated (day 2)	1	2.00 pm - 6.00 pm	Inflation of abdomen and blue-green changing of body color	Present but not intense	*Hister monitor, D. maculatus, Zophosis* sp., *C. chloropyga and Crematogaster* sp.
Active decay (day 3)	1	2.00 pm - 6.00 pm	Bursting of the abdomen to expose intestinal tissues, deflation of the body, gradual peeling of the skin.	Present and intense	*Hister monitor, D. maculatus, Zophosis*sp., *C. chloropyga and Crematogaster* sp.
Advanced decay (day 4 - 9)	6	2.00 pm - 6.00 pm	Loss of soft tissues, exposure of ribs, extensive peeling of skin, skin getting drier	Present but not intense	*Hister monitor, D. maculatus, Zophosis* sp., *C. chloropyga, Crematogaster* sp. *and Pheidole* sp.
Dry remain (day 10 - 14)	5	2.00 pm - 6.00 pm	No moisture on skin, skin very dry	None	*Hister monitor, D. maculatus, Zophosis* sp., *Crematogaster* sp. *and Pheidole* sp.

Suan Sunandha Science and Technology Journal
©2023 Faculty of Science and Technology, Suan Sunandha Rajabhat University

Table 8. Physical characteristics of slaughtered juvenile pig carcass shaded from sunlight at the decomposition stages.

Stages of decomposition	Period (days)	Sampling time	Physical changes	Odor presence and intensity	Dominant species
Fresh (day 0 - 1)	1	2.00 pm - 6.00 pm	Soft torsos and flexible limbs	None	*C. chloropyga and Anochetus* sp.
Bloated (day 2)	1	2.00 pm - 6.00 pm	Inflation of abdomen and blue-green changing of body color	Present but not intense	*H. monitor, D. maculatus, C. chloropyga, M. domestica, Anochetus* sp*. and C. maculatus*
Active decay (day 3)	1	2.00 pm - 6.00 pm	Bursting of the abdomen to expose intestinal tissues, deflation of the body, gradual peeling of the skin.	Present and intense	*H. monitor, D. maculatus, C. chloropyga, M. domestica, Anochetus* sp*., C. maculatus and Pheidole* sp.
Advanced decay (day 4 - 6)	3	2.00 pm - 6.00 pm	Loss of soft tissues, exposure of ribs, extensive peeling of skin, skin getting drier	Present and intense	*H. monitor, D. maculatus, C. chloropyga, M. domestica, Anochetus*sp*., C. maculatus and Pheidole* sp.
Dry remain (day 7 - 14)	8	2.00 pm - 6.00 pm	No moisture on skin, skin very dry	None	*H. monitor, D. maculatus, C. chloropyga, Anochetus* sp*., and Pheidole* sp.

4. Discussion

Five distinct decomposition stages on adult pig models and their associated arthropods have been reported in literature (Barton, Archer, Quaggiotto, & Wallman, 2019; Maisonhaute & Forbes, 2021; Ojianwuna et al., 2019; Timothy et al., 2022). The period of each decomposition stage as well as the associated cadaverous entomofauna have also been reported to be affected by factors such as geographical area, climate, body mass, cause of death among others. The decomposition of the carcasses (shaded and exposed) used for this study lasted for 14 days which is in a reasonable range for low body mass carcasses (Griffiths et al., 2020; Timothy et al., 2022; Viana et al., 2022). At the fresh stages of decomposition which lasted 0 – 1 day for both carcasses, the exposed carcass was colonized by insects from 5 families; Histeridae, Dermestidae, Calliphoridae, Muscidae and Formicidae while the shaded carcass was colonized by insects from 2 families; Calliphoridae and Formicidae. The presence of dipterans (Calliphoridae and Muscidea) as well as hymenopterans (Formicidae) at this stage buttresses the findings of Tembe and Mukaratirwa (2021). who reported sampling dipterans (largely Calliphoridae and Muscidae) and Ekanem & Dike (2010) who largely retrieved formicid hymenopterans at the fresh stage of decomposition. That more species colonized the exposed carcass at this stage may be attributed to the ease of visualization and accessibility by the insects as contrasted with the shaded carcass which may not have been as initially visible to the insects even though it was equally accessible. Both carcasses at this stage of decomposition had flexible limbs, soft torsos with no odor present as was also reported by Kelly, Van der Linde, & Anderson (2011) and Tembe & Mukaratirwa (2021).

The bloated stage for both carcasses was observed on day 2, corroborating the report of Barton et al. (2019) and also lasted only for the second day. At this stage both carcasses were slightly inflated, turned slightly blue-green especially at the abdominal region and had foul odors, which supports documented findings on the physical characteristic of carcasses at this stage of decomposition (Ojianwuna et al., 2019; Taleb, Tail, & Açıkgöz, 2017; Tembe & Mukaratirwa, 2021). Dominant insects colonizing both carcasses at this stage were from 3 orders: Coleoptera – Histeridae, Dermestidae and Tenebrionidae; Diptera – Calliphoridae and Muscidae; and Hymenoptera – Formicidae. Of interest is the fact that among the Formicidae family colonizing both carcasses, while *Crematogaster* sp. colonized the exposed carcass all through the decomposition stages, *Anochetus* sp. colonized the shaded carcass in the same manner. Although the activities of these ant species on pig carcasses have been documented (Bonacci, Zetto Brandmayr, Brandmayr, Vercillo, & Porcelli, 2011; Viana et al., 2022), their colonization of the respective carcasses which is hardly reported in this manner may be attributed to the proximity of their nests from the carcasses as *Anochetus* sp. was found to have nested on the tree serving as a shade for the colonized carcass. The observed increase in colonizing species at the boated stage vis-à-vis the fresh stage can be attributed to the presence of odor exhumed by the carcasses, as odor has been reported to play a vital role in the attraction of necrophagous insects (Timothy et al., 2022 Verheggen et al., 2017).

The active-decay stage for both carcasses was observed on the 3rd and also lasted for that day only. This contradicts reported findings of 5 - 10 days (Ojianwuna et al., 2019; Maisonhaute &

SuanSunandha Science and Technology Journal
©2023 Faculty of Science and Technology, SuanSunandhaRajabhat University

Forbes, 2021), and 7 - 12 days (Joseph, Mathew, Sathyan, & Vargheese, 2011). However, while our observation fairly agrees with the average of 2.33 days reported by Viana et al. (2022), it corroborates the reports of Griffiths et al. (2020) for carrion decomposition in tropical regions. Disparities in the period of occurrence of this stage can be largely attributed to body mass of the carcasses we used as well as differences in climatic and biogeographic factors. Supporting the report of Comstock, Desaulniers, LeBlanc, and Forbes (2015) the active-decay stage of both carcasses was characterized with bursting of the abdomen resulting to deflation of the carcass, intense putrefaction odor, massive maggot activities, slight peeling of the skin and massive invasion of cadaverous arthropods. Dominant arthropod families sampled from both carcasses at this stage included; Histeridae, Dermestidae, Tenebrionidae, Calliphoridae, Muscidae, and Formicidae (for exposed carcass). The aforementioned arthropod families, araenaens inclusive, were retrieved from the shaded carcass. Similar observations have been reported by Joseph et al. (2011), Griffiths et al. (2020) and Viana et al. (2022).

For both the shaded and exposed carcasses, the advanced-decay stage commenced on the 4th day. This stage lasted till day – 6 in the shaded carcass and till day – 9 in the exposed carcass. Observed differences in period length between the carcasses (exposed and shaded) might be attributed to differences in sun intensity to which the carcasses were exposed to. High sun intensity on the exposed carcass was also observed to have suppressed the abundance of visiting insects and the resulting rate of deterioration of the carcass due to reduced larval activities as the arthropods obviously avoided the upper portion of the carcass during the day but congregated underneath. Early commencement of this stage buttresses the findings of Griffiths et al. (2020) for carrion decomposition in tropical regions. Physical characteristics of the carcasses at this stage also agrees with the report of Tembe and Mukaratirwa (2021). who observed massive peeling of skin, loss of soft tissues, gradual drying of the skin and reduced odor intensity. Although both carcasses shared similar physical characteristics, the odor intensity in the shaded carcass at this stage was more intense. This may be attributed to higher aeration of the exposed carcass vis-à-vis the shaded. Dominant insect families associated with the carcasses at this stage include: Histeridae, Dermestidae, Tenebrionidae, Calliphoridae, Muscidae and Formicidae. Similar colonization of carrion by these insect families have been documented (Joseph et al., 2011; Matuszewski, Konwerski, Frątczak, & Szafałowicz., 2014; Viana et al., 2022).

The dry remain stage which was characterized by dry skin and relatively no odor for both carcasses was observed from day 10 - 14 for the exposed carcass and day 7 - 14 for the shaded carcass. Longer dry remain stage for the shaded carcass may also be attributed to sunlight intensity which is higher on the exposed carcass leading to its reduced dry remain period than in the shaded carcass. Dominant families associated with both carcasses at this stage were Histeridae, Dermestidae, Tenebrionidae, Calliphoridae and Formicidae. Consistency in represented dominant families for most of the decomposition stages can be attributed largely to the rapid decomposition of the carcasses favored by their relatively low body mass and the tropical climatic condition.

5. Conclusion

We observed that the dominant insect species colonizing the carcasses were *C. chloropyga*, *M. domestica* and *D. maculatus* (necrophagous), *Zophosis* sp. (predominantly predaceous), and *H. monitor*, *Anochetus* sp., *Crematogaster* sp. and *Pheidole* sp. (largely omnivorous). While it took 14 days for both carcasses to complete decomposition, the exposed carcass had a longer advanced-decay stage while the shaded carcass had a longer dry remain stage. Over 50% similarity exists between total sampled species from both carcasses. Little distinction exists on the succession pattern of invading carrion arthropods. This work will be helpful in estimating PMI for juvenile human remains and also provide information on the associated insects which could be useful for criminal investigations.

Acknowledgement

The authors would like to express their profound gratitude to Mr. Ishaku Musa of the Insect Museum of Ahmadu Bello University Zaria, Nigeria for identifying the arthropods collected during the study. Many thanks also to the staff of the Biological Garden, Federal University Wukari, who helped in setting up the study and the anonymous reviewers, whose constructive criticisms improved the manuscript.

Conflict of Interest

The authors do not report any financial or personal connections with anyone.

ORCID

Corresponding Author: Emmanuel Okrikata
https://orcid.org/0000-0002-9377-3058

SuanSunandha Science and Technology Journal
©2023 Faculty of Science and Technology, SuanSunandhaRajabhat University

Ethical Approval

At the time of the study, there was no ethical committee in relation to animal use in research in the Federal University Wukari, Nigeria. However, all the principles of 3Rs of the Guidance on the Operation of the Animals (Scientific Procedures) Act 1986 were observed.

References

Alboshabaa, S. H. H., & Al-Musawy, H. R. (2016). The taxonomic composition of the forensically important insects in the rabbit carcasses during two seasons in An-Najaf province–Iraq. *World Journal of Pharmaceutical Research*, *5*(4), 2068-2077.

Barton, P. S., Archer, M. S., Quaggiotto, M. M., & Wallman, J. F. (2019). Invertebrate succession in natural terrestrial environments. In J. H. Byrd, & J. K. Tomberlin (Eds.), *Forensic entomology* (pp. 141-153). Boca Raton, FL: CRC Press.

Bonacci, T., Zetto Brandmayr, T., Brandmayr, P., Vercillo, V., & Porcelli, F. (2011). Successional patterns of the insect fauna on a pig carcass in southern Italy and the role of *Crematogaster scutellaris* (Hymenoptera, Formicidae) as a carrion invader. *Entomological Science*, *14*(2), 125-132. doi:10.1111/j.1479-8298.2010.00423.x

Byrd, J. H., & Tomberlin, J. K. (2019). *Forensic entomology: The utility of arthropods in legal investigations* (3rd ed.). Boca Raton, FL: CRC Press.

Comstock, J. L., Desaulniers, J. P., LeBlanc, H. N., & Forbes, S. L. (2015). New decomposition stages to describe scenarios involving the partial and complete exclusion of insects. *Canadian Society of Forensic Science Journal*, *48*(1), 1-19. doi:10.1080/00085030.2014.929850

Ekanem, M. S., & Dike, M. C. (2010). Arthropod succession on pig carcasses in southeastern Nigeria. *Papeis Avulsos de Zoologia*, *50*(35), 561-570.

Emmanuel, O., Emmanuel Oludele, O., & Monday Unwabunne, U. (2019). Diversity, spatial and temporal distribution of above-ground arthropods associated with watermelon in the Nigerian southern guinea savanna. *Journal of Insect Biodiversity and Systematics*, *5*(1), 11-32.

Grassberger, M., & Frank, C. (2004). Initial study of arthropod succession on pig carrion in a Central European urban habitat. *Journal of Medical Entomology*, *41*(3), 511-523. doi:10.1603/0022-2585-41.3.511.

Griffiths, K., Krosch, M. N., & Wright, K. (2020). Variation in decomposition stages and carrion insect succession in a dry tropical climate and its effect on estimating postmortem interval. *Forensic Sciences Research*, *5*(4), 327-335. doi:10.1080/20961790.2020.1733830

Hammer, O., Harper, D. A. T., & Ryan, P. D. (2001). PAST: Paleontological statistics software package for education and data analysis. *Palaeontologia Electronica*, *4*, 1-9.

Joseph, I., Mathew, D. G., Sathyan, P., & Vargheese, G. (2011). The use of insects in forensic investigation: An overview on the scope of forensic entomology. *Journal of Forensic Dental Sciences*, *3*(2), 89-91. doi:10.4103/0975-1475.92154

Kelly, J. A., Van der Linde, T. C., & Anderson, G. S. (2011). The influence of wounds, severe trauma, and clothing, on carcass decomposition and arthropod succession in South Africa. *Canadian Society of Forensic Science Journal*, *44*(4), 144-157. doi:10.1080/00085030.2011.10768149

Keshavarzi, D., Zaimy, M. A., Yusuf, M. A., Shahriarinamadi, M., & Parkhideh, S. (2019). Insect succession on carrion in Fars Province, southwestern Iran. *Egyptian Journal of Forensic Sciences*, *9*(1), 1-6. doi:10.1186/s41935-019-0124-8

Maisonhaute, J. É., & Forbes, S. L. (2021). Decomposition process and arthropod succession on pig carcasses in Quebec (Canada). *Canadian Society of Forensic Science Journal*, *54*(1), 1-26. doi:10.1080/00085030.2020.1820799

Matuszewski, S., Hall, M. J. R., Moreau, G., Schoenly, K. G., Tarone, A. M., & Villet, M. H. (2020). Pigs vs people: the use of pigs as analogues for humans in forensic entomology and taphonomy research. *International Journal of Legal Medicine*, *134*, 793-810. doi:10.1007/s00414-019-02074-5

Matuszewski, S., Konwerski, S., Frątczak, K., & Szafałowicz, M. (2014). Effect of body mass and clothing on decomposition of pig carcasses. *International Journal of Legal Medicine*, *128*, 1039-1048. doi:10.1007/s00414-014-0965-5

Ojianwuna, C. C., Odibo, O. E., Akpan, A. U., & Egwaoje, K. I. (2019). Succession pattern of insects in relation to killing methods of *Rattus norvegicus* at Delta State University, Abraka, Nigeria. *Journal of Applied Science and Environmental Management*, *23*(3), 483-487. doi:10.4314/jasem.v23i3.18

SuanSunandha Science and Technology Journal
©2023 Faculty of Science and Technology, SuanSunandhaRajabhat University

Sonker, R., Rawat, S., & Singh, K. (2018). Factors affecting the arthropod succession on a dead animal. *International Journal of Scientific and Innovative Research*, *6*(1), 11-22.

Taleb, M., Tail, G., & Açıkgöz, H. N. (2017). Ecological roles of cadaveric fauna in relation with decomposition stages. *Congress of Ecology and Environment with International Participation* (pp. 399-408). *UKECEK 2017*.

Tembe, D., & Mukaratirwa, S. (2021). Insect succession and decomposition pattern on pig carrion during warm and cold seasons in KwaZulu-Natal Province of South Africa. *Journal of Medical Entomology*, *58*, 2047-2057. doi:10.1093/jme/tjab099

Timothy, C. A., & Emmanuel, O. (2020). Phototactic response of two spotted cricket (*Gryllus bimaculatus* De Geer) to electric bulb light colours and types. *International Journal of Sustainable Agricultural Research*, *7*(2), 66-72. doi:10.18488/journal.70.2020.72.66.72

Timothy, C. A., Okrikata, E., & Tidi, J. A. (2022). Impact of sunlight exposure status on the diversity and succession of insects associated with strangulated juvenile pig carcasses. *International Journal of Scientific Research in Multidisciplinary Studies*, *8*(10), 21-27.

Verheggen, F., Perrault, K. A., Megido, R. C., Dubois, L. M., Francis, F., Haubruge, E., ... Stefanuto, P. H. (2017). The odor of death: An overview of current knowledge on characterization and applications. *BioScience*, *67*(7), 600-613. doi:10.1093/biosci/bix046

Viana, G. S., Paula, M. C. D., Eulalio, A. D. M. D. M., Santos, P. G. D., Lima-Junior, S. E., & Antonialli-Junior, W. F. (2022). Formicidae fauna in pig carcasses contaminated by insecticide: implications for forensic entomology. *Revista Brasileira de Entomologia*, *66*. doi:10.1590/1806-9665-RBENT-2021-0085

Available online at https://li02.tci-thaijo.org/index.php/ssstj

Suan Sunandha Science and Technology Journal
©2023 Faculty of Science and Technology, Suan Sunandha Rajabhat University

Effect of Preparation Conditions on Crosslinking Behavior of Linseed Oil-Based Thermosetting Polymer

Piyapon Permpoontanalap, Wanchai Lerdwijitjarud*

[1]Department of Materials Science and Engineering, Faculty of Engineering and Industrial Technology, Silpakorn University, Nakhon Pathom 73000, Thailand

***Corresponding author e-mail: lerdwijitjarud_w@su.ac.th**

Received: *15 February 2023* / **Revised:** *24 April 2023* / **Accepted:** *5 May 2023*

Abstract

Bio-based materials have received more attention to replace materials from petroleum resources because of sustainability reasons. Plant oil is one of the most interesting raw materials to produce thermosetting polymers. A crosslinking reaction between epoxidized linseed oil and vegetable oil-based crosslinkers is investigated in the present study. Two types of crosslinker including fatty acid dimer and fatty acid trimer were reacted with epoxidized linseed oil. A rotational rheometer equipped with cone-and-plate geometry was used to monitor the progress of three-dimensional network formation. A curing phenomenon was illustrated by the increment in storage modulus of the reaction mixture. The trifunctional crosslinker was more effective than the functional crosslinker for an uncatalyzed system at the reaction temperature of 120°C. When the crosslinking temperature of the trimer-crosslinker system increased from 120°C to 140°C, the induction time for curing decreased around three times. The reaction between epoxidized oil and trimer acid was obviously accelerated by using 4-methyl amino pyridine as a catalyst. Increasing the catalyst content induced a monotonically reduction in the induction time of the curing process. The induction time of the reaction between epoxidized linseed oil and trimer acid with 2% catalyst at reaction temperature of 120°C was only 18 minutes, which was significantly shorter than that of an uncatalyzed system around seven times.

Keywords: Thermosetting polymer, Epoxidized linseed oil, Fatty acid trimer

1. Introduction

Thermosetting polymer is one class of important polymeric material. A three-dimensional network structure provides some better properties compared with thermoplastic polymers such as solvent resistivity, dimensional stability, and mechanical strength. Epoxy thermoset is commonly used in various fields such as electronic, coating, adhesive, composites and other fields due to its excellent thermal stability, mechanical properties, electrical insulation and chemical resistance (Zhao, An, & Wang, 2021). Nowadays, epoxy resin is a major share of thermosetting polymers business (Qi et al., 2018). Commercial epoxy resin is presently made from diglycidyl ether of bisphenol A (DGEBA) and epichlorohydrin (ECH), which were the petroleum-based materials (Tao et al., 2020). These raw materials of epoxy resin are suspected to have a negative impact on living organisms and ecosystems (Qi et al., 2018). The rapid decrease of nonrenewable resources has motivated the researchers and manufacturers to investigate bio-based and renewable feedstock as the alternative raw materials (Khandelwal, Sahoo, Kumar, & Manik, 2018).

There are several potential bio-based feedstocks such as cellulose, lignin, starch, natural oils and chitin. Bio-based oils can derive from plants and animals as vegetable oils and animal fats. Plant-based oils have gained interest as raw materials due to their low cost, environmental friendliness, availability, non-hazardous, renewability, and possible biodegradability. Triglyceride is a base chemical in plant oils. Natural plant oils typically contain some unsaturated carbon-carbon bonds in their fatty-acid part of triglyceride molecules. This unsaturated site enables direct polymerization and modification. There are various chemical modifications that are performed at unsaturated fatty acids, including acylation, ozonolysis, hydroformylation, dimerization, epoxidation and hydroxylation (Musik, Bartkowiak, & Milchert, 2022).

Suan Sunandha Science and Technology Journal
©2023 Faculty of Science and Technology, Suan Sunandha Rajabhat University

Among many vegetable oils, linseed oil (LO) is one of the most natural oils that exhibits a high degree of unsaturation. The composition of fatty acid in LO is 53% of linolenic acid, 16% of linoleic acid, and 22% of oleic acid (Janković, Govedarica, & Sinadinović-Fišer, 2020). It has approximately 6.6 carbon-carbon double bonds per molecule of triglyceride (Singh, Sethi, & Manik, 2022). Epoxidation process is potentially useful for increasing the reactivity of LO by the formation of epoxide rings. Epoxidized linseed oil (ELO) is possibly produced by epoxidation reaction between LO and peracid (Samper, Petrucci, Sánchez-Nacher, Balart, & Kenny, 2015). A high reactivity of epoxide groups in ELO can be easily reacted with other chemicals. ELO can be used as raw materials to prepare diluents, fillers, lubricants, coatings, and stabilizers in PVC, PLA and other polymers (Balart, Fombuena, Fenollar, Boronat, & Sánchez-Nacher, 2016; Thuy & Duc, 2020). Chemical reaction between ELO and crosslinking agent results in thermosetting polymer. Chemicals containing amine, anhydride or carboxylic acid functional groups can be possibly used as crosslinkers for ELO. Yahua Chen and co-workers (Chen, Xi, & Zhao, 2016) studied the preparation of thermoset from epoxidized soybean oil and crosslinking agent using 2-ethyl-4-methylimidazole as a catalyst. The bio-based maleopimaric acid crosslinker and two petroleum-based crosslinkers, including hexahydro-4-methylphthalic anhydride (MHHPA) and trimellitic anhydride (TMA), were compared. The thermosets formulated from bio-based crosslinker showed greater in elongation at break and ultimate tensile strength than thermoset derived from petroleum-based crosslinkers. Dimer and trimer of fatty acid is one of the interesting bio-based crosslinking compounds for epoxidized vegetable oil. They can be produced from condensation reactions of unsaturated fatty acids such as oleic acid (C18:1) and linoleic acid (C18:2) (dos Santos Martini, Braga, & Samios, 2009). Besides the types of thermosetting precursors, the crosslinking conditions such as time and temperature of curing, amount and type of catalyst have to be concerned. Different curing parameters undoubtedly result in thermosetting materials with different properties. The total production time of thermosets depends significantly on preparation conditions.

This study aims to develop plant oil-based thermosetting polymers from curing reaction between ELO and plant oil-based crosslinker, including dimer and trimer of fatty acid in this study. We focus on the influence of crosslinker type and crosslinking temperature on curing behavior of this all-plant-oil based epoxy resin. The effect of catalyst content on the induction time of three-dimensional network formation is also explored.

2. Materials and Methods

2.1 Materials

Linseed oil (Virgin grade, Tropicalife) was used as a base oil. Epoxidation reaction of oil was performed using hydrogen peroxide solution 30% w/w (AR, QRëC), formic acid (98.5% w/w, QRëC) and sulfuric acid (98% w/w, QRëC) as reagents. Toluene (99.5%, QRëC) was used as a solvent. Dimer acid (Pripol 1012, CRODA) and trimer acid (Pripol 1040, CRODA) were used as the difunctional and trifunctional crosslinking agents, respectively. The catalyst for crosslinking reaction was 4-dimethylamino pyridine (AR, Sigma-Aldrich).

2.2 Synthesis of epoxidized linseed oil

First, Linseed oil (300 g) was mixed and stirred with toluene (150 g) in a three-neck round-bottom flask equipped with a condenser. Then, Formic acid (35.4 g) was added at room temperature followed by adding sulfuric acid (1.5 ml) dropwise under stirring. The mixture temperature was raised to 60ºC. Hydrogen peroxide (251.1 g) was then added slowly to the solution by equivalent dropping funnel. The mixture was stirred and the temperature was maintained for 6 hours. After cooling down to room temperature, the mixture was separated into aqueous and oil phase. The oil phase was neutralized by washing with distillated water. The trapping water and excess solvent were removed by evaporation process with rotary evaporator. The epoxidized linseed oil was then characterized by FTIR spectroscopy and ^{1}H-NMR.

2.3 Characterization of linseed oil and epoxidized linseed oil

FTIR spectra of linseed oil and epoxidized linseed oil were recorded by FTIR spectrometer (Vertex70, BRUKER) in TR mode within the range from 4000 cm^{-1} to 500 cm^{-1} at a 4 cm^{-1} resolution.

^{1}H-NMR spectra were obtained from ^{1}H-NMR spectrometer (Advance III 300 MHz, BRUKER) using deuterated chloroform ($CDCl_3$) as a solvent. The epoxide content (%) was calculated by using this below equation (Saithai, Jonjanekieat, Chinpa, & Tanrattanakul, 2007; Xia, Budge, & Lumsden, 2015).

$$\%Epoxide = \frac{I_{2.8-3.0}}{I_{2.8-3.0}+I_{5.3-5.6}} \times 100 \qquad (1)$$

where $I_{2.8\text{-}3.0}$ and $I_{5.3\text{-}5.6}$ are integral areas from the ^{1}H-NMR spectrum at 2.8-3.0 ppm and 5.3-5.6 ppm respectively.

©2023 Faculty of Science and Technology, Suan Sunandha Rajabhat University

2.4 Investigation of crosslinking behavior by rheological analysis

The curing reaction between epoxidized linseed oil and crosslinking agents was investigated by using rotational rheometer (ARES-G2, TA instrument) equipped with cone-and-plate geometry. The rheological analysis was operated in oscillation time sweep mode at the fixed 5% strain and angular frequency of 1.0 rad/s. The progress of crosslinking reaction was monitored by tracking the increase in storage modulus with time. The epoxidized linseed oil was initially premixed with crosslinker at room temperature. The molar ratio between crosslinking agent and content of epoxide functional group of modified oil was fixed at 1/2. Two types of crosslinking agents, including dimer and trimer of fatty acid, were studied. The influence of crosslinker type on curing behavior was tested at temperature of 120ºC in an uncatalyzed system. The more efficient crosslinker in uncatalyzed system was then chosen to further examine the effect of crosslinking temperature, which was ranged from 120ºC to 140ºC. The network formation between epoxidized linseed oil and optimal crosslinker at optimal temperature was finally explored by varying the catalyst content from 0.0 to 2.0 weighted percent.

3. Results and Discussion

3.1 Characterization of epoxidized linseed oil

The epoxidized plant-based oil was obtained from an epoxidation reaction between linseed oil and performic acid. Hydrogen peroxide was firstly reacted with formic acid to produce peracid using sulfuric acid as a catalyst. The performic acid was subsequently reacted with double bonds of linseed oil to achieve epoxidized linseed oil. Scheme 1 proposes the epoxidation reaction.

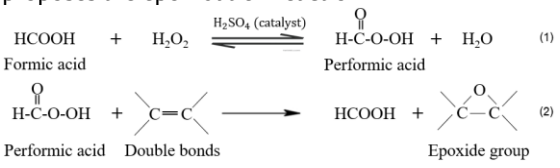

Scheme 1. Epoxidation reaction of performic acid with double bond of linseed oil.

The synthesized epoxidized linseed oil was investigated by FTIR spectroscopy. Figure 1 shows FTIR spectra of linseed oil and epoxidized linseed oil. FTIR spectrum of linseed oil displayed the characteristic peak of double bonds in unsaturated fatty acids structure at wavenumber 731 cm^{-1}, 1653 cm^{-1} and 3009 cm^{-1} related to *cis*-CH=CH stretching, C=C stretching and =CH stretching, respectively. The new peak at wavenumber 823 cm^{-1} corresponded to C-O-C vibration of oxirane ring was emerged in FTIR spectrum of epoxidized oil (Figure 1(b)) (López Téllez, Vigueras-Santiago, & Hernández-López, 2009; Nieto, Santiago, & López, 2021). Moreover, the reduction in the intensities of double-bonds characteristic peaks were fairly detected.

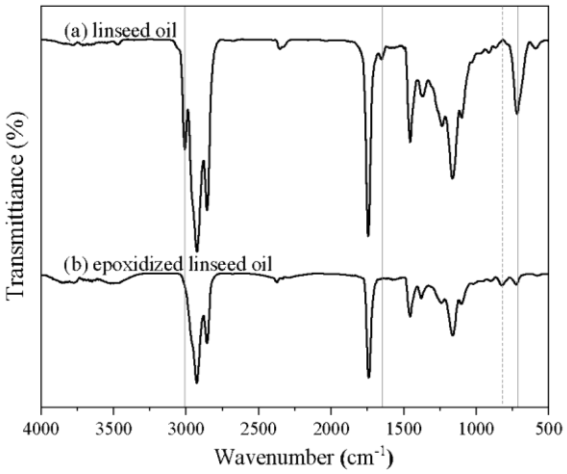

Figure 1. FT-IR spectra of (a) linseed oil and (b) epoxidized linseed oil.

The ^{1}H-NMR spectra of LO and ELO are depicted in Figure 2. In LO spectra, chemical shift (δ) at 2.1 ppm (5), 2.8 ppm (8) and 4.1-4.3 ppm (1) related to allyl protons (-C**H**$_2$-CH=CH-), hydrogens between two double bonds (-CH=CH-**CH**$_2$-CH=CH-) and methylene protons of hydrogens of glycerol (-CH-C**H**$_2$-O-) respectively. In ELO spectra, the characteristic epoxy hydrogens signals at δ equaled to 1.5 ppm (5) and around 2.8-3.0 ppm (6') assigned to protons adjacent to oxirane ring (-CH$_2$-O-CH$_2$-C**H**$_2$-) and hydrogens of epoxide group (-C**H**$_2$-O-C**H**$_2$-), respectively (Khandelwal et al., 2018; López Téllez et al., 2009). After epoxidation, the intensity of vinyl protons of alkene (-C**H**=C**H**-) at 5.3-5.6 ppm obviously decreased, which confirmed the successful epoxidation process. Based on chemical reaction (2) of Scheme 1, the carbon-carbon double bonds were changed to be epoxide groups during epoxidation reaction. The integral areas of protons at the positions of 2.8-3.0 ppm corresponded to protons of epoxide groups and those of 5.3-5.6 ppm corresponded to protons of alkene groups were effectively used to determine the epoxide content of the synthesized product. The carbon-carbon double bonds of LO were transformed to be epoxide groups around 87.5% (Salih et al., 2015), which was calculated based on equation 1.

Suan Sunandha Science and Technology Journal
©2023 Faculty of Science and Technology, Suan Sunandha Rajabhat University

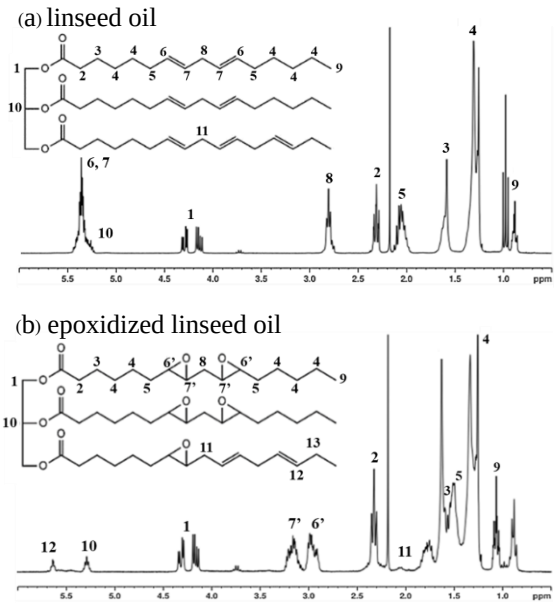

Figure 2. ^{1}H-NMR spectra of (a) linseed oil and (b) epoxidized linseed oil.

3.2 Influence of preparation conditions on crosslinking behavior

The effect of preparation conditions on crosslinking behavior of epoxidized plant-based oil was monitored by rheological analysis by using cone and plate rheometer. Storage modulus versus time was tracked in oscillation time sweep mode.

3.2.1 The effect of crosslinker type

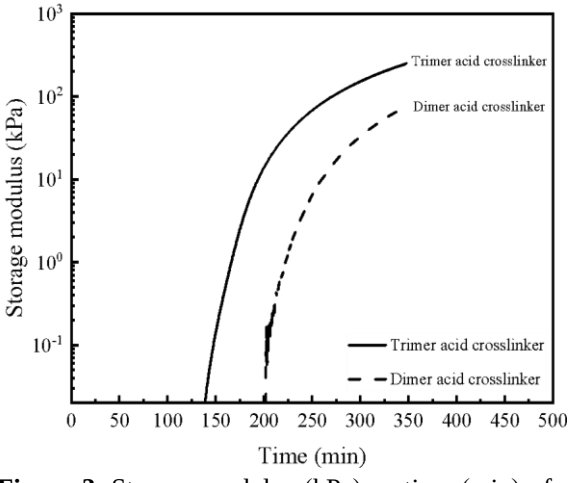

Figure 3. Storage modulus (kPa) vs time (min) of the reaction between epoxidized linseed oil and crosslinker in uncatalyzed system.

The comparison between using trimer acid and dimer acid as a crosslinking agent for ELO was studied by fixing curing temperature at 120ºC in an uncatalyzed system. The results are presented in Figure 3. The shorter induction time and also higher storage modulus were obviously detected for the reaction system using trimer acid as a crosslinking agent. The larger molecular size of trimer acid might retard the diffusion movement. However, it contained trifunctional active sites to react with the epoxide groups of ELO. Therefore, the results implied that the number of functional groups was more influential than the size of the crosslinker. Trimer acid was consequently an appropriate crosslinking agent for ELO.

3.2.2 The effect of crosslinking temperatures

The reaction between ELO and trimer acid at temperature of 120ºC and 140ºC in an uncatalyzed system was examined. The results are displayed in Figure 4. The results indicated that the reactivity of crosslinking reaction between trimer acid and ELO noticeably depended on temperature. The thermal energy could accelerate the diffusion ability of both ELO and trimer acid, which favored the formation of crosslinking networks. The decrease of induction time from 127 min to 44 min was observed when the crosslinking temperatures increased from 120ºC to 140ºC.

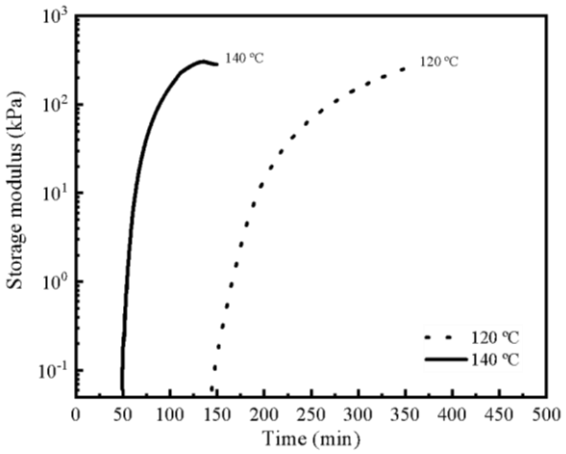

Figure 4. Storage modulus (kPa) vs time (min) of the reaction between epoxidized linseed oil and trimer acid at different temperatures.

3.2.3 The effect of catalyst content

The crosslinking mechanism of epoxidized linseed oil with trimer acids using 4-dimethylamino pyridine (DMAP) as catalyst is proposed in Scheme 2. The effect of catalyst contents on curing reaction was studied by fixing crosslinking temperature at 120ºC in trimer acids-crosslinker system. The results are illustrated in Figure 5. DMAP could significantly accelerate the network formation. In the present

©2023 Faculty of Science and Technology, Suan Sunandha Rajabhat University

study, the induction time is defined as the time interval required to detect a significant increase in storage modulus at the early stage of curing. The uncatalyzed systems exhibited the longest induction time of around 129 minutes. Figure 6 depicts the influence of catalyst content on induction time. The induction time decreased with increasing catalyst content. The induction time of the reaction mixture catalyzed by 2.0% DMAP was only 18 minutes, which was shorter than that of the uncatalyzed system around 7 times. However, the efficiency of the catalyst was alleviated in the systems with high catalyst concentration. The relationship between the induction time and catalyst were downward curves with decreasing slope. The rate of crosslinking reaction might be considered from the slope of the curve in Figure 5. The data revealed that the curing rate also increased with increasing catalyst content.

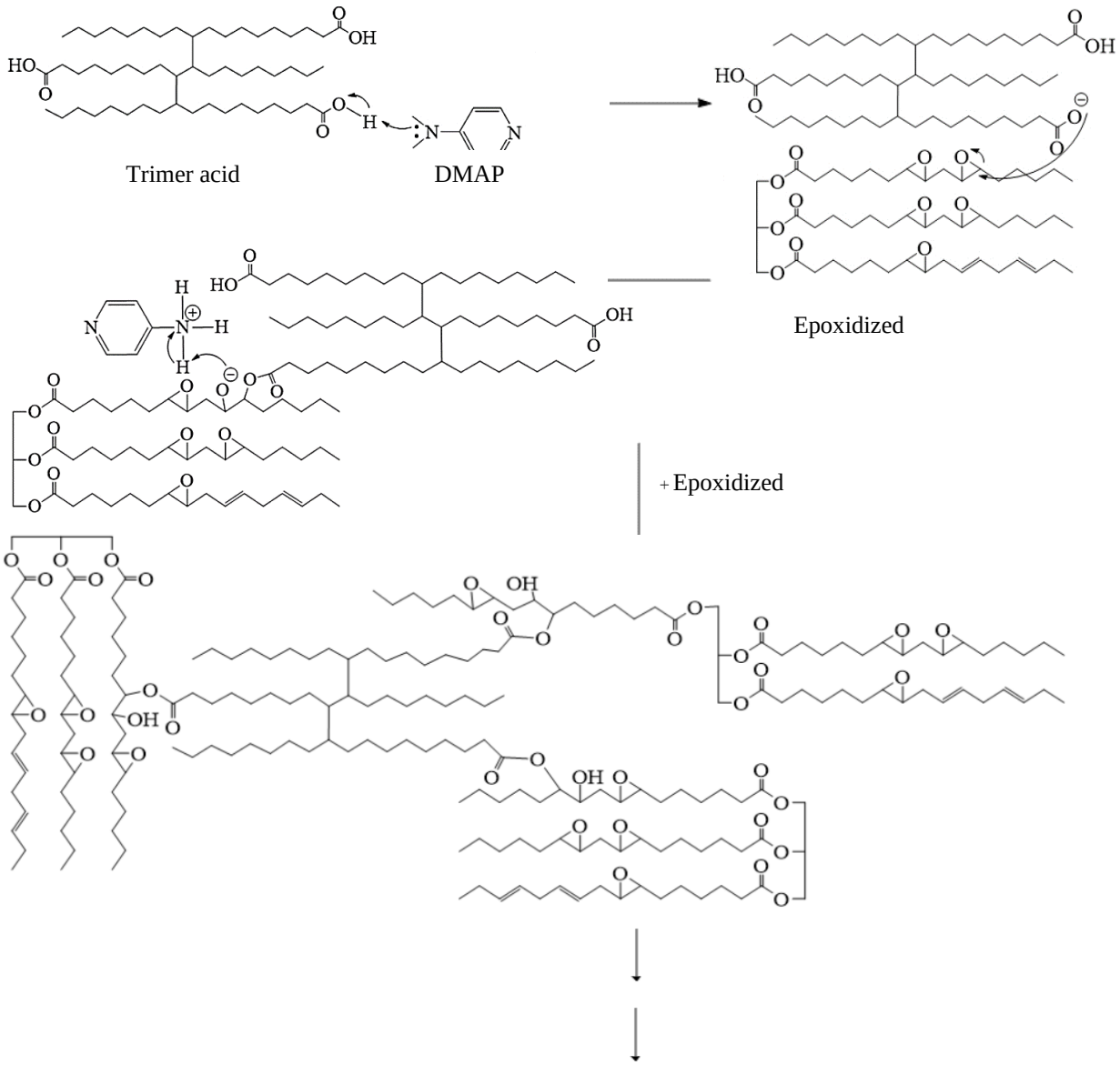

Scheme 2. Crosslinking reaction of epoxidized linseed oil with trimer acid.

©2023 Faculty of Science and Technology, Suan Sunandha Rajabhat University

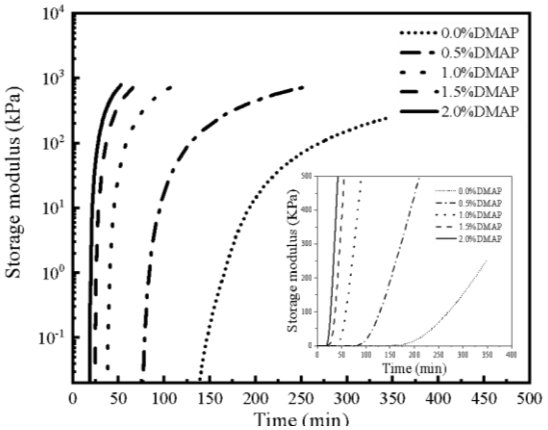

Figure 5. Storage modulus (kPa) vs time (min) of the crosslinking reaction between epoxidized linseed oil and trimer acid with different DMAP contents. [the insert represented the linear curve]

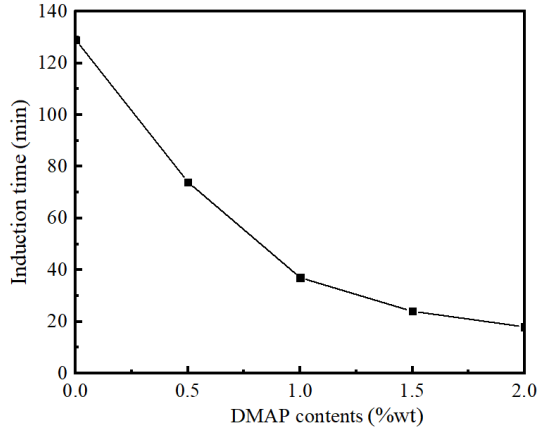

Figure 6. The induction time of the crosslinking reaction between epoxidized linseed oil with trimer acid at different DMAP contents.

4. Conclusions

In this work, the epoxidized linseed oil was synthesized via the in-situ epoxidation reaction and the achievement was confirmed by FTIR spectroscopy and ^{1}H-NMR. The obtained epoxidized linseed oil was subsequently crosslinked by trimer and dimer of fatty acid. Trimer acid crosslinker was more effective than dimer acid for an uncatalyzed system at the reaction temperature of 120ºC because of the higher number of active functional groups. The induction time for curing of an uncatalyzed system decreased around 3 times with increasing the crosslinking temperature from 120ºC to 140ºC. At reaction temperature of 120ºC, the induction time of the 2.0%-DMAP catalyzed system was only 18 minutes whereas that of the uncatalyzed system was 129 minutes. However, the efficiency of catalysts tended to decrease in the systems with high catalyst content.

Acknowledgments

The authors gratefully thank the support provided by the Department of Materials Science and Engineering, Faculty of Engineering and Industrial Technology, Silpakorn University. The assistance from Croda (Thailand) Co., Ltd. for chemical support is also acknowledged.

References

Balart, J. F., Fombuena, V., Fenollar, O., Boronat, T., & Sánchez-Nacher, L. (2016). Processing and characterization of high environmental efficiency composites based on PLA and hazelnut shell flour (HSF) with biobased plasticizers derived from epoxidized linseed oil (ELO). *Composites Part B: Engineering*, *86*, 168-177. doi:10.1016/j.compositesb.2015.09.063

Chen, Y., Xi, Z., & Zhao, L. (2016). New bio-based polymeric thermosets synthesized by ring-opening polymerization of epoxidized soybean oil with a green curing agent. *European Polymer Journal*, *84*(1), 435-447. doi:10.1016/j.eurpolymj.2016.08.038

dos Santos Martini, D., Braga, B. A., & Samios, D. (2009). On the curing of linseed oil epoxidized methyl esters with different cyclic dicarboxylic anhydrides. *Polymer*, *50*(13), 2919-2925. doi:10.1016/j.polymer.2009.03.058

Janković, M. R., Govedarica, O. M., & Sinadinović-Fišer, S. V. (2020). The epoxidation of linseed oil with *in situ* formed peracetic acid: A model with included influence of the oil fatty acid composition. *Industrial Crops and Products*, *143*. doi:10.1016/j.indcrop.2019.111881

Khandelwal, V., Sahoo, S. K., Kumar, A., & Manik, G. (2018). Electrically conductive green composites based on epoxidized linseed oil and polyaniline: An insight into electrical, thermal and mechanical properties. *Composites Part B: Engineering*, *136*, 149-157. doi:10.1016/j.compositesb.2017.10.030

López Téllez, G., Vigueras-Santiago, E., & Hernández-López, S. (2009). Characterization of linseed oil epoxidized at different percentages. *Superficies y Vacío*, *22*(1), 5-10.

Musik, M., Bartkowiak, M., & Milchert, E. (2022). Advanced methods for hydroxylation of vegetable oils, unsaturated fatty acids and their alkyl esters. *Coatings*, *12*(1). doi:10.3390/coatings12010013

Nieto, J. F., Santiago, E. V., & López, S. H. (2021). Determination of the number of epoxides groups by FTIR-HATR and its correlation with

Suan Sunandha Science and Technology Journal
©2023 Faculty of Science and Technology, Suan Sunandha Rajabhat University

^{1}H NMR in epoxidized linseed oil. *Advances in Analytical Chemistry*, *11(1)*, 1-8. doi:10.5923/j.aac.20211101.01

Qi, M., Xu, Y. J., Rao, W. H., Luo, X., Chen, L., & Wang, Y. Z. (2018). Epoxidized soybean oil cured with tannic acid for fully bio-based epoxy resin. *RSC Advances*, *8*(47), 26948-26958. doi:10.1039/c8ra03874k

Saithai, P., Jonjanekieat, S., Chinpa, W., & Tanrattanakul, V. (2007). Preparation of epoxidized soybean oil. *KMUTT Research & Development Journal*, *4*(1), 583-589.

Salih, A. M., Ahmad, M. B., Ibrahim, N. A., Dahlan, K. Z., Tajau, R., Mahmood, M. H., & Yunus, W. M. Z. W. (2015). Synthesis of radiation curable palm oil–based epoxy acrylate: NMR and FTIR spectroscopic investigations. *Molecules*, *20*(8), 14191-14211. doi:10.3390/molecules200814191

Samper, M. D., Petrucci, R., Sánchez-Nacher, L., Balart, R., & Kenny, J. M. (2015). New environmentally friendly composite laminates with epoxidized linseed oil (ELO) and slate fiber fabrics. *Composites Part B: Engineering*, *71*, 203-209. doi:10.1016/j.compositesb.2014.11.034

Singh, M., Sethi, S. K., & Manik, G. (2022). Pressure-sensitive adhesives based on acrylated epoxidized linseed oil: A computational approach. *International Journal of Adhesion and Adhesives*, *112*. doi:10.1016/j.ijadhadh.2021.103031

Tao, Y., Fang, L., Dai, M., Wang, C., Sun, J., & Fang, Q. (2020). Sustainable alternative to bisphenol A epoxy resin: High-performance recyclable epoxy vitrimers derived from protocatechuic acid. *Polymer Chemistry*, *11*(27), 4500-4506. doi:10.1039/d0py00545b

Thuy, N. T., & Duc, V. M. (2020). The epoxidized linseed oil as a secondary plasticizer in PVC processing. *Vietnam Journal of Chemistry*, *58*(4), 534-539. doi:10.1002/vjch.202000023

Xia, W., Budge, S. M., & Lumsden, M. D. (2015). New ^{1}H NMR-based technique to determine epoxide concentrations in oxidized oil. *Journal of Agricultural and Food Chemistry*, *63*(24), 5780-5786. doi:10.1021/acs.jafc.5b01719

Zhao, W., An, L., & Wang, S. (2021). Recyclable high-performance epoxy-anhydride resins with DMP-30 as the catalyst of transesterification reactions. *Polymers*, *13*(2). doi:10.3390/polym13020296

Available online at https://li02.tci-thaijo.org/index.php/ssstj

Suan Sunandha Science and Technology Journal
©2023 Faculty of Science and Technology, Suan Sunandha Rajabhat University

Investigation of Some Regular X-ray Imaging Parameters in Suggestive Radiography of Four Hospitals in Bangladesh

Sadeka Sultana Rubai[1], Santunu Purohit[1], Tanjim Siddiqua[2], Md. Shakilur Rahman[2], AKM Moinul Haque Meaze[1*]

[1]Department of Physics, University of Chittagong, Chittagong- 4331, Bangladesh
[2]Secondary Standard Dosimetry Laboratory, Institute of Nuclear Science & Technology, Bangladesh Atomic Energy Commission, Savar- 1100, Bangladesh
***Corresponding author e-mail: meaze@cu.ac.bd; mhqmeaze@yahoo.com**

Received: *17 November 2022* / **Revised:** *23 February 2023* / **Accepted:** *19 April 2023*

Abstract

Analytic radiography is a normal image testing technique which has been utilized for quite a long time. It is recommended by specialists so they can identify any problem in patients' bodies without a cut. Thinking about its wide use, the principle objective of this investigation is to give a top notch picture by keeping the radiation portion as low as conceivable through identifying any variety in quality control (QC) boundaries. In this work, some standard quality control boundaries, for example, voltage exactness, time precision test, tube yield linearity, half value layer (HVL) of x-beam were measured. These quality control (QC) boundaries were estimated by a dosimeter keeping a distance of 100 cm from source. The voltage precision went from 0.31% to 4.67% and the time exactness test went from 0% to 2.29%. The consequences of this investigation show that all the QC boundaries are inside the acceptable level which guarantees the advancement of the low portion conveyed to the patients.

Keywords: Diagnostic radiography, Quality control (QC), X-ray, HVL, Dosimeter

1. Introduction

Diagnostic x-ray is a common and frequently used procedure in any accidental case to check fracture or to monitor progression of diagnosed disease all over the world. A report has been made that medical imaging tests are increased at a rate of 5% per year with the whole world annual per capital dose of 0.4 mSv. So, diagnostic imaging becomes the largest source of man-made exposure to ionizing radiation in medical science (Abdulkadir, 2020). As the use of x-ray in medical science has been grown up everywhere, the execution of quality control of x-ray machines is of most important for justification and optimization of exposures (Al-Kinani & Mohsen, 2014). Optimization of dose is of most important for the quality and quantity of QC test on x-ray machines (Gholami, Nemati, & Karami, 2015). The World Health Organization (WHO) characterizes a quality assurance (QA) program in symptomatic radiology as a coordinated exertion by the staff working an office to guarantee that the indicative pictures delivered are of adequately excellent so they reliably give sufficient analytic data at the most reduced conceivable expense and with the most un-conceivable openness of the patient to radiation (Inkoom, Schandorf, Emi-Reynolds, & Fletcher, 2011). The initial responsibility of a medical physicist is to design and supervise a QA program which is stated by AAPM. The European Commission of protection published a guideline for QC in 1997 and main components of QC programs have been reported by AAPM in 2002 (Asadinezhad, Bahreyni Toossi, Ebrahiminia, & Giahi, 2017). QC is part of the QA program that is used to test and maintain the technical component of x-ray units. So, quality control techniques mainly focused on the instruments that can play an important role in imaging (Ismail, Ali, Omer, Garelnabi, & Mustafa, 2015). Patients and radiation workers in diagnosis face an estimated lifetime cancer risk of between 1 in 3500 and 1 in 7000. So, it is very important to know the amount of radiation exposure used during diagnosis so that it may lessen excessive radiation to patients (Rubai et al., 2018). Minimization of radiation exposure to have a high quality image is the main aim of QA. This can be done by routine checkup of some parameters like voltage and time accuracy, linearity of output, half value layer (Abd-Alla, Salih, & Albashir, 2019). The

©2023 Faculty of Science and Technology, Suan Sunandha Rajabhat University

quality assurances of diagnostic X-ray are based on the Basic Safety Standard – BSS and International Commission of Radiological Protection, and use of diagnostic reference levels (DRL for patients, ICRP-Report No. 46, 1966) (Taha, 2011). The main objective of this study is to decrease the delivered dose during imaging with a high quality image by investigating some important QC parameters which would also reduce the economic cost according to the IAEA Technical Report Series No. 457 (International Atomic Energy Agency [IAEA], 2007).

2. Materials and Methods

Three 500 mA digital x-ray systems (Shimadzu IEC60601-1-2-2001) of Delta Hospital Ltd., Mirpur, Dhaka, and KhwajaYunus Ali Medical College Hospital, Sirajgonj as well as one digital x-ray system (Siemens part8375545g2107) of National Institute of Cancer Research and Hospital (NIRCH), Dhaka, Bangladesh were used with inherent filtration 1.5 and 1 mm respectively in the present study. Dosimetry convention in this study was as indicated by the IAEA Specialized Report Arrangement No. 457 (IAEA, 2007). QC test were performed by using a dosimeter named DIAVOLT UNIVERSAL (T43014-001400) made by PTW-Freiburg. Its measuring quantities are practical peak voltages and air kerma. For making this, various quality control parameters such as output of x-ray, time accuracy, output linearity with mA, voltage accuracy, kV linearity with kV_p were investigated. The beam alignment was checked with field size of 10×10 cm^2. For measurements, the dosimeter was positioned in such a way that the focus to detector distance (FDD) was 100 cm.

Figure 1. Set-up representation of the radiation measurement geometry for 40, 50, 60, 80 and 100 kV.

2.1 Voltage accuracy test

For various tube currents which are commonly used in different organs image testing of the patients, tube voltage was tested. At field to surface distance (FSD) 100 cm kV_p was measured from 60-120 kV tube voltage for different currents in mA (Ranallo, 1998).

$$Voltage\ \ accuracy\ \ = \frac{kV(measured)-kV(nominal)}{kV(nominal)} \quad (1)$$

2.2 Time accuracy test

It was measured for 15 tube voltages at FSD 100 cm.

Linearity test with output

For mA linearity test 4 data was taken for using 80kV_p at a distance 100 cm from x-ray tube with exposure time 100 ms. The dose to mA ratio, X and the linearity coefficient L, can be determined for the formula (Ranallo, 1998):

$$X = \frac{Dose}{mAS}; L = \frac{X_{max}-X_{min}}{X_{max}+X_{min}} \quad (2)$$

2.3 Linearity with output

For output linearity as a function of tube voltage, air kerma was measured at constant tube current and exposure time. During the experiment three exposures was used at 160 mA and 100 ms. For each exposure FDD was 100 cm.

2.4 Half value layer

For the HVL computation, the air kerma corresponding to different thickness of aluminum filters are measured. To avoid scattering the aluminum filters were placed as close as possible to the x-ray tube. Data was also taken without a filter to get the initial doses to compute HVL for different potential. During this measurement the dosimeter was kept at a distance of 100 cm from the x-ray tube. This was done in two hospitals with two different x-ray machines. The effective energy (keV) can also be obtained by using an established empirical formula which was obtained by the interpolation value from Hubble mass attenuation coefficients (Rahman et al., 2008);

$$E = 22.03t^{0.341} + 0.1469t^{2.01}; t = HVL\ for\ Al \quad (3)$$

©2023 Faculty of Science and Technology, Suan Sunandha Rajabhat University

3. Results

3.1 Voltage accuracy test

Table 1 shows the precision of kV for various organ's imaging in three x-beam machines. Tube voltages in different organs were performed in accordance with published international standard (Health Canada, 2008) and well suited for patients' health. For machine 1 (Shimadzu IEC60601-1-2-2001) the varieties lay from 4.67% to 2.56% for tube voltage 60-90 kV. For machine 2 (Shimadzu IEC60601-1-2-2001) it was about 0% to 3.1% for tube voltage 60-120 kV and 0.31% to 2.1% for 65-120 kV in machine 3 (Shimadzu IEC60601-1-2-2001) individually. That was, for the majority of the tube voltage the variety was impressive.

Table 1. The accuracy of kV used for different organ's x-ray examination of three machines.

Name of organ	Machine 1 (Shimadzu IEC60601-1-2-2001)			Machine 2 (Shimadzu IEC60601-1-2-2001)			Machine 3 (Shimadzu IEC60601-1-2-2001)		
	Tube voltage (kV)	Mean kV_p	Deviation (%)	Tube voltage (kV)	Mean kV_p	Deviation (%)	Tube voltage (kV)	Mean kV_p	Deviation (%)
Chest	60	62.800	4.667	60	60	0	65	65.200	0.308
Cervical	60	61.00	1.667	-	-	-	-	-	-
Thorax	74	75.100	1.486	-	-	-	-	-	-
Abdomen	80	82.700	3.375	80	80.600	0.750	80	81.300	1.625
Head	90	92.300	2.556	100	103.100	3.100	90	91.600	1.780
							100	102.100	2.100
Skull	-	-	-	120	120.100	0.083	120	122.200	1.833

3.2 Time accuracy test

The accuracy of exposure time of three x-ray machines were carried out by setting the source to detector at 100 cm for different kV. The exposure time applied to the different organ imaging at two hospitals that ranged 50-125, 172-318 and 40-70 ms, and are presented in the Table 2. The time variation for machine 1 (Shimadzu IEC60601-1-2-2001) varies from 0% to 0.8%, for machine 2 (Shimadzu IEC60601-1-2-2001) it was from 0% to 1.18% and for machine 3 (Shimadzu IEC60601-1-2-2001) it was from 0.5% to 2.29%.

Table 2. The accuracy of time for different kVs of some organ's imaging test of three machines.

Organ	Machine 1 (Shimadzu IEC60601-1-2-2001)		Machine 2 (Shimadzu IEC60601-1-2-2001)		Machine 3 (Shimadzu IEC60601-1-2-2001)	
	Exposure time, measured time (ms)	Deviation (%)	Exposure time, measured time (ms)	Deviation (%)	Exposure time, measured time (ms)	Deviation (%)
Chest	71.000	0.420	220.000	0.270	45.000	1.100
	71.300		220.600		45.500*	
Cervical	100.000	0.000	-	-	-	-
	100.000					
Thorax	50.000	0.800	-	-	-	-
	50.400					
Abdomen,	100.000	0.500	220.000	0.273	70.000	2.290
Pelvis	100.500		220.600		71.600	
Head	125.000	0.240	-	-	40.000	0.500
	125.300				40.200	
Head	-	-	318.000	0	40.000	0.250
			318.000		39.900	
Skull	-	-	170.000	1.180	40.000	0.500
			172.000		40.200	

©2023 Faculty of Science and Technology, Suan Sunandha Rajabhat University

*It was taken at tube voltage of 65 kV.

3.3 Linearity of output as a function of time

All the measurements were performed at fixed exposure time and tube voltage 80 kV. The proportional variation of dose and mA for x-ray machines was checked at fixed exposure time as shown in Table 3. The coefficient of linearity for exposure time is 0.017.

Table 3. Linearity of output as a function of mA at exposure time 100 ms and tube voltage 80 kV.

Mean (kVp)	Tube current (mA)	Measured time (ms)	Air kerma (µGy)	Dose to mA ratio, X	Linearity, L
81.5	160	100.5	646.900±18.111	40.430	
81.6	200	100.8	781.600±21.884	39.080	
81.6	250	100.5	988.800±27.686	39.550	0.017
81.8	320	100.5	1274.000±35.672	39.810	

3.4 Linearity of output as a function of kV

At a constant exposure time and tube current, three exposures were performed with different tube voltages. Table 4 shows the measurement value for the linearity of output as a function of kV.

Table 4. Linearity values of output as a function of kV at fixed exposure time 100 ms and tube current 160 mA.

Tube voltage (kV)	Mean kVp	Air kerma (µGy)
60	60.2	344.7
100	101.9	1001.0
120	121.4	1385.0

3.5 Half Value Layer measurements

It was measured for two machines namely Machine 1 and 4 (Siemens part8375545g2107). The filtration of the x-ray unit for Machine 1 was measured for 40-100 kV,40 mAs and SSD 100 cm. The output dose was measured with a different thickness of Al sheet (1.5, 3, 3.5, 4 mm). Again, the x-ray filtration of Machine 4 was measured for 40-99 kV,10 mAs and source to detector distance was 100 cm. and the output dose was measured for different filter thickness of Al sheet (1.5, 3, 3.5, 4 mm). Then the dose was plotted as a function of thickness for each x-ray unit and the thickness for which the dose reduced to half gave the half value thickness. The thickness of aluminum needed to reduce the intensity of the beam to one half of its original values for Machine 1 and Machine 4 (Figure 2 and Figure 3). From the attenuation curve, HVL values were extracted which is given in Table 5 for Machine 1 and Machine 4 and Compared with the recommended value given by International Electrotechnical Commission 2008 IEC 2008 (Health Canada, 2008) of aluminum for x-ray tube voltages.

©2023 Faculty of Science and Technology, Suan Sunandha Rajabhat University

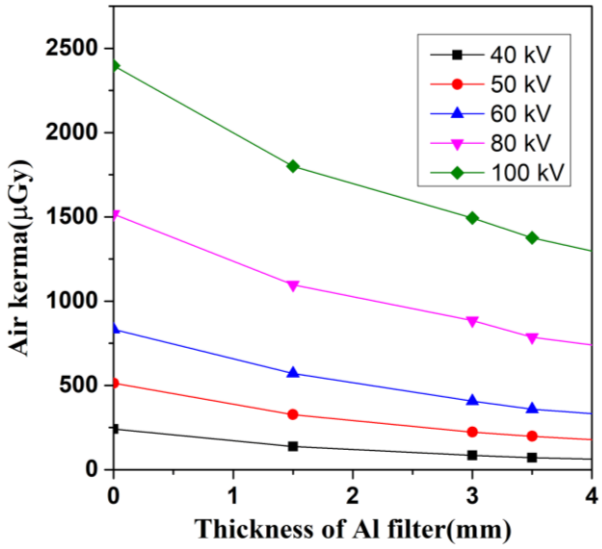

Figure 2. Graphical representation of dose as function of thickness for HVL measurements of Machine 1 (Shimadzu IEC60601-1-2-2001) for 40, 50, 60 80 and 100 kV respectively.

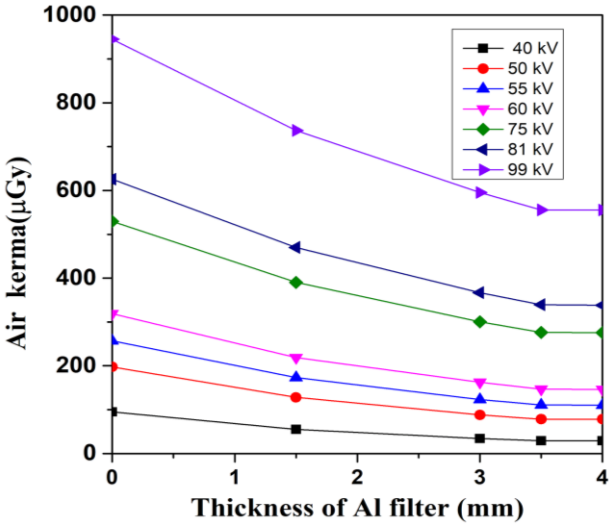

Figure 3. Graphical representation of dose as function of thickness for HVL measurements of Machine 4 (Siemens part8375545g2107) for 40, 50, 55, 60, 75, 81 and 99 kV respectively.

©2023 Faculty of Science and Technology, Suan Sunandha Rajabhat University

Table 5. Experimental value of HVL value and comparison with IEC.

Tube potential (kV)	Inherent filtration of 1.5 mm Al filtration, M1 (Shimadzu IEC60601-1-2-2001)	Inherent filtration of 1 mm Al filtration, M4 (Siemens part8375545g2107)	IEC 2008 (Health Canada, 2008)
40	1.89	1.89	1.42
50	2.41	2.52	1.78
55	-	2.85	1.96
60	2.87	3.14	2.14
75	-	3.97	2.68
80	3.81	-	2.90
81	-	4.33	2.90
99	-	5.38	3.55
100	4.68	-	3.60

4. Discussion

During radiological assessment, it is imperative to keep the openness portion low with great picture quality thinking about patients' constitution. Idea of QC assists with diminishing the fluctuation of the same sort of assessments. In this investigation the QC test has a decent concurrence with the suggested acknowledgment levels. In any case, there is a need to take care of the chest x-beam assessment of machine 1 as it is near acknowledgment level. The accuracy of kV is very good for three machines that lie within the acceptable limit $\pm 5\%$ (Ranallo, 1998). Though all the results were good, the deviation was very close to the boundary of the acceptance level at tube voltage 60 kV used for chest and at tube voltage 80 kV used for abdomen in the x-ray machine 1. During time accuracy tests there is higher deviation for abdomen in machine 3 than others. The accuracy of exposure time was found good in agreement with all settings for imaging lying within the tolerance limit ±5% (Ranallo, 1998). The coefficient of linearity for exposure time is 0.017 which does not exceed the recommended value, i.e. it is within the tolerance limit $\pm 5\%$ (International Commission on Radiation Units and Measurements, ICRU Report - 51, 1993) which indicates that there is no need to calibrate the machine urgently. From Table 5 it is seen that HVL is not less than the recommended value. For machine 1 with inherent filtration 1.5 mm, the HVL is 2.87 which is slightly close to the value 2.14. The effective energy (keV) can be evaluated by using the established empirical formula which was obtained by the interpolation value from Hubble mass attenuation coefficients (Rahman et al., 2008). The measured half value layer was used in this formula to determine the effective energy for two x- ray machines at two hospitals. Different effective energy corresponds to different HVL for different tube voltages. To evaluate an exposure dose, the effective energy of the x- ray is required for which the measurement of HVL is also needed.

5. Conclusions

The quality control test assumes a significant part to have a decent picture without reiteration of openness. Without appropriate exactness of x-beam boundaries utilized during imaging tests, there is likelihood that the patients and the radiation laborers can have additional portions. Sometimes excessive radiation can create inherent exposure to healthy cells. That is not only dangerous for patients but also for radiation workers (Doctors. Patients, nurse and Medical physicist). In this investigation, the outcomes are inside a worthy breaking point. In spite of the fact that it gives great outcomes, the utilization of new gear will assist with lessening the conveyed portion by utilizing legitimate radiological boundaries. This investigation mirrors not only the current circumstance of utilizing radiography framework in diagnostic radiology but also the safety measurement taken the Government republic of Bangladesh with the Secondary Standard Dosimetry Laboratory, Bangladesh Atomic Energy Commission, Dhaka, Bangladesh.

©2023 Faculty of Science and Technology, Suan Sunandha Rajabhat University

Acknowledgement

This research work was performed in collaboration with Four Government Medical colleges of Bangladesh in association with Bangladesh Atomic Energy Commission and Department of Physics, University of Chittagong. We acknowledged all team workers of different sectors at Radiology departments.

Authors email and ORCID

Sadeka Sultana Rubai: rubaisultana.91@gmail.com; 0000-0002-3977-8229
Santunu Purohit: santunupurohit@cu.ac.bd; 0000-0002-0029-995X
Tanjim Siddiqua: tanjim.siddiqua@gmail.com; 0000-0001-8920-340X
Md. Shakilur Rahman: shakilurssdl@baec.gov.bd; 0000-0002-7873-7999
*AKM Moinul Haque Meaze (Corresponding author): meaze@cu.ac.bd; mhqmeaze@yahoo.com; 0000-0002-1526-2113

References

Abd-Alla, A., Salih, S. M., & Albashir, F. A. (2019). Evaluation of X-ray machines Gezira state: Based quality control. *International Journal of Innovative Science, Engineering and Technology*, *6*(7), 68-71.

Abdulkadir, M. K. (2020). Quality assurance in medical imaging: A review of challenges in Nigeria. *Journal of Radiology Nursing*, *39*(3), 238-244. doi:10.1016/j.jradnu.2020.02.005

Al-Kinani, A. T., & Mohsen, Y. (2014). Study of the quality assurance of conventional X-ray units at medical city in Baghdad. *Arab Journal of Nuclear Sciences and Applications*, *47*(2), 129-137.

Asadinezhad, M., Bahreyni Toossi, M. T., Ebrahiminia, A., & Giahi, M. (2017). Quality control assessment of conventional radiology devices in Iran. *Iranian Journal of Medical Physics*, *14*(1), 1-7. doi:10.22038/ijmp.2017.19052.1173

Gholami, M., Nemati, F., & Karami, V. (2015). The evaluation of conventional X-ray exposure parameters including tube voltage and exposure time in private and governmental hospitals of Lorestan province, Iran. *Iranian Journal of Medical Phys*ics, *12*(2), 85-92. doi:10.22038/ijmp.2015.4770

Health Canada. (2008). *Safety Code 35: Safety procedures for the installation, use and control of X-ray equipment in large medical radiological facilities*. Health Canada.

Inkoom, S., Schandorf, C., Emi-Reynolds, G., & Fletcher, J. J. (2011). Quality assurance and quality control of equipment in diagnostic radiology practice-the Ghanaian experience. In I. Akyar (Ed.), *Wide spectra of quality control* (pp. 291-308). InTech. doi:10.5772/22591

International Atomic Energy Agency. (2007). *Technical Reports Series No. 457: Dosimetry in diagnostic radiology: An international code of practice*. Vienna, Austria: IAEA.

International Commission on Radiation Units and Measurements. (1993). *ICRU Report 51, Quantities, quantities and units in radiation protection dosimetry*. Bethesda, MD: ICRU.

Ismail, H. A., Ali, O. A., Omer, M. A, Garelnabi, M. E., & Mustafa, N. S. (2015). Evaluation of diagnostic radiology department in term of quality control (QC) of X-ray units at Khartoum state hospitals. *International Journal of Science and Research*, *4*(1), 1875-1878.

Rahman, M. S., Kim, G., Tsujimura, N., Yoshida, T., Kanai, K., & Kurihara, O. (2008). Influence of the PMMA slab and ISO water phantom in calibrating personal dosimeter in the energy range of 36-662 keV. *Journal of Nuclear Science and Technology*, *45*, 264-267. doi:10.1080/00223131.2008.10875838

Ranallo, F. N. (1998). Recommended standards for the routine performance testing of diagnostic X-ray imaging systems, IPEM Report No. 77. *Medical Physics*, *25*(8), 1556-1557. doi:10.1118/1.598335

Rubai, S. S., Rahman, M. S., Purohit, S., Patwary, M. K. A., Meaze, A. K. M. M. H., & Mamun, A. A. (2018). Measurements of entrance surface dose and effective dose of patients in diagnostic radiography. *Biomedical Journal of Science and Technical Research*, *12*(1), 1-5. doi:10.26717/BJSTR.2018.12.002186

Taha, T. M. (2011). Study the quality assurance of conventional X-ray machine using non-invasive KV meter. *Proceedings of the Tenth Radiation Physics and Protection Conference* (pp. 105-110). Cairo, Egypt.

Available online at https://li02.tci-thaijo.org/index.php/ssstj

Suan Sunandha Science and Technology Journal
©2023 Faculty of Science and Technology, Suan Sunandha Rajabhat University

Spatial Distribution of Crimes Against Property: A Case Study in Nakhon Pathom Province

Wichittra Phlicharoenphon[1*], Ornprapa Pummakarnchana Robert [2]

[1]Program in Forensic Science and Criminal Justice, Faculty of Science, Silpakorn University, 6, Rajamankha Nai Road., Mueang Nakhon Pathom, Nakhon Pathom, 73000, Thailand

[2]Department of Environmental Science, Faculty of Science, Silpakorn University, 6, Rajamankha Nai Road., Mueang Nakhon Pathom, Nakhon Pathom, 73000, Thailand

***Corresponding author e-mail: wichittra.phl@gmail.com**

Received: *11 January 2023* / **Revised:** *8 March 2023* / **Accepted:** *19 April 2023*

Abstract

Crimes against property were correlated with the recession of the economy. According to the Royal Thai Police report, crimes against property continue to increase. The criminal statistics showed that the second-highest number of crimes against property was found in Nakhon Pathom Province. The purposes of this study were to 1) examine the pattern of crimes against property using Moran's I, 2) investigate the spatial distribution of crimes against property using Getis-Ord Gi*, 3) find out the directional distribution of crimes against property using a standard deviational ellipse, and 4) explore the spatial relationship between crimes against property, land use, and population density. Secondary data on crime cases were collected from the Mueang Nakhon Pathom Police Station criminal report book between 2013 and 2018 and then converted to spatial data. The results of the study were as follows: 1) The pattern of the cases over 5 years was clustered; 2) the spatial distribution of cases revealed hotspot areas with a GiZscore greater than 1.65 over 5 years covering residential and village areas, city and town areas, commercial areas, entertainment venues, local education institutes, the boulevard, dark alleys, and deserted streets; 3) the directional distribution of the cases over 5 years was distributed to the west of the study area; and 4) urban and built-up land was discovered where most cases occurred. Overall, the crimes against property clustered around crowded residential areas and villages, dark alleys, and deserted streets. This study facilitates investigations, defense, and control of crimes against property.

Keywords: Crimes against property, Geo-statistic analysis, Moral's I, Getis-Ord Gi*, Standard deviational ellipse

1. Introduction

Thailand has developed from an agricultural to an industrial country. This change has impacts on the economy and society including the higher cost of living and unemployment. The rising cost of living and unemployment can cause higher crime. Moreover, the expansion of urbanization has affected more crime, more complex patterns, and violent tendencies, especially crimes against property (Phuaksomon, 2020).

Crimes against property have become a major problem affecting peace and social security in Thailand (Phuaksomon, 2020). The statistics report of arrested crimes divided by cases and provinces in Thailand between 2007 and 2016 revealed the highest number of the cases were crimes against property including robbery and embezzlement (National Statistical Office, 2016). Similarly, the National Economic and Social Development Council data reported that overall criminal cases in the third quarter of 2021 increased, as did the 17.3% increase in crime against properties (12,623 cases), with the highest number of theft (45.4%) (Royal Thai Police, 2021). The criminal cases discovered in Nakhon Pathom Province between 2007 and 2018 were the following; 91.18% of theft cases, 4.72% of snatching cases, 3.20% of robbery, and 0.90% of gang robbery cases (Rattanapongs & Gulabutr, 2020).

In the criminal code of Thailand, crimes against property were categorized into 11 major groups (Dharmniti, 2019): 1) theft, the taking of

©2023 Faculty of Science and Technology, Suan Sunandha Rajabhat University

another person's property by dishonesty (Article 334), 2) robbery, the stealing in front of the owner (Section 336), 3) extortion, the compelling others to allow oneself or others to gain an advantage in an asset way by threatening to harm life, body, liberty, reputation, or property (Section 337), 4) robbery, the getting something, especially money, from someone by using force or threats (Section 338), 5) stealth, theft "by force" (Article 339), 6) gang robbery, a robbery by committing more than three people offences (Section 340), 7) fraud, the deceiving other people by displaying false statements or concealing true statements (Section 341), 8) embezzlement, the possession of another person's property and then corruptly claiming that property as one's own or a third person (Section 352), 9) offenses of receiving stolen property, helping to conceal, sell, help to take away, buy, pledge, or otherwise accept (Section 357), 10) mischief, damaging, destroying, depreciating, renders useless" of property belonging to another person (Section 358), and 11) trespassing, the entering into someone else's immovable property, to take possession of that immovable property, in whole or in part, or to do any act that disturbs the normal possession of the immovable property (Article 362) (Thailand Lawyer, 2020).

To our knowledge, the geo-spatial analysis approach is widely applied in spatial analysis. (Paramasivam & Venkatramanan, 2019). Hence, the characteristics of crimes can be considered geographically using crime mapping and the geo-statistical analysis techniques. Autocorrelation Moran's I, which is one of the geo-statistical analysis techniques, can be used to identify the clustering of crimes across the study area (on a global scale) (Mitchell, 2005; Prasannakumar, Vijith, Charutha, & Geetha, 2011) applied this technique to observe the overall pattern of crime incidents. Getis-Ord Gi* referred to as a geo-statistical method can be applied to identify specific clusters of high or low-crime incidents.

Standard Deviational Ellipse (SDE) is one of the standard methods to facilitate investigations and the prioritization of police work, crime prevention, and suppression planning (Balogun, Okeke, & Chukwukere, 2014; Srithamarong, 2016; Yiampisan & Srivanit, 2010) employed Moran's I approach to evaluate crime-risk areas and crime patterns. High-incident areas known as hotspots (In-ain, 2018) were identified by using the Getis-Ord Gi* technique. Srithamarong (2016) further studied the directional distribution of crime incidents using the Standard Deviational Ellipse (SDE). SDE allowed us to see if the distribution of crimes was elongated and hence had a particular orientation (Wang, Shi, & Miao, 2015). Dechsiri and Robert (2019) also investigated crime-risk areas of drug smuggling based on Moran's I, Getis-Ord Gi*, and SDE. Mohammed and Baiee (2020) identified the riskiest area for Baltimore City using the Getis-Ord Gi* technique. Achu, Aju, Suresh, Manoharan and Reghunath (2019) investigated the spatial and temporal patterns of road accidents using autocorrelation in Moran's I and Getis-Ord Gi*. Chutia et al. (2020) analyzed spatio-temporal incidents of crime in Shillong, Meghalaya, India. Incremental autocorrelation in Moran's I technique made it possible to explain the pattern of crime, and Getis-Ord Gi* described clusters of high- or low-crime incidents. Ahmed and Salihu (2013) disclosed the spatial pattern of crimes in the area of Dala L.G.A, Kano State, Nigeria, using Moran's I and Getis-Ord Gi*. The results showed that the crime rate was higher than outside the city wall, and more hotspots were found outside the city because of the absence of police stations.

The objectives of this research were 1) to examine the pattern of offences against property cases, 2) to investigate the spatial distribution of offences against property cases, 3) to determine trends and directions of distribution of offences against property cases, and 4) to discover the spatial relationship between a crime against property, land use, and population density. The study area was Nakhon Pathom Province, the 9th province with the most crimes against property reported in 2011 (National Statistical Office, 2011) and the 2nd highest crimes against property found between 2013 and 2017

2. Materials and Method

2.1 Materials

Table 1 explains the data used in this investigation. The study area is Mueang Nakhon Pathom, as seen in Figure 1. The statistics of criminal data including cases, arrest points, and date and time of incidents reported, were secondary data retrieved from the Criminal Statistics Reported Book of Mueang Nakhon Pathom Police Station between 2013 and 2018. After that, the criminal-reported books were converted to .xlsx and spatial.

©2023 Faculty of Science and Technology, Suan Sunandha Rajabhat University

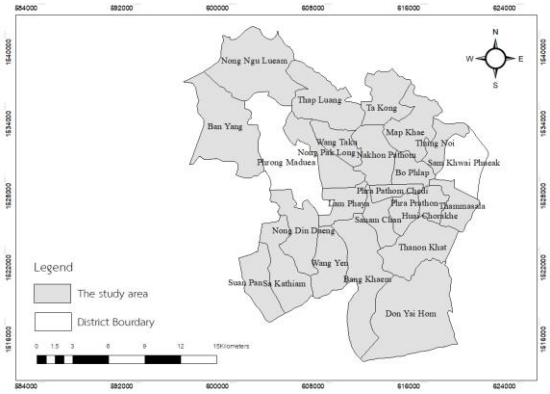

Figure 1. Responsibility area of Mueang Nakhon Pathom Police Station, the study area.

Figure 2. Methodology of the study consists of the following steps: first, input criminal data (.xlsx). After that, the criminal data was converted to a suitable .shp before 4 steps of analysis: 1) Global geo-statistic, Moran's I to evaluate the pattern of similar correlation overall in the study area. 2) Local geo-statistic, Getis-ord Gi* for evaluation of a specific area. Then, hotspot results were continued to be analyzed with 3) Directional distribution for predicting the trend and distribution of crime. Finally, 4) Find the spatial relationship between land use, population density, and crime.

2.2 Methods

Figure 2 displays the workflow of this study, which is 2.2.1) identifying patterns of crimes against property using Moran's I, 2.2.2) finding the prevalence of crimes against property using Getis-Ord Gi*, 2.2.3) determining trends and direction of distribution of crimes against property using standard deviational ellipse, and 2.2.4) discovering the spatial relationship between crimes against property, land use, and population density.

Table 1. Data and data source of the study.

Data	Detail	Data source / Year
Crimes Statistics Reported of Mueang Nakhon Pathom Police Station, Nakhon Pathom Province, 2013 to 2018	cases, arrest point, date and time of reporting, date and time of arrest	Crimes Statistics Reported book of Mueang Nakhon Pathom Police Station, Nakhon Pathom Province, retrieved from 2013 to 2018
Administrative district	The administrative district of Mueang Nakhon Pathom, Nakhon Pathom Province, ratio 1:25,000 (.shp)	Land Development Department (2015 and 2017)
Land use	The administrative district of Mueang Nakhon Pathom, Nakhon Pathom Province, ratio 1:25,000 (.shp)	Land Development Department (2010 to 2017)
Population density	Population per yearly, per sub-district (.xls)	Department of Provincial Administration (2013 to 2017)

2.2.1 Identifying patterns of crime against property using Moran's I

Moran's I is a correlation coefficient that is used for finding patterns in complicated data sets. Moran's I result shows a value from -1 to 1. If the value approaches 1, the data is clustered. If the value is close to -1, the data is scattered, and if the value approaches 0, the distribution is random (Dechsiri & Robert, 2019), as seen in equation (1).

$$I = \left(\frac{n}{\sum_{i=1}^{n}\sum_{j=1}^{n}\omega_{ij}} \right) \frac{\sum_{i=1}^{n}\sum_{j=1}^{n}\omega_{ij}\left(x_i-\bar{X}\right)\left(x_j-\bar{X}\right)}{\sum_{i=1}^{n}\left(x_i-\bar{X}\right)^2} \quad (1)$$

Where I = Moran's I Index value

$\sum_{i=1}^{n}\left(x_i-\bar{X}\right)^2$ = The sum of the squares of the difference between the event value and mean, where xi and xj are the statistics of crime against property cases in Mueang Nakhon Pathom Police Station's responsibility area

©2023 Faculty of Science and Technology, Suan Sunandha Rajabhat University

$\bar{x}$ = Mean of arrests for crime against property cases in the Mueang Nakhon Pathom Police Station's responsibility area from 2013 to 2017

N = The scope of the study

$\sum_{i=1}^{n}\sum_{j=1}^{n}\omega_{ij}$ = Sum of polygons enclosed which matched in the study. The area obtained from the weighted matrix of the i and j where a value approaching 1 means i and j are neighbors meanwhile a value approaching 0 means i and j are not together

$\sum_{i=1}^{n}\sum_{j=1}^{n}\omega_{ij}\left(x_i-\bar{X}\right)\left(x_j-\bar{X}\right)$ = The weighted value of the difference between the event values and meaning of neighbours where X_i and X_j are the numbers of occurrences of the interest factor in i and j

2.2.2 Finding the prevalence of crime against property using Getis-Ord Gi*

Getis-Ord Gi* or Hot Spot Analysis based Getis-Ord Gi* is a specific spatial statistic used to identify high- and low-incident areas the study area. If the value of GiZscore is greater than 1.65, the study area has a very high incidence and if the value of GiZscore is less than -1.65, it means the study area has a very low incidence (Abdulhafedh, 2017) as shown in equation (2).

$$G_i^*(d)=\frac{\sum_j w_{ij}(d)x_j-w_i^*\bar{X}}{S\left\{\left[\left(nS_{ij}^*\right)-W_X^{*2}\right]/(n-1)\right\}^{1/2}} \quad (2)$$

where x_j = value of variable x at location j

w_{ij} = elements of the weight matrix

n = the number of crimes

S = the variance of Getis-ord Gi* where

$$S=\sqrt{\frac{\sum_j x_j^{\,2}}{n}-\left(\bar{X}\right)^2}$$

$\bar{x}$ = mean of the variable x

2.2.3 Determining trends and direction of distribution of crime against property cases using Standard Deviational Ellipse

Directional distribution (Standard Deviational Ellipse or SDE), is the dispersion direction analysis for measuring the distribution of crime points by calculating distances in x- and y-axis directions; the values of x- and y- can determine the ellipse's axis size and thus show the distribution of incidents and also indicate the rotation angle of the ellipse or the distribution direction of the data as demonstrated in equations (3) and (4) (ESRI, 2009a, 2009b, 2009c).

$$SDE_y=\sqrt{\frac{\sum_{i=1}^{n}\left(y_i-\bar{Y}\right)^2}{n}} \quad (3)$$

$$SDE_x=\sqrt{\frac{\sum_{i=1}^{n}\left(x_i-\bar{X}\right)^2}{n}} \quad (4)$$

where x_i = crimes point at I position and x axial

y_i = crimes point at I position and y axial

$\bar{x}$ = mean center of crime along the x-axis

$\bar{y}$ = mean center of crime along the y-axis

n = number of crimes point.

the determine of rotation angle as shown in equations (5) to (8), respectively.

$$\tan\Theta=\frac{A-B}{C} \quad (5)$$

$$A=\left(\sum_{i=1}^{n}\bar{X}_i^2-\sum_{i=1}^{n}\bar{Y}_i^2\right) \quad (6)$$

$$B=\sqrt{\left(\sum_{i=1}^{n}\bar{X}_i^2-\sum_{i=1}^{n}\bar{Y}_i^2\right)^2+4\left(\sum_{i=1}^{n}\bar{X}\bar{Y}\right)^2} \quad (7)$$

$$C=2\sum_{i=1}^{n}\bar{X}_i\bar{Y}_i \quad (8)$$

where $\bar{x}_i$ = deviation of x position from the central mean

$\bar{Y}_i$ = deviation of Y position from the central mean

2.2.4 Discovering the spatial relationship between crime against property, land use and population density

The spatial relationship between land use and the occurrence of crime against property was analyzed using the overlay technique, i.e., hot and cold spots of crime acquired from Getis-Ord Gi*

©2023 Faculty of Science and Technology, Suan Sunandha Rajabhat University

were spatially overlaid with land use data to investigate spatial relationships. Afterward, population density data were included discover the spatial relationship between crime incidents and population density.

3. Results and Discussion

3.1 Patterns of crime against property

The patterns of crime against property between 2013 and 2017 in Mueang Nakhon Pathom were all clustered according to Moran's I value, which was discovered at 0.32, 0.27, 0.29, 0.27, and 0.23, as shown in Figures 3-7. The pattern results were concentrated in the city center, with some scattered in villages and on deserted roads with insufficient lighting. Spatial autocorrelation analysis results were displayed in Figures 8-12, respectively.

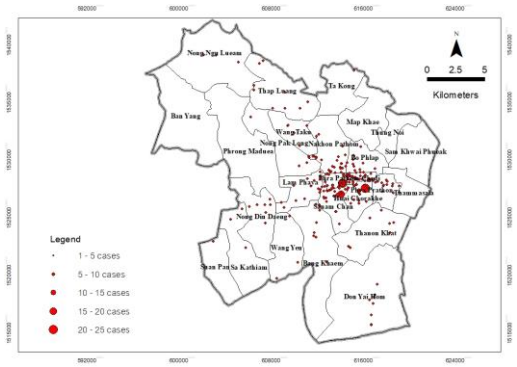

Figure 3. The crime against property pattern in 2013.

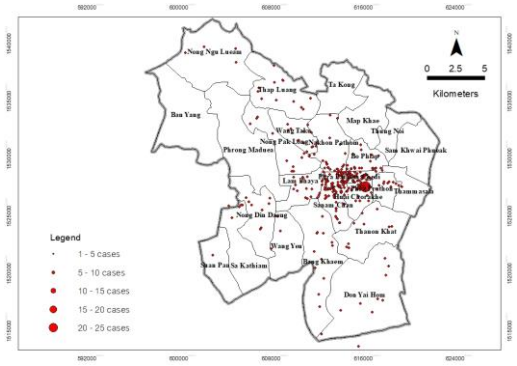

Figure 4. The crime against property pattern in 2014.

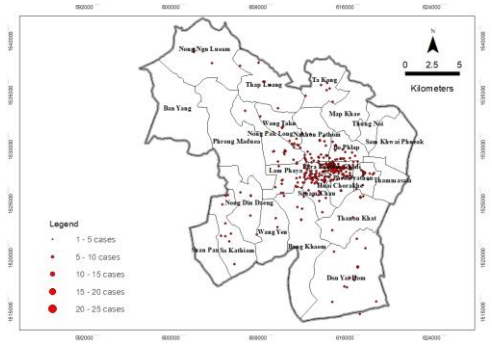

Figure 5. The crime against property pattern in 2015.

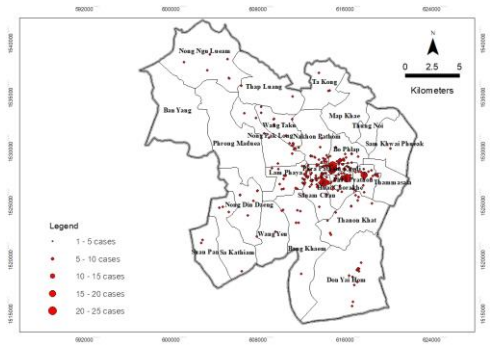

Figure 6. The crime against property pattern in 2016.

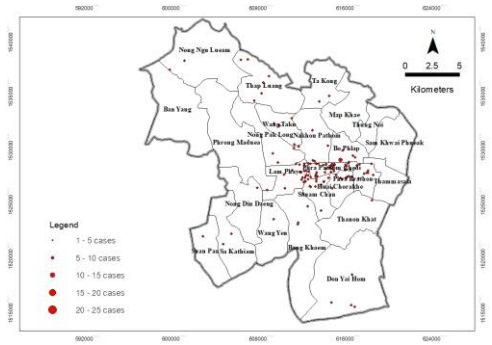

Figure 7. The crime against property pattern in 2017.

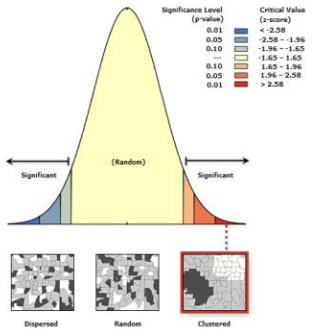

Figure 8. Spatial autocorrelation report of crime against property in 2013.

Available online at https://li02.tci-thaijo.org/index.php/ssstj
Suan Sunandha Science and Technology Journal
©2023 Faculty of Science and Technology, Suan Sunandha Rajabhat University

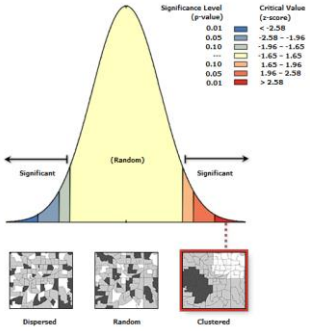

Figure 9. Spatial autocorrelation report of crime against property in 2014.

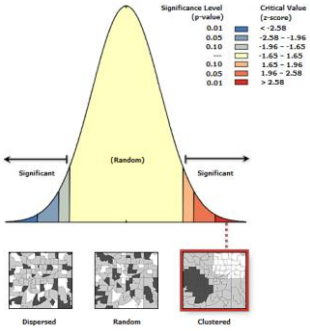

Figure 10. Spatial autocorrelation report of crime against property in 2015.

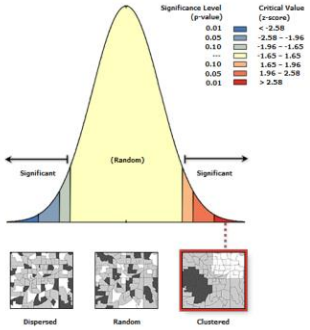

Figure 11. Spatial autocorrelation report of crime against property in 2016.

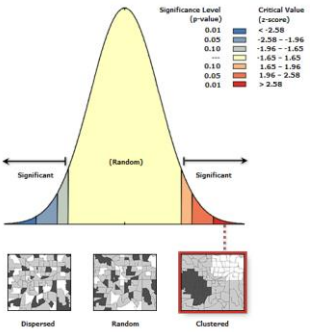

Figure 12. Spatial autocorrelation report of crime against property in 2017.

3.2 Hotspot analysis of crime against property based Getis-Ord Gi*

The crime against property cases from 2013 to 2017 in Mueang Nakhon Pathom were discovered high-incidence areas with a GiZscore greater than 1.65. In this case, those areas were as follows: Huai Chorakhe, Phra Prathon, and Thammasala district in 2013 (Figure 13); Huai Chorakhe, Bo Phlap, Thammasala, Phra Prathon, and Thanon Khat district in 2014 (Figure 14); Huai Chorakhe and Phra Prathon district in 2015 (Figure 15); Bo Phlap, Phra Phathom Chedi, Phra Prathon, Sanam Chan, Huai Chorakhe and Thanon Khat district in 2016 (Figure15); Huai Chorakhe and Phra Prathon district in 2017 (Figure 16); The results indicate that, a high incidence of crime was around the city and slightly towards the Mueang Nakhon Pathom borderland and adjacent provinces.

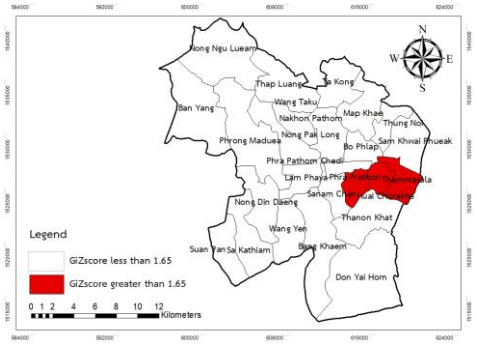

Figure 13. Hotspot analysis of crime in 2013.

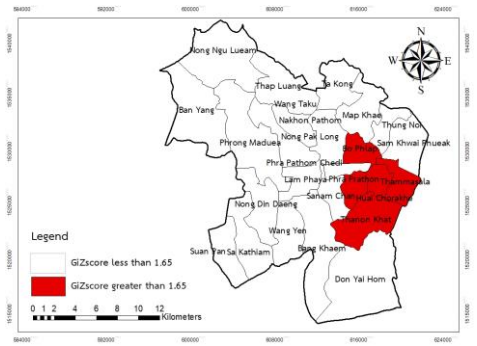

Figure 14. Hotspot analysis of crime in 2014.

Available online at https://li02.tci-thaijo.org/index.php/ssstj
Suan Sunandha Science and Technology Journal
©2023 Faculty of Science and Technology, Suan Sunandha Rajabhat University

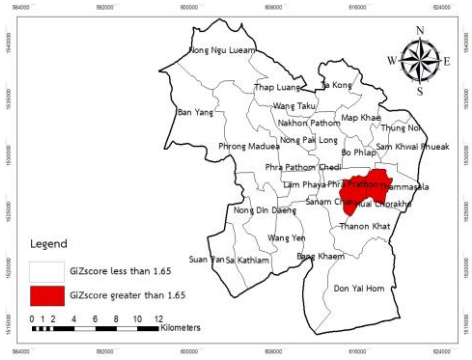

Figure 15. Hotspot analysis of crime in 2015.

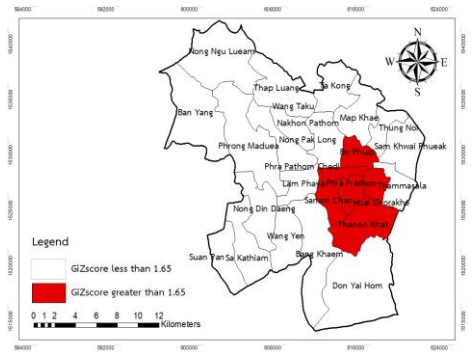

Figure 16. Hotspot analysis of crime in 2016.

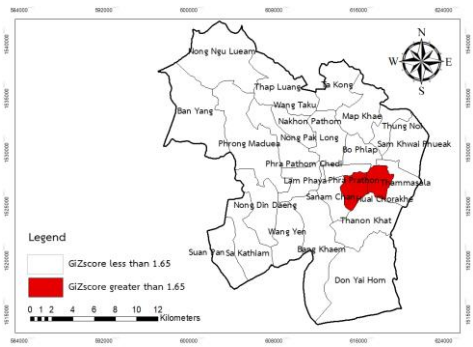

Figure 17. Hotspot analysis of crime in 2017.

3.3 Direction distribution results of crime against property with standard deviational ellipse

The trend and distribution of crime against property cases in Mueang Nakhon Pathom revealed that all of the distribution directed to the west covered Bo Phlap, Phra Prathon, Phra Prathom Chedi, Huai Chorakhe, and Thanon Khat districts in 2013 (Figure 18); the rotation value of 115.58 covered Bo Phlap, Phra Prathon, Phra Prathom Chedi, Huai Chorakhe, and Thanon Khat districts in 2014 (Figure 19). The rotation value of 143.09 covered Bo Phlap, Phra Prathon, Phra Prathom Chedi, Huai Chorakhe, Thanon Khat, Nakhon Pathom, and Sanam Chan districts in 2015 (Figure 20). The rotation value of 125.43 covered Bo Phlap, Phra Prathon, Phra Prathom Chedi, Huai Chorakhe, Thanon Khat, and Nakhon Pathom districts in 2016 (Figure 21). The rotation value of 144.34 covered Bo Phlap, Phra Prathom Chedi, Phra Prathon, Huai Chorakhe, Thanon Khat, Nakhon Pathom, and Sanam Chan districts in 2017 (Figure 22). All of the distribution had a direction to the west of the study area, covering the town center and heading to the borderland to adjacent provinces, the main, long roads to Bangkok, and Samut Sakhon Provinces, which sometimes did not have enough light.

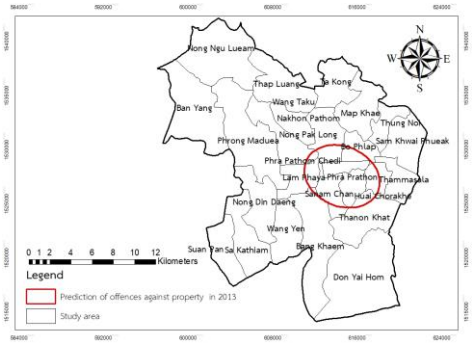

Figure 18. Trend and distribution of crime against property in 2013.

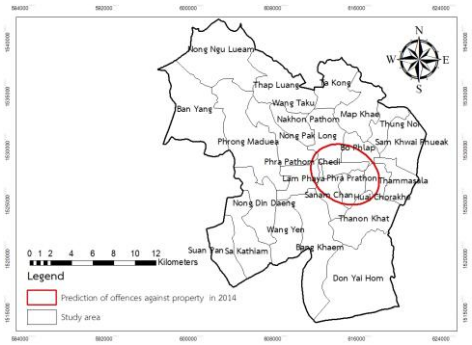

Figure 19. Trend and distribution of crime against property in 2014.

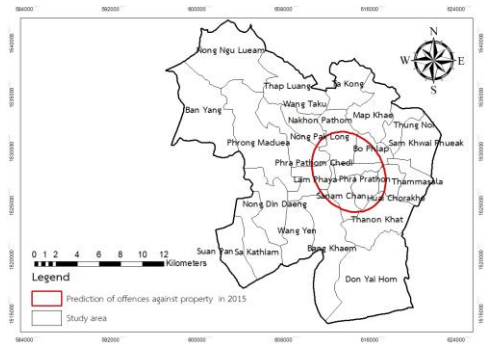

Figure 20. Trend and distribution of crime against property in 2015.

Available online at https://li02.tci-thaijo.org/index.php/ssstj
Suan Sunandha Science and Technology Journal
©2023 Faculty of Science and Technology, Suan Sunandha Rajabhat University

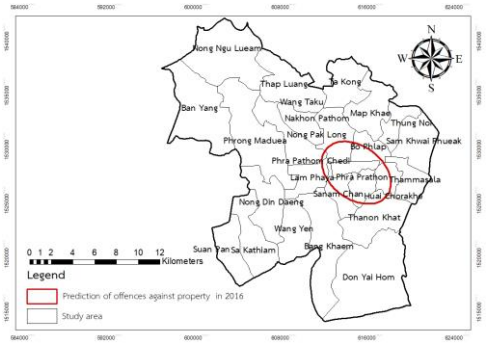

Figure 21. Trend and distribution of crime against property in 2016.

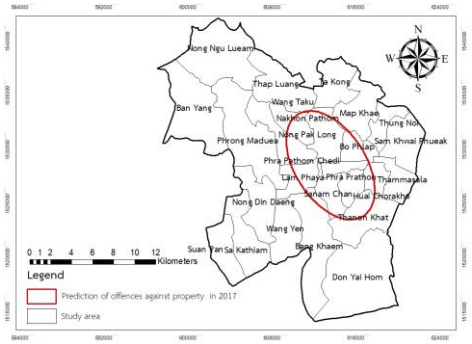

Figure 22. Trend and distribution of crime against property in 2017.

Table 2. Analysis results of crime against property using standard deviational ellipse.

Years	Center X	Center Y	X Std Dist	Y Std Dist	Rotation
2013	100.05710	13.81252	0.034028	0.025081	110.14535
2014	100.06022	13.81491	0.031438	0.023738	115.57669
2015	100.05246	13.81789	0.035852	0.029069	143.09139
2016	100.06135	13.81553	0.032435	0.022277	125.43046
2017	100.04804	13.82184	0.051394	0.030611	144.33950

3.4 Validation of predicted spatial trend and distribution of crime incidents

The spatial trend and distribution of crime incidents were validated using predicted cases and actual incidents, as shown in Table 3. The average of crime incidents from 2013 to 2017 was used to validate actual crime cases discovered in 2018. The result of the average rotation was 127.72 degrees toward the west direction. The spatial distribution of actual crime incidents in 2018 was at a 108.40-degree rotation. This explained why the precision of the predicted spatial trend and distribution of crime was 94.18%.

Table 3. The result of the validation of the analysis.

Crime against property cases	Rotation
predict of cases	127.71668
actual cases	108.40097

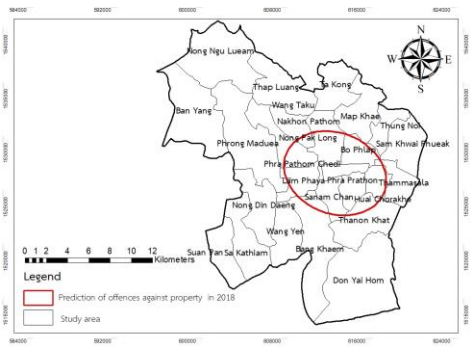

Figure 23. Trend and distribution of crime against property in 2018.

3.5 Spatial relationship between crime against property, land use and population density

The spatial relationship between the occurrence of crime against property and land use in the same years (2015 and 2017) was analyzed. The data for 2015 showed 453 crimes against property cases with 219 incident coordinates in urban and built-up areas (48.34%) (Figure 24). Similarly, the data for 2017 showed 348 crimes against property cases with 158 incident coordinates in urban and built-up areas (45.40%) (Figure 25). In addition, the results showed incidents of crime were almost exclusively found in cities, towns, and commercial areas (49.44%), institutions (18.74%), and villages (15.12%), respectively.

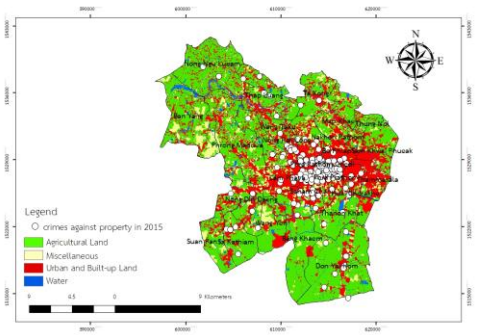

Figure 24. The relationship between land use and crimes against property in 2015.

©2023 Faculty of Science and Technology, Suan Sunandha Rajabhat University

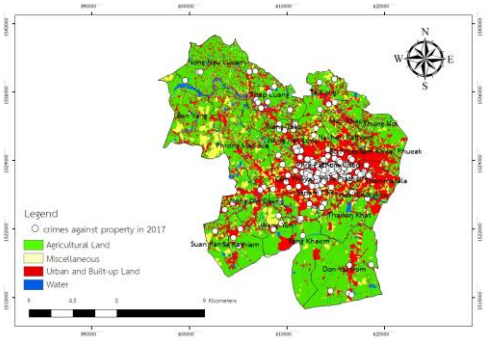

Figure 25. The relationship between land use and crime against property in 2017.

Moreover, the spatial relationship between a crime against property and population density was analyzed. The result showed a spatial relationship between population density and a crime against property in the Phra Pathom Chedi district, the location of the city center consists of tourist attractions, schools, residences, villages and community malls (Figure 26). The results showed a correlation in Sanam Chan district, where there is a low population density but a large number of temporary residents, a passive population, and a cluster of entertainment venues and on-premise and off-premise alcohol retailers because Sanam Chan district is located near universities, schools, dormitories that are always crowded, and a large number of commercial establishments (Figure 27).

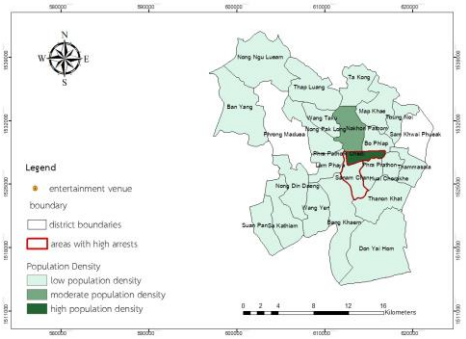

Figure 26. The spatial relationship between land use and crimes against property.

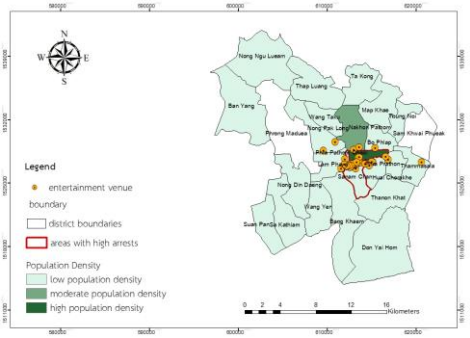

Figure 27. The spatial relationship between crimes against property, land use, and entertainment venues.

4. Conclusions

The geo-spatial analysis of crime against property in Mueang Nakhon Pathom was a great approach to examining the patterns, hotspots, trends and distribution direction, and spatial relationships of crimes. The results of this analysis revealed that the pattern of cases involving crimes against property in the responsibility area of Mueang Nakhon Pathom Police Station from 2013 to 2017 was clustered. The pattern of crime against property is obviously clustered around the center of Mueang Nakhon Pathom, where schools, universities, residences, villages, markets, communities, dormitories, entertainment venues, alcohol stores, tourist attractions, and deserted and dark roads are located. Hot spot analysis showed high incidence areas that had a GiZscore more than 1.65 as follows. the center of the city, the place that consists of a large number of villages, community malls, markets, schools, universities, the bypass road, and slightly towards the borderland, forward to adjacent provinces, heading to Bangkok and Samut Sakhon, farm, and deserted place. The trends of crimes showed the direction of the distribution to the west, directed to the main road to Bangkok and Samut Sakhon, the long, deserted road toward Bangkok and Samut Sakhon Provinces, which sometimes did not have enough light. The spatial relationship between the occurrence of crime against property and land use in 2015 and 2017 showed the most incidences in urban and built-up areas (92.66% and 94.61%, respectively). Evidence indicates that crowded villages and communities are obviously risk and a thief attraction. Moreover, the results illustrated the relationship between crime against property and the population density area in the center of Mueang

©2023 Faculty of Science and Technology, Suan Sunandha Rajabhat University

Nakhon Pathom, where crowded, markets, schools, universities, community malls, tourist attractions, and government offices are located. The Sanam Chan district showed high crime incidents because of the many passive populations and a cluster of entertainment venues. Property crime is always associated with crowded, deserted, and dark places, as well as built-up and community areas. In addition, the results showed incidents of crime were almost found in cities, towns, and commercial areas (49.44%), institutions (18.74%), and villages (15.12%), respectively. Finally, the overall results of this study help make relevant staff and police officials aware of the overall crime incident so that they can predict and develop prevention plans, suppression strategies, and deterrence tactics for crime reduction.

Acknowledgement

The authors would like to thank Mueang Nakhon Pathom Police Station, Nakhon Pathom Province for contributing crime data. We are also grateful to the Program in Forensic Science and Criminal Justice, Faculty of Science, Silpakorn University for the support throughout this research.

References

Abdulhafedh, A. (2017). A novel hybrid method for measuring the spatial autocorrelation of vehicular crashes: Combining Moran's Index and Getis-Ord G_i* statistic. *Open Journal of Civil Engineering*, *7*(2), 208-221. doi:10.4236/ojce.2017.72013

Achu, A. L., Aju, C. D., Suresh, V., Manoharan, T. P., & Reghunath, R. (2019). Spatio-temporal analysis of road accident incidents and delineation of hotspots using geospatial tools in Thrissur district, Kerala, India. KN - *Journal of Cartography and Geographic Information*, *69*, 255-265. doi:10.1007/s42489-019-00031-1

Ahmed, M., & Salihu, R. (2013). Spatiotemporal pattern of crime using Geographic Information System (GIS) approach in Dala L.G.A of Kano State, Nigeria. *American Journal of Engineering Research (AJER)*, *2*(3), 51-58.

Balogun, T. F., Okeke, H., Chukwukere, C. I. (2014). Crime mapping in Nigeria using GIS. *Journal of Geographic Information System*, *6*(5), 453-466. doi:10.4236/jgis.2014.65039

Chutia, D., Santra, M., Nishant, N., Singh, P. S., Chouhan, A., & Raju, P. L. N. (2020). Mapping of crime incidences and hotspot analysis through incremental auto correlation – A case study of Shillong city, Meghalaya, India. *Journal of Geomatics*, *14*(1), 61-71.

Dechsiri, B., & Robert, O. P. (2019). Drug trafficking estimation based on geo-statistics. *Defence Technology Academic Journal*, *1*(3), 52-61.

Dharmniti. (2019). *Against property according to the Criminal Code*. Retrieved from https://www.dharmniti.co.th/

ESRI. (2009a). *How spatial autocorrelation (global Moran's I) works*. Retrieved from https://www.pro.arcgis.com/

ESRI. (2009b). *How hot spot analysis (Getis-Ord Gi*) works*. Retrieved from https://www.pro.arcgis.com/.

ESRI. (2009c). *Standard deviational ellipse (Spatial statistics)*. Retrieved from https://pro.arcgis.com/en/

In-ain, T. (2018). *Developing a spatial database for the application of GIS in drug offences analysis*. Retrieved from https://www.agi.nu.ac.th/nred/Document/is-PDF/2561/geo_2561_018_FullPaper.pdf

Mitchell, A. (2005). *The ESRI guide to GIS analysis, volume 2: Spatial measurements and statistics*. Retrieved from https://www.esri.com/en-us/esri-press/

Mohammed, A. F., & Baiee, W. R. (2020). Analysis of criminal spatial events in GIS for predicting hotspots. *IOP Conference Series: Materials Science and Engineering*, *928*, 1-8. doi:10.1088/1757- 899X/928/3/032071

National Statistical Office. (2011). *Top 10 statistics.* Retrieved from http://service.nso.go .th /nso/nsopublish/TopTen/Top_othsoc.html

Nation Statistical Office. (2016). *Statistics of reported and arrested for the crimes of interest group by type of reported cases and province: 2007-2016*. Retrieved from http://statbbi.nso.go.th/staticreport/

Paramasivam, C. R., & Venkatramanan, S. (2019). An introduction to various spatial analysis techniques. In S. Venkatramanan, M. V. Prasanna, & S. Y. Chung (Eds.), *GIS and geostatistical techniques for groundwater science* (pp. 23-30). Amsterdam, Netherlands: Elsevier.

Phuaksomon, K. (2020). *People participation in preventing crimes in Hatyai Municipality, Hatyai District, Songkhla Province* (Master's thesis). Kasetsart University, Thailand.

Prasannakumar, V., Vijith, H., Charutha, R., & Geetha, N. (2011). Spatio-temporal clustering of road accidents: GIS based analysis and assessment. *Procedia - Social and Behavioral Sciences*, *21*, 317-325. doi:10.1016/j.sbspro.2011.07.020

©2023 Faculty of Science and Technology, Suan Sunandha Rajabhat University

Rattanapongs, P., & Gulabutr, V. (2020). Safety management from crime: against properties of students living dormitories in Salaya district, Nakhon Pathom Province. *Journal of MCU Buddhapanya Review*, *5*(3), 114-129.

Royal Thai Police. (2021). *Cracking down on the crime problem in 2011, escalating non-stop, social threats aggravate the people during the Covid period*. Retrieved from https://www.thairath.co.th/scoop/theissue/2262011

Srithamarong, T. (2016). *Crime risk area assessment based geo-spatial statistics* (Master's thesis, Silpakorn University). Retrieved from http://www.sure.su.ac.th/xmlui/handle/123456789/20686

Thailand Lawyer. (2020). *Criminal code*. Retrieved from https://library.siam-legal.com/thai-law

Wang, B., Shi, W., & Miao, Z. (2015). *Confidence analysis of standard deviational ellipse and its extension into higher dimensional Euclidean space*. *PLoS ONE, 10*(3). doi:10.1371/journal.pone.0118537

Yiampisan, M., & Srivanit, M. (2010). Using the Kernel density estimation surface for criminal pattern: A case study in Phranakhon District, Bangkok. *Journal of Architectural/Planning Research and Studies*, *7*(1), 87-102.

Available online at https://li02.tci-thaijo.org/index.php/ssstj

Suan Sunandha Science and Technology Journal
©2023 Faculty of Science and Technology, Suan Sunandha Rajabhat University

Factors Affecting Oil Palm Productivity in Surat Thani Province

Orawan Suebsen

Mathematics, Faculty of Science and Technology, Surat Thani Rajabhat University,
Surat-Nasan Road, Khun Thale Subdistrict, Mueang District, Surat Thani 84000, Thailand
Corresponding author e-mail: orawan.sue@sru.ac.th

Received: *11 November 2022* / **Revised**: *7 March 2023* / **Accepted:** *21 April 2023*

Abstract

This paper was a study of factors affecting oil palm productivity in Surat Thani Province. The objectives were to study the relationship between factors including oil palm prices in Surat Thani Province, the average number of hours of sunshine in Surat Thani, average temperatures in Surat Thani Province, the relative humidity in Surat Thani Province, oil palm productivity in Surat Thani Province, rainfall, fertilizer price and plantation area, as well as the factors affecting oil palm productivity in Surat Thani Province. Collected secondary data for the study from 1996 to 2022, a total of 30 years, and used multiple regression analysis. The results showed that two independent variables related to fertilizer price (X_6) and plantation area (X_7) were in a positive direction, affecting oil palm productivity in Surat Thani Province, which increased with statistical significance at the 0.05 level and had the following form of the multiple regression equation:

$$\hat{Y} = 14337.399 + 58.943(X_6) + 0.000253\ (X_7)$$

Keywords: Oil palm, Productivity, Fertilizer price, Plantation area, Surat Thani Province

1. Introduction

Oil palm originated in West Africa. Oil palm was introduced to Asia by the Portuguese. It was planted in the Botanical Garden of Bogor, Indonesia, around 1848, and then spread to Sumatra between 1853 and 1857, when it became a serious trade. In 1911 and 1918, there were 22,500 rai of palm oil plantations in Sumatra. Around 1870, the Singapore Botanic Gardens were the first place to plant oil palms. Later, it received attention, and the first research was conducted in Selangor State. It began to grow as a trade for the first time in the year 2460 and continues to do so till now. Oil palm plantations have covered approximately 34.04 million hectares in Indonesia and Malaysia since 1929. Oil palm was brought to Thailand for planting at the Kho Hong Rubber Testing Station in Songkhla Province (Krovis & Srikul, n.d.). The palm family is the second-largest plant family known and used by humans after the grass family. It must be seasonal if it does not rain throughout the year. Asia has made the most use of the palm's multiple parts, from food to shelter as well as clothing and medicine. Palms are monocotyledons that are mostly found in the tropics. There are many types of palms; some are bushes, and some are ivy. When seeds germinate, there is only one cotyledon, and the trunk has only one shoot and no branching. It has large, palmate, or feathery leaflets with distinct bracts and petioles, and leaves often form new clusters at the tip of the stem. The young leaves in the first stage combine to form a long stick that resembles a sword. Inflorescences are sheathed. The first flowering is called Tangjan. In the germination stage, the part of the sapling inside the seed expands and grows, known as the "jaw" (Pinkham, 2017).

The southern region has the most oil palm plantations, followed by the central region, the northeastern region, and the northern region. The efficiency of oil palm productivity shows that the productivity per unit of production is uncertain. The important and urgent production problem is the price and low quality of fertilizer. Surat Thani's oil palm had a perennial area of 915,255 rai and a productivity of 2.42 million tons in 2018, rainfall was about 135.4 millimeters, GPP was about 133,415 million baht, and the average oil palm price was 4.32 baht per kilogram. In 2019, the perennial area was approximately 1.34 million rai, the productivity was approximately 3.84 million tons,

Suan Sunandha Science and Technology Journal
©2023 Faculty of Science and Technology, Suan Sunandha Rajabhat University

the rainfall was approximately 132 millimeters, the GPP was approximately 210,396 million baht, and the average price of oil palm was 2.82 baht per kilogram (Office of Agricultural Economics 8 Surat Thani, 2019).

In addition, the COVID-19 situation affects the economy, causing farmers in Surat Thani Province to have the most difficult time regarding the volatility of oil palm prices, followed by no set selling price based on palm quality. Furthermore, there is a lack of aid from government organizations as well as manufacturing issues (Coronavirus Disease 2019 News Operation Center, 2019). As a result, the government should assist farmers by assuring the price of fresh palm fruit so that it can be sold at a fixed price. Farmers requested that fertilizer costs and the supply of high-quality fertilizers be controlled. Furthermore, they need financial help to extend planting areas and the provision of planting areas for farmers who want to grow the oil palm. Many farmers wish to extend their growing area but there is a lack of funds and land. a palm quality criterion for use in palm trading based on the quality class of The Palm Farmers Fund and the Rubber Plantation Aid Fund were established to provide farmers with systematic assistance. Additionally, organizing training classes on production and marketing for farmers, such as analyzing palm planting areas, the effective use of fertilizers and soil, and maintaining and improving palm plantation quality can be considered as another kind of aid that they received . Increasing productivity, lowering costs, and ensuring proper harvesting are the reasons that make researchers interested in researching the factors influencing the price of oil palm in Surat Thani Province. The information here can be useful in agriculture as well as solving production problems and providing guidelines for future development.

Research objectives

The research objective was to study the factors affecting oil palm productivity in Surat Thani Province.

2. Materials and Methods

2.1 Researched data

Secondary data were collected yearly from 1996 to 2022 for a total period of 30 years, and multiple regression equations were used to estimate the coefficients of the independent variables on the dependent variables. The dependent variable was the oil palm productivity data (unit: kilogram per rai), and seven independent variables were as follows:

X_1	the oil palm price in Surat Thani Province	(Unit : kilogram per rai)
X_2	average number of hours of sunshine in Surat Thani	(Unit : hour)
X_3	average temperatures	(Unit: Celsius)
X_4	relative humidity in Surat Thani Province	(Unit : Percent)
X_5	rainfall in Surat Thani Province	(Unit : millimeter)
X_6	fertilizer price in Surat Thani Province	(Unit : baht per kilogram)
X_7	plantation area in Surat Thani Province	(Unit : rai)

2.2 Data collection

Factors Affecting Oil Palm Prices in Surat Thani Province Data is collected from studies and research papers, related articles, and websites as secondary information. Data on dependent variables (Y) and independent variables (X) were collected for research purposes by collecting the following data:

Table 1. Contains statistical data for dependent and independent variables.

Variables	Items	Source
Y	oil palm productivity (Unit: kilogram per rai)	Office of Agricultural Economics 8 Surat Thani (2019)
X_1	oil palm price in Surat Thani Province (Unit : baht per kilogram)	
X_2	average number of hours of sunshine in Surat Thani province (Unit : hour)	Office of Agriculture and Cooperatives, Surat Thani Province (2020)
X_3	average temperatures (Unit: Celsius)	
X_4	relative humidity in Surat Thani Province (Unit : Percent)	
X_5	rainfall in Surat Thani Province (Unit : millimeter)	
X_6	fertilizer price in Surat Thani Province (Unit : baht per kilogram)	
X_7	plantation area in Surat Thani Province (Unit : rai)	

2.3 Data Analysis

Forecasting equations for palm oil prices were constructed with seven independent variables by multiple linear regression analysis. Creating a forecast equation involves the following steps (Wanichbancha, 2008):

Suan Sunandha Science and Technology Journal
©2023 Faculty of Science and Technology, Suan Sunandha Rajabhat University

2.3.1 Verify the distribution of the dependent variable (Y) to see if there is a normal distribution or not. By plotting the histogram for skewness and using the Lilliefors test, if the dependent does not have a normal distribution, the dependent variable (Y) must be converted to have a normal distribution.

1) If the distribution of the dependent variable (Y) was positively skewed, it would be converted to log Y.

2) If the distribution of the dependent variable (Y) was negatively skewed, it would be converted to Y^2.

2.3.2 The following was the multiple regression analysis assumption:

1) All independent variables were independent of each other. Determine the tolerance of every independent variable in the equation. The value was close to 1, and the value of VIF (Variance Inflation Factor) was not more than 10, indicating that the independent variables in each equation were independent.

2) Tolerance values must have a normal distribution as determined by plotting the NPP (Normal Probability Plot) and Lilliefors's test of residual values. If the NPP (Normal Probability Plot) curve tends to a straight line and Lilliefors's test cannot reject the main hypothesis (H_0), this indicates that the discrepancy is a normal distribution.

3) Verify the mean of the error E(e) because, in calculating the regression, the relationship between the independent set of variables and the dependent variable must be a linear relationship. The project developer uses the least squares error method to minimize the sum of squares of error values, which makes the sum. As a result, the total mean of error E(e) is zero, as well, or $\sum e_i$ = 0. For that reason, there is no need to check this requirement.

4) Examination of the variability of static displacement for all independent variables (X_i) or check the difference between actual Y_i and $\hat{Y}$ from the forecasts based on the generated multiple regression equations $e_i = Y_i - \hat{Y}$. Or is it a check to determine if e_i is spread around that is equal to 0? When X or Y change, or changes or does not change. If e_i does not change, then the variance of the fixed error satisfies the condition. However, if e_i changes with the change in the value of X or Y, heteroscedasticity can be solved by using the weighted least squares method when estimating the regression using the ordinary least squares method.

5) Based on the Durbin-Watson statistic, an autocorrelation-independent test that can be checked from independent variables with no intrinsic correlation, known as "non-problem." Autocorrelation. Using the Durbin-Watson value to test whether the independent variables are correlated or not with the Durbin-Watson measurement criteria, as follows:-

The values are in the range of 0–1.4, indicating that there is a positive correlation.

The values are in the range of 1.5–2.5, indicating that they are independent of each other.

The values are in the range of 2.6–4.0, indicating that there is a negative correlation.

However, if the value of Durbin-Watson is less than 1.5 and greater than 2.5 indicates that autocorrelation, or independent variables with self-correlation, makes the calculation of multiple regression equations problematic.

2.4 Interpreting the results of multiple regression analysis

When the assumption in the multiple regression analysis passed, the order of interpretation of the analysis results was as follows (Wanichbancha, 2008):

1. Examination of dependent variables and independent variables for a linear relationship. Therefore, the overall regression coefficient is tested using the F-test statistic from the ANOVA table. The assumptions will be set as follows:

H_0 : factors unrelated to palm oil prices in Surat Thani Province.

H_1 : Factors related to palm oil prices in Surat Thani Province

2. Checking the significance of the individual constants and coefficients in the equations and tables Coefficients. Each regression coefficient was tested using a statistical value of t-test significance at the 0.05 level. The assumptions were made as follows:

Suan Sunandha Science and Technology Journal
©2023 Faculty of Science and Technology, Suan Sunandha Rajabhat University

H_0 : The regression coefficient is zero.

H_1 : The regression coefficient is not equal to zero.

3. To create the form of the regression equation from the coefficients obtained from the coefficients table, the data from the β (the regression coefficient of the independent variable in the raw score form equation) would be written in the form of an equation prediction.

4. Summarizing the regression equations obtained from the Model Summary table by combining the multiple correlation coefficients, forecast coefficients, and standard error values together with the regression equations obtained as follows:

4.1 The multiple correlation coefficients (R) indicate the relationship between all independent variables and dependent variables.

4.2 The forecast coefficient (R^2) is an index that tells the percentage change of variables as a result of all independent variables.

4.3 The standard error of the estimate in the forecast of the resulting forecast equation.

2.5 Create multiple regression equations

According to the following model (Meejang, 2014)

$$Y = a + b_1X_1 + b_2X_2 + b_3X_3 + \dots b_nX_n \quad (1)$$

Where

Y	mean	dependent variable
a	mean	Constant-coefficient or vertical-axis intercept coefficient.
b	mean	The coefficient of the independent variable, which represents the percentage of change when the change in the independent variable affects the change, is also known as the class coefficient.
X_i	mean	independent variables i = 1,2,…,n

3. Results and Discussion

Descriptive statistics analysis results

In this study, data on palm oil prices in Surat Thani province were collected for 30 years, from 1996 to 2022. Seven variables and related factors were collected as follows:

1. Oil palm price in Surat Thani Province (X_1)
2. Average number of hours of sunshine (X_2)
3. Average temperatures (X_3)
4. Average relative humidity (X_4)
5. Rainfall (X_5)
6. Fertilizer price (X_6)
7. Plantation area (X_7)

The results of the descriptive statistical analysis of the variables consisting of mean, minimum, maximum, and standard deviation are shown in Table 2.

Table 2. Descriptive statistical analysis results

Variables	Mean	Minimum	Maximum	Std. dev.
Y	2765.90	1891.00	3536.00	410.48
X_1	3.50	1.15	7.80	1.53
X_2	151.71	52.90	202.70	26.83
X_3	27.16	26.50	27.60	0.25
X_4	81.12	75.00	86.00	3.54
X_5	1626.93	1227.10	2060.20	196.80
X_6	14.19	7.57	25.80	4.99
X_7	2014664.00	240212.00	4066640.00	1243043.34

Table 2: Summary of preliminary data from data collection on oil palm productivity in Surat Thani province by yearly data collection from 1996 to 2022, totaling a period of 30 years. The preliminary results were summarized as follows:

The average oil palm productivity (Y) was 2765.90 kilogram per rai; the lowest was 1891 tons, the highest was 3536 kilogram per rai, and the standard deviation was 410.48.

The average oil palm price (X_1) was 3.50 baht per kilogram, the lowest price was 1.15 baht per kilogram, the highest price was 7.80 baht per kilogram, and the standard deviation was 1.53.

The average number of hours of sunshine (X_2) was 151.71 hours, the lowest average was 52.90 hours, the highest average was 202.70 hours, and the standard deviation was 26.83.

The average temperature (X_3) was 27.16°C, the lowest average was 26.50°C, the highest average was 27.60°C, and the standard deviation was 0.25.

The average relative humidity (X_4) was 81.12 percent; the lowest average was 75 percent; the highest average was 86 percent; and the standard deviation was 3.54.

The rainfall (X_5) was 1626.93 millimeter; the lowest average was 1227.10 millimeter; the highest average was 2060.20 millimeter; and the standard deviation was 196.80.

Suan Sunandha Science and Technology Journal
©2023 Faculty of Science and Technology, Suan Sunandha Rajabhat University

The fertilizer price (X_6) was 14.19 baht per kilogram; the lowest average was 7.57 baht per kilogram; the highest average was 25.80 baht per kilogram; and the standard deviation was 4.99.

The plantation area (X_7) was 2014664 rai; the lowest average was 240212 rai; the highest average was 4066640 rai; and the standard deviation was 1243043.34.

Assumption Test for Multiple Linear Regressions

1. Tests for independent and dependent variables

Variables must have an interval scale or above, data on independent and dependent variables were collected on a yearly basis from 1996 to 2022, a period of 30 years. The data used on the interval scale is a measure that can divide the variables into groups and arrange them in order, and the measuring range will have the same distance.

2. Test data for independent and dependent variables

Variables must be randomized from a normal distribution population that can be tested using the Lilliefors method based on statistical testing. The Shapiro-Wilk test statistic was used to test the normal distribution data (Meejang, 2014).

Table 3. Tests of normality for independent and dependent variables.

Variables	Kolmogorov-Smirnov			Shapiro-Wilk		
	statistic	df	Sig.	statistic	df	Sig.
Y	.140	30	.137	.960	30	.317
X_1	.105	30	.200	.932	30	.056
X_2	.149	30	.089	.933	30	.059
X_3	.132	30	.193	.950	30	.165
X_4	.136	30	.167	.943	30	.110
X_5	.090	30	.200	.973	30	.621
X_6	.148	30	.092	.937	30	.074
X_7	.132	30	.195	.936	30	.070

The results from Table 3 showed that there were 8 normal distributions as follows:

1. The fact that the oil palm productivity (Y) has a sig = 0.317, which is greater than α=0.05, shows that the main hypothesis was accepted. As a result, the oil palm productivity variables (Y) had a normal distribution.

2. The fact that the oil palm price (X_1) has a sig = 0.056, which is greater than α=0.05, shows that the main hypothesis was accepted. As a result, the oil palm price (X_1) had a normal distribution.

3. The average number of hours of sunshine (X_2) has a sig = 0.059, which is greater than α=0.05, shows that the main hypothesis was accepted. As a result, the average number of hours of sunshine (X_2) had a normal distribution.

4. The average temperatures (X_3) have a sig = 0.165, which is greater than α= 0.05, shows that the main hypothesis was accepted. As a result, the average temperature (X_3) had a normal distribution.

5. The average relative humidity (X_4) has a sig = 0.110, which is greater than α=0.05, shows that the main hypothesis was accepted. As a result, the average relative humidity (X_4) had a normal distribution.

6. The Rainfall (X_5) has a sig = 0.621, which is greater than α=0.05, shows that the main hypothesis was accepted. As a result, the Rainfall (X_5) had a normal distribution.

7. The Fertilizer price (X_6) has a sig = 0.074, which is greater than α=0.05, shows that the main hypothesis was accepted. As a result, the Fertilizer price (X_6) had a normal distribution.

8. The Plantation area (X_7) has a sig = 0.070, which is greater than α=0.05, shows that the main hypothesis was accepted. As a result, the Plantation area (X_7) had a normal distribution.

3. Test of multicollinearity

If the independent variables are not independent, multicollinearity will occur. The method used for verification of the multicollinearity correlation coefficient between the independent variables can be determined by the tolerance of all independent variables in the equation approaching 1 and the VIF (Variance Inflation Factor) being less than 10, showing that the independent variable in the equation is independent and the Pearson correlation being more than 0.8. Using the Stevens criterion, it may be assumed that the pair of independent variables' many correlations should be addressed (Meejang, 2014).

Suan Sunandha Science and Technology Journal
©2023 Faculty of Science and Technology, Suan Sunandha Rajabhat University

Table 4. Relationship between independent variables with Pearson Correlation.

Variables	Y	X_1	X_2	X_3	X_4	X_5	X_6	X_7
Y	1	0.591**	0.108	.626	-0.056	-0.115	0.785**	0.791**
X_1		1	0.168	.0900	0.006	0.078	0.093	0.068
X_2			1	-0.015	0.304	0.143	0.238	0.226
X_3				1	-0.259	-0.201	0.021	0.640
X_4					1	0.095	0.024	0.144
X_5						1	-0.050	-0.191
X_6							1	0.089
X_7								1

**** P < 0.01**

Table 4 shows that all independent variables were uncorrelated and that we can take into account each independent variable's tolerance in the equation. A value closest to one, and VIF (Variance Inflation Factor) is less than 10. Therefore, the independent variables in the equation are independent of each other.

4. Relationship between independent variables coefficients

Table 5 shows that all independent variables are independent and can be determined by the tolerance of the independent variables in the equation with values approaching 0, where the calculated variable is the minimum at 0.218 and maximum 0.851. As a result, because the values of all independent variables in the equation are close to zero, it can be concluded that each independent variable is independent of the other. The value of the VIF (Variance Inflation Factor) must not be exceeded 10 (Kleinbaum, 1998), where all the variables obtained from the calculation are not more than 10. It can be concluded that each independent variable is independent of the others.

Table 5. Relationship between independent variables coefficients.

Variables	Tolerance	VIF
X_1	0.341	2.935
X_2	0.711	1.407
X_3	0.635	1.576
X_4	0.316	3.166
X_5	0.851	1.176
X_6	0.218	4.587
X_7	0.262	3.822

5. Assumption of normality

Figure 1 shows that the normal probability plot graph represents the normal distribution of the error values. Therefore, if the points are aligned along a straight line, the error is assumed to have a normal distribution. From the analysis of the data, the points in the normal probability plot graph are aligned close to the straight line. Concluded that the error has a normal distribution.

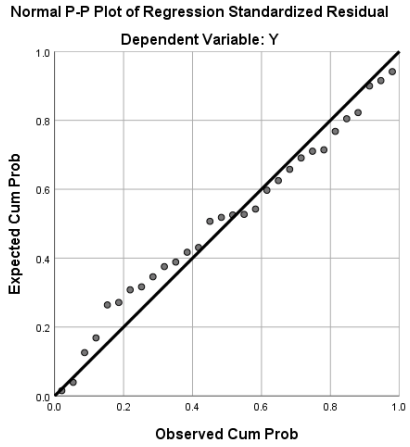

Figure 1. Normal probability plot graph.

6. Test of the Residuals Statistics E(e)

Table 6 shows that the mean error E(e) can be determined using the residual statistics, in which the mean is 0.000. It was determined that residual statistics E(e) = 0 and from testing problems with heteroskedasticity with the Breusch-Pagan-Godfrey method. It is a general test for the unstable variance of the residuals obtained from the model estimation by the least-squares method. The test results were found to be statistically insignificant at the 0.05 level (Sig. = 0.2593 > α = 0.05), so the obtained equations were not problematic for heteroskedasticity.

Table 6. Residuals statistics.

	Minimum	Maximum	Mean	Std. Deviation	N
Predicted Value	2220.00	3331.2217	2765.90	366.834	30
Residual	-468.385	338.86746	.00000	184.202	30
Std. Predicted Value	-1.488	1.541	.000	1.000	30
Std. Residual	-2.164	1.565	.000	.851	30

Suan Sunandha Science and Technology Journal
©2023 Faculty of Science and Technology, Suan Sunandha Rajabhat University

7. Tests for constancy of error variance

Figure 2 shows the scatter of data points. Data from the north and south were both scattered near the 0.0 level. They have similar areas and are rectangular. This indicates that the data discrepancies have constant variance.

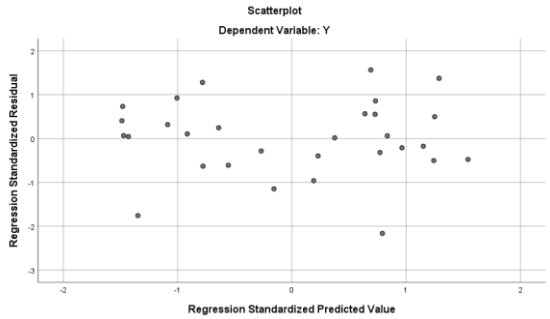

Figure 2. Scatterplot graph.

8. Test of autocorrelation

The Durbin-Watson statistic can be examined for independent variables that have no intrinsic correlation or autocorrelation by using Durbin-Watson values to test whether independent variables have a relationship among themselves or not. The criteria for measuring Durbin-Watson are as follows (Meejang, 2014):

The range 0 – 1.4 Correlated in a positive direction

The range 1.5 – 2.5 Independence

The range 2.6 – 4.0 Correlated in a negative direction

However, if the Durbin-Watson was less than 1.5 and more than 2.5, it was autocorrelation, which means that independent variables are correlated with themselves. This results in the problem of calculating multiple regression equations. In addition, the researcher has also tested autocorrelation using the Breusch–Godfrey serial correlation LM test and found that the value of F-statistics = 0.4048, which is greater than $\alpha = 0.05$, indicates that the variable does not have autocorrelation problems (Table 7).

Table 7. Test of Autocorrelation with Breusch–Godfrey serial correlation LM test.

F-statistics	0.946562
Prob.F (2,20)	0.4048
Obs*R-squared	2.594136
Prob. Chp-Square (2)	0.2733

Table 8 shows that Durbin-Watson found Durbin-Watson = 1.704 in the range of 1.5 to 2.5, indicating that the independent variables used in the test were not correlated with themselves.

Table 8. Test for independence of error (Model summary).

Model	R	R Square	Adjusted R Square	Std. Error of The Estimate	Change Statistics					Durbin-Watson
					R Square Change	F Change	Df1	Df2	Sig. F Change	
1	.894	.799	.722	216.46327	.799	10.411	8	21	0.000	1.704

9. Multiple regression analysis results

Table 9 Multiple regression analysis found that F-test = 10.411 (Sig. = 0.000 < α = 0.05) shows some independent variables affecting oil palm productivity in Surat Thani province; details are as follows:

1. The fertilizer price (X_6) in Surat Thani Province has a positive correlation with oil palm productivity in Surat Thani Province, which is statistically significant at 0.05 levels. When all other variables are held constant, the coefficient of 58.943 denotes that if the fertilizer price increases, affecting oil palm productivity in Surat Thani province, it increases by 58.943 baht per kilogram. If the fertilizer price decreases, affecting oil palm productivity in Surat Thani province, it decreases by 58.943 baht per kilogram.

2. The plantation area (X_6) in Surat Thani Province had a positive correlation with oil palm productivity in Surat Thani Province, which was statistically significant at 0.05 levels. When all other variables are held constant, the coefficient of 0.000253 denotes that if the fertilizer price increases, affecting oil palm productivity in Surat Thani province, it increases by 0.000253 rai. If the fertilizer price decreases, affecting oil palm productivity in Surat Thani province, it decreases by 58.943 0.000253 rai.

The results of the multiple regression analysis can be written in the equation as follows:

Suan Sunandha Science and Technology Journal
©2023 Faculty of Science and Technology, Suan Sunandha Rajabhat University

$$\hat{Y} = 14337.399 + 58.943(X_6) + 0.000253\,(X_7) \quad (2)$$

R-squared and adjusted R-squared can explain the variability of dependent variables. R-squared = 0.799, according to the results of the multiple regression analysis. This equation's independent variables and related factors can explain 79.90 percent of the variation in oil palm productivity in Surat Thani province. The remaining 20.01% was caused by other factors that were not analyzed. Adjusted R-squared = 0.722, which is close to the R-squared value. Most of the variables were able to explain the factors that correlate well with oil palm productivity in Surat Thani province. Therefore, the R-squared and adjusted R-squared obtained from the analysis were acceptable values. From the multiple regression equations using the enter method, it was found that the four factors consisting of oil palm price, average number of hours of sunshine, average temperature, and relative humidity have an influence on oil palm productivity, indicating that if one wants to have more oil palm productivity, all four factors must be controlled to be appropriate.

Table 9. Multiple regression analysis.

Variable	b	Std. Error	Beta	t	Sig.
Constant	14337.399	6216.068	-	2.307	.031
Oil palm prices (X_1)	-25.385	45.109	-.094	-.563	.580
Average number of hours of sunshine (X_2)	-2.607	1.777	-.170	-1.467	.157
Average temperatures (X_3)	-379.065	198.093	-.235	-1.914	.069
Relative humidity (X_4)	-24.474	20.178	-.211	-1.213	.239
Rainfall (X_5)	.098	.221	.047	.444	.661
Fertilizer price (X_6)	58.943	17.258	.716	3.415*	.003
Plantation area (X_7)	.000	.000	.765	3.995*	.001

R-Square = 0.799 Adjusted R-squared = 0.722 S.E. of regression = 216.463
F = 10.411 Sig. = 0.000 Durbin-Watson = 1.704 * $p < 0.05$

Discussion

In this study, factors affecting oil palm productivity in Surat Thani province consisted of fertilizer price (X_6) and plantation area (X_7). The effect of these factors on oil palm productivity in Surat Thani province was 79.90%. Each factor can be discussed as follows:

1. Fertilizer prices affect oil palm productivity in Surat Thani Province. In the first year, the oil palm requires a small amount of nutrients, while in the second and third years, it requires a much higher amount of nutrients**.** Especially potassium and nitrogen. Because it is a period of rapid growth both above and below ground, the need for fertilizer each year is quite stable after planting for 3 years or more. Oil palm normally requires more potassium than nitrogen and needs a higher amount in the pre**-**production period**.** However, nitrogen, potassium, phosphorus, magnesium, and boron are the plant nutrients that oil palm require in large or very large amounts (Suratthani Oil Palm Research Center, 2020). Fertilizer is an important production factor for growing Thai agricultural crops. the demand for fertilizer is mainly based on the quantity of crops, which more than doubled in 2022, had the direct impact on farmers who grow the most oil palm. Compared to other main crops, oil palm has a fertilizer application rate per rai as high as 120 kilograms per rai (Kasikorn Research Information Center, 2022). Therefore, the price of fertilizer directly affects oil palm productivity in Surat Thani Province because fertilizer is one of the production costs for farmers**.** If fertilizer prices are higher, farmers will have to pay more for fertilizer cost. Or in some cases, there may be a reduction in the quantity of fertilizer orders to meet the cost**.** However, reducing the amount of fertilizer will affect oil palm productivity and consistent with the research of Klaiyoo et al. (Klaiyoo, Sattayanuwat, & Premashthira, 2018), they studied factors affecting the efficiency of oil palm production. The results showed that factors affecting the efficiency of oil palm production include increasing the efficiency of fertilizer use and improving soil quality. Selection of good palm seedlings, increasing the supply chain in income variables, and training and management of palm plantations are all important factors to increase the efficiency of oil palm production. when they will provide farmers with important knowledge about an analysis of the economic worthiness of investment in production factors and the payment of oil palm production price subsidies based on the net present value of return (NPV), thus it could increase Competition in an investment of different

©2023 Faculty of Science and Technology, Suan Sunandha Rajabhat University

production factors. Consistent with Chatsirapop (2017), a study of factors affecting palm oil prices in Thailand in 2017 found that if the price of palm oil quality in the country increases by 17%, it would increase the price of refined palm oil in the country by 0.55 baht. The price of crude palm oil in the country would increase by 1 baht, which could affect the price of refined palm oil in the country, by 0.85 baht. For pure palm wax or stearin, an increase of 1 baht in the country would increase the price of refined palm oil by 2.78 baht. The refined palm oil exported from FOB Malaysia will increase by 1 baht. This would increase the price of refined palm oil in the country by 1.57 baht and create policy issues. The government's domestic refined palm oil stockpile was a direct factor affecting palm oil prices in Thailand in 2017.

2. The plantation area affects oil palm productivity in Surat Thani Province**.** The planting of oil palm is most prevalent in the southern region (Suratthani Oil Palm Research Center, 2020). However, having a large area of oil palm plantations gives the opportunity to increase the yield**.** However, the output of palm oil per ton of production is uncertain due to a variety of factors. So the more palm plantation areas, would obviously bring the more income from palm production**.** In addition, there are farmers who grow other crops but are turning to plant oil palm due to the high price of the product (Surat Thani Provincial Statistical Office, 2017). This is consistent with the research of Sowana (2009), who studied the suitability of peatlands for palm plantations. they presented that most of the peatlands were unsuitable or less suitable for oil palm planting due to the soil conditions being acidic and marshy, and the bottom soil layer being sandy soil with severe acidity. Therefore, in order for oil palms to grow well, good management is required. This leads to the high cost of oil palm plantations. In addition, the current agricultural production behavior has shifted from subsistence production to commercial production that focuses more on the quantity and quality of the product, leading to the selection of crops that provide higher economic value, such as palm oil, rubber, etc and consistent with the research of Thongpradab (2010), who found that oil palm plantations instead of rice in the South. This is because oil palm is an economic crop that is more important economically, while rice is less important because rice production in the south is highly uncertain, resulting in lower yields and poorer quality.

4. Conclusions

Summarizing the results of the correlation analysis, it was found that the only two independent variables related to oil palm productivity in Surat Thani province were fertilizer price (X_6) and plantation area (X_7) they were moving in a positive direction, affecting oil palm productivity in Surat Thani Province, which increased with statistical significance at the 0.05 level. The most influential factor was plantation area (X_7) (Beta = 0.765), followed by fertilizer price (X_6) (Beta = 0.716)

The results of the multiple regression analysis can be written in the equation as follows:

$$\hat{Y} = 14337.399 + 58.943(X_6) + 0.000253\ (X_7) \quad (3)$$

Suggestions for this research; The variables that the researcher brought into the study for the recommendation of this research were those that were directly related to the concepts, theories, and facts arising from the study of relationships, as well as those that were related to the oil palm productivity in Surat Thani Province. However, there may be additional factors influencing the amount of oil palm output in Surat Thani province that should be considered**.** Those interested in undertaking more research may take into account political and policy variables for the growth of the government's agriculture sector as secondary data; this research investigates the relationship and factors associated with the oil palm productivity in Surat Thani province. The whole term is 30 years, beginning in 1996 and ending in 2022. As a result, the amount of data collected in future studies should be increased and may utilize monthly, daily, or weekly data.

Acknowledgements

Thank you to Surat Thani Rajabhat University, which provides funding for research.

References

Chatsirapop, U. (2017). *Factors affecting palm oil prices in Thailand in 2017.* Retrieved from https://so04.tci-thaijo.org/index.php/SSRUJPD/article/view/249026/169157

Coronavirus Disease 2019 News Operation Center. (2019). *News report on corona virus infection 2019.* Retrieved from https://covid19.dms.go.th/?StartWeb=1

Kasikorn Research Information Center. (2022). *Price of chemical fertilizer (urea) year 2022.* Retrieved from https://www.kasikornresearch.com/en/analysis/k-econ/business/Pages/Fertilizer-z3325.aspx

Klaiyoo, Y., Sattayanuwat, W., & Premashthira, A. (2018). Factors affecting the enhancement of palm oil production efficiency. *Veridian E-Journal, Silpakorn University*, *11*(3), 2458-2472.

©2023 Faculty of Science and Technology, Suan Sunandha Rajabhat University

Kleinbaum, D. G. (1998). *Applied regression analysis and other multivariable methods*. Massachusetts: Duxfury Press.

Krovis, C., & Srikul, S. (n.d.). *History and importance.* Retrieved from https://www.doa.go.th/oard8/wp-content/uploads/2019/08/km3.pdf

Meejang, S. (2014). *Advanced statistics for research: Theory and practice*. Bangkok: Chulalongkorn University.

Office of Agricultural Economics 8 Surat Thani. (2019). *Prices of palm oil in Surat Thani Province.* Retrieved from https://data.go.th/dataset/datasetoae-1504

Office of Agriculture and Cooperatives, Surat Thani Province. (2020). *Oil palm production*. Surat Thani: Office of Agriculture and Cooperatives, Surat Thani Province.

Pinkham, K. (2017). *History of palm trees.* Retrieved from https://km.raot.co.th/km-knowledge/detail/366

Sowana, A. (2009). *Research project on people participation development in Saiburi River Basin management, oil palm plantation in deserted rice fields*. Bangkok: The Thailand Research Fund (TRF).

Suratthani Oil Palm Research Center. (2020). *Fertilizer application based on soil and leaf analysis in oil palm production*. Retrieved from http://www.doa.go.th/fc/palmsurat/wp-content/uploads/2020/06/คำแนะนำปุ๋ยปาล์มน้ำมัน3.pdf

Surat Thani Provincial Statistical Office. (2017). *Summary of the trend situation and important strategies of Surat Thani Province.* Retrieved from http://www.oic.go.th/FILEWEB/CABINFOCENTER20/DRAWER003/GENERAL/DATA0000/00000201.PDF

Thongpradab, A. (2010). *An analysis of the impact on household food security from area change. rice fields are other economic crops in Karaket Subdistrict, Chien Yai District, Nakhon Si Thammarat Province* (Doctoral dissertation). Prince of Songkla University, Thailand.

Wanichbancha, K. (2008). *Analysis: Statistics for administration and research* (11th ed.). Bangkok: Chulalongkorn University.

Available online at https://li02.tci-thaijo.org/index.php/ssstj

Suan Sunandha Science and Technology Journal
©2023 Faculty of Science and Technology, Suan Sunandha Rajabhat University

Literature Study on Conditions of Sea Surface Temperature and Seawater Rise in Indonesia Detected by Remote Sensing

Agnes Sri Mulyani

Department of Civil Engineering, Faculty of Engineering, Universitas Kristen Indonesia, Jakarta 13620, Indonesia

Corresponding author e-mail: agnes.mulyani@uki.ac.id

Received: *2 February 2023* / **Revised:** *20 February 2023* / **Accepted:** *19 April 2023*

Abstract

The Sea Surface Temperature (SST) is an important parameter for climate dynamic issues either globally or regionally as well as for global warming issues. In some condition the parameter can cause melting glaciers that will influence the rise of the sea levels. The further effect will be the climate change with the weather phenomena such as storms, hurricanes and heavy rains. As the result, the changes of the planting seasons occur and all of these will harm human life on earth. If there is no prevention with the condition of the parameter it is predicted that by 2040 the sea levels will rise highly because of the melting polar ice caps that will cause the sink of the islands. The SST has been detecting using remote sensing methods for 32 years in Indonesia. The trend has increased to reduce the damage of infrastructure and the activity disturbance of coastal communities. Indonesian country optimistically commits to achieve the target of net zero emission by 2060. The Indonesian government has stated nationally the climate target commitments determined for Indonesia and will strive to maintain the main target of reducing greenhouse gas emission into 41% by 2030.

Keywords: Sea surface temperature, Global warming, Sea-level rise, Remote sensing

1. Introduction

Remote sensing is one of the technologies to overcome some problems mostly occurred in archipelagic countries. The technology of remote sensing can perform encroachment on territorial boundaries, determine the location of natural resources, and carry out early detection of natural disaster. The technology can also measure effectively the Sea Surface Temperature (SST) as a very important parameter of climate dynamics issues either globally or regionally as well as for global warming issues (Mulyani, 2021a). The measurement outcome can be carried out spatially and timely in a short time on a wider scale. Hence, in this case, very broad information can be obtained on a global scale. The satellite capabilities can make the remote sensing technology capture the mapping images of an area based on its specifications. By using the remote sensing techniques, the information needed for areas or places that are difficult to reach will be obtained more easily. This process can be done without having to collect data directly because the remote sensing system can detect objects on the earth's surface from the satellite sensors. The system works when the electromagnetic radiation emitted by objects on earth' s surface is detected by the satellite sensors.

The increase of average temperatures in the atmosphere, at the sea, and on the land of the earth's surface can cause global warming. According to the scientists, there are many human activities contributing to global warming that makes the excessive amounts of greenhouse gases to the atmosphere. The greenhouse gases such as carbon dioxide can build up in the atmosphere. The heat of the gasses is trapped and normally released into the atmosphere. The heat is then absorbed by seawater that increases the SST which can cause global warming. Sequentially the effects of global warming are melting glaciers, climate change, extreme weather, and decreasing food quality that will harm human life. The melting glaciers can change the climate that makes the weather phenomena become extreme. There can be much more storms, hurricanes, heavy rains and changes in planting

Suan Sunandha Science and Technology Journal
©2023 Faculty of Science and Technology, Suan Sunandha Rajabhat University

seasons. In addition, threat of tropical storms, tsunamis, floods, landslides, and droughts which can increase the potential causes of fires can occur. Moreover, various types of fishes can become extinct, coral reefs can be damaged, and there can be clean water crisis that can increase the spread of parasitic diseases (Mulyani, 2021a; Triana, 2008). Scientists who are members of the Intergovernmental Panel on Climate Change IPCC) from several countries have observed the temperature changes on earth. It turned out to the various problems. They found that within 15 years from 1990 to 2005 the temperature on earth was evenly increased with the range from 0.15^0C to 0.3^0C. As a result, the melting ice in Greenland and Antarctica occurred and caused the rising sea levels approximately 1 meter every year that sank small islands. Based on the research performed by scientists who are members of the Antarctic Survey Institute, more than one million hectares of icebergs in the western part of Antarctica can be melted or broke. It indicates that the condition in Antarctica or the southern polar circle will change rapidly due to the increase of the earth's temperature. If this situation continues, it is predicted that in 2040 the polar ice caps will melt, the sea levels will rise, and the islands will sink; of course, it is a serious disaster of the earth and everything in it (Al Tanto, 2020).

The lifestyle and the irregular increase of population growth can make various human activities that influence the earth's temperature to become warmer which can damage the environment (Mulyani, 2021b). Hence, many human activities including deforestation and forest burning, motorized vehicles, industrial pollution can become the trigger of global warming. Besides, acidification of seawater, extreme weather, and excessive heat absorption of the oceans will occur and worsen the condition. Human behavior and other factors can impact the increase of ocean temperature that sequentially causes the melting of ice in Antarctica and the rising of sea levels. In fact, the process of global warming has begun even since hundreds of years ago. The effects, however, start to happen and can be felt nowadays. They are climate instability, heat energy, water vapor in the atmosphere, much higher rainfall, larger hurricanes, shifts in the rainy and dry seasons as well as unpredictable and extreme weather changes anomalies. The climate instability can cause storms and high waves that disrupt fishing activities. The rising sea levels can increase floods in cities closed to the coast.

The other impact continues that global warming can disrupt agricultural products because of the extreme weather which can causes severe drought during the dry season in tropical countries. The drought can dry up most of the agricultural lands. Meanwhile, the extreme weather can also make viruses as well as bacteria grow and multiply stronger and faster that can cause new diseases. As global warming has been getting worse, the solution must be started immediately by converting barren land into green land and educating people to live with a healthy and energy-efficient lifestyle.

The remote sensing technology that is developed increasingly can be used to detect surface water temperature related to SST. It is the first step to detect the possibility of disaster on earth because SST is one of the important indicators of climate change. As a consequence of global warming, people must adapt themselves to live in condition of hot air. Alternatively, the triggers of global warming must be reduced. It is necessary to take action or attempt to reduce emissions and greenhouse gases.

This paper aims to detect SST waters in Indonesia for 32 years and sea-level conditions in some waters also in Indonesia using remote sensing methods with data obtained from satellite imagery. The changes of symptoms and temperature are needed to be monitored regularly to analyze the distribution pattern of SST. The initial results of surface temperature detection are intended to anticipate disasters through policies carried out by the competent authorities. The method used is a literature study obtained from scientific reviews that have been previously carried out and published as scientific journals.

Suan Sunandha Science and Technology Journal
©2023 Faculty of Science and Technology, Suan Sunandha Rajabhat University

2. Materials and Methods

Materials-Literature Review

NO	Author, Year	Research result
1.	Al Tanto, (2020)	This research uses a literature review method on detection. Indonesia's average sea surface temperature is around 26ºC - 31ºC (NOOA estimation 1993-2003), with an accuracy of > 90%; the difference between SST measurements with the field and the estimation results is 0.2ºC. SST conditions in Indonesia were quite high in July 2015, around 29.1ºC-29.8ºC (MODIS estimate), with a correlation coefficient of r = 0.72 and Root Mean Square Error (RMSE) 0.72ºC. In the eastern waters of Indonesia (north of Papua), the MODIS (Aqua) estimation results are 29.10ºC - 29.36ºC. MODIS (Terra) of 28.88ºC - 29.19ºC. The RMSE values obtained from MODIS image interpretation are 0.2461ºC (Aqua) and 0.4854ºC (Terra). In these waters, the average SST value is 29.11ºC-29.65ºC (NOAA estimates, 2010 - 2012) with a bias of -0.43 and an average RMSE of 0.2228ºC. The accuracy of the microwave sensor in SST reaches 0.5ºC, free from the influence of cloud cover. The distribution of SST TRMM (Tropical Rainfall Measuring Mission/Microwave in 2008) in Indonesian waters is 21ºC-31ºC. Correlation coefficient value of 0.95 and an RMSE value of 0.24 K. It turns out that there are differences in the estimated values in the use of some of the satellite imagery data used. In general, a better SST value is found in the NOOA-AVHRR satellite measurement with a fairly low bias and RMSE, but it is at risk because it is affected by cloud cover. The use of the TRMM (Microwave) sensor has slightly higher accuracy but is not affected by cloud cover.
2.	Alfajri, Mubarak, & Mulyadi, (2017)	The study was conducted in Sumatera Barat Waters using Aqua Modis to determine the fluctuation and distribution of SST and the factors causing it. The study was carried out from March to April 2016, with daily results observed from February 15, February 20, February 25, March 2, March 7, and March 12, 2016. The results show that the highest temperature was 34.54ºC occurred on February 15, and the lowest temperature of 27.41ºC occurred on March 12, 2016. Meanwhile, the average SST between April 2015 and March 2016 was 27.07ºC - 34.98ºC.
3.	Ariani, (2018)	Data observed from the Topex/Poseidon, Jason 1, Jason 2, Jason 3 altimetry satellite reference missions used to analyze the trend of sea-level rise in Indonesia and its spatial distribution. After doing the least square intercalibrated and seasonal-trend decomposition procedure based on loess, it is known that the sea level rise rate in Indonesia is 4.6 ± 0.2 mm/year in the period 1993-2018. The linear trend is positive; it shows that the sea level in Indonesia will continue to increase with the equation y = 4.6x - 9133.5. Where y is the sea level anomaly in mm, and x is the time in years. Based on the analysis of the spatial distribution of sea-level rise with a 3x3º grid, it is known that the fastest sea-level rise occurs around the islands of Madura and Bali, as well as parts of Flores Island at a speed of 7.4 mm/year.
4.	Azizah & Wibisana, (2020)	The research results from 2018-2020 are that the temporal variation of SST using Terra Modis in the coastal area of Malang has increased. SST in 2018 ranged from 25ºC-26ºC, and in 2019 the SST value ranged from 26ºC-27ºC, while in 2020 the SST value ranged from 30ºC-31ºC. The highest SST value occurred on May 23, 2020, with an average temperature reaching 30.8ºC. The lowest SST occurred on May 22, 2018, at 25.7ºC. The distribution of SST was made by mathematical modeling, and the most optimum mathematical model was at 667 nm wavelength occurred on May 23, 2020, with the equation model Y = -0.498 ln x + 27.936, which results

Suan Sunandha Science and Technology Journal
©2023 Faculty of Science and Technology, Suan Sunandha Rajabhat University

		in a correlation value of R = 0.6561.
5.	Cheng et al., (2021)	The SST reached a new record in 2019 with the warmest level recorded history, reaching 228 Zettajoules (ZJ), above 1981 to 2010 average temperature and 25 ZJ above 2018. The research results in 2020, with temperature measurements at a depth of 2000 meters, show that SST reached higher values than the data in 2019. At the top of the world's oceans, it absorbs 20 Zettajoules more than the previous year (1 Joules=1.0E-21 Zettajoules). The researchers took the data from various sources then used it to calculate the temperature of seawater, especially seawater, at a depth of 0 to 2,000 meters.
6.	Dwi Ayu, Sukojo, & Jaelani, (2011)	The research was conducted in Java, Madura and Bali islands using Aqua Modis. The results showed that the average SST in 2005 it was 26.89ºC, in 2006 it was 26.25ºC, in 2007 it was 29.89ºC, in 2008 it was 28.87ºC, in 2009 it was 28.22ºC and in 2010 it was 22.9ºC. In 2010 the average SST decreased because the rainy season was so long that clouds covered the earth.
7.	Emiyati, Setiawan, Manopo, Budiman, & Hasyim, (2014).	SST analysis was carried out temporally and spatially in 2009-2013 using MODIS (Moderate Resolution Imaging Spectroradiometer) Aqua Terra, the research site was divided into two, namely the northern waters of Lombok and South Lombok. The maximum SST value in the northern waters of Lombok and the southern waters of Lombok occurs in April, and the minimum value occurs in August. The distribution of SST for one year in Lombok waters forms a sinusoidal pattern, and SST in northern Lombok waters has a higher value than southern Lombok waters. The SST trend for five years in the waters north of Lombok and south of Lombok tends to decrease.
8.	Gaol, Tambunan, Osawa, Pasaribu, & Nurjaya, (2017)	Satellite altimetry data for 23 years (1993-2016), tide gauges, and Digital Elevation Model (DEM) data are used to determine the impact caused by an average sea-level rise. Sea-level rise on the east coast of North Sumatra has a significant negative impact on coastal activities and ecosystems. The regional mean sea level trend during the period estimated from satellite altimetry is 5.0 mm/year. The potential loss of coastal areas in these areas due to 1 m and 2 m inundation can range from 11.9 km2 to 63.8 km2, respectively.
9.	Mansawan, Lumban-Gaol, & Panjaitan, (2016)	The study was conducted in the coastal waters of Cilacap and Bali with analysis of Envisat satellite altimetry data for the period 2003 to 2010 plus data collected from various altimetry satellites from 2006 to 2014. Tidal data was used as a comparison of altimetry satellite data. More than 90% of satellite altimetry data in the waters of Cilacap and Benoa can be used to assess variations and sea-level rise during the 2003-2010 period. The rate of sea-level rise in both tidal data and satellite altimetry shows the same figure is 3.5 mm/year in Cilacap; in Benoa, it is 4.7 mm/year and 5.60 mm/year.
10.	Mayasari & Handoko, (2010)	Utilization of Topex/Poseidon altimetry satellite data and SST data from 2002-2005 is expected to correlate between changes in sea level position and sea surface temperature to know changes in sea-level rise in Indonesian Waters. Binary data processing from the Topex/Poseidon altimetry satellite using the Basic Radar Altimetry Toolbox (BRAT) 2.0.0 software. The previous data processing used Matlab software to compare the BRAT software.
11.	Mujadida, Setiyono, Handoyo, Hariyadi, & Marwoto, (2021)	This study aims to analyze the dynamics of sea-level change in the Java Sea and predict future data using a machine learning approach with a Recurrent Neural Network (RNN) network architecture. The main data used is data on

Suan Sunandha Science and Technology Journal
©2023 Faculty of Science and Technology, Suan Sunandha Rajabhat University

		sea-level anomalies in the Java Sea from 1993 to 2019 published by the Copernicus Marine Environment Monitoring Service (CMEMS) supported by a map of the Indonesian Earth and a map of surface currents in the Java Sea. The analysis results show that there has been an increase in sea level values since 1993, around 37,545 mm/year. The fastest trend of sea-level rise in the Java Sea reached a value of 72,313 mm in 2015-2016, while the slowest trend occurred in 2002-2005 at around 16.7 mm. Due to El Nino and La Nina phenomena, changes in extreme sea level trends occurred in 1996-1998 and 2010-2016. Evaluation of the RNN model obtained an MSE value of 0.000343, an RMSE value of 0.0058564, an R2 value of 0.993, and an MAE (Mean Absolute Error) value of 0.0045024. The evaluation results show a very small error value, so it can conclude that the RNN model is very accurate in predicting the sea surface dynamics.
12.	Putra, Karang, & Putra, (2019)	Putra et al. (2019) used AVHRR (Advanced Very High Resolution Radiometer), to monitor SST in Indonesian marine waters. In general, it was found that there was an increasing trend of 0.28ºC SST in Indonesian marine waters for 32 years (1981 - 2012). The domain is located at 14ºC North Latitude – 15ºC South Latitude and 90º East Longitude – 145º East Longitude. While the amount of SST ranges from 26.8ºC-29.1ºC
13.	Syaifullah, (2015)	Syaifulah was conducted SST observation research to know the relationship between the increase in SST and global warming in Indonesian waters. The data used in SST data for 32 years (1982 - 2014) is made in time series with spatial analysis and temporal analysis methods. During a period of 32 years, it turns out that there have been changes in temperature in Indonesian waters that vary. In general, the southern region of Java waters increased in SST for 32 years, as well as the waters of West Sumatra increased in SST for 32 years, and lastly, the South China waters also increased in SST for 32 years, but the increase was lower than the waters of Java and waters of West Sumatra. The greatest increase in temperature occurred in the waters of the western Pacific Ocean to the north of Papua. SST anomalies were also found, namely deviations from the sea surface temperature from its normal/historical value at a certain time, while sea surface temperatures in Indonesia ranged from 26ºC - 31.5ºC.
14.	Sulaiha, Handoko, & Yuwono, (2020)	Sea level variations observed in the Java Sea and the South China Sea using Altimetry satellites, Jason 1, Jason 2, and Jason 3 from 2002-2019 showed a sea-level rise rate of 4.1 mm/year, where high velocity occurred around the North or South Java Sea, with a value of 7-9 mm/year.
15.	Tampubolon, & Gustin, (2016)	Aqua Modis was used in Riau Islands Province to monitor of temperature, symptoms of changes, and their distribution can be well described by channels 20, 31, and 32. The validation test carried out was worth 88.6%; this shows that the SST image processing results represent the real condition. The results are presented in an SST information map, and the temperature distribution is presented in web-based spatial information.

The method used in this study is a literature study approach taken from scientific journal publications**.** The monitoring of SST in Indonesian territorial waters becomes the materials to find out whether there is an increase of temperature and the rise of sea**-**levels using remote sensing methods. Consequently, if the increase of sea surface temperature that can cause disasters occurs, the anticipation must be done to prevent such disasters**.** For this research, a study of scientists' findings is carried out as much as possible to get the best results.

Suan Sunandha Science and Technology Journal
©2023 Faculty of Science and Technology, Suan Sunandha Rajabhat University

3. Results and Discussion

Scientists performed the studies that have been carried out for approximately 32 years in various waters in Indonesia including Java, Madura, Bali, West Sumatra, South China, the Pacific Ocean at North of Papua, Lombok, and Malang**.** It turns out that the SST in most of the waters in Indonesia has increased**.** The lowest SST value occurred in 2008, that was around 21^0C, and the highest value in the same year reached 31^0C. Between April 2015 and March 2016 the lowest SST value was 27.07^0C and the highest SST value was 34.98^0C, and in 2020 the SST value was between 30^0C and 31^0C. Based on those data, it turns out that the lowest value occurred from year to year has increased. It started at 21^0C in 2008, then it became 27.07^0C between April 2015 and March 2016, and finally it reached 30^0C in 2020. The highest SST value was 34.98^0C that occurred between April 2015 and March 2016 (Alfajri et al., 2017). These findings observed by scientists are serious matter because SST is an important measure to determine the impact of climate change**.** The ocean can absorb more than 90% of the heat from the greenhouse gases generated by burning fossil fuels, forest fires, and other human activities**.** The condition of hot seawater over a long period is an important indicator of climate change both in the past and present.

The increase of temperature on earth is caused by various factors carried out mostly by humans. They include the burning of fossil fuels, the industrial sector, transportation, deforestation, agricultural and livestock activities**.** These human activities produce carbon emissions that impact the greenhouse effect as the cause of the increasing temperature on the earth**'**s surface. As the further result, it can disrupt the balance condition of ecosystem which is actually necessary to harmonize all living things with their environment. Obviously, the damage of the environment can disturb the balance condition of ecosystem that become a catastrophe which makes living things miserable. It turns out that human activity is the dominant element of ecosystem disturbances**.** All human beings must participate in the restoring process of the environmental balance**.** Humans are the God**'**s intelligence creatures who are responsible to create good environment (Mulyani, 2021b).

Global warming has started since the industrial revolution with the emission of greenhouse gases caused by human activities. The increase of the greenhouse gases is trapped in the atmosphere that has disrupted the flow of natural energy causing imbalance of the energy system on earth. The ocean absorbs more than 90% of heat due to greenhouse gases resulted from burning fossil fuels, forest fires, and other human activities. This condition can cause melting ice and rising sea levels that prove the change of the climate meaning that global warming occurs**.** It is a warning for Indonesia to be always vigilant due to the possible adverse effects. One of the consequences of global warming is the rising of sea**-**level that make the small islands sink. This is a very bad impact for developing archipelagic countries such as Indonesia. The rate of the sea**-**level rise for both tidal data and satellite altimetry in Cilacap is 3.5 mm / year; while in Benoa they are 4.7 mm/year and 5.60 mm/year (Mansawan et al., 2016).

To prevent the global warming, there are several activities that can be performed**.** Reducing the use of fossil fuels can reduce energy consumption. It can be implemented by reducing the use of motorized vehicles because they consume much energy and cause air pollution**.** The individual users of motorized vehicles can be encouraged to use public transportation to carry out them for their daily activities**.** Meanwhile, the public transportation must be supported with good facilities including security guide and standard comfortable requirements for passengers. All of the supporting facilities must be available to make people decide to use the public transportation instead of their own motorized vehicles**.** Currently, the Indonesian government has provided various public transportation**.** There are LRT (Light Rail Transit), MRT (Mass Rapid Transport), Trans Jakarta Buses, and other public transportation especially in big cities where air pollution is very worrying due to excessive use of motorized vehicles**.** Another policy in the field of energy**-**saving is the use of alternative energy that has been implementing in Indonesia and has started to be widely applied. The use of sunlight, hydropower, and wind power can become the alternative energy to reduce air pollution and the greenhouse effect. The preventive action can also be programmed for deforestation that must be followed by reforestation without burning the forests to avoid air pollution. The use of eco**-**friendly material must be encouraged to support the program of reforestation.

Suan Sunandha Science and Technology Journal
©2023 Faculty of Science and Technology, Suan Sunandha Rajabhat University

The phenomenon of sea-level rise (Sea Level Rise or SLR) is an issue that arises along with the problem of global warming. The phenomenon of global warming can lead to thermal expansion and variations of water mass caused by previous results such as melting glaciers and polar ice caps as well as the changes of global average sea level. The rising of sea levels will certainly inundate sloping coastal land and those that can also fall due to land subsidence. This effect is important since it will influence socio-economic impact, infrastructure, disruption of human activities especially in coastal areas with their environment. As the result, the coastal area with more than 10% of the world's population living on the coast, especially for Indonesia as an archipelagic country, can become decreased because of the land loss around the area. The coastal area that will be suffered from the threatens of sinking land is inhabited by 60% of the population. Since the late 19th century, the changes of seawater position have been observed from tidal stations along the coastline. However, the observations have limitations in terms of number, distribution, and range as well as their contribution to land subsidence. Therefore, the presence of altimetry satellites can really help to monitor the sea-level rise. The rising of sea-level that occurs every year can be caused by unstable climate change. It happens when the earth's temperature is increased as the impact of the increasing greenhouse gases.

Based on the findings of several scientists, sea-level rise on the east coast of North Sumatra has a significant negative impact on coastal activities and ecosystems. The regional mean of sea level trend for 23 years, i.e. 1993 - 2016, estimated from altimetry satellite, is 5.0 mm/year, and the potential loss of coastal areas in these areas due to 1 m and 2 m inundation can range from 11.9 km^2 to 63.8 km^2 (Gaol et al., 2017). The study results during the years 2002 - 2005 showed that the lowest sea-level rise of 1.83 mm/year was in the Flores Sea, while the fastest rising of sea level trend that reached a value of 72.313 mm was in the Java Sea area occurred in 2015 (Mujadida et al., 2021).

From the altimetry satellite, the observation data used for reference mission is provided by Topex/Poseidon, Jason 1, Jason 2, and Jason 3 to analyze the trend of sea-level rise in Indonesia and its spatial distribution. It turned out that the sea-level rise rate in Indonesia was 4.6 ± 0.2 mm/year for the period of 1993 - 2018. The positive linear trend with the equation of $y = 4.6x - 9133.5$ where y is the sea-level anomaly in mm and x is the time in years, indicates that the sea-level in Indonesia will continue to increase (Ariani, 2018; Handoko, Yuwono, & Ariani, 2020). Another impact of sea-level rise is that the coastline advances to the mainland can make the waves erode the harbor pier and wave barrier that can decrease the strength of building structures on the coast. According to these results, the decision-maker can carry out pre-event planning to prevent the impact of the sea-level rise in the future. The changes of SST must be informed early; therefore, it is necessary to monitor temperature symptoms temporarily in order to analyze the changes of surface temperature patterns. The early detection of surface temperature must be implemented as soon as possible to take strategic actions or real steps to anticipate disasters.

The remote sensing technology is very helpful for scientists to monitor the earth's surface, water temperature, and sea-level rise that the desired SST data can be obtained quickly on a global scale and even in a large area. As the archipelagic country with a very wide sea level, Indonesia really needs to be able to detect SST early to determine the condition of sea waters. Based on the results of research carried out by scientists, in general the SST in Indonesia has been increasing every year; this is a very serious problem that can become a challenge for Indonesia. The policy to reduce the negative impacts caused by the condition of SST can be considered by Indonesian government to be able to overcome the problems. As the indicator of climate change, the SST is important to avoid hot temperature and air on earth that can cause global warming. The strategic action should be determined to reduce the causes by lowering SST which can be followed by lowering the earth's surface and air temperature.

Indonesia maintains its headline target to lower greenhouse gas emission not more than 41% by 2030 with the international assistance. Indonesian government has updated its adaptation measures and included a new long-term development strategy for low carbon. For the energy sector, Indonesian government plans to stop using coal, oil, and gas by 2060 and aims to have 85% of its energy needs from renewable sources and the rest from nuclear energy (Reuters, 2021). Indonesia is also looking for utilizing energy storage and hydrogen fuel cell technology. A mega hydropower plant in North

Suan Sunandha Science and Technology Journal
©2023 Faculty of Science and Technology, Suan Sunandha Rajabhat University

Kalimantan has been expected to start construction since October 2022 to support renewable energy contribution. While in 2020 Indonesia had reduced deforestation to its lowest level in the last decade, it should step up the efforts to address the climate crisis.

4. Conclusions

Based on the description above, the conclusions can be made in statements as follows:

a. The SST trends in Indonesia that were detected in some of the water areas using remote sensing methods for 32 years has increased.
b. Global warming has already happened in Indonesia with the climate change in the form of extreme weather that causes disasters such as hurricanes, extreme rains, landslides, and floods**.** The impact continues with the melting process of polar ice caps as the cause of sea level rise that can make the sinking process of small islands. As an archipelagic country, there is a possibility that Indonesia can have big losses with the sinking of small islands if the impact occurs caused by the rising of sea level.
c. The sea level in Indonesia has been increasing for some periodical time that in some conditions can damage infrastructure and disturb the activities of coastal communities. It is also the threat for small islands and coastal areas being submerged.

Acknowledgements

I am profoundly thankful to the Head of Research Institute and Community Service in Universitas Kristen Indonesia for the help and support in the process to complete this research.

ORCID

Author

Ir. Agnes Sri Mulyani, M.Sc.
Education and Qualification
Bachelor **(**Surveying/Teknik Geodesi**)**, Universitas Gadjah Mada, Indonesia**.**
Master of Science, Interdisciplinary Natural Resources Development and Management Program, Asian Institute of Technology, Bangkok, Thailand.
https://orcid.org/0000-0003-0491-5200
Scopus Author ID:57362008100
http://www.scopus.com/inward/authorDetails**.** url?authorID=57362008100&partnerID=MN8TOARS

References

Al Tanto, T. (2020). Deteksi suhu permukaan laut (SPL) menggunakan satelit. *Jurnal Kelautan: Indonesian Journal of Marine Science and Technology*, *13*(2), 126-142. doi:10.21107/jk.v13i2.7257

Alfajri, A., Mubarak, M., & Mulyadi, A. (2017). Analisis spasial dan temporal sebaran suhu permukaan laut di perairan Sumatera Barat. *Dinamika Lingkungan Indonesia*, *4*(1), 65-74. doi:10.31258/dli.4.1.p.65-74

Ariani, R. (2018). *Analisa kenaikan muka air laut di perairan Indonesia menggunakan data altimetri Topex/Poseidon dan Jason Series tahun 1993-2018, Tugas Akhir*. Institut Sepuluh Nopember Surabaya. Retrieved from https://repository.its.ac.id/55856/7/03311440000049-Undergraduate_Thesis.pdf

Azizah, A., & Wibisana, H. (2020). Analisa temporal sebaran suhu permukaan laut tahun 2018 hingga 2020 dengan data citra Terra Modis. *Jurnal Kelautan*, *13*(3), 196-205. doi:10.21107/jk.v13i3.7550

Cheng, L., Abraham, J., Trenberth, K. E., Fasullo, J., Boyer, T., Locarnini, R., ... Zhu, J. (2021). Upper oceans temperatures hit record high in 2020. *Advances in Atmospheric Science*, *38*(4), 523-530. doi:10.1007/s00376-021-0447-x

Dwi Ayu, R. A., Sukojo, B. M., & Jaelani, L. M. (2011). Studi perubahan suhu permukaan laut menggunakan satelit Aqua Modis. *Geoid*, *7*(1), 073-078. doi:10.12962/j24423998.v7i1.4223

Emiyati, Setiawan, K. T., Manopo, A. K. S., Budiman, S., & Hasyim, B. (2014). Analisis multitemporal sebaran suhu permukaan laut di perairan Lombok menggunakan data penginderaan jauh MODIS. *Buku Prosiding Seminar Nasional Penginderaan Jauh* (pp. 470-479). Retrieved from http://repositori.lapan.go.id/1557/1/Prosiding_E miyati_Pusfatja_2014.pdf

Suan Sunandha Science and Technology Journal
©2023 Faculty of Science and Technology, Suan Sunandha Rajabhat University

Gaol, J. L., Tambunan, E., Osawa, T., Pasaribu, B., & Nurjaya, I. W. (2017). Sea level rise impact on eastern coast of North Sumatra, Indonesia. *2nd International Forum on Sustainable Future in Asia, 2nd NIES International Forum.* Bali, Indonesia. Retrieved from http://repository.ipb.ac.id/handle/123456789/103633

Handoko, E. Y., Yuwono, & Ariani, R. (2020). Analysis kenaikan muka air laut Indonesia tahun 1993-2018 menggunakan data altimetri. *Geoid*, *15*(1), 58-64. doi:10.12962/j24423998.v15i1.3958

Mansawan, A. A., Lumban-Gaol, J., & Panjaitan, J. P. (2016). Variation and trend of sea level derived from altimetry satellite and tide gauge in Cilacap and Benoa coastal areas. *International Journal of Remote Sensing and Earth Sciences*, *13*(1), 59-66 doi:10.30536/j.ijreses.2016.v13.a2703

Mayasari, O. S., & Handoko, E. Y. (2010). Analisa sea level rise dari data satelit altimetri Topex/Poseidon dan data Sea Surface Temperature menggunakan software BRAT 2.0.0; Studi kasus perairan Indonesia. *Geoid*, *5*(1), 39-47. doi:10.12962/j24423998.v5i1.7329

Mujadida, Z., Setiyono, H., Handoyo, G., Hariyadi, H., & Marwoto, J. (2021). Analisis dinamika permukaan laut di Laut Jawa dengan Recurrent Neural Network periode 1993 sampai 2019. *Indonesian Journal of Oceanography*, *3*(1), 100-110. doi:10.14710/ijoce.v3i1.10661

Mulyani, A. S. (2021a). Antisipasi terjadinya pemanasan global dengan deteksi dini suhu permukaan air menggunakan data satelit. *Centech*, *2*(1), 22-29. doi:10.33541/cen.v2i1.2807

Mulyani, A. S. (2021b). Pemanasan global, penyebab, dampak dan antisipasinya. Retrieved from http://repository.uki.ac.id/4908/1/PEMANASANGLOBAL.pdf

Putra, I. N. J. T., Karang, I. W. G. A., & Putra, I. D. N. N. (2019). Analisis temporal suhu permukaan laut di perairan Indonesia selama 32 tahun (Era AVHRR). *Journal of Marine and Aquatic Science*, *5*(2), 234-246. doi:10.24843/jmas.2019.v05.i02.p11

Reuters. (2021). *Indonesia optimistic of reaching net zero emissions by 2060 or earlier*. Retrieved from https: / / www. reuters. com/ business/ environment/ indonesia- optimistic-reaching- net- zero- emissions- by- 2060- or-earlier-2021-07-27/

Sulaiha, F., Handoko, E. Y., & Yuwono, Y. (2020). Studi variasi permukaan laut Jawa dan laut China selatan tahun 2002-2019 menggunakan data altimetri Jason. *Geoid*, *15*(2), 172-178. doi:10.12962/j24423998.v15i2.6953

Syaifullah, M. D. (2015). Suhu permukaan laut perairan Indonesia dan hubungannya dengan pemanasan global. Jurnal Segara, 11(2), 103-113. doi:10.15578/segara.v11i2.7356

Tampubolon, A. B., & Gustin, O. (2016). *Pemetaan suhu permukaan laut Menggunakan Citra Satelit Aqua Modis di perairan Provinsi Kepulauan Riau*. Politeknik Negeri Batam. doi:10.13140/RG.2.2.11693.08161

Triana, V. (2008). Pemanasan global. *Jurnal Kesehatan Masyarakat*, *2*(2), 159-163. doi:10.24893/jkma.v2i2.26

Available online at https://li02.tci-thaijo.org/index.php/ssstj

Suan Sunandha Science and Technology Journal
©2023 Faculty of Science and Technology, Suan Sunandha Rajabhat University

Comparison of the Effectiveness of Two Histochemical Staining Techniques for Steatosis Detection in Liver Tissue and Application in Forensic Autopsy: A Case Study

Yasudama Chaimad[1*], Woratuch Witchuvanich[2]

[1]Program in Forensic Science and Criminal Justice, Faculty of Science, Silpakorn University, Mueang Nakhon Pathom District, Nakhon Pathom Province 73000, Thailand
[2]Faculty of Forensic Science, Royal Police Cadet Academy, Sampran District, Nakhon Pathom 73100, Thailand
***Corresponding author e-mail: yasudama2929@gmail.com**

Received: *1 February* 2023 / **Revised:** *21 March 2023* / **Accepted:** *19 April 2023*

Abstract

Oil Red O (ORO) stain is lipophilic for stain fat and lipid components, it is one of the chemical reagents which have the potential to be utilized for forensic medicine to identify asphyxia deaths from pulmonary emboli, that are frequently occurred following an accident or sudden death. Consequently, it can increase forensic pathologists' confidence and lower the cost of delivering ORO stains to other units. Therefore, the authors were interested in comparing the effectiveness of commercial ORO-C and homemade ORO-HM in steatosis samples. Tissue samples were collected and divided into two groups namely with fixative and without any preservative. Assessment of the persistence efficiency of ORO-HM at different storage periods was performed by four experts with a blind testing method. The results were compared by assessing the efficiency of two histochemical stains using the SPSS software. The results showed that ORO-HM in both fresh and formalin-fixed tissues represented decent efficiency in fatty changed detection which was in line with the results from ORO-C. However, the ORO-HM data in formalin fixative tissues was clearer than fresh tissue ($p < 0.05$). This study presents that the ORO-HM method expresses promising results, that is useful for the diagnosis of steatosis as same as ORC-C. Furthermore, it should be performed in slides of no longer than 72 h storage time because the efficiency of the dye would deteriorate significantly. In conclusion, ORO-HM stain in this study provided compatible results with PRC-C and could be utilized in forensic medicine.

Keywords: Fatty change, Oil Red O, Fat embolism, Histochemical staining, Forensic medicine

1. Introduction

Oil Red O (ORO) is a lysochrome (a fat-soluble dye) diazo dye uses for staining of neutral triglycerides, fatty acids, and lipids on frozen sections and some lipoproteins on paraffin sections. Alexandre Beaudoin discovered it in 2004, and its structural formula is $C_{26}H_{24}N_4O$ (Figure 1) (Bumbrah, Sodhi, & Kaur (2019). ORO stains complex phospholipids and glycolipids with polar groups poorly, which means it does not stain myelin, peripheral nerves, or biological membranes and thus highlights only fat droplets. The staining has to be performed on fresh samples, as alcohol fixation removes most lipids (Definition of Oil Red O, 2021). Some benefits of ORO stains; pathologists use ORO stains in muscle biopsies to assess the amount of sarcoplasmic lipid droplets and to look for lipid storage diseases, primary carnitine deficiency, neutral lipid storage disease with myopathy, assessing steatosis in liver transplant biopsy (Riva et al., 2018). It was used in cytopathology to raise the levels of lipid-laden macrophages (Quan, Hoerger, Mullins, & Kuhn, 2022), in lung transplant biopsies (Marangu et al., 2018), various respiratory conditions, including chronic smoking, gastroesophageal reflux (Hopkins et al., 2010), lipoid pneumonia (Nguyen & Oh, 2013), fat embolism, pulmonary alveolar proteinosis and pulmonary aspiration (Bandla, Davis, & Hopkins, 1999). In clinical pathology, it is used to fecal fat test which is a test for indicating abnormal fat absorption (Fine & Ogunji, 2000) and study lipid metabolism in worms (Wang & Ching, 2021). In addition to forensic science or forensic medicine, ORO is used for fat emboli detection in tissue (Milroy & Parai, 2019; Turkmen Samdanci et al., 2019) or the

Suan Sunandha Science and Technology Journal
©2023 Faculty of Science and Technology, Suan Sunandha Rajabhat University

development of latent fingerprints on porous exhibits that are dry or wet, such as paper, cardboard (Bumbrah et al., 2019), etc.

In current practice, forensic histopathology laboratory of Institute of Forensic Medicine Police hospital, has a role to support the work of forensic medicine in determining the cause of death. Based on the principles of histology and pathology. As mentioned above, in forensic science, fat emboli detection techniques are commonly used in cases of unexpected death or sudden death when the autopsy and the determination of the cause of death by the hematoxylin and eosin stain technique (H and E) cannot explain the exact cause of death. Fat emboli can be seen in other organs, including the brain, kidneys, and heart muscle (Turkmen Samdanci et al., 2019). There is a mechanism by fat droplets obstruction of blood vessels and / or by biochemical methods, i.e. lipolysis into free fatty acids induce an inflammatory response (Parai & Milroy, 2018). For instance, death from cardiopulmonary resuscitation (CPR) is an emergency procedure for maintaining blood circulation and oxygenation during cardiac arrest (Deliliga, Chatzinikolaou, Koutsoukis, Chrysovergis, & Voultsos, 2019), Lipoplasty or liposuction, the surgical process of removing excess fat or orthopedic surgery. Trauma in general, and particularly fractures of long bones or ribs (after cardiopulmonary resuscitation (CPR)) or accident and intra-medullary nailing (Voisard, Schweitzer, & Jackowski, 2013), Blunt injury of adipose tissue, fatty liver and pancreatic necrosis as well as other factors such as severe toxicity that causes liver failure are additional suspected or proven triggers of fat embolism. Furthermore, it can also be seen in sudden deaths caused by a fat embolism in the lungs in patients with miliary tuberculosis, which 90% of the people with incidents such as those listed above showed a microscopically visible fat embolism. (Chinen & Ito, 2019). Therefore, detection of a fat embolism in autopsy requires the history, clinical and laboratory findings along with autopsy investigations to determine its relevance.

According to data from the Institute of Forensic Medicine Police Hospital, there are approximately 5,600 autopsies performed each year. In 3,350 cases (accident 1,306 cases), an unknown cause of death was discovered. To support forensic medicine practice and reduce the cost of sending ORO to external agencies. Therefore, the researcher is interested in preparing a histochemical stain for fat emboli detection called ORO in-house (ORO-Homemade, ORO-HM), with the aim of comparing the efficacy of ORO in-house with ORO commercial (ORO-C stain sets). As far as we know, it has been recommended that tissue stained with Oil Red O must be examined within 24 hours because the quality of the ORO will fade due to lipids that may be accused of distorting and floating together because of the lower surface tension of the lysochrome organic solvent. Therefore, the researcher was interested in studying the stability of the ORO-HM dye at 48 h, 72 h, 7 days, 1 mo, and 2 months. If the lipid drops in Oil Red O stained tissue, it will keep its original position and color over time. (Christoffersen & Thomsen, 2014).

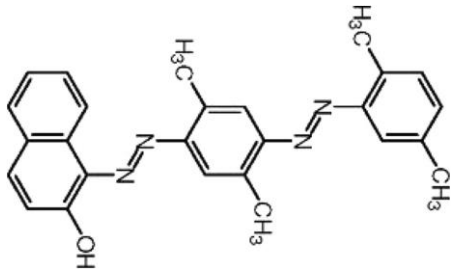

Figure 1. Schematic representation of the structure formula of Oil Red O ($C_{26}H_{24}N_4O$) (Bumbrah, Sodhi, & Kaur (2019).

As a result, the goal of this study is to (1) compare the quality of fat stains in tissue between the ORO-HM and ORO-C stain sets. (2) To assess the ability to report the diagnosis of steatosis or a fatty change in tissue between the ORO-HM and ORO-C stain sets, (3) To assess the persistence of ORO-HM at different time intervals.

2. Materials and Methods

2.1 Chemicals

All reagents used were at least analytical reagent (AR) grade. Isopropyl alcohol was supplied by Lab scan (Thailand). Oil Red O-HM was supplied by Sigma-Aldrich (Thailand) and Oil Red O–Commercial set was supplied by Bio-Optica. 40% formaldehyde was supplied by the Government Pharmaceutical Organization. O.C.T. Compound embedding medium for cryostat was supplied by Bio-Optica. Mayer Hematoxylin was supplied by Thermo Fisher Scientific (Thailand).

Suan Sunandha Science and Technology Journal
©2023 Faculty of Science and Technology, Suan Sunandha Rajabhat University

2.2 Instruments

Embedding tissue was performed by Medite model TES Valida, Microtome section was done by Epredia™ model HM 355S, Automatic slide strainer was Intelsint model AUS-1, Microscope was Nikon model Ni-U and Cryostat Microtome (Frozen section) was Leica model CM1860 UV Cryostat in which temperature range of 0°C to -60°C was used for frozen fresh tissue.

2.3 Methods for preparing reagents and ORO-HM dyes

Methods for the preparation of ORO-HM dyes, (a) Preparation of Oil Red O stock solution, 0.5g of Oil Red O powder was dissolved with 100 ml of isopropyl alcohol and mix until homogeneous achieved; (b) preparation of Oil Red O working solution, 3 ml of stock Oil Red O with 2 ml of distilled water mixed well and leaved at room temperature for about 30 min; and (c) filter before used; this dye cannot be reused.

Methods for 60% isopropyl alcohol, 30 ml of isopropyl alcohol was measured and mixed with 20 ml of distilled water.

Methods for the gelatin jelly, 10 g of gelatin weighted and mixed with 52.5 ml of distilled water, melted by heat and added glycerin and phenol when it was completely dissolved. Mix together and leave to cool to form a jelly. It was Preserved in the refrigerator.

2.4 Samples / study population

This research was a case-control study. Samples of cadavers' tissues had been granted by the Institute of Forensic Medicine, Police Hospital. All samples were blinded for ethical issues. The study was approved by the Human Research Ethics Committee Silpakorn University Certificate with issue number of COE 63.0325-024. By collecting samples from liver organs, criteria for consideration were included such as the appearance of a fatty liver or fat accumulation in the liver cells, the appearance of the surface as bulges of various sizes or smooth, yellowish-green, non-rotten condition and with rotten tissue being the exclusion criterion**.** Evaluation of pathological characteristics by a pathologist were performed by dividing into 2 types, liver tissue fixed in 10% formalin and fresh tissue samples. All tissue samples were stored at 4-8°C until analysis. The samples were collected between 14 May 2022 to 31 May 2022 with a total number of 30 cases.

- Preparation of liver tissue samples was done by cutting the liver tissue samples into 2 pieces with a sizing of 0.5x0.5x0.5 mm. Then fixed them with a desired preservative 1 piece and left the rest for a fresh sample group.
- Normal liver tissue samples or no fatty liver tissues were used as a negative control group.
- Positive fatty changes in liver tissue samples were used as a positive control group.

In assessing the quality of both sets of dyes, four experts were invited to assess the quality of both sets of dyes by random blind testing procedures on the following issues: (1) assess the quality of the fat stain; (2) ability to detect changes of fatty changes in the liver tissue of patients with steatosis; (3) evaluate the durability of ORO-HM dyes over time; and (4) suitability of ORO-HM dye to be used in a forensic medicine.

2.5 A comparison of the fat stain quality and ability to diagnose steatosis between the ORO-HM and ORO-C stain sets

2.5.1 Tissue preparation by histological technique

(a) Dissected tissue of the desired size was placed into the tissue cassettes, and then brought it into the automatic tissue processing according to the machine's working program which were as follows: (1) tissue fixation with 10% formalin, dehydration with 95% alcohol and ethanol, (2) clearing tissue sample with xylene simmering, and (3) infiltration with paraplast. Total time required was approximately 22 to 24 hours; and (b) hematoxylin and eosin staining (H and E) process was started with an automatic slide staining machine according to the machine's working program as follows:(1) deparaffinization with xylene simmering, (2) rehydration with ethanol and 95% alcohol, (3) hematoxylin nuclear staining and eosin counterstaining, (4) dehydration with 95% alcohol and ethanol. In order to make sure that the slices were clear, the final step was utilized with the process of sample clearing with xylene. Total time was roughly 30 minutes.

2.5.2 Procedure for staining liver slides with ORO

Firstly, the fresh liver and liver were fixed by 10% formalin with a sizing of 0.3x0.3x0.2 mm then they were sliced into thin tissues by a cryostat machine. The obtained slides were then stained with

Suan Sunandha Science and Technology Journal
©2023 Faculty of Science and Technology, Suan Sunandha Rajabhat University

Oil Red O according to the following procedure. (1) Oil Red O homemade (ORO-HM) staining, (2) the slides were dipped in 60% isopropyl alcohol and (3) stained with working Oil Red O for 20 minutes before being differentiated in 60% isopropyl alcohol until the background color was completely removed and (4) washing with running tap water. (5) The slide was then counterstained with hematoxylin for 1-2 minutes before being washed for 5 minutes under running tap water. In the final process, slides were wiped dry and coated with gelatin jelly glass lacquer, a solution used exclusively for tissue lipid staining.

Secondly, standard Oil Red O commercial staining sets (ORO-C stain sets) were as follow; (1) slice section was submerged into distilled water, (2) place the ORO solution in a coplin jar, and (3) immerse the slides for 20 minutes before washing quickly in tap water. (4) Drain the slide and place it on hematoxylin solution for 30 seconds before washing in running tap water for 3 minutes, Final step was to drain and mount in gelatin jelly.

2.6 Assessment of ORO-HM dyes persistence over time

Take slide sections from point 2.5 of each sample were examined and photographed at x40 magnification within 24 h after staining. After that, all slides were stored in small plastic boxes. At the same time, all of the samples were analyzed, and they were all kept at the same steady ambient temperature in a dark location. examination and photography were repeated, using the same microscope at 24 h, 48 h, 72 h, 7 days, 1 month, and 2 months, respectively. Each time, photos of the identical area of each sample were taken. Finally, the pictures were compared in order to ascertain if the lipids in each sample had migrated from their initial positions as well as to assess the color quality.

2.7 Statistical analysis

The data were expressed as the mean and comparative mean differences in fatty tissue staining ability and the reporting of hepatic steatosis between ORO-HM stain and ORO-C stain sets, and the stability color of the ORO-HM stain was assessed using the SPSS program. The analysis was performed by one-way ANOVA and Chi-square tests. Differences were considered to be statistically significant at $p < 0.05$.

3. Results and Discussion

3.1 Assessment of hepatic steatosis samples by hematoxylin and eosin (H and E) methods

Hepatocytes, which are large polygonal cells with eosinophilic (pink) cytoplasm and round nuclei, present in Figure 2a as histopathological features of the normal liver. The portal tracts (PT) consist of the hepatic artery (HA), portal vein (PV), and bile duct (BD). The CV is lined by a single layer of endothelial cells and drains blood coming from the portal tracts (PT) via sinusoids. Hepatocyte plates extend toward the portal tracts from the central vein (CV) (PT) in the picture on the right. Histopathological features of the abnormal liver demonstrated fatty changes or steatosis, which represents the intracytoplasmic accumulation of triglycerides. The hepatocytes present small fat vacuoles and macrovesicular fatty change (Figure 2b) (Liver Fellow Network, 2020).

A total of 30 liver tissue samples were examined using hematoxylin and eosin (H and E) staining by two pathologists. According to histology, 16 cases of steatosis show liver parenchyma with markedly diffuse small and large droplet infiltration, no inflammatory cell or malignancy is seen. In addition, fibrosis of the liver parenchyma and cirrhosis were also found, and 14 cases of non-steatosis show liver parenchyma composed of small lobules of roughly hexagonal shape with portal tracts at the apices. Inside the lobules, the hepatocytes are arranged as cords of cells connecting the portal tracts in the periphery to the central veins. In addition, in some cases, liver cells are also found to be inflamed.

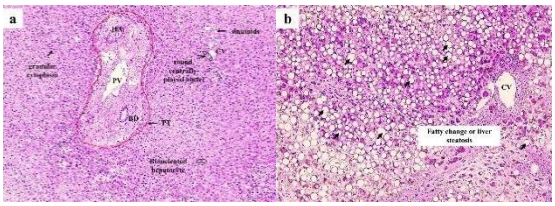

Figure 2. Histopathological comparison images of liver tissue samples. a) normal liver showed the central vein (CV), portal tracts (PT), hepatic artery (HA), portal vein (PV) and bile duct (BD) b) abnormal liver showed fatty changes or steatosis (shown with arrows, 10x).

Suan Sunandha Science and Technology Journal
©2023 Faculty of Science and Technology, Suan Sunandha Rajabhat University

3.2 Assessment of quality of fat stain between ORO-HM and ORO-C stain sets

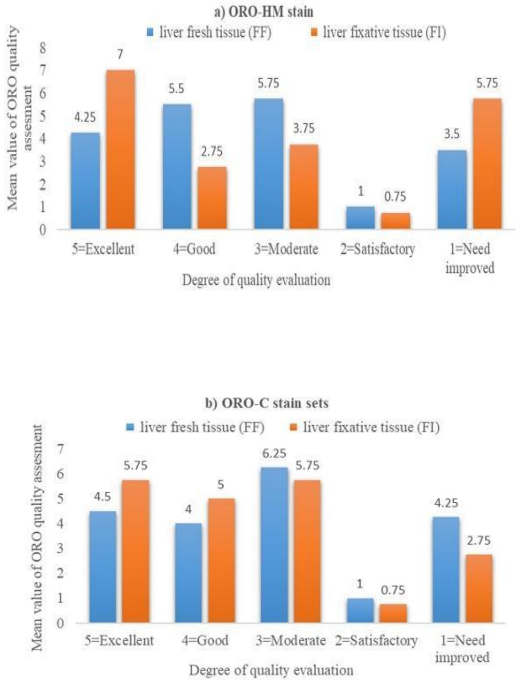

Figure 3. The mean qualitative assessment results between a) ORO-HM and b) ORO-C stain sets in the liver samples for both types, (ORO, Oil Red O), (ORO-Homemade, ORO-HM), (ORO-C stain sets, ORO-C), (FF, fresh tissue or non-fixative), (FI, fixative tissue).

Figure 3 shows the average results of the quality evaluation of the two ORO lipid dyes for both types. Four experts evaluated liver samples based on the type of specimen as follows: 3a) presented, the staining quality of ORO-HM in the fresh liver sample showed excellent staining quality of ORO-HM 4.25 (21%), good 5.5 (27%), moderate 5.75 (29%), satisfactory 1 (5%), and needs improvement 3.5 (18%), respectively. Likewise, ORO-C stain set lipid quality in non-fixed liver samples showed that the staining quality was excellent 4.5 (23%), good 4 (20%), moderate 6.25 (31%), satisfactory 1 (5%) and need improved 4.25 (21%). As for the fixative liver samples, the staining quality of the ORO-C stain set was excellent 5.75 (28%), good 5 (25%), moderate 5.75 (29%), satisfactory 0.75 (4%) and need improved 2.75 (14%), respectively.

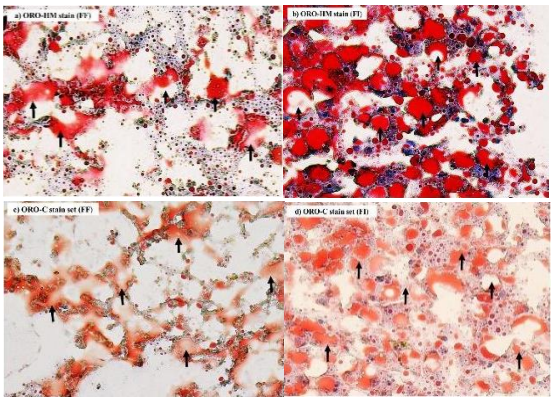

Figure 4. Photographs of liver fatty changes by ORO-HM and ORO-C stain sets between fresh and fixative tissue samples a) ORO-HM stain (fresh tissue), b) ORO-HM stain (fixative tissue), c) ORO-C stain sets (fresh tissue) and d) ORO-C stain sets (fixative tissue) x10 magnification., (ORO, Oil Red O), (ORO-Homemade, ORO-HM), (ORO-C stain sets, ORO-C), (FF, fresh tissue or non-fixative), (FI, fixative tissue).

Figure 4, shows the histopathology of liver steatosis by the histochemical stain in 4 groups. Morphologic and shade of color differentiation was easily assessed the fatty change using the ORO-HM stain (fixative tissue) and the ORO-C stain sets (fixative tissue). Unlike the ORO-HM (fresh tissue) stain, the ORO-C (fresh tissue) stain series is difficult to diagnose due to the altered shape of the liver cells. Poor nuclear staining obscures hepatocyte boundaries. In Figures 3 and 4, it can be seen when liver steatosis was stained with ORO-HM and ORO-C stain sets in fresh autopsy samples, the quality was not different at all levels, i.e., excellent at 4.25 and 4.5, good at 5.5 and 4.0, moderate at 5.75 and 6.25, satisfactory at 1 and 1, and need improved at 3.5 and 4.25, respectively. However, the ORO-C stain sets had a higher mean quality improvement than the ORO-HM. This was due to the non-fixative in tissue specimens, which caused specimens to be easily degenerative, difficult to frozen section, easily folding and wrinkled, and deteriorating the nucleus structure. When examined under a microscope, the nuclei were not clearly stained, and cell boundaries were unclear. As illustrated in Figures 4a) and 4c), this makes fatty change diagnosis difficult. In contrast, when staining liver steatosis with ORO-HM and ORO-C stain sets in fixative specimens, the quality of the stain was consistent with fresh tissue samples at all levels; thus, excellent was 4.25 and

Suan Sunandha Science and Technology Journal
©2023 Faculty of Science and Technology, Suan Sunandha Rajabhat University

4.5, good was 5.5 and 4.0, moderate was 5.75 and 6.25, satisfactory was 1 and 1, and need improved was 3.5 and 4.25, respectively, but the fixative tissue samples were able to diagnose fatty change more easily than fresh tissue samples, as shown in Figures 4b and 4d.

Table 1 shows the results of the statistical analysis of fat stain quality between ORO-HM and ORO-C stain sets on liver tissue slides. When comparing ORO-HM in fresh tissue samples, it was found that the quality had no difference at all levels with ORO-C stain sets in both fixative and fresh. However, when only comparing ORO-HM, found that ORO-HM in fresh tissue samples showed significantly different dye quality at every level from ORO-HM in fixative tissue samples. Statistically, the value is 0.009 ($p < 0.05$).

Table 1. The statistical analysis of qualitative assessment results between ORO-HM and ORO-C stain sets on liver tissue slides.

Type of ORO	Type of ORO	Mean Different	Std. Error	Sig.
ORO-HM (FF)	ORO-C (FF)	-.300	.227	.187
	ORO-HM (FI)	-.600*	.227	.009*
	ORO-C (FI)	-.425	.227	.062
ORO-C (FF)	ORO-HM (FF)	.300	.227	.187
	ORO-HM (FI)	-.300	.227	.187
	ORO-C (FI)	-.125	.227	.582
ORO-HM (FI)	ORO-HM (FF)	.600*	.227	.009*
	ORO-C (FF)	.300	.227	.187
	ORO-C (FI)	.175	.227	.441
ORO-C (FI)	ORO-HM (FF)	.425	.227	.062
	ORO-C (FF)	.125	.227	.582
	ORO-HM (FI)	-.175	.227	.441

*The mean difference is significant at the 0.05 level., (ORO, Oil Red O), (ORO-Homemade, ORO-HM), (ORO-C stain sets, ORO-C), (FF, fresh tissue or non-fixative), (FI, fixative tissue)

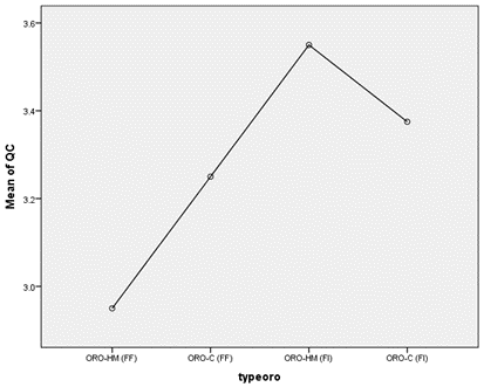

Figure 5. The means plot of qualitative assessment results between ORO-HM and ORO-C stain sets in the liver samples for both types., (ORO, Oil Red O), (ORO-Homemade, ORO-HM), (ORO-C stain sets, ORO-C), (FF, fresh tissue or non-fixative), (FI, fixative tissue).

Figure 5 shows the average results of four experts who evaluated the quality of the two ORO lipid dyes for both types of liver samples as follows: they concluded that the best quality staining of ORO is ORO-HM in fixative tissue samples (ORO-HM (FI)) = 3.55, ORO-C stain sets in fixative tissue samples (ORO-C (FI)) = 3.38, ORO-C stain sets in fresh tissue samples (ORO-HM (FF)) = 3.25 and ORO-HM in fresh tissue samples (ORO-HM (FF)) = 2.95, respectively.

Although the qualitative assessment results of the four lipid dye groups in parts of their frequency distribution (Figure 3) and histopathological results are shown in Figure 4, did not differ at all levels of qualitative assessment, it is clear that all four levels of quality are trending in the same direction. ORO-HM results for fresh and fixative tissue samples are excellent (4.25 and 7.0), good (5.5 and 2.75), moderate (5.75 and 3.75), satisfactory (1.75 and 1.0), and need to be improved at 3.5 and 5.75, respectively. ORO-C stain sets, both fresh and fixative tissue samples, yielded excellent results of 4.5 and 5.75, good results of 4.0 and 5.0, moderate results of 6.25 and 5.75, satisfactory results of 1.0 and 0.75, and needed improvements of 4.25 and 2.75, respectively. From the study results, it can be seen that both the ORO-HM and ORO-C stain sets had a relatively high level of need for improvement, and changes in the structure of the nucleus, and cell boundaries are unclear, which interferes with the detection of fatty changes. However, when evaluating the quality of the four dye groups using one-way ANOVA statistics, the results were found to be in the same direction as the frequency distribution for only the three groups, which is the quality of ORO-HM dyes for both fresh and fixative tissue samples. There was no difference at all levels when compared with ORO-C stain sets. However, ORO-HM in fixative tissue samples showed different levels of quality than ORO-HM in fresh tissue samples, as shown in Table 1, in which ORO-HM fixative tissue samples showed better staining quality than ORO-HM in fresh tissue samples, and ORO-C stain sets in both fresh and fixative tissue samples are shown in Figure 5. Therefore, in order to make a reliable diagnosis of steatosis with ORO dye, ORO-HM can be used in fixative specimens because the staining quality is similar to that of ORO-C stain sets.

3.3 Assessment of the diagnostic competency of steatosis between ORO-HM and ORO-C stain sets.

According to the results of the detection of fatty changes on liver steatosis slides stained with ORO-HM, the positive results ranged from mild to severe, with the most moderate yield being 56.9%, while the positive effects of the ORO-C stain sets were also

Suan Sunandha Science and Technology Journal
©2023 Faculty of Science and Technology, Suan Sunandha Rajabhat University

positive in the mild to severe range, with the most severe effect being 54.7%. As shown in Table 2.

Table 2. Comparison of levels of diagnostic competency for fatty liver disease between ORO-HM and ORO-C stain sets.

Tissue slides	ORO type		Grading steatosis				
			Not found	Mild	Moderate	Severe	Total
Liver steatosis	ORO-HM	Count	66	22	33	31	160
		%Grading steatosis	53.2 %	42.3 %	56.9 %	45.3 %	50 %
	ORO-C stain sets	Count	58	30	25	47	160
		%Grading steatosis	46.8 %	57.7 %	43.1 %	54.7 %	50 %

(ORO, Oil Red O), (ORO-Homemade, ORO-HM), (ORO-C stain sets, ORO-C), (FF, fresh tissue or non-fixative), (FI, fixative tissue)

Table 3. Statistical analysis of fatty changes detected on liver tissue slides.

	Value	df	Asymp. Sig. (2 sides)
Pearson Chi square	3.595[a]	3	.309
Likelihood Ratio	3.604	3	.307
Linear-by-Linear Association	.662	1	.416
N of Valid Cases	320		

Chi-squared test, *p*-value < 0.05 statistically significant., (ORO, Oil Red O), (ORO-Homemade, ORO-HM), (ORO-C stain sets, ORO-C), (FF, fresh tissue or non-fixative), (FI, fixative tissue)

The results of statistical differential analysis by SPSS using the chi-square test showed that the fatty changes of ORO-HM and ORO-C stain sets in liver steatosis tissues were not significantly different at the 0.05 level, as shown in Table 3.

3.4 Evaluation of ORO-HM dye quality stability over time

The image shows the persistent quality of ORO-HM dye in fresh and fixative tissue samples over time. It was discovered that the dye's quality can be found to be good for a period of 24 to 72 hours. Macrovesicular steatosis has a single, large vacuole of fat with clear boundaries, which are indicated with black arrows. The color persistence quality of ORO-HM in fresh and fixed tissue samples from day 7 to 2 months showed a deterioration in quality, small fat droplets were found scattered throughout, and patchy artifacts were indicated with yellow arrows. Specifically, in the fresh tissue samples, agglutination of fat droplets (red circles) was observed. The hepatocyte boundaries were not clear; the color was faded, but in the fixative tissue specimen, the appearance of the fat vesicle was still evident. The cell boundaries were still evident, and the color has faded slightly.

The image presented in Figure 6 is an example taken from the same sample that was stored in the same slide box with no moisture and not exposed to sunlight, it was used to check the persistence quality of ORO-HM dye by collecting data for 24 h, 48 h, 72 h, 7 days, 1 month, and 2 months, respectively. Based on previous knowledge, it is recommended that fatty changes should be read immediately or no later than 24 hours for the diagnosis of fatty changes with ORO, which provides the most reliable diagnosis (Christoffersen & Thomsen, 2014).

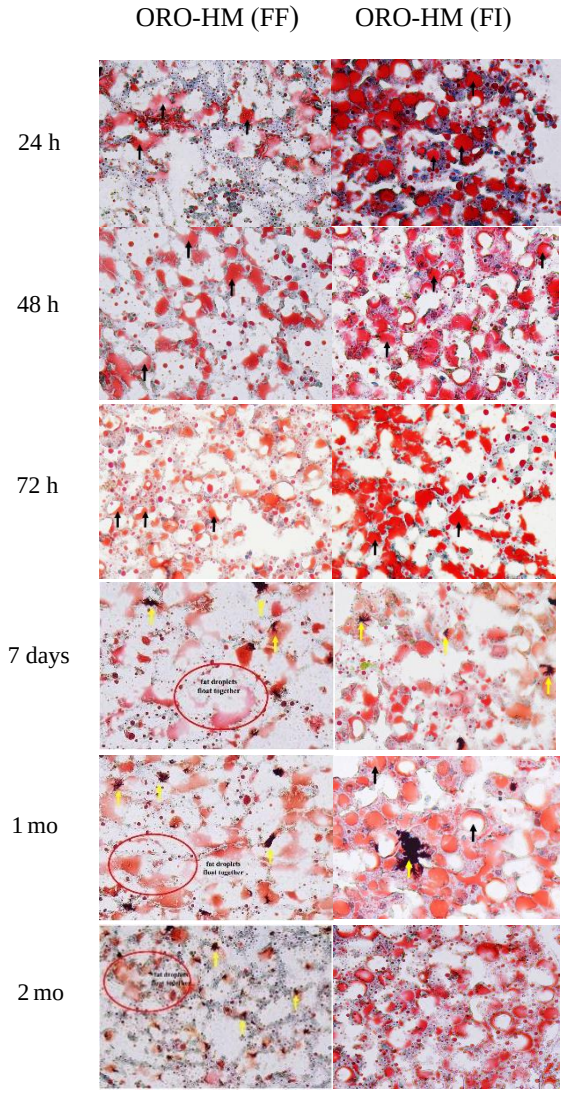

Figure 6. A section stained with Oil Red O-HM in the liver samples for both types followed over time., (ORO, Oil Red O), (ORO-Homemade, ORO-HM), (FF, fresh tissue or non-fixative), (FI, fixative tissue).

From the experiments, it can be seen that ORO-HM can be used to detect fatty changes well in 24 to 72 hours, and the slides should not be reinterpreted when stored for more than 1week because the color quality decreases and there is a precipitation. From

©2023 Faculty of Science and Technology, Suan Sunandha Rajabhat University

the experiments, it can see that ORO-HM can use to detect fatty changes well in a period of 24 to 72 hours, and the slides should not be reinterpreted when stored for more than 1 week because the color quality decreases and there is a precipitation. There is an agglomeration of pigments. The color of the nucleus faded, and there were scattered fat droplets, which hampered interpretation of the results. To determine the effectiveness of the fat stain, all ORO-HMs were found to be consistent with the quality and reportability of the results, i.e., the ORO-HM stain could be used for the diagnosis of steatosis in fixative tissue samples, which provides good quality and can extend the color sticking life for a long time.

3.5 Apply ORO-HM stain in forensic autopsy: Case study

Female, 29 years old, overweight, cause of autopsy due to unnatural death from undergoing breast augmentation liposuction surgery at a clinic. Dead at the hospital, have a history of resuscitation. The first hospital performed an autopsy and found that the cause of death was due to sepsis or septicemia. However, relatives are still suspicious about the cause of death. Therefore, they offered to have the police freeze the corpses and sent the corpses to the second hospital for a thorough autopsy again ("Relatives are fascinated by a woman", 2020)

Autopsy finding, the condition of the body was examined. The external examination of the corpse found wounds on the upper right arm, left arm, under the left breast, right leg, right leg, and left leg. There were no abnormalities discovered during an internal corpse examination of the head, neck, and abdomen. A large bruise wound in the chest spread across the chest area. Tissue samples were sent to the laboratory for hematoxylin and eosin and Oil Red O stain techniques.

Histopathology findings by hematoxylin and eosin methods found that the brain has subcerebral hemorrhage, edema, neuron degeneration, and cell death. Congestive heart edema and inflammation, lungs hemorrhage in the alveoli. The liver and pancreas found fat infiltrates in cells and acute kidney failure. The uterus and ovary had some hemorrhagic patches. ORO-HM stained in lung autopsy showed fat emboli positive within the alveolar space and small patches along the alveolar wall (Figures 7 c and 7d). In addition, they found blood clots within the alveoli of the lungs.

Although death from fat emboli can be tested in multiple organs such as the brain, heart, liver, or kidney in forensic medicine, the lung is the most appropriate organ to use because it is an organ related to the respiratory system and can explain the death most clearly (Turkmen Samdanci et al., 2019). Figure 7 shows the histopathological results of the case study in that the pathologist who sent the stain for histological examination used the Oil Red O color. The laboratory uses a lung fixative tissue autopsy sample for testing. Figures 7c and 7d demonstrate that the ORO-HM dye clearly stained both small and large fat droplets within the alveoli, and found blood congestion in the alveoli that was spread throughout the lung tissue. It is assumed that the mechanism of death in the case study was caused by fat droplets from the liposuction process that escaped into the circulatory system and eventually obstructed the trachea and caused asphyxia. The liver tissue was used as a negative control and a positive control, as shown in Figures 7a and 7b, respectively.

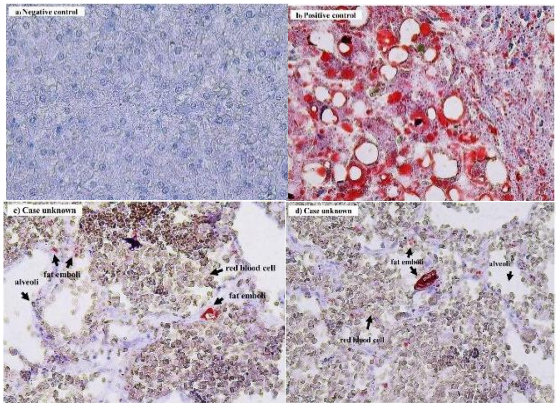

Figure 7. Frozen section autopsy microscopy in samples a) liver: negative control ORO-HM (10X), b) liver: positive control ORO-HM and c and d) lung: Oil red O staining showing large and small fat droplets within the alveolar space (40X)., (ORO, Oil Red O), (ORO-Homemade, ORO-HM).

4. Conclusions

A comparative study of dye efficacy between ORO-homemade (ORO-HM) and commercial ORO (ORO-C stain sets) was performed using liver tissue samples with steatosis and normal liver pathology. A comparison was also made between fresh and fixative liver tissue samples, which was characterized by the samples which were confirmed by a pathologist. The study consisted of assessing the quality of ORO to detect hepatocyte fatty changes, which rating on a 4 scale: excellent, good, moderate, and needing improvement. It was found that the staining quality of fatty changes in hepatocytes in both fresh and fixative tissue samples with ORO-HM was not different from that of ORO-C stain sets. However, ORO-HM in fixative tissue samples had better staining quality than ORO-HM in fresh liver samples. Because fresh tissue samples have a chance to rot easily, the cellular structure changes to an unclear extent. The nucleus begins to partially die. When considering the persistence and quality of ORO-HM in liver cells in both fresh and

©2023 Faculty of Science and Technology, Suan Sunandha Rajabhat University

fixative tissue samples at different times were examined, it was discovered that ORO-HM stained liver cells from 24 to 72 hours can best fatty changes in the liver in the better condition. Compared with the time period of 1 week to 2 months, the persistence of the ORO-HM dye was observed in both fresh and fixative tissue samples and markedly decreased. Especially in ORO-HM fresh tissue samples, fatty changes fusion was found, cell nuclei deteriorated, and cell boundaries were not clearly visible. In addition, in both ORO-HM in fresh and fixative tissue samples, the quality of the dye is faded color and contaminated, which interferes with the diagnosis. The final efficacy assessment of the ORO stain was its ability to report steatosis, found that the ORO-HM stain detects fatty changes at levels of severe steatosis (45.3%) less than ORO stain sets (54.7%) and can report cases where fatty changes were not found at 53.2% and 46.8%, respectively. When the correlation was analyzed by SPSS, it was found that ORO-HM's ability to diagnose steatosis was not different from that of ORO-C stain sets. Therefore, when the ORO-HM dye was used to explain the cause of death in a case study where the preliminary autopsy results could not find a cause of death, Analysis of the cause of death with histochemical staining techniques can detect fat droplets inserted within the alveoli and spreading to different parts of the lung tissue. This technique can support the doctors concluding the cause of death in the case study was due to circulatory failure and asphyxiation from fat droplets becoming obstructed in the trachea, a condition known as a fat embolism. Thus, from all studies, it can be concluded that a fat dye prepared in-house in the laboratory (ORO-HM) is as effective as ORO-C stain sets for elucidating the cause of mortality in unexplained cases. However, the tissue samples should be fixative, and the result should be diagnosed within 3 days to make the interpretation accurate and the most reliable.

Acknowledgements

We would like to express our gratitude to all three experts as well as Police Colonel Pakorn Wisinrat, Deputy Commander of the Institute of Forensic Medicine. Police Hospital, Police Lieutenant Ratchakorn Anantapada, Doctor Pathologist at Pathology Division, Police Hospital, and Dr. Tharinthorn Chansoon, Head of Histopathology Laboratory, Department of Pathology, Faculty of Medicine Ramathibodi Hospital, and we would like to thank the forensic histopathology laboratory at the Institute of Forensic Medicine, Police Hospital, and the pathology laboratory in the Police Hospital for their support and excellent work next to their daily routine and some other authors cited in the text for making literature accessible and for the stimulating discussions.

Ethical Approval

The study was approved by the Human Research Ethics Committee. From the Human Research Ethics Committee Silpakorn University (Date 25 March 2020). Number of ethics COE 63.0325-024

References

Bandla, H. P. R., Davis, S. H., & Hopkins, N. E. (1999). Lipoid pneumonia: A silent complication of mineral oil aspiration. *Pediatrics*, *103*(2), 1-4. doi:10.1542/peds.103.2.e19

Bumbrah, G. S., Sodhi, G. S., & Kaur, J. (2019). Oil Red O (ORO) reagent for detection of latent fingermarks: A review. *Egyptian Journal of Forensic Science*, *9*(3), 1-7. doi:10.1186/s41935-018-0107-1

Chinen, K., & Ito, K. (2019). Sudden death caused by pulmonary fat embolism in a patient with miliary tuberculosis. *Autopsy and Case Reports*, *9*(1), 1-10. doi:10.4322/acr.2018.059

Christoffersen, S. D., & Thomsen, J. L. (2014). Can examination of tissue stained with Oil red O be postponed up to three months? *Scandinavian Journal of Forensic Science*, *20*(2), 50-52. doi:10.2478/sjfs-2014-0005

Definition of Oil Red O. (2021). Retrieved from https://www.pathologyoutlines.com/topic/stainsoilredo.html

Deliliga, A., Chatzinikolaou, F., Koutsoukis, D., Chrysovergis, I., & Voultsos, P. (2019). Cardiopulmonary resuscitation (CPR) complications encountered in forensic autopsy cases. *BMC Emergency Medicine*, *19*(1), 1-7. doi:10.1186/s12873-019-02345-5

Fine, K. D., & Ogunji, F. (2000). A new method of quantitative fecal fat microscopy and its correlation with chemically measured fecal fat output. *American Journal of Clinical Pathology*, *113*(4), 528-534. doi:10.1309/0t2w-nn7f-7t8q-5n8c

Hopkins, P. M., Kermeen, F., Duhig, E., Fletcher, L., Gradwell, J., Whitfield, L., … McNeil, K. (2010). Oil red O stain of alveolar macrophages is an effective screening test for gastroesophageal reflux disease in lung transplant recipients. *The Journal of Heart and Lung Transplantation*, *29*(8), 859-864. doi:10.1016/j.healun.2010.03.015

Suan Sunandha Science and Technology Journal
©2023 Faculty of Science and Technology, Suan Sunandha Rajabhat University

Liver Fellow Network. (2020). *Normal liver histology 101*. Retrieved from https://liverfellow.org/post/normal-liver-histology-101

Marangu, D., Pillay, K., Banderker, E., Gray, D., Vanker, A., & Zampoli, M. (2018). Exogenous lipoid pneumonia: an important cause of interstitial lung disease in infants. *Respirology Case Reports*, *6*(7), 1-7. doi:10.1002/rcr2.356

Milroy, C. M., & Parai, J. L. (2019). Fat embolism, fat embolism syndrome and the autopsy. *Academic Forensic Pathology*, *9*(3-4), 136-154. doi:10.1177/1925362119896351

Nguyen, C. D., & Oh, S. S. (2013). A case of exogenous lipoid pneumonia. *Respiratory Care*, *58*(3), 23-27. doi:10.4187/respcare.01727

Parai, J. L., & Milroy, C. M. (2018). The utility and scope of forensic histopathology. *Academic Forensic Pathology*, *8*(3), 426-451. doi:10.1177/1925362118797602

Quan, M. A., Hoerger, J. L., Mullins, E. H., & Kuhn, B. T. (2022). A 66-year-old man with subacute cough and worsening dyspnea previously diagnosed with COVID-19 pneumonia. *Journal of Investigative Medicine High Impact Case Reports*, *10*, 1-4. doi:10.1177/23247096211055334

Relatives are fascinated by a woman who died as a result of breast augmentation liposuction, whether done by the doctor or the clinic staff. (2020). *Thairath On Line*. Retrieved from https://www.thairath.co.th/news/crime/1921503

Riva, G., Villanova, M., Cima, L., Ghimenton, C., Bronzoni, C., Colombari, R., … Eccher, A. (2018). Oil Red O is a useful tool to assess donor liver steatosis on frozen sections during transplantation. *Transplantation Proceedings*, *50*(10), 3539-3543. doi:10.1016/j.transproceed.2018.06.013

Turkmen Samdanci, E., Reha Celik, M., Pehlivan, S., Celbis, O., Turkkan, D., Ozdemir Kara, D., & Pamukcu, E. (2019). Histopathological evaluation of autopsy cases with isolated pulmonary fat embolism (IPFE): Is cardiopulmonary resuscitation a main cause of death in IPFE? *Open Access Emergency Medicine*, *11*, 121-127. doi:10.2147/OAEM.S194340

Voisard, M. X., Schweitzer, W., & Jackowski, C. (2013). Pulmonary fat embolism-A prospective study within the forensic autopsy collective of the Republic of Iceland. *Journal of Forensic Science*, *58*, 105-111. doi:10.1111/1556-4029.12003

Wang, F. Y., & Ching, T. T. (2021). Oil Red O staining for lipid content in *Caenorhabditis elegans*. *Bio-protocol*, *11*(16), 1-9. doi:10.21769/BioProtoc.4124

Available online at https://li02.tci-thaijo.org/index.php/ssstj

Suan Sunandha Science and Technology Journal
©2023 Faculty of Science and Technology, Suan Sunandha Rajabhat University

Synthesis and Characterization of TiN Thin Films by DC Reactive Magnetron Sputtering

Siriwat Alaksanasuwan[1,3], Nirun Witit-anun[2,3*]

[1]Faculty of Science and Technology, Phranakhon Si Ayutthaya Rajabhat University, Phranakhon Si Ayutthaya 13000, Thailand
[2]Department of Physics, Faculty of Science, Burapha University, Chonburi 20131, Thailand
[3]Thailand Center of Excellence in Physics (ThEP), MHESI, Bangkok 10400, Thailand
***Corresponding author e-mail: nirun@buu.ac.th**

Received: *7 December 2022* / **Revised:** *11 May 2023* / **Accepted:** *19 June 2023*

Abstract

In this work, the titanium nitride (TiN) thin films were prepared on Si-wafers by using the DC reactive magnetron sputtering from a pure titanium target. The influence of N_2 flow rates, in the range of 1.0-4.0 sccm, on the as-deposited TiN film's structure was characterized by several techniques. (i) The crystal structures were studied by GI-XRD. (ii) The film's thicknesses, microstructures, and surface morphologies were analyzed by FE-SEM. (iii) The elemental composition of films was measured by EDS. (iv) The hardness was measured by the nano-indentation. (v) The color was identified by a UV-VIS spectrophotometer. The results showed that the as-deposited films were polycrystalline of B1-NaCl structure. The lattice constants were ranging from 4.211-4.239 Å. The as-deposited films showed a nano crystal size in the range of 17.8-24.6 nm. The thickness decreases from 1254 nm to 790 nm with following in the N_2 flow rates. The concentration of Ti and N depended on the N_2 flow rates. The cross-sectional analysis showed that the films had a compact-columnar structure. The hardness increased from 4 to 19 GPa with increasing in the N_2 flow rates. The close to the color of 24K gold thin films in the CIE L*a*b* system was obtained by deposition in optimal N_2 flow rates.

Keywords: TiN thin film, N_2 flow rates, Reactive magnetron sputtering

1. Introduction

The scientific research on the novel and high-performance industrialized materials are unstoppable. Many researchers from all over the world have pushed the performances of materials beyond their theoretical limits, in order to achieve the best results possible. Surface coating is one of the best ways to improve the materials' properties or durability, especially for those exposed to extreme working conditions and aggressive environments (Santecchia et al., 2015).

Hard coatings or hard thin films based on metals, ceramics, and related compounds have been utilized often during the past few decades as a surface treatment for effectively enhancing structural performance (Gao & Sun, 2019). Many of the hard coatings based on transition metal nitrides (such as TiN, CrN, and ZrN) have been investigated and widely used in surface modification, which is now common material in the coating industry (Mitterer, 2014).

Among these coatings, titanium nitride (TiN) is very interesting due to its very hard and chemically resistant ceramic material that has long been used for corrosion, erosion, and wears protective coatings (Jithin, Ganapathi, Vikram, Udayashankar, & Mohan, 2018). TiN is widely used in many applications, such as coated on cutting tools. Additionally, TiN exhibits biocompatible qualities leading to its usage in medical implants such as orthopedic and dental prosthesis.

TiN film is a well-known hard coating that has crystallized in the B1-NaCl structure, which is a solid solution as the nitrogen concentration is in the range of 37.5-50.0% (Santecchia et al., 2015). Nowadays, TiN is mainly used as a coating material in order to extend the lifespan of cutting tools that are made of high-speed steels or sintered carbides. As compared to the non-modified cutting tools, the use of TiN films allows an increase in the cutting speed and feed during machining (Lepicka et al., 2019). Typically, the TiN showed beautiful colored films: pale yellow, gray, brownish yellow, or red which depending on the stoichiometry. The TiN film

Suan Sunandha Science and Technology Journal
©2023 Faculty of Science and Technology, Suan Sunandha Rajabhat University

has a high hardness ranging from 20-22 GPa, and excellent thermal and mechanical stability (Grosso et al., 2017).

There are many methods of physical vapor deposition (PVD) and chemical vapor deposition (CVD) that have been used to deposit TiN films. Nevertheless, CVD requires the use of high substrate temperature (in excess of 900°C); which is not appropriate for sensitive substrates (Kumar, Kumar, Kalaiselvam, Thangappan, & Jayavel, 2018). In contrast, the PVD method uses a lower substrate temperature (around 400-550°C). Generally, PVD involves the deposition of Ti atoms on the substrate surface by sputtering or evaporation followed by a subsequent reaction with nitrogen at the substrate surface (Kim et al., 2009). Among this PVD, reactive magnetron sputtering is a commonly used technique to deposit thin films for surface uniformity and good adhesion (Thampi, Bendavid, & Subramanian, 2016).

It is well known that the quality of the sputtered deposited thin films depends upon several parameters such as nitrogen concentration in the chamber during deposition, sputtering power, base pressure, working pressure, substrate temperature, gas flow rates, and bias voltage (Ponon et al., 2015). These parameters included the N_2 flow rate used for deposit films are known to impact the grain growth and crystallographic orientation, which result in microstructure and properties of the as-deposited films (Ajenifuja, Popoola, & Popoola, 2019). It has been reported that the microstructure, surface morphology, and preferred orientation of TiN thin films deposited by reactive magnetron sputtering are mainly controlled by the ratio of deposited nitrogen ions to titanium atoms, which is vital to determine the performance of the films (Zhang et al., 2019). For example, the N_2 flow rate is strongly impacted on the grain size, crystal orientation and chemical state of TiN films. The results showed that the grain size and atomic ratio of N/Ti decreased with increase of the N_2 flow rate and the diffraction peak were reformed as (111) to (200) orientation (Zhou, Liu, Zhang, Ouyang, & Suo, 2016). Moreover, many properties of the hard nitride films such as hardness, stoichiometry or wear resistance may depend on the concentration of nitrogen in the film (Zhang et al., 2019).

The aim of this work is to study the effects of N_2 flow rates on the structure of TiN films, which are prepared by the reactive DC magnetron sputtering. The main characteristics of the as-deposited films such as crystal structures, microstructures, surface morphologies, and elemental compositions as well as the hardness and the color were investigated. The results of this research would be useful for the hard coating industrial applications.

2. Materials and Methods

2.1 Thin films preparation

The TiN thin films were deposited on Si wafers substrates by the homemade DC reactive unbalanced magnetron sputtering system, which is shown in Figure 1. A pure titanium disc of 50 mm in diameter and 3 mm in thickness served as the sputtering target and was mounted on a magnetron cathode that cooled by water. Prior to deposited thin films, all substrates were cleaned with acetone in an ultrasonic container for 10 min. Subsequently, they were rinsed in deionized water and dried with N_2 gas. After cleaning, the substrates were immediately inserted into the sample holder in the deposition chamber. The target-to-substrate distance was at 100 nm. The high purity of Ar (99.999%) and N_2 (99.999%) were used as the sputtering gas and reactive gasses, respectively. The Ar flow rate was set as a constant value of 20 sccm. Whereas in this work, the N_2 flow rates were set as a variable parameter in the range of 1.0-4.0 sccm, which was controlled by mass flow controllers.

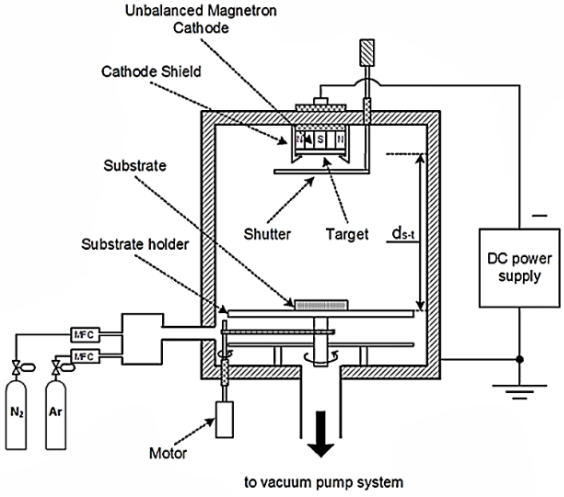

Figure 1. The homemade DC magnetron sputtering coater diagram.

Suan Sunandha Science and Technology Journal
©2023 Faculty of Science and Technology, Suan Sunandha Rajabhat University

Table 1. Thin films deposition conditions.

Parameters	Details
Sputtering target	Ti (99.97%)
Substrate temperature	room temperature
Target to substrate distance	100 mm
Base pressure	$5.0x10^{-5}$ mbar
Working pressure	$5.0x10^{-3}$ mbar
Sputtering power	300 W
Ar flow rate	20 sccm
N_2 flow rates	1, 2, 3, 4 sccm
Deposition time	30 min

Prior deposition the chamber was evacuated to a base pressure of $5.0x10^{-5}$ mbar by a diffusion pump backed with a rotary pump, before feeding the working gasses (Ar and N_2). The coating system employed an unbalanced magnetron powered by a homemade DC power supply. Before starting the deposition, the target was pre-sputtering for 5 min, with a shutter between the target and the substrate. During all depositions, the total working pressure and the sputtering power were kept fixed at $5.0x10^{-3}$ mbar and 300 W, respectively. The deposition time for each film was 30 min. The deposition conditions shown in Table 1.

2.2 Thin films characterization

The phase and crystal structures of the as-deposited films were analyzed by grazing incidence X-ray diffraction (GIXRD: BRUKER D8) in the continuous scanning mode using Cu Kα radiation (λ=0.154 nm). The diffraction angles were in the range of 20 - 80°. Scanning speed and grazing incidence angle was 2°/min and 3°, respectively. The crystal size can be calculated from the FWHM data acquired from the XRD pattern using Scherrer's equation. The microstructure, surface morphologies, cross-sectional morphologies, and thickness of the films were observed by a field emission scanning electron microscope (FE-SEM: Hitachi s4700). The composition of the films is examined by energy-dispersive X-ray spectroscopy (EDS: EDAX). The film's colors are measured by the UV-VIS spectrophotometer (UV-VIS: Shimadzu UV2600) in CIE L*a*b* system. The hardness was measured from a nanoindentation system (BRUKER: Hysitron TI Premier) at room temperature. The indentation was performed by using a Berkovich indent probe under depth-control mode. The indentation depth was controlled less than 1/10 of the film thickness, so that the influence from the substrate can be neglected, with maximum load at 9 mN.

3. Results and Discussion

3.1 Crystal structure

In this work, the as-deposited TiN thin films were successfully prepared on the substrates at room temperature by the reactive DC unbalanced magnetron sputtering, with N_2 flow rates ranging from 1.0-4.0 sccm. The crystal structure of as-deposited thin films was identified by the XRD technique at different N_2 flow rates presented in Figure 2. The results are showing that several diffraction peaks appeared at 2θ of 36.7°, 42.6°, 61.9°, and 74.1°. It corresponded to the polycrystalline of TiN at (111), (200), (220), and (311) planes (JCPDF no. 65-2899). The diffraction angles which corresponded to standard planes were found at N_2 flow rates of 1.0-4.0 sccm as the aberration of angles about ±0.3° for the as-deposited films. It has been shown that the crystal structure of films was a good agreement from the JCPDS standard.

Moreover, it was found the changing intensities of a diffraction peak with varying of the N_2 flow rates. As the lowest N_2 flow rates (1.0 sccm), the as-deposited thin films showed the low-crystallinity. The several phases appeared as the N_2 flow rates increased to 2.0 sccm, which corresponded to the polycrystalline of TiN at (111), (200), (220), and (311) planes. These phases still appeared as the N_2 flow rate increased to a higher value, but it showed an obviously preferred orientation of (111). The results showed that the orientation growth behavior was strongly related to the N_2 flow rate in the sputtering process. Additionally, the preferred orientations were controlled by the opposition of surface energy and strain energy. For example, the lowest surface energy caused to the (200) preferred orientation, whereas the lowest strain energy caused to the (111) preferred orientation (Pelleg, Zevin, Lungo, & Croitoru, 1991). In this work, the crystal sizes were analyzed by using the Scherrer formula from the FWHM of the XRD peaks; it was found that the crystal sizes of films ranged from 17.8 to 24.6 nm. The lattice constants of the films were in the range of 4.211-4.239 Å *(*the lattice constants of standard TiN are 4.238 Å*)*, which confirmed that the obtained films were complete of TiN structure.

Suan Sunandha Science and Technology Journal
©2023 Faculty of Science and Technology, Suan Sunandha Rajabhat University

In this work, the variation of N_2 flow rates is the result of the growing of crystallinity for the TiN films. In summary, the crystal sizes and the lattice constants of the films are shown in Table 2.

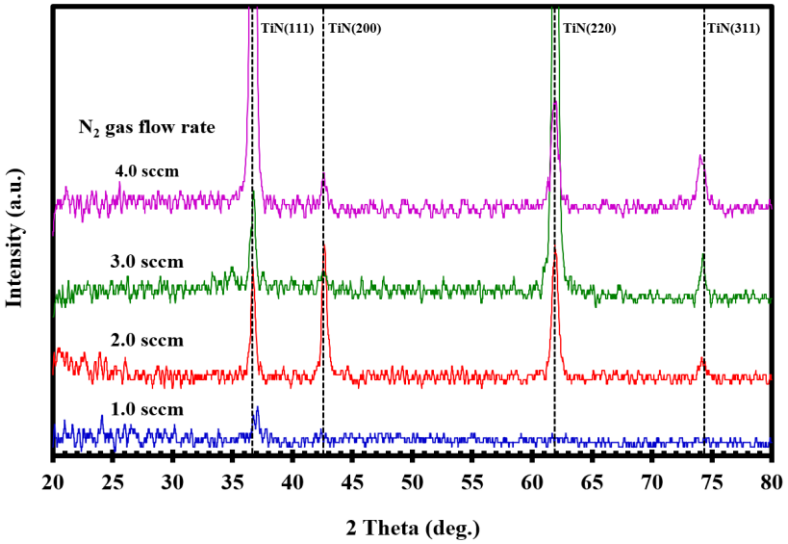

Figure 2. XRD pattern of the TiN thin films deposited at different N_2 flow rates.

Table 2. Crystal size and lattice constant of the as-deposited TiN thin films at different N_2 flow rates.

N_2 flow rates	Crystal size [nm]				Lattice constants [Å]			
(sccm)	(111)	(200)	(220)	(311)	(111)	(200)	(220)	(311)
1.0	17.8	-	-	-	4.211	-	-	-
2.0	22.6	21.3	19.7	19.2	4.234	4.234	4.236	4.234
3.0	23.9	20.3	21.5	23.2	4.233	4.239	4.235	4.234
4.0	24.6	20.3	20.1	20.3	4.233	4.233	4.236	4.237

3.2 Microstructure and surface morphology

Figure 3 showed the microstructure and surface morphology of the as-deposited TiN films at different N_2 flow rates ranging from 1.0-4.0 sccm. It is clearly presented that the films had a small grain and smooth surface, when deposited at the lowest N_2 flow rates as shown in Figure 3(a). Whereas the different sizes of the large grains were randomly distributed on the film's surface, when deposited at higher N_2 flow rates (Figure 3(b) to 3(d)). As the N_2 flow rate increased, the grain's size on the surface of the as-deposited film became smaller compared to the film deposited at a low N_2 flow rate. The result in this work may be described by the fact that the increase in N_2 flow rate declines the energy of bombarding ions, reduces the mobility of sputter atoms, and decreases the grain size (Zhou et al., 2016).

The cross-sectional analysis of the as-deposited TiN thin films observed by FE-SEM presented in Figure 4. It was revealed that the film's thickness decreased from 1254 to 790 nm with an increase in the N_2 flow rates (Table 3). It has been revealed that increasing the N_2 flow rates reduced the deposition rate. This effect is well known as for the reactive sputtering, the increasing of reactive gas during the deposition process intensely reduces the sputtering yield of a Ti-target due to target poisoning. On the other hand, since the concentration of the gas mixture was constant, an increase in the concentration of nitrogen followed by a decrease in the concentration of argon. Therefore, the sputtering yield of the target was reduced owing to the lower momentum transfer of nitrogen compared to argon (Zhang et al., 2000).

The as-deposited TiN thin films showed the dense structure at the N_2 flow rate of 1 sccm (Figure 3). When the N_2 gas flow rate increased to 2.0 sccm, the columnar structure appeared. It still achieved deposits at 3.0 and 4.0 sccm. This structure continuously grows throughout the thin film's growth, which corresponds to the zone 2 of the Thornton's structure zone model (SMZ) (Kusano, 2019). The columns are less defective and regularly facet at the surface of films. In summary, the microstructure of the TiN films in this work also show dense to compact-columnar.

Suan Sunandha Science and Technology Journal
©2023 Faculty of Science and Technology, Suan Sunandha Rajabhat University

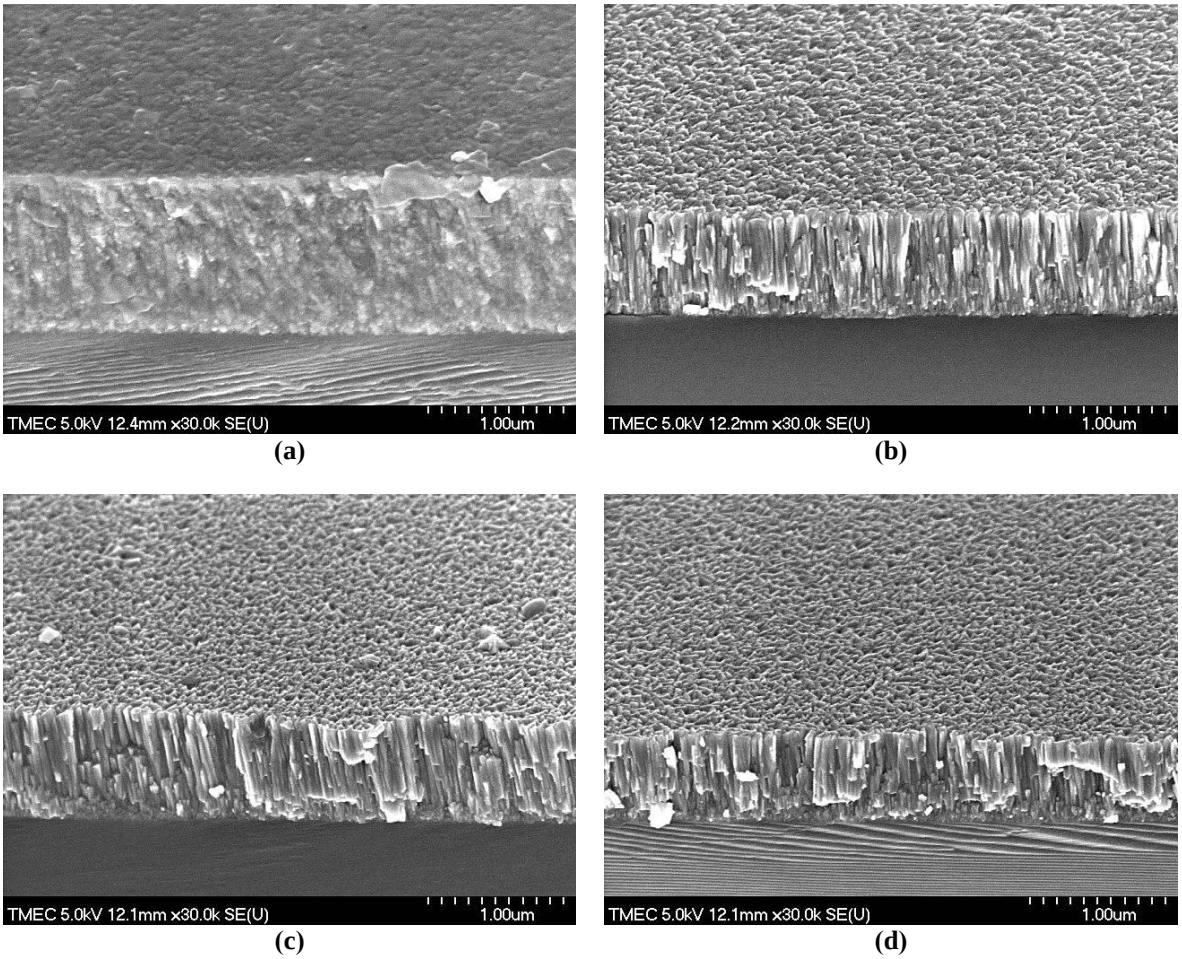

Figure 3. FE-SEM micrograph of TiN thin films deposited at different N_2 flow rates; (a) 1.0 sccm, (b) 2.0 sccm, (c) 3.0 sccm, (d) 4.0 sccm.

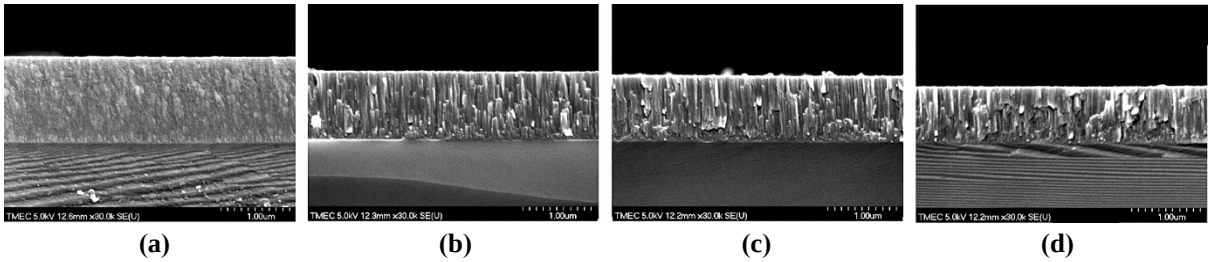

Figure 4. Cross-sectional analysis of TiN thin films deposited at different N_2 flow rates; (a) 1.0 sccm, (b) 2.0 sccm, (c) 3.0 sccm, (d) 4.0 sccm.

Table 3. Some properties of the TiN thin films with different N_2 flow rates.

N_2 flow rate (sccm)	Thickness (nm)	Deposition rate (nm/min)	Structure	Hardness (GPa)	Color
1.0	1254	42	dense	4.5	grey
2.0	991	33	columnar	18.7	like-gold
3.0	865	29	columnar	19.0	like-gold
4.0	790	26	columnar	19.4	like-gold

Suan Sunandha Science and Technology Journal
©2023 Faculty of Science and Technology, Suan Sunandha Rajabhat University

3.3 Elemental composition

The elemental composition of the TiN thin films at various N_2 gas flow rates was analyzed by the energy dispersive spectroscopy (EDS) shown in Table 4 the N content increased from 43.8 to 53.7 at.% following on N_2 flow rates from 1.0 to 4.0 sccm. Actually, in this work, the Ti content decreased from 56.2 to 46.3 at.%, oppositely to the N content. Moreover, it also shows the ratio x of Ti content defined as x is Ti/(Ti+N), the ratio y of N content defined as y is N/(Ti+N), and the film composition defined as Ti_xN_y, respectively. It was found that the ratio of Ti and N content of films deposited at N_2 gas flow rate of 2.0 to 4.0 sccm was equally values of about 0.5 leading to the film composition in these cases being $Ti_{0.5}N_{0.5}$. Additionally, the ratio of Ti:N was approximately 1 indicating that the as-deposited TiN thin films in this case were stoichiometry.

Table 4. Elemental composition and film composition as a function of the N_2 gas flow rates.

N_2 flow rate (sccm)	Ti (at. %)	N (at. %)	x (Ti/Ti + N_2)	y (N/Ti + N_2)	Films composition (Ti_xN_y)
1.0	56.2	43.8	0.6	0.4	$Ti_{0.6}N_{0.4}$
2.0	47.2	52.8	0.5	0.5	$Ti_{0.5}N_{0.5}$
3.0	46.9	53.1	0.5	0.5	$Ti_{0.5}N_{0.5}$
4.0	46.3	53.7	0.5	0.5	$Ti_{0.5}N_{0.5}$

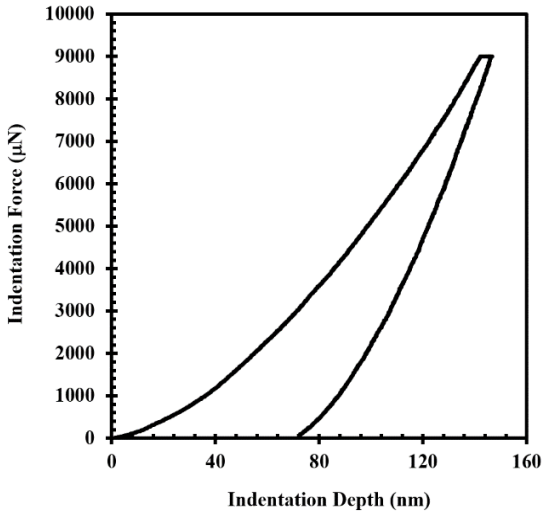

Figure 5. Sample of the load-displacement curve of TiN thin films.

3.4 Hardness

The hardness of TiN films was calculated from the load-unload displacement curve (Figure 5) and Table 3. It is accepted that the ratio of the indentation depth is around tenth of the total thickness by the nano-indentation technique.

In this study, the hardness was calculated for each unloading curve with values of 4.5 to 19.4 GPa. The maximum hardness of TiN films achieved to deposit at the highest N_2 flow rates (4.0 sccm), which showed the highest crystallinity of TiN (111). These results are consistent with another study. Zhang et al. (2019) reported that the TiN thin film with a high N_2 gas flow rate showed an obvious preferred orientation of TiN (111), which is the close-packed plane in the face-centered-cubic (fcc) crystal structure. Thus, at the high N_2 gas flow rate, TiN film showed the lowest compressive residual stress among other films.

3.5 Color

The as-deposited thin film's color was measured and identified in the CIE L*a*b* system. From Figure 6, it is shown that the film's color in this work was grey to gold-like as an increase of N_2 flow rates (Table 3). The close to 24K gold films was obtained by using the N_2 gas flow rates at 3.0 and 4.0 sccm with L* around 60, a* around 6, and b* around 26 - 28. The results are in good agreement with a study that the film's color changes totally from grey to golden as the change in the N/Ti ratio (Grosso et al., 2017). In addition, the golden color is obtained as the stoichiometric titanium nitride. Depending on the stoichiometry variations in the number of free-electron are obtained that play a role in the reflection of light (Bendavid, Martin, Netterfield, & Kinder, 1996).

Suan Sunandha Science and Technology Journal
©2023 Faculty of Science and Technology, Suan Sunandha Rajabhat University

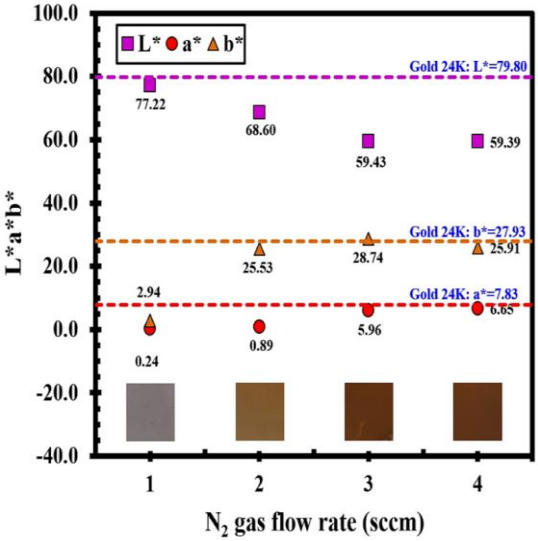

Figure 6. The Color of TiN films measured in the CIE L*a*b* system as a function of the N_2 flow rates.

4. Conclusion

The TiN thin films were successfully prepared by using DC reactive magnetron sputtering at different N_2 flow rates at 1.0-4.0 sccm in 1.0 sccm increments. The crystal structures, microstructures, surface morphologies, elemental compositions, and color were strongly influenced by the N_2 gas flow rates. The results showed the as-deposited thin films had a B1-NaCl structure of TiN(111), TiN(200), TiN(220), and TiN(311). The lattice constants were in the range of 4.211-4.239 Å. The crystal sizes were as small as below 25 nm. The thickness reduced from 1254 nm to 790 nm, with opposite change of the N_2 flow rate. The concentration of Ti and N in the films (Ti and N contents) depended on the N_2 flow rates. From the cross-sectional analysis, the films showed the changing of the structure from the dense to the compact columnar. The hardness obtained by the nano-indentation technique was increased from 4 - 19 GPa with following in the N_2 flow rates. The color close to 24K gold thin films was obtained by using the N_2 gas flow rates at 3.0 and 4.0 sccm.

References

Ajenifuja, E., Popoola, A. P. I., & Popoola, O. M. (2019). Thickness dependent chemical and microstructural properties of DC reactive magnetron sputtered titanium nitride thin films on low carbon steel cross-section. *Journal of Materials Research and Technology*, *8*(1), 377-384. doi:10.1016/j.jmrt.2018.02.010

Bendavid, A., Martin, P. J., Netterfield, R. P., & Kinder, T. J. (1996). Characterization of the optical properties and composition of TiN_x thin films by spectroscopic ellipsometry and X-ray photoelectron spectroscopy. *Surface and Interface Analysis*, *24*(9), 627-633. doi:10.1002/(SICI)1096-9918(19960916)24:9<627::AID-SIA149>3.0.CO;2-R

Gao, F., & Sun, W. (2019). Nonlinear finite element modeling and vibration analysis of the blisk deposited strain-dependent hard coating. *Mechanical Systems and Signal Processing*, *121*, 124-143. doi:10.1016/j.ymssp.2018.11.028

Grosso, S., Latu-Romain, L., Berthome, G., Renou, G., Le Coz, T., & Mantel, M. (2017). Titanium and titanium nitride thin films grown by dc reactive magnetron sputtering Physical Vapor Deposition in a continuous mode on stainless steel wires: Chemical, morphological and structural investigations. *Surface and Coatings Technology*, *324*, 318-327. doi:10.1016/j.surfcoat.2017.05.089

Jithin, M., Ganapathi, K. L., Vikram, G. N. V. R., Udayashankar, N. K., & Mohan, S. (2018). Pulsed DC magnetron sputtered titanium nitride thin films for localized heating applications in MEMS devices. *Sensors and Actuators A: Physical*, *272*, 199-205. doi:10.1016/j.sna.2017.12.066

Suan Sunandha Science and Technology Journal
©2023 Faculty of Science and Technology, Suan Sunandha Rajabhat University

Kim, S. H., Park, H., Lee, K. H., Jee, S. H., Kim, D. J., Yoon, Y. S., & Chae, H. B. (2009). Structure and mechanical properties of titanium nitride thin films grown by reactive pulsed laser deposition. *Journal of Ceramic Processing Research*, *10*(1), 49-53.

Kumar, D. D., Kumar, N., Kalaiselvam, S., Thangappan, R., & Jayavel, R. (2018). Film thickness effect and substrate dependent tribo-mechanical characteristics of titanium nitride films. *Surfaces and Interfaces*, *12*, 78-85. doi:10.1016/j.surfin.2018.05.002

Kusano, E. (2019). Structure-zone modeling of sputter-deposited thin films: A brief review. *Applied Science and Convergence Technology*, *28*(6), 179-185.

Lepicka, M., Gradzka-Dahlke, M., Pieniak, D., Pasierbiewicz, K., Krynska, K., & Niewczas, A. (2019). Tribological performance of titanium nitride coatings: A comparative studyon TiN-coated stainless steel and titanium alloy. *Wear*, *422-423*, 68-80.

Mitterer, C. (2014). PVD and CVD hard coatings. In V. K. Sarin (Ed.), *Comprehensive hard materials* (pp. 449-467). Oxford, UK: Elsevier. doi:10.1016/B978-0-08-096527-7.00035-0

Pelleg, J., Zevin, L. Z., Lungo, S., & Croitoru, N. (1991). Reactive-sputter-deposited TiN films on glass substrates. *Thin Solid Films*, *197*(1-2), 117-128. doi:10.1016/0040-6090(91)90225-M

Ponon, N. K., Appleby, D. J. R., Arac, E., King, P. J., Ganti, S., Kwa, K. S. K., & O'Neill, A. (2015). Effect of deposition conditions and post deposition anneal on reactively sputtered titanium nitride thin films. *Thin Solid Films*, *578*, 31-37. doi:10.1016/j.tsf.2015.02.009

Santecchia, E., Hamouda, A. M. S., Musharavati, F., Zalnezhad, E., Cabibbo, M., & Spigarelli, S. (2015). Wear resistance investigation of titanium nitride-based coatings. *Ceramics International*, *41*(9), 10349-10379. doi:10.1016/j.ceramint.2015.04.152

Thampi, V. V. A., Bendavid, A., & Subramanian, B. (2016). Nanostructured TiCrN thin films by Pulsed Magnetron Sputtering for cutting tool applications. *Ceramics International*, *42*(8), 9940-9948. doi:10.1016/j.ceramint.2016.03.095

Zhang, D. H., Yang, T. L., Ma, J., Wang, Q. P., Gao, R. W., & Ma, H. L. (2000). Preparation of transparent conducting ZnO:Al films on polymer substrates by r. f. magnetron sputtering. *Applied Surface Science*, *158*(1-2), 43-48. doi:10.1016/S0169-4332 99 00591-7

Zhang, H., Li, Z., Ma, C., He, W., Cao, X., & Li, Y. (2019). The anti-sand erosion performance of TiN films fabricated by filtered cathodic vacuum arc technique at different nitrogen flow rates. *Ceramics International*, *45*(8), 10819-10825. doi:10.1016/j.ceramint.2019.02.157

Zhang, S., Yan, F., Yang, Y., Yan, M., Zhang, Y., Guo, J., & Li, H. (2019). Effects of sputtering gas on microstructure and tribological properties of titanium nitride films. *Applied Surface Science*, *488*, 61-69. doi:10.1016/j.apsusc.2019.05.148

Zhou, T., Liu, D., Zhang, Y., Ouyang, T., & Suo, J. (2016). Microstructure and hydrogen impermeability of titanium nitride thin films deposited by direct current reactive magnetron sputtering. *Journal of Alloys and Compounds*, *688*, 44-50. doi:10.1016/j.jallcom.2016.06.278

Available online at https://li02.tci-thaijo.org/index.php/ssstj

Suan Sunandha Science and Technology Journal
©2023 Faculty of Science and Technology, Suan Sunandha Rajabhat University

A Risk Prediction Model of Road Accidents During Long Holiday in Thailand Using Ensemble Learning with Decision Tree Approach

Paranya Palwisut*

Department of Data Science, Faculty of Science and Technology, Nakhon Pathom Rajabhat University,
85 Malaiman Road, Mueang Nakhon Pathom, Nakhon Pathom 73000, Thailand
***Corresponding author e-mail: paranya@npru.ac.th**

Received: *21 February 2023* / **Revised:** *11 May 2023* / **Accepted:** *13 June 2023*

Abstract

The rate of injury and death from traffic accidents during the New Year and Songkran Festival each year has high and are continuously on the increase. The researchers, therefore, has decided to study and develop a model for predicting the road accident risk during the holiday season with ensemble learning based on decision tree approach. The aim is to help reduce accidents and loss of life caused by road accidents. The dataset used in this research is traffic accidents resulting in injury and death data during the long holiday from 2008 to 2015 from hospitals across the country, accumulatively recorded by the National Institute for Emergency Medicine. This research compared the efficiency of data classification to find the best ensemble model for predicting traffic accident risk. The methods studied included Adaptive Boosting (AdaBoost), and Random Forest, and the decision tree techniques used in the experiment were J48, ID3, and CART. The results of experiment and comparisons of classification efficiency showed that the Random Forest algorithm with J48 decision tree was the most efficient model, providing an accuracy of up to 93.3%.

Keywords: Road accident, Decision tree, Ensemble learning

1. Introduction

Traffic accidents are a major problem in Thailand. There are a large number of victims of traffic accidents each year in the form of injury, disability, and fatality. Moreover, the incidence tends to become more increased. Road accidents are the leading cause of death in Thailand, particularly during long holiday. For the New Year and Songkran Festival, there are 7 dangerous days. This refers to the period when the statistic of road accidents, the number of casualties and injury has peaked to the highest point due to the highest rate of road travel (Sonwongsa, Pinpoo, & Wongkhae, 2016). According to the report of injuries and deaths from traffic accidents during the New Year and Songkran Festival, it was found that most of the accident victims were drivers and accompanying passengers, resulting in an increasing number of deaths. During the new year festival of 2022 (Accident Prevention Network, 2022), there were 2,707 road accidents, which killed 333 people and injured 2,672 others, from statistics found that there are still many accidents every year. Currently, various techniques have been used for road traffic accident data analysis, such as data mining algorithms. This process involves exploring large amounts of data to find patterns and relationships hidden in the dataset, with techniques and methods for predicting, classifying, and managing the data (Esenturk, Turley, Wallace, Khastgir, & Jennings, 2022; Parathasarathy, Soumya,Das, Saravanakumar, & Merjora, 2019). Because of the exponential rising number of road accidents on the New Year and Songkran Festival, the researchers decided to study and construct the risk prediction model of road accidents during the holiday season with ensemble learning method using decision tree approach. The researcher studied the theories and literatures related to this research as follows:

Suan Sunandha Science and Technology Journal
©2023 Faculty of Science and Technology, Suan Sunandha Rajabhat University

1.1 Decision Tree Technique

Decision Tree (Njoku, 2019) is a technique that presents outcomes in a tree-like graph. The data are partitioned based on their features travestying the tree structure to terminal class. The tree model is the collection of nodes. Each node denotes a test on a particular feature. Each branch denotes the possible value of the tested feature, while each leaf at the bottom of the decision tree denotes class labels, which is the outcome of prediction. The node at the top most of the tree is called root node. The structure of decision tree is shown in Figure 1.

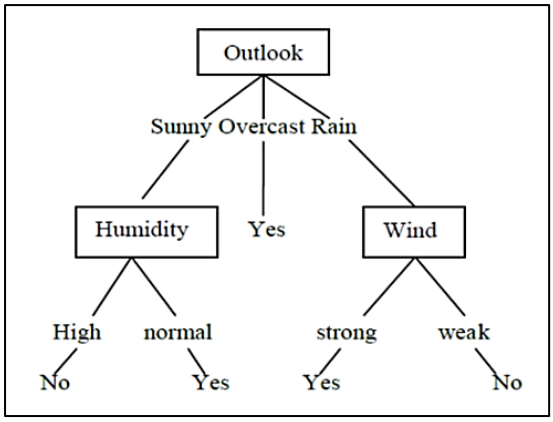

Figure 1. Decision Tree Structure (Njoku, 2019).

The decision tree measures the impurity of each features or variables as follows:

Gini Index is a value that indicates what features or variables should be used for classification algorithm J48 and CART.

$$Gini(t_i) = 1 - \sum_{i=1}^{N}[p(t_i)]^2 \qquad (1)$$

Entropy is the degree of uncertainty in the dataset which is classified based on the identification of ID3 algorithm,

$$Entropy(t_i) = 1 - \sum_{i=1}^{N}[p(t_i)]log_2 p(t_i) \qquad (2)$$

where

t_i is the feature selected to measure the entropy

$P(t_i)$ is proportion of number of group i members and the total number of sample group

Each algorithm gives different outcomes. The decision tree algorithms employed in this research are as follows:

- J48 or C 4.5 is an algorithm to create a tree model from a set of training data. The accuracy value of each data feature is used as a criterion to classify the data into subsets based on entropy values. The feature with the highest normalized information gain is chosen to make the decision (Panigrahi & Borah, 2018).

- Iterative Dichotomiser 3 or ID3 is an algorithm to generate a decision tree based on information gain. The data are split into subsets based on the entropy or the information gain of each feature. The decision tree is built according to selected features in order of gain value from high to low (Ogheneovo & Nlerum, 2020).

- Classification and Regression Trees (CART) is an algorithm to build a binary decision tree consisting of one or two branches for each node. This technique divides records of training data into subsets given the same target value (Zacharis, 2018).

1.2 Ensemble learning

Ensemble learning is a process by which multiple independent classifiers are combined or voted for decision making to boost the classification efficiency, as shown in Figure 2.

The following steps are performed:

(1) Generate new data from the original data

(2) Build classifiers from the generated data

(3) Combine the classifiers to find out the answer

There are many ensemble techniques available, but the most common methods used in this research are boosting and bagging.

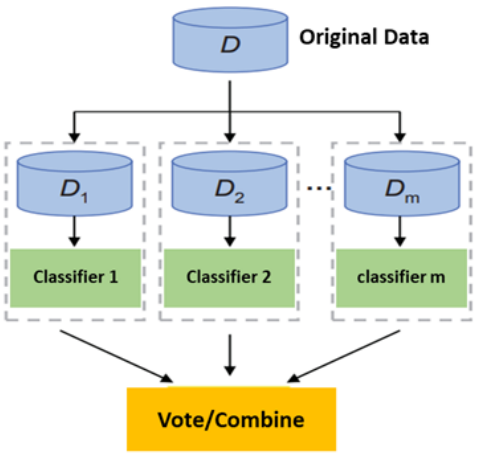

Figure 2. Basic structure of ensemble learning.

Suan Sunandha Science and Technology Journal
©2023 Faculty of Science and Technology, Suan Sunandha Rajabhat University

1.2.1 Boosting Method is a general ensemble method to build a model by weighing training samples. Boosting focuses on finding errors that arise from the learning process, called "weak learning". Finally in the last step, it combines the classifiers based on the mean weight and votes for a single accurate learner.

The adaptive boosting or AdaBoost algorithm proposed by Freund and Schapire in 1997 is one of the most widely used. Initially, all weights of each instance in the training datasets are set equally. On each round the weights of correct instances are lessen, while more weight is given to incorrectly classified instances to increase a chance of distribution in the next round (Tanha, Abdi, Samadi, Razzaghi, & Asadpour, 2020). Boosting Method is shown in Figure 3.

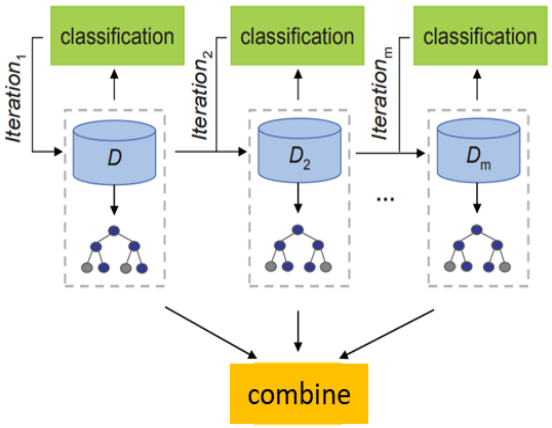

Figure 3. Boosting method (Yang, Yang, Zhou, & Zomaya, 2010).

1.2.2 Bagging Method, or Bootstrap Aggregating, is an effective ensemble algorithm introduced by Breiman, L. It is usually applied together with decision tree methods. The samples of each dataset are randomly drawn to generate several different models. Finally, majority vote is conducted to find the final model which is the best answer.

Random Forest is one of the most popular ensembles learning algorithms and also a notable improvement of bagging; it constructs an extensive collection of de-correlated trees and averages them. It creates multiple decision tree models to support decision making and votes to choose the best outcome. However, Random Forest adds a function of random feature selection from the sample set. This can reduce the correlation between features (Njoku, 2019). The method is shown in Figure 4.

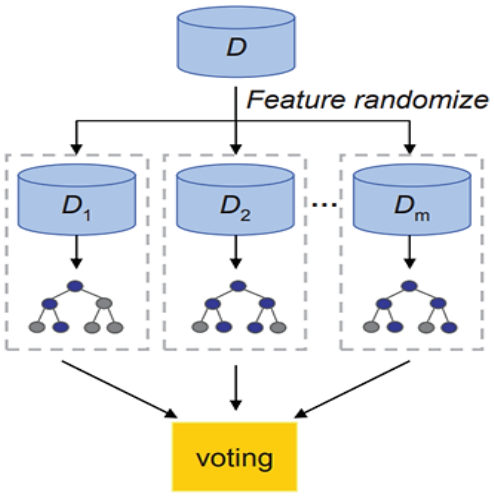

Figure 4. Random forest method (Yang et al., 2010).

1.3 Model efficiency measurement

1.3.1 The efficiency of model is measured by confusion matrix, which summarizes the number of correct and incorrect classified data, as shown in Figure 5.

		Predicted Class	
		Positive	Negative
Actual Class	Positive	TP	FN
	Negative	FP	TN

(a)

		Predicted Class			
		C_1	C_2	...	C_N
Actual Class	C_1	$C_{1,1}$	FP	...	$C_{1,N}$
	C_2	FN	TP	...	FN
	...	...	...	...	...
	C_N	$C_{N,1}$	FP	...	$C_{N,N}$

(b)

Figure 5. Confusion matrix examples.
(a) Binary classification problem confusion matrix.
(b) Multiclass classification problem confusion matrix (Markoulidakis et al., 2021).

where
TP is correct prediction value of the target group
FP is incorrect prediction of the target group
TN is correct prediction value of other groups
FN is incorrect prediction value of other groups

Suan Sunandha Science and Technology Journal
©2023 Faculty of Science and Technology, Suan Sunandha Rajabhat University

To measure the effectiveness of the proposed method, the following details are described: (Markoulidakis et al., 2021)

(1) Accuracy is a value that indicates how close of the predictive value to the actual value, as shown in Equation (3).

$$Accuracy = \frac{TP+TN}{TP+FP+FN+TN} \quad (3)$$

(2) Precision is the ratio of correctly predicted data to the total number of retrieval data. It also can be defined as the value denoted information retrieval and how predictive data is likely correct, as explained in Equation (4).

$$Precision = \frac{TP}{TP+FP} \quad (4)$$

(3) Recall is ratio of data that meet the requirements and are retrieved to all observed data, or the value that represents the retrieved data mostly responding to the user's needs, as in Equation (5).

$$Recall = \frac{TP}{TP+FN} \quad (5)$$

(4) F-Measure is the harmonic mean of precision and recall and can be expressed in Equation (6).

$$F\text{-}Measure = \frac{2*Precision * Recall}{Precision + Recall} \quad (6)$$

1.3.2 Mean Absolute Error (MAE) is a measure of the average size of the mistakes in a collection of predictions, without taking their direction into account. It is measured as the average absolute difference between the predicted values and the actual values, as in Equation (7).

$$MAE = (1/n) * \Sigma|y\_i - \hat{y}\_i| \quad (7)$$

where

n is the number of observations in the dataset.

y_i is the true value.

$\hat{y}$_i is the predicted value.

1.4 Relevant research

Zamzuri and Qi (2022) studied the decision tree model to classify the severity levels of traffic accidents in Malaysia. This study aims to identify the main factors that drive the occurrence of road accidents in Malaysia. The Classification and Regression Tree (CART) and Chi-square Automatic Interaction Detector (CHAID) techniques are used to identify the effects of factors in this study. The performances of the two classification models are compared based on prediction accuracy and model reliability. It is found that CHAID performs slightly better than CART and offers richer information in terms of influential factors and decision rules.

Nedjmedine and Tahar (2022) studied the decision tree model to analyze road accidents in Algeria. With the enormous number of death and injuries, this problem pushes governments to create solutions to reduce those statistics. Then, the decision tree model compares with similar works using accuracy as a performance evaluation metric. This work can help government and traffic safety entities to improve road safety and minimize the number of accidents.

Chen and Chen (2020) studied statistical and nonparametric data mining techniques for road accidents, namely, logistic regression (LR), classification and regression tree (CART), and random forest (RF), to compare their prediction capability, identify the significant variables (identified by LR) and important variables (identified by CART or RF) that are strongly correlated with road accident severity, and distinguish the variables that have significant positive influence on prediction performance. In this study, three prediction performance evaluation measures, accuracy, sensitivity, and specificity.

Boonraksa and Thongkam (2018) studied the effectiveness of models in predicting road accidents in Khon Kaen Province, Thailand. Five modeling techniques were used, which included Linear Regression (LR), Artificial Neural Network (ANN), Sequential Minimal Optimization for Regression (SMOReg), Support Vector Machine Regress (SVMR), and Gussian Process (GP). The predictive efficiency of the models was measured with mean absolute error (MAE) and root mean square error (RMSE). The results indicated that SVMR technique is effective in building a predictive model of road accidents with the lowest error value, compared to LR, ANN, SMOreg, and Gussian Process models.

Taamneh, Alkheder, and Taamneh (2017) studied data mining techniques for traffic accidents modeling and predictions in the United Arab Emirates. Four classification algorithms were

Suan Sunandha Science and Technology Journal
©2023 Faculty of Science and Technology, Suan Sunandha Rajabhat University

employed, included: Decision Tree (J48), Rule Induction (PART), Naïve Bayes (NB), and Multilayer Perceptron (MLP). The results showed that the overall accuracy of The J48, PART, and MLP classifiers in predicting the severity of severity injury resulting from traffic accidents, using 10-fold cross-validation was similar. The results revealed that the 18-30-year-old age group was most vulnerable to traffic accidents. Drivers were more frequently involved in traffic accidents than passengers and pedestrians. Male drivers are more involved in traffic accidents than female drivers.

According to recent researches, data mining techniques, especially decision tree, are widely used to analyze data and given satisfactory results. Therefore, the researchers adopted the principle of decision tree to build a risk prediction model of road accidents during the New Year and Songkran Holiday.

2. Materials and Methods

In this study, the risk prediction model of road accidents during long holiday was constructed with ensemble learning using decision trees as a fundamental algorithm. The overall work process is shown in Figure 6.

2.1 Data collection

Data of road accidents during long holiday were complied. The dataset used in this study is the record of injury and death from road accidents during the New Year and Songkran Holiday from 2008 to 2015 from hospitals across the country, collected by the National Institute for Emergency Medicine. Examples of road accident data, as shown in Figure 7.

2.2 Data preparation

The selection of inputs is the most important aspect of creating a useful prediction, as it represents all of the knowledge that is available to the model to base the prediction. The 13 features were selected for use in model construction from the total number of 18 features, which have removed unwanted features such as hospital code, hospital name, transporting the injured, number of days of treatment, and province name. Unwanted data is duplicate or irrelevant data. This redundant data should be removed as it is of no use and will only increase the amount of data and the time to train the model. The Feature 13 result of the accident was employed to classify the dataset. There are 417,122 complete records. Ignoring the tuple was applied to the records with missing values. Dataset descriptions are shown in Table 1.

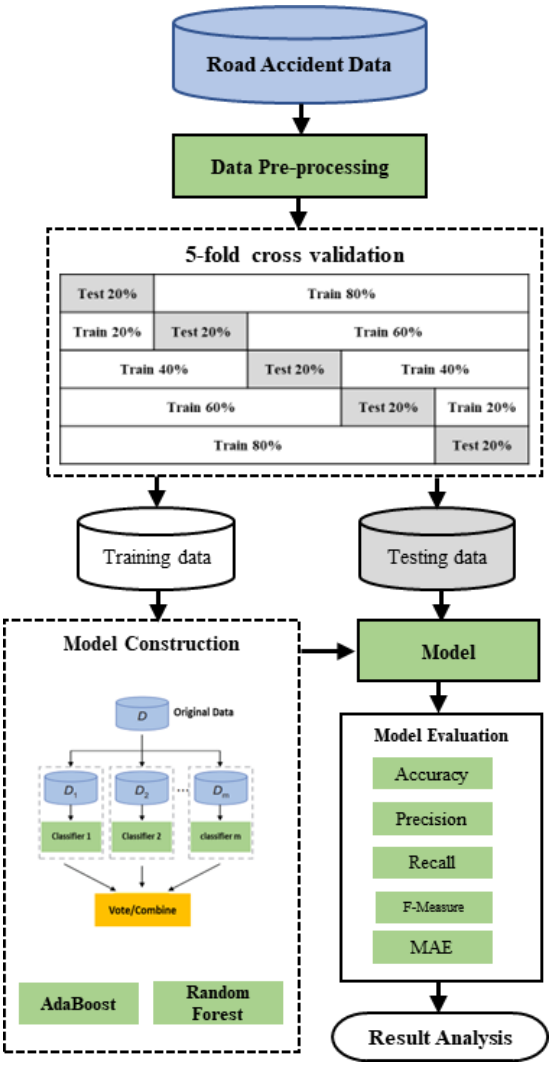

Figure 6. Research procedure.

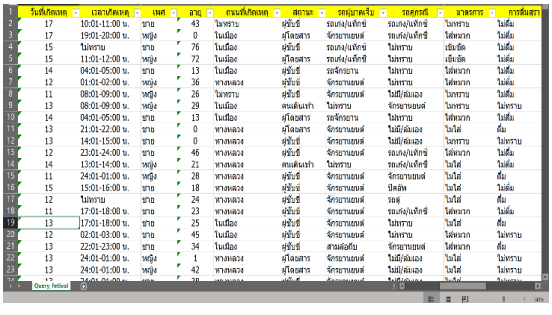

Figure 7. Examples of road accident data.

Suan Sunandha Science and Technology Journal
©2023 Faculty of Science and Technology, Suan Sunandha Rajabhat University

Table 1. Feature description.

No.	Feature Name	Description
1	Holiday	Type of holiday 1 = New Year 2 = Songkran
2	Province	Province code where the accidents happened 10 = Bangkok 11 = Samutprakarn : 97 = Buengkan
3	Date	In what day in 7-dangerous days that the accidents happened 1 = Day 1 2 = Day 2 3 = Day 3 : 7 = Day 7
4	Time	Time when the accidents happened 1 = 00.01-01.00 2 = 01.01-02.00 : 24 = 23.01-24.00
5	Sex	1. Female 2. Male
6	Age	1. <=10 2. 11-20 3. 21-30 4. 31-40 5. 41-50 6. 51-60 7. 61-70 8. 71-80 9. >80
7	Roadacc	Types of road where the accidents happened 1 = City road 2 = Rural road 3 = Highway 4 = No information
8	Status	1 = Driver 2 = Passenger 3 = Pedestrian
9	Injured_car	1 = None/Falling 2 = Motorcycle 3 = Pick-up 4 = Private car/Taxi 5 = four-wheel passenger car 6 = Big bus 7 = Bicycle 8 = Van 9 = Truck 10 = Motor-tricycle 11= Tricycle 12 = Other
10	Parties_car	1 = None/Falling 2 = Motorcycle 3 = Pick-up 4 = Private bar/Taxi 5 = four-wheel passenger car 6 = Big bus 7 = Bicycle 8 = Van 9 = Truck 10 = Motor-tricycle 11= Tricycle 12 = Other
11	Protection	1 = Wearing seatbelts 2 = Wearing helmets 3 = Not-wearing seatbelts or helmets 4 = No information
12	Alcohol	1 = Yes 2 = No 3 = No information
13	Result	Accident severity 1 = Injury/Recovery 2 = Death

2.3 Model construction

In this research, the models constructed based on AdaBoost and Random Forest using decision tree techniques such as J48, ID3, and CART, each with a different 5-fold cross validation partitioning of road accident dataset were compared to the prediction efficiency.

The random variables are selected to create differences in the training sets, consisting of N number of constructed models. The randomly generated data set is called Bootstrap. The probability of teaching instances can be explained in Equation (8).

$$n_i = 1 - \left(1 - \frac{1}{m}\right)^m \qquad (8)$$

where

n_i is a randomly generated set of data

m is the total number of sample data in the training set

In this section, experiments were performed to determine the parameters and optimize the parameters for models. The minimum number of experiments was 20 to evaluate the parameter optimization of models. The details of model construction are explained as follows:

2.3.1 Adaptive Boosting Method (AdaBoost)

The parameters in the experiment were:

Number of Model: 10, 30, 50, 80, 100

According to the experiments, the number of models with the highest efficiency of each decision tree technique is presented in Table 2.

Suan Sunandha Science and Technology Journal
©2023 Faculty of Science and Technology, Suan Sunandha Rajabhat University

Table 2. Parameter of AdaBoost.

Algorithms	Number of Model
J48	80
ID3	100
CART	100

2.3.2 Random Forest

The parameters in the experiment were:

- Number of Model: 10, 30, 50, 80, 100
- Number of Feature: 2, 4, 6, 8,10

As in the experiments, the parameters with the highest efficiency of each decision tree technique are shown in Table 3.

Table 3. Parameter of Random Forest.

Algorithms	Number of Model	Number of Feature
J48	80	6
ID3	100	6
CART	80	8

3. Results and Discussions

In this research, the data were classified with ensemble learning to predict the risk of road accidents during holiday season. The efficiency measurement was conducted by comparing accuracy, recall, precision, f-measure, and MAE of the constructed models. The results are as follows:

3.1 AdaBoost modeling

The results of model construction from AdaBoost algorithm are explained in Table 4.

Table 4. Data analysis by AdaBoost.

	J48	ID3	CART
Accuracy	87.5%	83.3%	76.7%
Precision	0.871	0.843	0.769
Recall	0.875	0.833	0.767
F-Measure	0.872	0.831	0.767
MAE	0.090	0.108	0.156

According to Table 4, the J48 decision tree technique of the Number 80 parameter had the highest efficiency with accuracy of 87.5%, precision of 0.871, recall of 0.875, f-measure of 0.872, and MAE of 0.090.

3.2 Random forest modeling

The results of model construction from Random Forest are presents in Table 5.

Table 5. Data analysis by Random Forest.

	J48	ID3	CART
Accuracy	93.3%	82.5%	74.2%
Precision	0.934	0.868	0.734
Recall	0.933	0.850	0.742
F-Measure	0.931	0.833	0.733
MAE	0.042	0.117	0.181

According to Table 5, with the J48 decision tree, the Number 80 parameter and Number 6 Feature expressed the highest efficiency with accuracy of 93.3 %, precision of 0.934, recall of 0.933, f-measure of 0.931, and MAE of 0.042.

3.3 Comparison of accurate efficiency

In this research, accurate efficiency obtained from the experimental results of predictive model construction from AdaBoost and Random Forest techniques. The results are shown in Table 6 and Figure 8.

Table 6. Comparison of accuracy.

Algorithms	Boosting (AdaBoost)	Bagging (Random Forest)
J48	87.5%	93.3%
ID3	83.3%	82.5%
CART	76.7%	74.2%

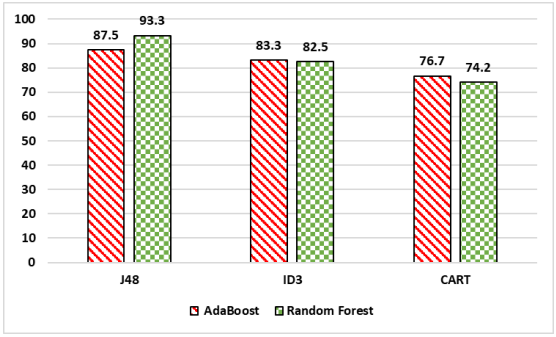

Figure 8. Results of accuracy comparison.

According to Table 6 and Figure 8, the J48 decision tree technique with Random Forest modeling has the highest efficiency with the

Suan Sunandha Science and Technology Journal
©2023 Faculty of Science and Technology, Suan Sunandha Rajabhat University

accuracy of 93.3%. Therefore, the model is suitable to employ for risk prediction of road accidents during holiday season.

4. Conclusions

This research aimed to propose a risk prediction model of road accidents during the holiday season based on ensemble learning using decision tree as a basic algorithm. The results revealed that:

The risk prediction model constructed from J48 algorithm with Random Forest Method had the highest prediction efficiency with accuracy of 93.3%. When comparing the accurate efficiency of the two techniques, Random Forest mostly expressed more accuracy than Boosting Method. It is because the Random Forest is added the random function to select data features for analysis, which reduces the correlation between each feature. The features were independent when building the decision trees. The As a result, the constructed decision trees are varied, small-structured, rapid processing, and highly efficient. In conclusion, the constructed model from Random Forest is suitable for predicting road accident risk during the next holiday season.

However, the model proposed by the researchers has focused on model construction by ensemble classification using Boosting and Bagging Methods. There are many other methods have not been mentioned, e.g. Stacking, Voting, Random Subspace, and Hybrid Experts, etc. Furthermore, the application of new algorithms for data classification, such as Artificial Neural Network algorithm (deep learning), can be employed to enhance the accuracy; and the hybrid algorithms can be used to improve the efficiency of data classification.

References

Accident Prevention Network. (2022). *Traffic accident statistics report: New Year - Songkran Festival 2022*. Retrieved from http://www.accident.or.th/ index.php/2017-12-04-07-32-28/289-2565

Boonraksa, P., & Thongkam, J. (2018). Performance comparison of the road occurrence accidents prediction models using time series techniques. *Journal of Technology Management Rajabhat Maha Sarakham University*, *4*(2), 39-46.

Chen, M.-M., & Chen, M.-C. (2020). Modeling road accident severity with comparisons of logistic regression, decision tree and random forest. *Information*, *11*(5), 270. doi:10.3390/info11050270.

Esenturk, E., Turley, D., Wallace, A., Khastgir, S., & Jennings, P. (2022). A data mining approach for traffic accidents, pattern extraction and test scenario generation for autonomous vehicles. *International Journal of Transportation Science and Technology*. doi:10.1016/j.ijtst. 2022.10.002

Markoulidakis, I., Rallis, I., Georgoulas, I., Kopsiaftis, G., Doulamis, A., & Doulamis, N. (2021). Multiclass confusion matrix reduction method and its application on net promoter score classification problem. *Technologies*, *9*(4), 81. doi:10.3390/technologies9040081

Nedjmedine, O., & Tahar, M. (2022). Analysis of road accident factors using Decision Tree Algorithm: A case of study Algeria. *5th International Symposium on Informatics and its Applications (ISIA)*. M'sila, Algeria. doi:10.1109/ISIA55826.2022.9993530.

Njoku, O. C. (2019). *Decision trees and their application for classification and regression problems* (Master's thesis). MSU Graduate Theses. Retrieved from https://bearworks. missouristate.edu/theses/3406

Ogheneovo, E. E., & Nlerum, P. A. (2020). Iterative Dichotomizer 3 (ID3) decision tree: A machine learning algorithm for data classification and predictive analysis. *International Journal of Advanced Engineering Research and Science (IJAERS)*, *7*(4), 514-521. doi:10.22161/ijaers.74.60

Panigrahi, R., & Borah, S. (2018). Rank allocation to J48 group of decision tree classifiers using binary and multiclass intrusion detection datasets. *Procedia Computer Science*, *132*, 323-332. doi:10.1016/j.procs.2018.05.186

Parathasarathy, G., Soumya, T. R., Das, Y. J., Saravanakumar, J., & Merjora, A. A. (2019). Using hybrid data mining algorithm for analysing road accidents data set. *3rd International Conference on Computing and Communications Technologies (ICCCT)* (pp. 7-13). Chennai, India. doi:10.1109/ICCCT2.2019.8824860

Suan Sunandha Science and Technology Journal
©2023 Faculty of Science and Technology, Suan Sunandha Rajabhat University

Sonwongsa, R., Pinpoo, S., & Wongkhae, K. (2016). Severity analysis of car accidents during "7 dangerous days" of New Year and Songkran festival. *The 12th Mahasarakham University Research Conference* (pp. 39-47). Thailand.

Taamneh, M., Alkheder, S., & Taameh, S. (2017). Data-mining techniques for traffic accident modeling and prediction in the United Arab Emirates. *Journal of Transportation Safety & Security*, *9*(2), 146-166. doi:10.1080/19439962.2016.1152338

Tanha, J., Abdi, Y., Samadi, N., Razzaghi, N., & Asadpour, M. (2020). Boosting methods for multi-class imbalanced data classification: An experimental review. *Journal of Big Data*, *7*(1), 1-47. doi:10.1186/s40537-020-00349-y

Yang, P., Yang, Y. H., Zhou, B. B., & Zomaya, A. Y. (2010). A review of ensemble methods in bioinformatics. *Current Bioinformatics*, *5*(4), 296-308. doi:10.2174/157489310794072508

Zacharis, N. Z. (2018). Classification and Regression Trees (CART) for predictive modeling in blended learning. *International Journal of Intelligent Systems and Applications*, *3*, 1-9. doi:10.5815/ijisa.2018.03.01

Zamzuri, Z. H., & Qi, K. Z. (2022). Classifying the severity levels of traffic accidents using decision trees. *Proceedings of the International Conference on Mathematical Sciences and Statistics 2022 (ICMSS 2022)*. doi:10.2991/978-94-6463-014-5_17

Available online at https://li02.tci-thaijo.org/index.php/ssstj

Suan Sunandha Science and Technology Journal
©2023 Faculty of Science and Technology, Suan Sunandha Rajabhat University

Influence of Annealing and Etching on Physical and Wetting Properties of Acrylic Surface

Wattikon Sroila, Nidchamon Jumrus, Jongrak Jompaeng, Arisara Panthawan, Tewasin Kumpika, Ekkapong Kantarak, Pisith Singjai, Wiradej Thongsuwan*

Department of Physics and Materials Science, Faculty of Science, Chiang Mai University 50200, Thailand
***Corresponding author e-mail: wiradej.t@cmu.ac.th**

Received: *3 May 2023* / **Revised:** *12 June 2023* / **Accepted:** *16 June 2023*

Abstract

The objective of this research aims to study the surface modification of acrylic for superhydrophobic applications. The acrylics were modified by annealing for 1h at 50, 75 and 100 °C. To study the effect of the etching on the surface morphology, chloroform and tetrahydrofuran (THF) with their concentration of 99.8 % v/v were used as etching acids. The annealed acrylics were then etched with THF and chloroform for 1 min. The annealing and wet chemical etching effects on morphology, optical properties and wettability can be characterized using atomic force microscopy, scanning electron microscopy, Vickers hardness tester, UV/Vis spectroscopy and water contact angle measurement. This result shows that the hardness of acrylic increases with increasing the annealing temperature. Furthermore, the wet chemical etching plays an important role in the wetting property on acrylics due to the changing of surface roughness.

Keywords: Acrylic, Tetrahydrofuran, Wettability, Annealing, Etching

1. Introduction

Polymers are often found in every materials used in our life, such as windows, lens and packaging (Kaczmarek & Chaberska, 2006; Mohajerani, Farajollahi, Mahzoon, & Baghery, 2007). Acrylic is a transparent polymer that has been used as a substitute for glass. Because it is more durable and lighter than glass (Al-Qahtani & Haralur, 2020). Annealing and wet chemical etching processes are widely used to modify the physical, mechanical and wetting properties. It is well known that the wetting property is the ability of a liquid to maintain contact with a solid surface, and it is controlled by the balance between the intermolecular interactions of adhesive type (liquid to surface) and cohesive (liquid to liquid) (Moldoveanu & David, 2017). Wet chemical etching processes that use liquid chemicals or etchants to remove materials from a wafer involve multiple chemical reactions that consume the original reactants and produce new reactants (Nayak, Islam, & Logeeswaran, 2012). In 2020, Jumrus et al. (2020) reported that annealing assisted etching technique can modified the roughness in nanoscale by reducing residual and hardness. Due to the fact that acrylic is the hardest thermoplastic polymer that softens when heated and harden upon cooling. Its effect on crystal structure, hardness, internal stresses and strength has been studied in the literature (Aadila et al., 2016). Moreover, tetrahydrofuran (THF) is one of the interesting acids which can be used to create high surface roughness (Ebert & Bhushan, 2012). The enhancement of surface roughness play an important role in superhydrophobicity (Sriboonruang et al., 2019).

In this work, we aim to modify physical and wetting properties on the acrylic surface by annealing and etching methods. Their methods were simple and low-cost to change surface roughness. Morphology, hardness and optical properties of acrylic were characterized by scanning electron microscopy (SEM), atomic force microscopy (AFM), micro Vickers hardness tester and UV-Vis spectroscopy. Moreover, wetting property can be investigated using the water contact angle (WCA) measurement.

Suan Sunandha Science and Technology Journal
©2023 Faculty of Science and Technology, Suan Sunandha Rajabhat University

2. Materials and Methods

2.1 Preparation

The commercial acrylic sheets (Pan Asia Industrial Co., Ltd) were cut into 10x30x1 mm^3. 2 acids (tetrahydrofuran (THF) and chloroform, 99.8% purity, RCI Labscan Ltd) with similar conditions used to compare the change on the acrylic surface. The samples were annealed under atmospheric pressure at 50°C (A50), 75°C (A75), and 100°C (A100) for 1 h. The annealed samples were then etched by the chosen acid for 1 min.

2.2 Characterization

Morphology of samples was characterized by scanning electron microscopy (SEM, JEOL JSM-IT300) and atomic force microscopy (AFM, Digital Instruments, Inc.) The Vickers microhardness (STARTECH, SMV-1000) used 0.98 N of load for annealed samples. The optical transmittance was measured by UV-Vis spectroscopy (Hitashi U-4100) from 200 to 800 nm. The wetting property was estimated by the WCA measurement using a pendant drop tensiometer with 3 µL of water droplet at five different areas for each sample.

3. Results and Discussion

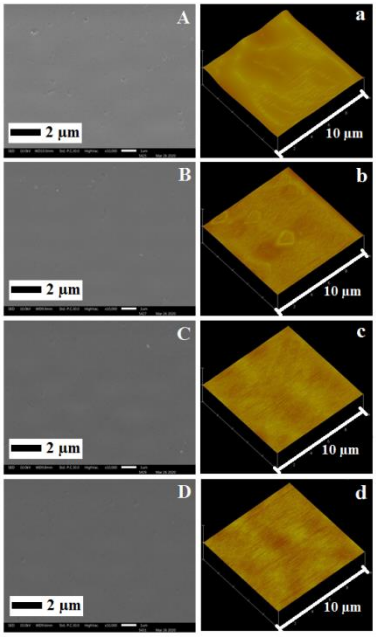

Figure 1. SEM and AFM images of, RT (A and a), A50 (B and b), A75 (C and c) and A100 (D and d).

Figure 1 shows SEM and AFM images of the acrylic surface after annealing with different temperatures. The surface roughness of all samples slightly changes in the nanoscale, as measured by AFM but not significantly in SEM. The surface roughness of bare acrylic (RT) is 5.024 and annealed acrylics at A50, A75 and A100 are 0.706, 0.447 and 0.344 nm, respectively. It has been reported that annealing at a temperature lower than the transition glass temperature (T_g = 105°C) plays an essential role in the reduction of surface roughness (Aadila et al., 2016).

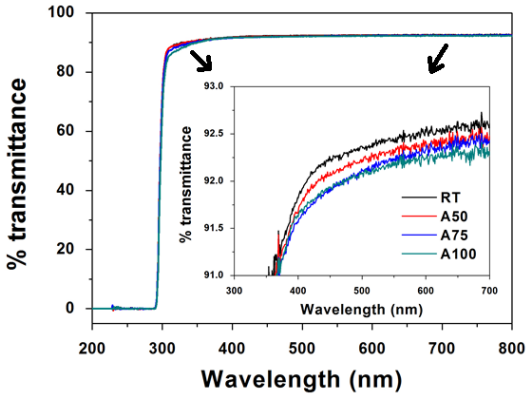

Figure 2. The spectra of transmittance after annealing at different temperatures.

The transmission of the samples with the wavelength from 200 to 800 nm is exhibited in Figure 2. Interestingly, the high transparency of the bare and annealed acrylics in the UV and visible regions is observed. This is because a small roughness change does not exceed the wavelength of incident light (< 100 nm), as indicated by the Mie scattering effect (Zhang et al., 2017).

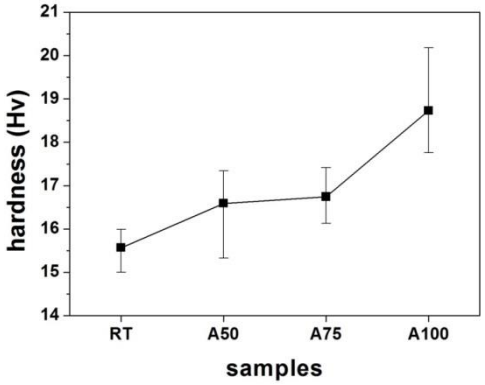

Figure 3. Micro-vickers hardness evolution after annealing at different temperatures.

The variation of micro-vickers hardness as a function of annealing temperature from room temperature to 100°C is shown in Figure 3. The

Suan Sunandha Science and Technology Journal
©2023 Faculty of Science and Technology, Suan Sunandha Rajabhat University

hardness increased from 15.6 to 16.6, 16.8, and 18.7 Hv with increasing the annealing temperature from RT to 50°C, 75°C and 100°C, respectively. This is in good agreement with Khodabakhshi et al. result (Khodabakhshi, Kazeminezhad, Azarnush, & Miran, 2011). Interestingly, the hardness was increased with increasing the annealing temperature lower than T_g of acrylic due to the gentle and independent vibrations in acrylic molecules (Wu et al., 2013). Whereas annealing temperature higher than T_g shows a decreasing of hardness due to rapid grain growth in acrylic.

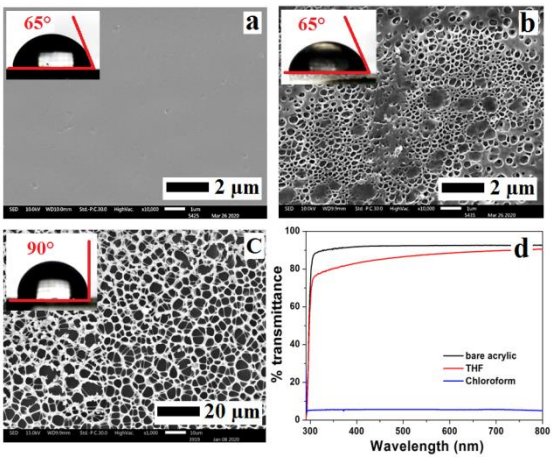

Figure 4. SEM images of (a) bare acrylic, (b) etched with THF, (c) etched with chloroform, and (d) transmittance spectra.

Figure 4 (b and c) shows the morphology of acrylic substrates for the etching of two different acids between THF and chloroform used, as affected by the increasing of surface roughness. The surface of bare acrylic is very smooth, with a WCA of 65°, as shown in Figure 4 (a). Although the surface morphology of the etched acrylic changed by THF but did not change in WCA (Figure 4 (b)). This is due to the THF etching is uncontrolled in the reaction and the roughness on the surface, as confirmed by figure 4 (d). Whereas the WCA of etched acrylic by chloroform increased to 90° (Figure 4 (c)). The chemical reaction of chloroform is better than THF due to its low boiling point, which affected to surface roughness (Kim et al., 2017). The molecular structure on the etched surface leads to a change in the WCA and their adhesion force (Hiratsuka, Emoto, Konno, & Ito, 2019). However, chloroform has highly hazardous acid and the average transmittance spectra is reduce to 5% which is compared to the spectrum of the THF etched sample of 83%, as seen in Figure 4 (d) (Yeh, Wu, Huang, Lee, & Jeng, 2019).

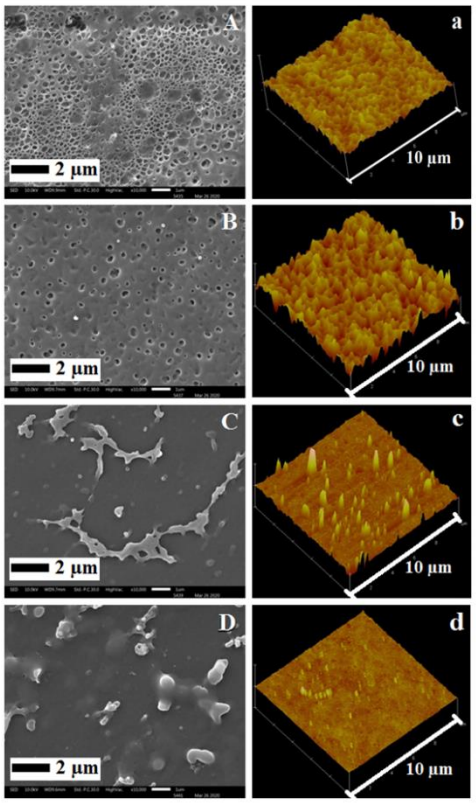

Figure 5. SEM and AFM images of, (A and a) bare acrylic (RT-THF), (B and b) annealed and etched (A50-THF), (C and c) annealed and etched (A75-THF), and (D and d) A100-THF.

The SEM and AFM images of THF etching samples are shown in Figure 5. The bare acrylic (RT-THF) surface roughness is 10.355 nm, while the roughness of the annealed and etched samples (A50-THF, A75-THF and A100-THF) are 26.691, 8.778 and 2.461 nm, respectively. It is noted that the annealed samples at room temperature (RT) rapidly etched while etching ability was decreased with the annealed samples at a higher RT. This result is in good agreement with the microhardness result (see in Figure 3).

Suan Sunandha Science and Technology Journal
©2023 Faculty of Science and Technology, Suan Sunandha Rajabhat University

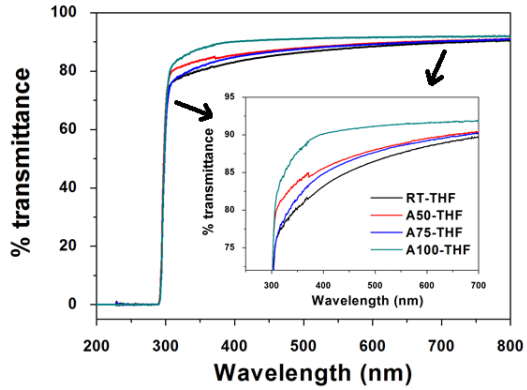

Figure 6. Transmission of the etched samples after annealed at different annealing temperatures.

The optical property of the annealed and etched samples is shown in Figure 6. From the figure, the sample A100-THF exhibits the highest transmittance because the surface roughness is the lowest. Interestingly, the sample A50-THF shows high transparency, although (Figure 6) it has the highest surface roughness**.** Thus, the transmittance not only depends on surface roughness in the micro-scale but also on the changing of morphology in the nano-scale, as shown in the AFM images (Figure 5 (a-d)). This is in good agreement with our previous paper (Jumrus et al., 2021). It is noted that THF etching creates both micro and nano-roughness on the acrylic surface, which depends on the hardness after annealing.

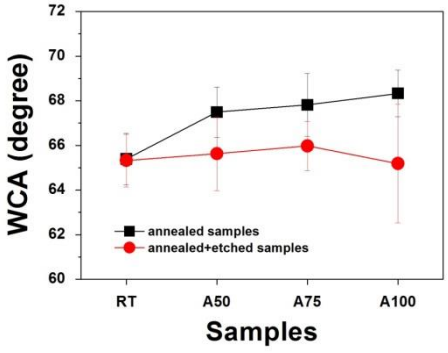

Figure 7. Variation of WCA after annealing in different temperature and etching.

Figure 7 shows the wettability of the samples**.** The annealed samples have a WCA that is slightly increased with increasing of the annealing temperature. This can be indicated that the annealing has direct effect on leaving some hydroxyl ions from the surface and lead to improving surface stability (Wu, Xu, Yang, & Zhang, 2016). However, some low surface energy will be eliminated from the annealed acrylic that was etched with THF. This is due to the annealed and etched acrylic's WCA not changing significantly.

4. Conclusions

Facile wet chemical etching techniques and annealing were modified using the wetting property of the acrylic surface. The annealing temperature and acid for etching are the main factors explaining the transparency and optimum surface roughness**.** These developments result in the creation of superhydrophobic applications. The acrylic materials are valuable because they are lighter than glass, but they also impact weather-resistant and have high transparency. This is an alternative material which can be used as a substitute for glass in the future.

Acknowledgements

This work was supported by Department of Physics and Materials Science, Faculty of Science, Chiang Mai University.

Conflict of Interest

The authors would like to declare that there is no conflict of interest in this paper.

Ethical Approval

Not applicable.

Publication Ethic

Submitted manuscripts must not have been previously published by or be under review by another print or online journal or source.

References

Aadila, A., Afaah, A. N., Asib, N. A. M., Mohamed, R., Rusop, M., & Khusaimi, Z. (2016). Effect of annealing temperature on the morphology and optical properties of PMMA films by spin-coating method, *AIP Conference Proceedings*, *1733*, 020045. doi:10.1063/1.4948863

Al-Qahtani, M., & Haralur, S. B. (2020). Influence of different repair acrylic resin and thermocycling on the flexural strength of denture base resin. *Medicina*, *56*(2), 50. doi:10.3390/medicina56020050

Ebert, D., & Bhushan, B. (2012). Transparent, superhydrophobic, and wear-resistant coatings on glass and polymer substrates using SiO_2, ZnO, and ITO nanoparticles. *Langmuir*, *28*(31), 11391-11399. doi:10.1021/la301479c

Suan Sunandha Science and Technology Journal
©2023 Faculty of Science and Technology, Suan Sunandha Rajabhat University

Hiratsuka, M., Emoto, M., Konno, A., & Ito, S. (2019). Molecular dynamics simulation of the influence of nanoscale structure on water wetting and condensation. *Micromachines*, *10*(9), 587. doi:10.3390/mi10090587

Jumrus, N., Chaisen, T., Sriboonruang, A., Panthawan, A., Kumpika, T., Kantarak, E., … Thongsuwan, W. (2020). A facile methodology to make the glass surface superhydrophobic. *Materials Letters*, *264*, 127347. doi:10.1016/j.matlet.2020.127347

Jumrus, N., Jompeang, J., Panthawan, A., Kumpika, T., Wiranwetchayan, O., Sanmuangmoon, P., … Thongsuwan, W. (2021). Transparency and water resistance of a superhydrophobic acrylic surface prepared using THF/IPA etching-assisted SiO_2 NPs. *Materials Letters*, *304*, 130618. doi:10.1016/j.matlet.2021.130618

Kaczmarek, H., & Chaberska. H. (2006). The influence of UV-irradiation and support type on surface properties of poly(methyl methacrylate) thin films. *Applied Surface Science*, *252*(23), 8185-8192. doi:10.1016/j.apsusc.2005.10.037

Khodabakhshi, F., Kazeminezhad, M., Azarnush, M., & Miran, S. H. (2011). Effect of post annealing treatment on nano-structured low carbon steel sheets processed by constrained groove pressing. *Materials Science Forum*, *667-669*, 1009-1014. doi:10.4028/www.scientific.net/MSF.667-669.1009

Kim, S. M., Park, S. B., Bedair, T. M., Kim, M. H., Park, B. J., Joung, Y. K., & Han, D. K. (2017). The effect of solvents and hydrophilic additive on stable coating and controllable sirolimus release system for drug-eluting stent. *Materials Science and Engineering C*, *78*, 39-46. doi:10.1016/j.msec.2017.04.024

Mohajerani, E., Farajollahi, F., Mahzoon, R., & Baghery, S. (2007). Morphological and thickness analysis for PMMA spin coated films. *Journal of Optoelectronics and Advanced Materials*, *9*(12), 3901-3906.

Moldoveanu, S. C., & David, V. (2017). *Selection of the HPLC method in chemical analysis*. Amsterdam: Elsevier.

Nayak, A. P., Islam, M. S., & Logeeswaran, V. J. (2012) Wet etching. In B. Bhushan (Ed.), *Encyclopedia of nanotechnology*. doi:10.1007/978-90-481-9751-4_431

Sriboonruang, A., Kumpika, T., Kantarak, E., Sroila, W., Singjai, P., Lawan, N., … Thongsuwan, W. (2019). Isomer effect on chemical reactivity and superhydrophobicity of chlorosilane modified SiO_2 nanoparticles prepared by one-step reaction. *Materials Letters*, *248*, 227-230. doi:10.1016/j.matlet.2019.04.047

Wu, H., Xu, D., Yang, M., & Zhang, X. (2016). Surface structure of hydroxyapatite from simulated annealing molecular dynamics simulations. *Langmuir*, *32*(18), 4643-4652. doi:10.1021/acs.langmuir.5b04667

Wu, R., Chen, R., Gao, Y., Zhang, G., Xiao, L., & Jia, S. (2013). Annealing temperature dependence of the nanosized pits on poly(methyl methacrylate) surface. *Japanese Journal of Applied Physics*, *52*, 125501. doi:10.7567/JJAP.52.125501

Yeh, S. C., Wu, C. H., Huang, Y. C., Lee, J. Y., & Jeng, R. J. (2019). In search of a green process: Polymeric films with ordered arrays via a water droplet technique. *Polymers*, *11*(9), 1473. doi:10.3390/polym11091473

Zhang, Y., Dong, B., Wang, S., Zhao, L., Wan, L., & Wang, E. (2017). Mechanically robust, thermally stable, highly transparent superhydrophobic coating with low-temperature sol–gel process. *RSC Advances*, *7*, 47357-47365. doi:10.1039/c7ra08578h

Available online at https://li02.tci-thaijo.org/index.php/ssstj

Suan Sunandha Science and Technology Journal
©2023 Faculty of Science and Technology, Suan Sunandha Rajabhat University

The Glass Produced from Recycled Soda-Lime Glass Cullet by Slip Casting Technique

Parinya Chakartnarodom[1*], Ekdanai Deeprasertwong[1], Pitcharat Ineure[2], Nutthita Chuankrerkkul[3], Edward A. Laitila[4], Nuntaporn Kongkajun[5]

[1]Department of Materials Engineering, Faculty of Engineering, Kasetsart University, Bangkok 10900, Thailand
[2]Glass Bridge Company Limited, Bangkok 10230, Thailand
[3]Metallurgy and Materials Science Research Institute, Chulalongkorn University, Bangkok 10330, Thailand
[4]Department of Materials Science and Engineering, Michigan Technological University, Houghton, MI 49931, USA
[5]Department of Materials and Textile Technology, Faculty of Science and Technology, Thammasat University, Pathumthani 12120, Thailand
***Corresponding author e-mail:** fengpryc@ku.ac.th

Received: *8 May 2023* / **Revised:** *7 June 2023* / **Accepted:** *12 June 2023*

Abstract

Slip casting is a ceramic processing technique that can be utilized for creating ceramic objects with complex shapes. In this study, slip casting was employed to fabricate green samples measuring 70 mm × 10 mm × 15 mm from recycled soda-lime glass. A slip with 60% solid loading was prepared from 100 g of recycled cullet, 1 g of sodium silicate as a binder, 50 ml of DI water, and 16.7 ml of deflocculant. A 0.1 wt% sodium tripolyphosphate solution was used as the deflocculant for slip casting. After the slip casting process, the samples were dried at room temperature for 3 days. Subsequently, they were sintered at 680, 700, and 720 °C for 1 and 2 hours with a heating rate of 5°C/min. Statistical analysis of the results revealed a high degree of variation in the flexural strength, which is attributed to the high closed porosity and pore-size variation of the samples. Therefore, the glass produced from slip casting is not suitable for load-bearing applications. Nevertheless, this technique can still be utilized to create other art products, such as Buddha amulets.

Keywords: Glass, Cullet, Recycle, Slip casting, Four-points bending test, Weibull modulus

1. Introduction

The glass industry in Thailand is substantial, with an annual production capacity of 3 million tons for glass-bottle manufacturing and 1 million ton for flat-glass manufacturing. The production process generally involves mixing raw materials such as silica sand (SiO_2), limestone ($CaCO_3$), and soda ash (Na_2CO_3), which are then melted at approximately 1500 °C and formed into products such as glass bottles or flat glass. Natural gas is a common source of heating in the glass industry and contributes to 75% to 85% of the total greenhouse gas emissions. Additionally, 15% to 25% of greenhouse gas emissions result from the chemical reactions of raw materials.

Cullet is recycled glass, and its properties remain unchanged even after several recycling cycles. When cullet is melted, there are zero greenhouse gas emissions, making it an environmentally friendly alternative to virgin materials. Thus, substituting virgin materials with cullet is an effective method to reduce greenhouse gas emissions and the consumption of non-renewable natural resources in the glass industry. Furthermore, reducing the operating temperature is another approach to further reduce greenhouse gas emissions (Deeprasertwong et al., 2022; Editors, 2021).

Slip casting is a forming method used to create ceramic products. A slurry, consisting of ceramic powder, deflocculant, and water, is prepared and poured into a plaster of Paris mold. The water from the slip is absorbed by the mold, resulting in the formation of a solid layer on the mold's walls. Once the solid layer reaches the desired thickness, excess slip is poured out, leaving behind the green product. Slip casting is particularly useful for producing complex-shaped ceramic products, including pottery

Suan Sunandha Science and Technology Journal
©2023 Faculty of Science and Technology, Suan Sunandha Rajabhat University

and sculptures (Askeland, Fulay, & Wright, 2010; Callister Jr, & Rethwisch, 2014; Tempelman, Shercliff, & van Eyben, 2014). Slip casting has been utilized by various research groups as a sample fabrication method for glass composite systems, including the cordierite/glass powder system (Marghussian & Geramian, 1999; Mei, Yang, & Ferreira, 2003), and hydroxyapatite/ borosilicate glass powder system (Hu & Miao, 2004).

Soda-lime glass is a commonly used commercial glass to produce glass bottles and flat glass. In Thailand, approximately 924,019.55 tons of glass bottles and 722,944.01 tons of flat glass were produced in 2017. Unfortunately, after their use, these glass products are often disposed of in landfills, contributing to environmental issues.

In the previous research, we investigated the use of soda-lime glass cullet recycling through the powder pressing method to form samples. The findings revealed that the samples sintered at 700°C, with a heating rate of 5°C/min and soaking time of 1 hour, exhibited the best properties. Additionally, due to the lower temperature used in the process, there was a significant reduction in greenhouse gas emissions compared to conventional glass manufacturing methods (Deeprasertwong et al., 2022).

The objective of this study was to assess the feasibility of utilizing the slip casting technique for the recycling of soda-lime glass cullet. The mechanical and physical properties of the sintered samples, including flexural strength, shrinkage, and porosity, were examined, and correlated with the observed microstructure. The results were subjected to a statistical analysis to evaluate the viability of this technique for glass recycling.

2. Materials and Methods

The ground cullet used in this study was prepared from waste soda-lime glass, which was crushed using ball milling for a duration of 16 hours. The waste soda-lime glass was obtained from Glassbridge Co., Ltd. The average particle size of the ground cullet was determined to be 891±22 µm using a laser particle size analyzer (Malvern mastersizer 3000). The particle size distribution of the ground cullet is illustrated in Figure 1. The chemical composition of the ground cullet was analyzed using an x-ray fluorescence spectrometer (XRF, Bruker s8 tiger), and the results are presented in Table 1.

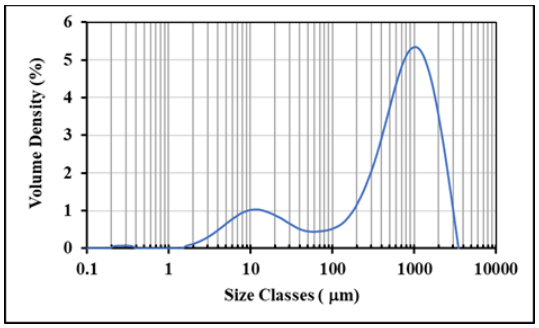

Figure 1. the particle size distribution of the ground cullet.

Table 1. the chemical composition of the ground cullet.

Oxide	wt%	Oxide	wt%
SiO_2	69.9	MgO	4.17
Na_2O	14.1	Al_2O_3	1.50
CaO	8.78	Others	1.55

To prepare the slip, a mixture of 100 g of ground cullet, 1 g of binder (sodium silicate), 50 ml of water, and 16.7 ml of deflocculant was used. The slip had a solid loading of 60%. The deflocculant utilized was a 0.1 wt% sodium tripolyphosphate solution, provided by Source Runner Enterprise Co., Ltd.

The slip was carefully poured into plaster molds to create green samples with dimensions of 70 mm × 10 mm × 15 mm. Figure 2 (a) depicts the plaster molds filled with the slip. Once the casting process was completed, the green samples were extracted from the molds, as shown in Figure 2 (b) and left to air dry for a period of 3 days. Subsequently, the dried samples were subjected to sintering, as depicted in Figure 2 (c). The sintering process involved temperatures of 680°C, 700°C, and 720°C, with soaking times of 1 and 2 hours, and a heating rate of 5°C/min.

(a)

Suan Sunandha Science and Technology Journal
©2023 Faculty of Science and Technology, Suan Sunandha Rajabhat University

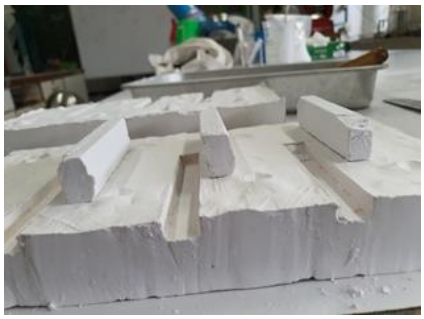

(b)

(c)

Figure 2. the different stages of the sample preparation process: (a) the plaster molds filled with the slip, (b) the green samples just after being removed from the molds, and (c) the green samples prior to undergoing the sintering process.

The flexural strength of the sintered samples was evaluated using a four-point bending test performed on a universal testing machine (UTM, Instron 5969). Additionally, the microstructure of the sintered samples was analyzed using a scanning electron microscope (SEM, Hitachi SU3500). To determine the closed porosity of the sintered samples, the Archimedes method was employed, and the calculation was carried out using the following equation:

$$CP = TP - AP \quad (1)$$

where CP, TP, and AP refer to the closed, true, and apparent porosity of the samples, respectively. As AP represents interconnected pores, and TP represents both interconnected pores and closed pores, the CP of a sample can be calculated using Equation (1).

TP and AP can be calculated using Equations (2) and (3) as follows:

$$TP = [(\rho - BD)/\rho] \times 100 \quad (2)$$

$$AP = [(W_2 - W_1)/(W_2 - W_3)] \times 100 \quad (3)$$

ρ represents the true density of soda-lime glass, which is approximately 2.47 g/cm³ (Ashby, 2013; Deeprasertwong et al., 2022), while BD, as obtained from Equation (4), represents the bulk density.

$$BD = W_1/(W_2 - W_3) \quad (4)$$

where W_1 represents the dry weight of the sample, W_2 represents the weight of the sample just after being removed from the water, and W_3 represents the weight of the sample measured in water (Askeland et al., 2010).

For each test on mechanical and physical properties, three samples from each experimental condition were used.

Statistical analysis was conducted on the flexural strength data. The probability of sample failure (F), due to the applied stress (σ) is (Askeland et al., 2010)

$$F = 1 - e^{(-[\sigma/\sigma_o]^{m_o})} \text{ or} \quad (5)$$

$$ln\left\{ln\left[\frac{1}{1-F}\right]\right\} = m_o(ln(\sigma) - ln(\sigma_o)) \quad (6)$$

In the equation, σ_o represents a parameter that depends on the size and shape of the sample, and m_o denotes the Weibull modulus.

According to Askeland et al. (2010); the Weibull modulus of a set of flexural strength data can be determined by ranking the data from lowest to highest. For a set of n samples, each sample is assigned a numerical rank from i = 1 to n, with i = 1 representing the sample with the lowest flexural strength. F is then assigned to each sample, and for sample i, F can be calculated as i / (n + 1). Afterward, a graph is created with the y-axis representing ln{ln(1/(1-F))} and the x-axis representing ln(σ). The Weibull modulus can be determined by applying linear regression analysis to the graph. In the context of a load-bearing ceramic part, a large value of the Weibull modulus is desirable as it indicates a narrow range of flaw sizes within the material.

3. Results and Discussion

Figure 3(a) depicts the samples before and after the sintering process, revealing a significant shrinkage following sintering. The volume shrinkage of each sintered sample is presented in Figure 3(b). Notably, the volume shrinkage remains relatively consistent across both soaking times (1 and 2 hours) and all sintering temperatures (680, 700, and 720 °C). Figure 4 illustrates that the sintered samples possess a porous structure with varying pore sizes. The closed porosity of each

Suan Sunandha Science and Technology Journal
©2023 Faculty of Science and Technology, Suan Sunandha Rajabhat University

sample is displayed in Figure 5, demonstrating a similar trend to the volume shrinkage, with consistent closed porosity observed across both soaking times and all sintering temperatures.

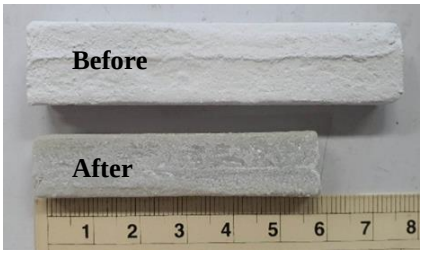

(a)

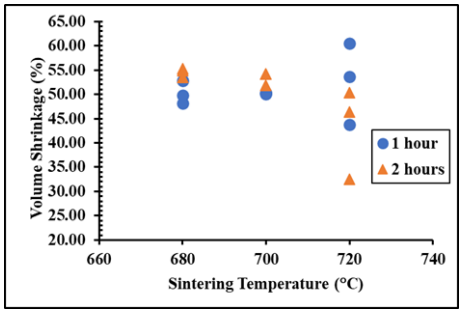

(b)

Figure 3. (a) a comparison of the sample size before and after sintering (b) the volume shrinkage that takes place after sintering.

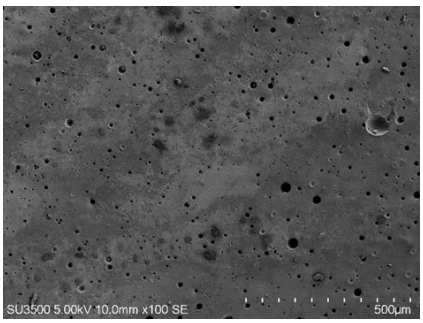

(a)

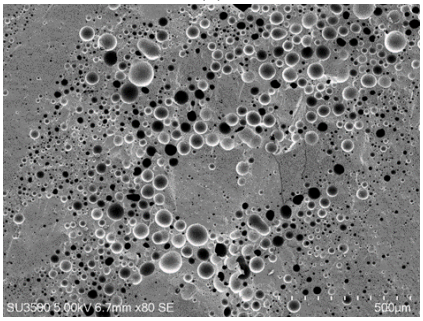

(b)

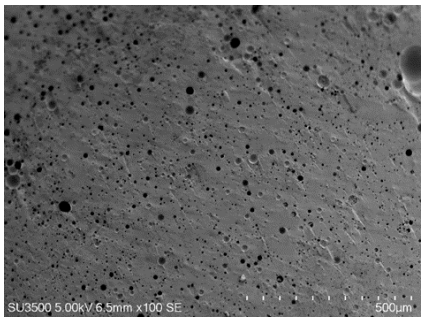

(c)

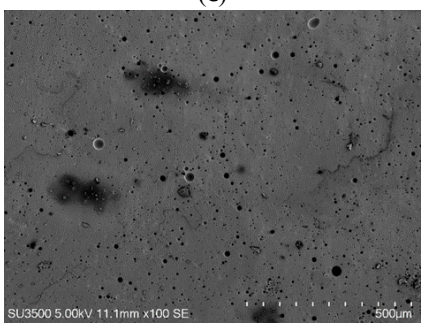

(d)

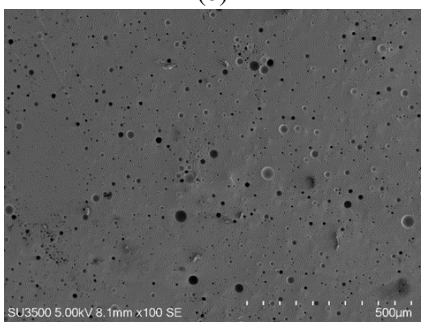

(e)

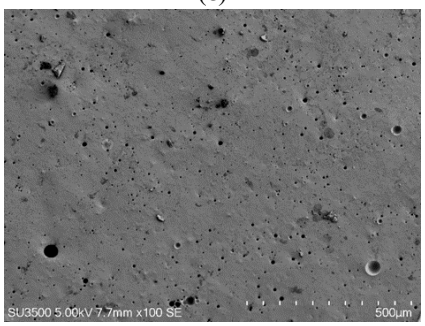

(f)

Figure 4. the microstructure of the samples after sintering at different temperatures and holding times. The images show the microstructures for the following conditions: (a) 680°C and 1 hr (b) 680°C and 2 hrs (c) 700°C and 1 hr (d) 700°C and 2 hrs (e) 720°C and 1 hr (f) 720°C and 2 hrs.

Suan Sunandha Science and Technology Journal
©2023 Faculty of Science and Technology, Suan Sunandha Rajabhat University

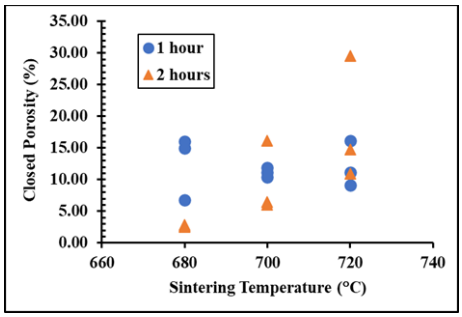

Figure 5. the closed porosity of the sintered samples.

According to Askeland et al. (2010), defects can be generated inside ceramics and glasses during the manufacturing process. Additionally, microcracking on the glass surface may occur due to the interaction between glass and water vapor in the air. The size and distribution of internal defects have a significant impact on the strength of ceramics and glasses.

Figure 6(a) illustrates the flexural strength of each sample. The data from both soaking times and various sintering temperatures were used to generate the straight line for Weibull statistical analysis, as shown in Figure 6(b). The Weibull modulus (m_o from Equation (6)) represents the slope of the straight line in Figure 6(b), which is calculated to be 1.409. Conventionally-prepared alumina typically exhibits a Weibull modulus around 4.7, while advanced ceramics can have Weibull moduli ranging from 10 to 20 (Askeland et al., 2010). Therefore, the Weibull modulus obtained in this work is considerably low. This low Weibull modulus suggests a high variation in flexural strength, which is likely due to the presence of high closed porosity and variations in pore size resulting from the sintering process (Figures 4 and 5).

Considering the low Weibull modulus observed in glass samples produced from recycled soda-lime glass cullet through slip casting, it is evident that these materials are not suitable for load-bearing applications. However, it should be noted that slip casting is widely employed in the creation of various art products. In this study, we utilized slip casting to produce art pieces such as the Buddha amulets depicted in Figure 7. These amulets demonstrate the capability of the glass slip casting technique for recycling glass and crafting intricate and aesthetically pleasing glass objects with artistic value.

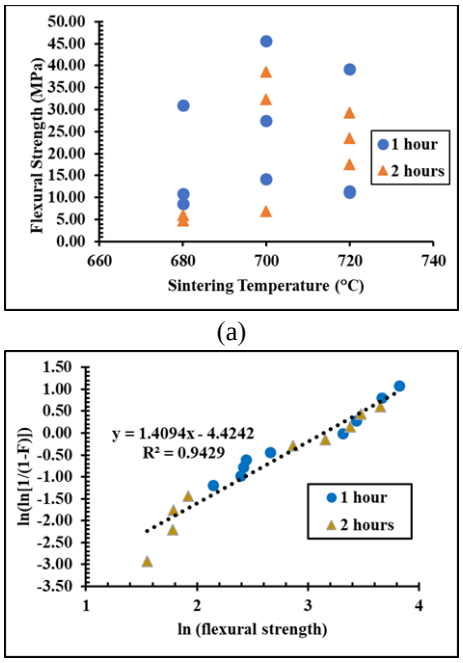

(a)

(b)

Figure 6. (a) flexural strength of the sintered samples and (b) Weibull statistical analysis on flexural strength data.

(a)

(b)

Figure 7. (a) Buddha amulets before and after sintering (b) various Buddha amulets.

Suan Sunandha Science and Technology Journal
©2023 Faculty of Science and Technology, Suan Sunandha Rajabhat University

4. Conclusions

Slip casting was investigated as a method for recycling soda-lime glass. The process involved crushing the waste soda-lime glass using ball milling, sieving it, and then mixing it with a binder, deflocculant, and water to prepare the slip for slip casting. The green samples obtained after casting were subsequently sintered. Statistical analysis of the flexural strength data of the sintered samples revealed a significant variation in strength, indicating that the glasses produced through slip casting were not suitable for load-bearing applications. As a result, the glass slip casting process was employed to create art products, such as Buddha amulets.

Acknowledgement

This work was supported by:

- Faculty of Engineering, Kasetsart University (Grant No. 63/06/MAT/INNOVATION),
- Department of Materials Engineering, Faculty of Engineering, Kasetsart University,
- Department of Materials and Textile Technology, Faculty of Science and Technology, Thammasat University, and
- Glass Bridge Company Limited.

Conflict of Interest

The authors declare that they have no known competing financial interests or personal relationships that could have appeared to influence the work reported in this paper.

ORCID

Parinya Chakartnarodom
https://orcid.org/0000-0002-4873-7285
Ekdanai Deeprasertwong
https://orcid.org/0000-0002-3137-0026
Pitcharat Ineure
https://orcid.org/0000-0002-0179-2690
Nutthita Chuankrerkkul
https://orcid.org/0000-0002-0327-3608
Edward A. Laitila
https://orcid.org/0000-0003-4868-9305
Nuntaporn Kongkajun
https://orcid.org/0000-0002-0856-5837

References

Ashby, M. F. (2013). *Materials and the environment* (2nd ed.) (pp. 459-595). UK: Butterworth-Heinemann.

Askeland, D. R., Fulay, P. P., & Wright, W. J. (2010). *The science and engineering of materials* (6th ed.). USA: Cengage Learning.

Callister Jr, W. D., & Rethwisch, D. G. (2014). *Materials science and engineering: An introduction* (9th ed.). NJ, United States: John Wiley & Sons.

Deeprasertwong, E., Ineure, P., Kongkajun, N., Borwornkiatkaew, W., Laitila, E. A., Chuankrerkkul, N., & Chakartnarodom, P. (2022). Properties of the glass formed from ground glass cullet via sintering. *Materials Today: Proceedings*, *65*, 2461-2466. doi:10.1016/j.matpr.2022.06.391

Editors. (2021). Glass is the hidden gem in a carbon-neutral future. *Nature*, *599*, 7-8. doi:10.1038/d41586-021-02992-8

Hu, Y., & Miao, X. (2004). Comparison of hydroxyapatite ceramics and hydroxyapatite/borosilicate glass composites prepared by slip casting. *Ceramics International*, *30*(7), 1787-1791. doi:10.1016/j.ceramint.2003.12.119

Marghussian, V. K., & Geramian, M. J. (1999). Fabrication of cordierite glass ceramics by slip casting of glass powders. *British Ceramic Transactions*, *98*(3), 133-140. doi:10.1179/096797899680345

Mei, S., Yang, J., & Ferreira, J. M. F. (2003). Comparison of dispersants performance in slip casting of cordierite-based glass-ceramics. *Ceramics International*, *29*(7), 785-791. doi:10.1016/S0272-8842(02)00231-6

Tempelman, E., Shercliff, H., & van Eyben, B. N. (2014). *Manufacturing and design* (pp. 227-250). UK: Butterworth-Heinemann.

Available online at https://li02.tci-thaijo.org/index.php/ssstj

Suan Sunandha Science and Technology Journal
©2023 Faculty of Science and Technology, Suan Sunandha Rajabhat University

XANES, XPS and Raman Studies of Hafnium Oxide Thin Films fabricated by RF Magnetron Sputtering at Different Power

Ekachai Chongsereecharoen*, Yotin Kallayalert, Wichai Kongsri

Faculty of Science and Technology, Valaya Alongkorn Rajabhat University under The Royal Patronage, Pathum Thani 13180, Thailand
***Corresponding author e-mail: ekachai@vru.ac.th**

Received: *23 May 2023* / **Revised:** *15 June 2023* / **Accepted:** *20 June 2023*

Abstract

Hafnium oxide layer was deposited on unheated silicon wafer and glass substrates at different power by using RF magnetron sputtering technique. The structural property was investigated by Raman spectroscopy. Moreover, HfO_2 structure in monoclinic major phase especially at high RF power was found from the Raman spectra in vibrational modes. In addition, oxidation state of hafnium oxide thin films was gained by synchrotron-based X-ray absorption spectroscopy (XAS) using Hf L3-edge of XANES techniques and X-ray photoelectron spectroscopy (XPS) as well. The XANES and XPS results show that the oxidation state of HfO_2 films is unchanged at different powers. The thin film prepared at higher power tends to have lower oxygen vacancy.

Keywords: Hafnium oxide thin films, Raman spectroscopy, XANES, XPS

1. Introduction

Hafnium oxide (HfO_2) has been considered as an alternative metal oxide material besides SiO_2 for high κ-gate dielectric material because of its great dielectric constant, excellent chemical and thermal stabilities, and high bandgap (Park & Kang, 2006). HfO_2-based materials are also a promising candidate for high index optical coatings, resistive-switching memory and ferroelectric field effect transistors (FeFET) (Ali et al., 2020). Semiconductor company introduced hafnium-based oxides as a replacement for silicon oxide in field-effect transistors' gate insulators. There are three phases of HfO_2: cubic, tetragonal, and monoclinic. The lowest energy structure of them is monoclinic HfO_2. Nevertheless, the implementation of Hafnium Oxide encounters various obstacles, including elevated defect density, increased threshold voltage, and concerns regarding dependability. Recent research has indicated that oxygen vacancies are the most active defects. The creation of oxygen vacancies in hafnia films and bulk samples can occur as a result of growth, deposition, and doping procedures. The presence of an oxygen vacancy in defective HfO_2 results in the emergence of a defect level situated at the edge of the conduction band. The electronic transition is obviously impacted by the new defect level. The presence of principal traps in HfO_2 implies that the optimal approach for deposition and postprocessing conditions should involve the elimination or neutralization of these defects (Gangqiang, Sanqi, & Tingting, 2013; Xiong, Robertson, Gibson, & Clark, 2005). Due to their simple binary oxide with non-perovskite structure and ferroelectric properties after doping by various dopants, such as Si, Zr, Al, and La, Hafnia –based materials have attracted considerable interest in the research field of ferroelectrics (Böscke, Müller, Bräuhaus, Schröder, & Böttger, 2011). The advantage of HfO_2 for transistors is its high dielectric constant, which is greater than SiO_2 (Luo et al., 2019). In recent times, several methods exist for producing HfO_2 thin films (Kukli et al., 2002). Magnetron sputtering is one of suitable methods to fabricate HfO_2 thin films because the film properties are controllable (Aygun & Yildiz, 2009; Cantas, Aygun, & Basa, 2014). The dielectric constant and other properties of a material are dependent on its deposition method, composition, and microstructure (Biswas, Sinha, & Chakraborty, 2016; Gao et al., 2016).

To gain a better understanding of the evolution of power dependent properties of Hafnia thin films fabricated by RF sputtering, in this work, we conducted detailed structural study using Raman

Suan Sunandha Science and Technology Journal
©2023 Faculty of Science and Technology, Suan Sunandha Rajabhat University

spectroscopy and chemical composition study by X-ray photoelectron spectroscopy (XPS) and X-ray absorption near edge structure (XANES) analysis. The structural sensitivity of X-ray diffraction techniques diminishes when the particle size of films achieves a few nanometers or when the films exhibit amorphous characteristics with short-range order. XPS is a well-known measurement method for probing the chemical environment and the electronic structure of a wide range of samples. X-ray absorption spectroscopy (XAS) is an essential elemental characterization technique due to its exceptional sensitivity to the local electronic and atomic structure. This technique effectively addresses the challenge of characterizing the local structure and electronic properties of diminutive, poorly crystalline, or low-conductive film/powder samples.

2. Experimental Details

Hafnium oxide layers were deposited on cleaned glass and silicon substrates by RF magnetron sputtering at room temperature by using HfO_2 ceramic target (99.999%, 3-inch diameter). Before deposition, the background pressure in the chamber was evacuated to about 1×10^{-4} Pa. The deposition pressure was controlled at 1×10^{-4} Pa. Argon was employed as sputtering gas and fixed at 10 sccm of flow rate. The spatial separation between target and substrate was kept at 70 mm. The operating time was set for 60 min. The RF sputtering power used during the deposition process varied between 50 to 200 Watt.

The structural study of the prepared films was examined by Raman spectroscopy (SENTERRA, Bruker). Raman spectra were obtained utilizing a 532 nm laser excitation, 25 mW power, and 25 μm ×1000 μm window, with a Raman shift resolution of 0.5 cm^{-1} over a range of 50–2700 cm^{-1}. The chemical composition was analyzed by means of XPS and XANES. XPS measurements were conducted utilizing a PHI5000 Versa probe II (ULVAC-PHI, Japan) that was installed with a hemispherical electron energy analyzer at Chiang Mai university, Thailand. A monochromatic Al Kα X-ray gun operating at an energy of 1486.6 eV was employed as the excitation source. The survey scans of XPS acquired over a range of 0 to 1400 eV with pass energy of 117.40 eV and energy step of 1.0 eV. High resolutions XPS spectra were gathered with pass energy of 46.95 eV and energy step of 0.05 eV to probe the elements of interest. The calibration of the binding energy for all XPS spectra was conducted utilizing the C1s peak at 284.8 eV. The peak deconvolution process involved the application of the Sherly background subtraction method and the linear combinations of Gaussian-Lorentzian function. Moreover, the local structure was investigated by synchrotron-based XANES with electron energy of 1.2 GeV at the BL5.2: SUT-NANOTEC-SLRI XAS beamline of the Synchrotron Light Research Institute, Thailand. The XANES measurements were performed by fluorescent mode at room temperature. The spectra of Hafnium L3-edge were obtained within an energy range of 9530-96400 eV, with a 0.2 eV energy increment. The XAS data was normalized and subtracted background by the ATHENA program included in the IFEFFIT package.

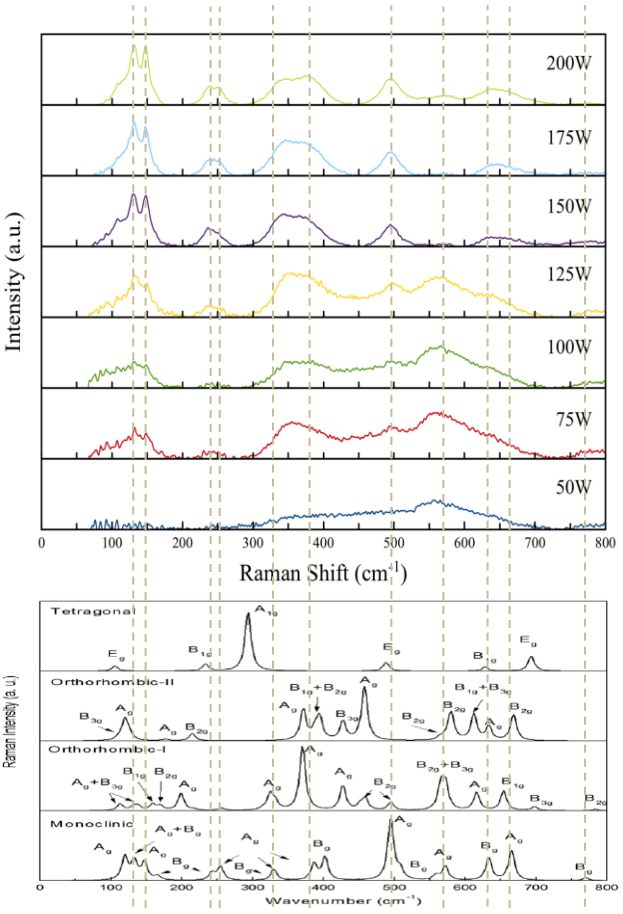

Figure 1. The RF power dependent Raman spectra of Hafnium oxide thin films compared with the calculation results from Zhou et al.'s work (Zhou, Shi, Zhang, Su, & Jiang, 2014).

Suan Sunandha Science and Technology Journal
©2023 Faculty of Science and Technology, Suan Sunandha Rajabhat University

3. Results and Discussion

Raman spectra of the HfO_2 thin films with different sputtering power are investigated as shown in Figure 1. The Raman experimental result was compared with the calculation results from Zhou et al.'s work (Zhou et al., 2014). The results revealed that all films are in a monoclinic/ orthorhombic-I phase mixture. In the preparation with the sputtering power more than 100W, HfO_2 film structure is obviously the majority in Monoclinic phase (Wu et al., 2012). As the sputtering power increased, the amount of activated Ar+ ions per unit time raised. As a result, more target atoms with higher average kinetic energies were sputtered per unit of time. As a result, the deposition rate rises linearly with sputtering power. The extra energy will be transmitted to the substrate and released as heat since the density of the film cannot be indefinitely increased. When temperature during deposition in the chamber is higher, a partial transformation into the monoclinic phase occurs (Pathak et al., 2020).

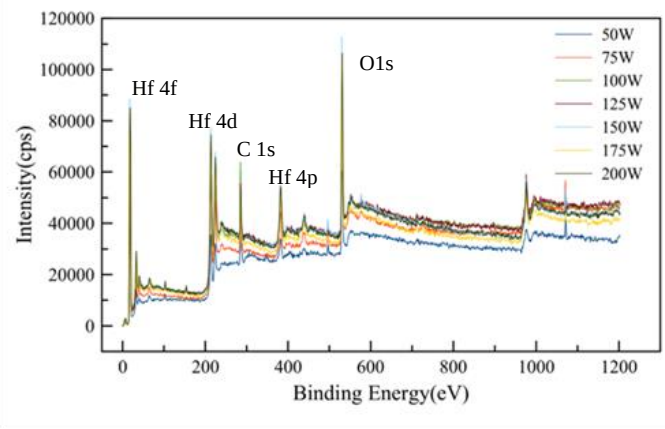

Figure 2. Survey XPS spectra of Hafnium oxide thin films prepared at different RF power.

XPS was utilized to examine the surface compositions of Hafnium oxide film samples. In Figure 2, the XPS survey spectra shows that Hf (4f, 4d, 4p), O and C are present on all films' surfaces. XPS typically has an analysis depth of less than 5 nanometers. There is no surface contamination observed in all samples within sensitivity of the instrument. The adsorption of atmospheric carbon on the surface is expected to be responsible for the presence of carbon. The high-resolution XPS spectra at Hf4f and O1s binding energy regions are shown in figures 3 and 4, respectively. The Hf 4f 7/2 and Hf 4f 5/2 peaks of all films were observed at binding energies of about 16.6 and 18.4 eV, respectively, confirming the formation of HfO_2 on the surfaces (Lin & Liao, 2013; Luo et al., 2018). The O1 s peaks of all films were deconvoluted into two peaks at the binding energies of 530.3 and 532.0 eV which are associated with the Hf–O bond of O–Hf–O and the O–O bond of non-lattice oxygen, which was made possible by the suboxides with Hf, respectively. The large proportion of the non-lattice oxygen peak in the O 1s spectra indicates that the HfO_2 film layer surface contained more defects (Biswas et al., 2016; Luo et al., 2018; Perevalov, Aliev, Gritsenko, Saraev, & Kaichev, 2013). The XPS result in figure 4 shows that the intensity of non-lattice oxygen peak decreased with increasing sputtering power. Therefore, it is noted that the HfO_2 films with low RF power have more defects.

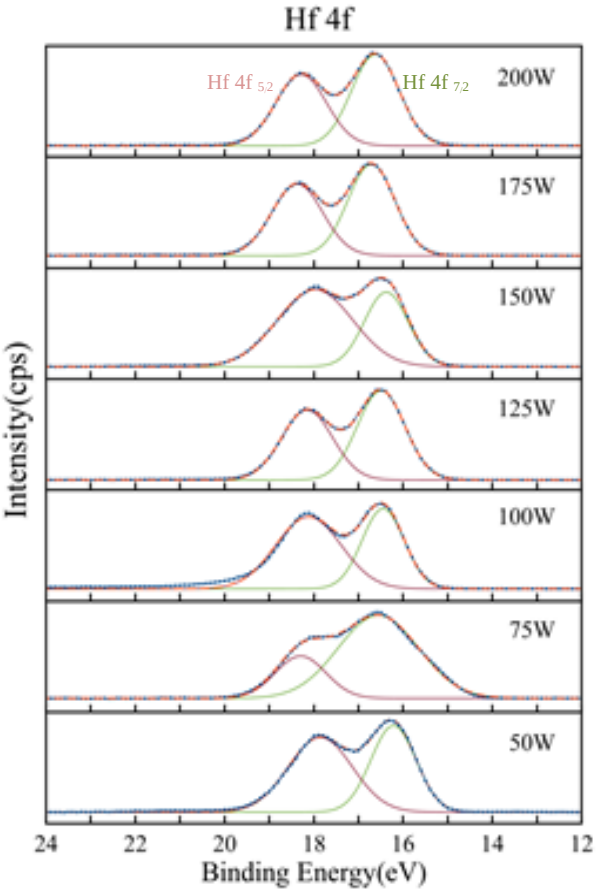

Figure 3. Hf 4f XPS spectra of the Hafnium oxide films prepared at various power.

The normalized Hf L3-edge XANES spectra of the Hafnium oxide films prepared at different power are shown in Figure 5. The benefit of XANES is that it is sensitive to the local environment surrounding the probing atoms and can therefore be used to determine the chemical composition and oxidation states of the probing atoms. It is evident from Figure 5, XANES spectra of all samples reveal similar features and identical energy position of Hf L3-edge.

Suan Sunandha Science and Technology Journal
©2023 Faculty of Science and Technology, Suan Sunandha Rajabhat University

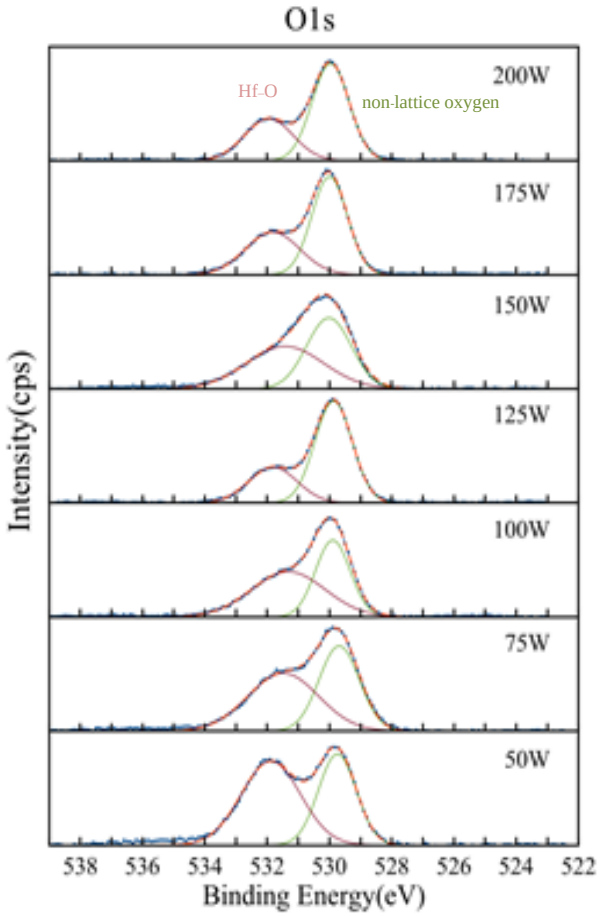

Figure 4. O1s XPS spectra of the Hafnium oxide films prepared at various powers.

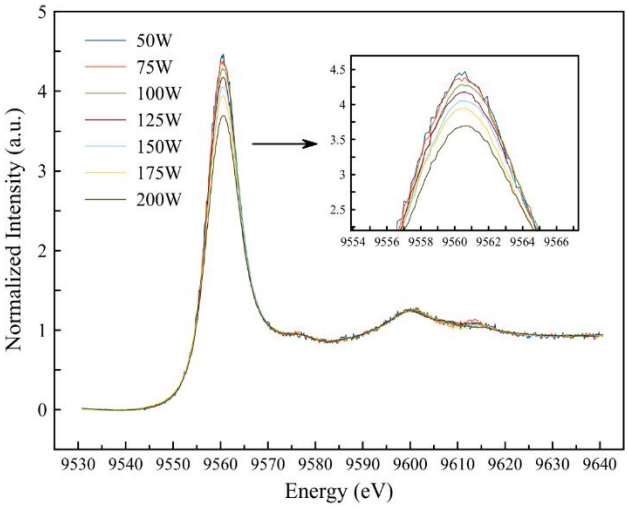

Figure 5. The normalized Hf L3-edge XANES spectra of the Hafnium oxide films are prepared at various powers.

The edge energy of Hf L3-edge was found at 6559.05eV. Additionally, the position of the absorption edge in all samples is similar to that of the HfO_2 standard, indicating that the valence state of Hf in Hf -O clusters is +4. The highest peaks at 9560 eV relate to the Hf 2p3/2 →5d transition and features above 9570 eV are due to the transition to the 6sd continuum (Botti et al., 2020; Cho, Jung, & Hwang, 2010). A significant decrease in intensity of the white line feature reflects the decrease of oxygen vacancy contents. Additionally, this XANES result is in good agreement with the previous XPS results.

4. Conclusion

Hafnium oxide thin films synthesized at different RF power by RF magnetron sputtering are in a monoclinic/ orthorhombic-I phase mixture. The majority Monoclinic structure was obtained in all samples which were confirmed by Raman and XANES results. XPS and Hf L3-edge XANES techniques were investigated, and they show well agreement with the same oxidation state of HfO_2. The samples prepared at greater power tend to have lower oxygen vacancy.

Acknowledgement

The authors would like to thank the Synchrotron Light Research Institute (Public Organization) (BL5.2), Thailand for their provision of the XAS measurement and laboratory facilities**.**

References

Ali, F., Zhou, D., Ali, M., Ali, H. W., Daaim, M., Khan, S., … Sun, N. (2020). Recent progress on energy-related applications of HfO_2-based ferroelectric and antiferroelectric materials. *ACS Applied Electronic Materials*, *2*(8), 2301-2317. doi:10.1021/acsaelm.0c00304

Aygun, G., & Yildiz, I. (2009). Interfacial and structural properties of sputtered HfO_2 layers. *Journal of Applied Physics*, *106*(1), 014312. doi:10.1063/1.3153953

Biswas, D., Sinha, A. K., & Chakraborty, S. (2016). Effects of oxygen partial pressure and annealing temperature on the residual stress of hafnium oxide thin-films on silicon using synchrotron-based grazing incidence X-ray diffraction. *Applied Surface Science*, *384*, 376-379. doi:10.1016/j.apsusc.2016.05.015

Suan Sunandha Science and Technology Journal
©2023 Faculty of Science and Technology, Suan Sunandha Rajabhat University

Böscke, T. S., Müller, J., Bräuhaus, D., Schröder, U., & Böttger, U. (2011). Ferroelectricity in hafnium oxide thin films. *Applied Physics Letters*, *99*(10), 102903. doi:10.1063/1.3634052

Botti, L., Kondrat, S. A., Navar, R., Padovan, D., Martinez-Espin, J. S., Meier, S., & Hammond, C. (2020). Solvent-activated hafnium-containing zeolites enable selective and continuous glucose–fructose isomerisation. *Angewandte Chemie*, *132*(45), 20192-20198. doi:10.1002/ange.202006718

Cantas, A., Aygun, G., & Basa, D. K. (2014). *In-situ* spectroscopic ellipsometry and structural study of HfO_2 thin films deposited by radio frequency magnetron sputtering. *Journal of Applied Physics*, *116*(8), 083517. doi:10.1063/1.4893708

Cho, D. Y., Jung, H. S., & Hwang, C. S. (2010). Structural properties and electronic structure of HfO_2-ZrO_2 composite films. *Physical Review B*, *82*(9). doi:10.1103/physrevb.82.094104

Gangqiang, Z., Sanqi, T., & Tingting, T. (2013). Electronic structure and optical properties of monoclinic HfO_2 with oxygen vacancy. *Rare Metal Materials and Engineering*, *42*(8), 1576-1580. doi:10.1016/s1875-5372(13)60093-4

Gao, J., He, G., Deng, B., Xiao, D. Q., Liu, M., Jin, P., … Sun, Z. Q. (2016). Microstructure, wettability, optical and electrical properties of HfO_2 thin films: Effect of oxygen partial pressure. *Journal of Alloys and Compounds*, *662*, 339-347. doi:10.1016/j.jallcom.2015.12.080

Kukli, K., Ritala, M., Sundqvist, J., Aarik, J., Lu, J., Sajavaara, T., … Hårsta, A. (2002). Properties of hafnium oxide films grown by atomic layer deposition from hafnium tetraiodide and oxygen. *Journal of Applied Physics*, *92*(10), 5698-5703. doi:10.1063/1.1515107

Lin, S. S., & Liao, C. S. (2013). The hydrophobicity and optical properties of the HfO_2-deposited glass. *Ceramics International*, *39*(1), 353-358. doi:10.1016/j.ceramint.2012.06.033

Luo, J. D., Zhang, H. X., Wang, Z. Y., Gu, S. S., Yeh, Y. T., Chung, H. T, … Cheng, H. C. (2019). Improvement of ferroelectric properties in undoped hafnium oxide thin films using thermal atomic layer deposition. *Japanese Journal of Applied Physics*, *58*. doi:10.7567/1347-4065/ab0ded

Luo, X., Li, Y., Yang, H., Liang, Y., He, K., Sun, W., … Feng, Z. (2018). Investigation of HfO_2 thin films on Si by X-ray photoelectron spectroscopy, Rutherford backscattering, grazing incidence X-ray diffraction and variable angle spectroscopic ellipsometry. *Crystals*, *8*(6), 248. doi:10.3390/cryst8060248

Park, P. K., & Kang, S. W. (2006). Enhancement of dielectric constant in HfO_2 thin films by the addition of Al_2O_3. *Applied Physics Letters*, *89*(19), 192905. doi:10.1063/1.2387126

Pathak, S., Das, P., Das, T., Mandal, G., Joseph, B., Sahu, M., … Siruguri, V. (2020). Crystal structure of monoclinic hafnia (HfO_2) revisited with synchrotron X-ray, neutron diffraction and first-principles calculations. *Acta Crystallographica Section C: Structural Chemistry*, *76*(11), 1034-1042. doi:10.1107/s2053229620013960

Perevalov, T. V., Aliev, V. Sh., Gritsenko, V. A., Saraev, A. A., & Kaichev, V. V. (2013). Electronic structure of oxygen vacancies in hafnium oxide. *Microelectronic Engineering*, *109*, 21-23. doi:10.1016/j.mee.2013.03.005

Wu, R., Zhou, B., Li, Q., Jiang, Z., Wang, W., Ma, W., & Zhang, X. (2012). Elastic and vibrational properties of monoclinic HfO_2 from first-principles study. *Journal of Physics D: Applied Physics*, *45*(12), 125304. doi:10.1088/0022-3727/45/12/125304

Xiong, K., Robertson, J., Gibson, M. C., & Clark, S. J. (2005). Defect energy levels in HfO_2 high-dielectric-constant gate oxide. *Applied Physics Letters*, *87*(18), 183505. doi:10.1063/1.2119425

Zhou, B., Shi, H., Zhang, X. D., Su, Q., & Jiang, Z. Y. (2014). The simulated vibrational spectra of HfO_2 polymorphs. *Journal of Physics D: Applied Physics*, *47*(11), 115502. doi:10.1088/0022-3727/47/11/115502

Available online at https://li02.tci-thaijo.org/index.php/ssstj

Suan Sunandha Science and Technology Journal
©2023 Faculty of Science and Technology, Suan Sunandha Rajabhat University

The System Recognizes the Digital Image of Pistol Shell Casings by Developing Algorithms Combined with Deep Learning

Aree Jivorarak[1*], Kittikhun Meethongjan[2], Narong Kunides[1],

[1]Department of Forensic Science, Graduate School, Suan Sunandha Rajabhat University, U-thong Nok Road, Dusit, Bangkok 10300, Thailand
[2]Faculty of Science and Technology, Suan Sunandha Rajabhat University, U-thong Nok Road, Dusit, Bangkok 10300, Thailand
***Corresponding author e-mail:** Aree.khlong3@gmail.com

Received: *4 August 2022* / **Revised:** *28 February 2023* / **Accepted:** *14 May 2023*

Abstract

Gun-related violence in Thailand is in a high rate. Resume reports showed that most of them caused by gun-shooting. Thus, Firearms and bullets are important evidence in the judicial process to link the events and the perpetrators. Therefore, the aim of this study was to present the system recognizes the digital image of pistol shell casings by developing algorithms combined with deep learning. The objectives of this forensic study were to 1) analyze, design, and develop a Pistol Identification System (PIS) based on breech face marks of cartridge case digital images, and 2) achieve a guideline or an alternative method for facilitating an expert to investigate firearms linked to the offender. In this research the PIS that was designed with programming language applied to develop algorithms for identification of the breech face marks of cartridge case digital images. In addition to that, MATLAB's tools were applied in the deep learning process to achieve the final PIS model. The steps of deep learning technique were composed of designing a training and repeat the experiments over multiple cycles (Epoch) for the purpose of confirming, test and adjust the proportions of the hidden layers until reaching the ratio of 80:10:10 and accomplishing a satisfied averaged accuracy rate. The PIS model was subsequently used for comparison and predict the image pair through database management technology. Materials used in this study were composed of 50,000 images of rear plates of .38 Cartridge case, Camera, Mobile Phone, Computer, MATLAB language and Microsoft Access software. The findings showed that the PIS developed is of satisfactory accuracy capable of accurately matching the pairs of images stored in the database and could also be traced back to the gun used at the scene and gun owners. The results of this study would apply as the alternative or guideline to PIS and even would help forensic practitioners to cross-checking and investigating firearms in relation to the offender.

Keywords: Pistol, Shelling gun, Breech Face Digital Image, Image of pistol shell casings

1. Introduction

Investigations are carried out until the perpetrators are arrested and punished in accordance with the legal procedure. It is an extremely important task for law enforcement. This task requires the knowledge and competence of experts in the field of forensic work. The use of science and technology tools combined with forensics is essential to facilitate the accurate, accurate and timely work of experts. It affects the acceptance of stakeholders. And it can bring the wrong people to punishment. Forensic science is therefore useful to conclude the case based on the evidence correctly. From the above points. Police Forensic Science Center7 (2015) therefore discusses the scope of applying forensic science in general, such as (1) crime scene investigations and forensics, (2) fingerprinting, palmprint, footprint, (3) documents such as signatures, handwriting, (4) forensic ballistics, (5) forensic chemistry, such as the chemical composition of a variety of substances, (6) forensic physics, such as

Suan Sunandha Science and Technology Journal
©2023 Faculty of Science and Technology, Suan Sunandha Rajabhat University

vehicle collision detection, (7) biological trace evidence such as hair, blood, sperm (8) forensic medicine, including forensic pathology, forensics, biochemistry, personal proof, medical imaging.

In Thailand, there is evidence of firearms, with relevant research such as “Breech Face Digital Images Recognition System” by developing an algorithm for identifying the identity of the digital trace image of the end plate of the shell casing to be used to in-depth the prediction of the image of the end plate of the shell casing. The results from the dual image predictions are quite accurate (Jivorarak, Meethongjan, & Kunides, 2021). “Firearm Identification System based on Bullet Image Analysis”. It is a firearms verification system based on bullet head images. Find attribute values based on derived lines. To analyze the surface characteristics of an image in two different ways: two-dimensional spectrum and GLCM. Then compare the results to find an appropriate method. The results from the dual image predictions are quite accurate (Thammavarin, 2013). “Firearm identification based on fir system characterizing rotation invariant features of cartridge case image” This research proposes a method for examining firearms based on a limited impulse response system that shows unchanged properties based on the rotation of the shell casing image. The vehicle inspects firearms using Fisher's linear classification function. The effectiveness of the proposed method can be demonstrated by the results of experiments with verification of firearms from sample casings on crimes committed with firearms (Prasit, 2010). February 22, 2016. The Elite+ (2016) indicates a population ratio of 100,000, the country with the highest gun-related deaths is the Philippines (7.42). Thailand (4.45) is higher than the United States (3.85), and the Asian Correspondent website (2016) recently reported that Thailand also has a high record of firearms crimes. Most motives are identified as "faceless" or "business conflicts."

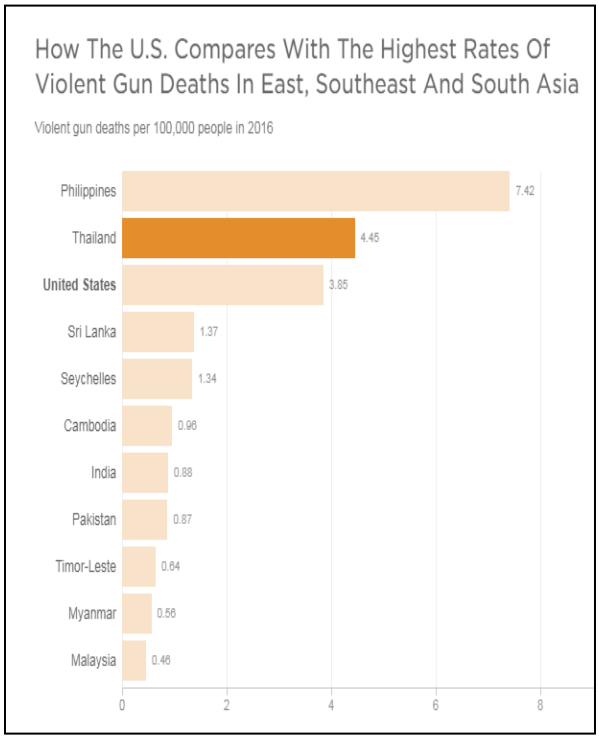

Figure 1. Statistics on firearm deaths in 2016 in Asia and the United States of America per 100,000 population (NPR, 2016).

According to the study, life-threatening mischief Property and peace of the people of Thailand Some of the perpetrators were found to have used firearms in the attack, as evidenced by statistics from the Royal Thai Police between 2005 and 2015. The Royal Thai Police More and more firearms can be arrested. At present, there is evidence related to cases used in forensic science, such as firearms information, cartridge cases, information about gun owners, etc. Forensic examination of witnesses is generally based on the eyes and the individual. This leaves them vulnerable to deviations and impacts the investigative process to find the culprit. Practical procedures should enable experts to identify connections automatically. “the system recognizes the digital image of pistol shell casings by

Suan Sunandha Science and Technology Journal
©2023 Faculty of Science and Technology, Suan Sunandha Rajabhat University

developing algorithms combined with deep learning". That could be an option for facilitating specialists.

Table 1. Statistics on firearm arrests 2005 to 2015.

Year	Catch/Case		Catch/Person	
	Firearms	Weapon of war	Firearms	Weapon of war
2005	17,777	1,242	18,924	1,182
2006	18,701	1,455	19,535	1,411
2007	21,023	1,049	21,846	1,161
2008	22,169	773	23,190	882
2009	25,087	855	25,798	900
2010	21,463	699	22,214	759
2011	23,941	546	25,740	667
2012	28,134	605	30,257	796
2013	34,895	620	37,015	815
2014	35,280	713	37,554	931
2015	31,232	570	33,420	755

Source: National Statistical Office (2016).

2. Research Methodology

In this research, the researchers researched and compiled academic papers containing the contents of the pistol verification system from digital trace photographs of the end of the shell casings to be framed. Designs and applications in research. consist of theoretical concepts connected with projectiles. Bullets, shell casings Traces formed on the end plate of the shell casing. Bullet Comparison Machine and automatic shell casings, database theory, digital images, digital image processing with MATLAB languages, converting image data in two dimensions, Scrolling of images, artificial intelligence, machine learning, neural network with MATLAB language, deep learning, related research, and the conceptual framework of research. Then create a database and store the data, firearm information, shell casing information, and gun owner information. Then find the identity of each image using an algorithm developed using language MATLAB to pass on to the system for in-depth learning. This research used 50,000 learning samples, there was a rotating image, each of which was added to noise, 80% samples were used in training, 10% in validation and 10% in testing and 50 Hidden had complex calculations for highly performing work, image classification. It can predict visual pairs by providing a higher level of accuracy, so deep learning algorithms are required to work.

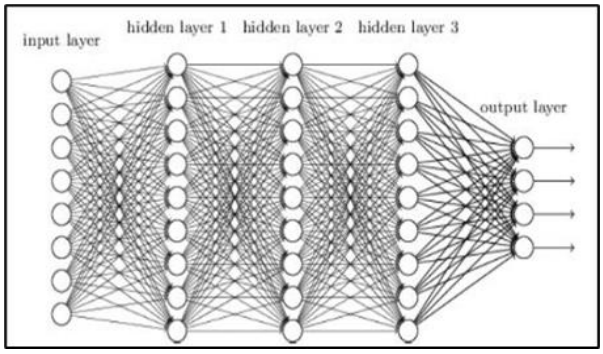

Figure 2. Training deep neural networks (Towards Data Science, 2018).

3. Research Framework

Based on the conceptual framework, it can be described as Firing pin marks and Breech Marks. It can be used through an algorithm to determine the uniqueness of the bullet casing footplate image, which includes the area of the explosion from the slate needle, the length of the circumference, the width and length of the image where the explosion occurred. The widest length of the image that exploded. The average sum of RGB colors in the middle, store it in the database, and then go through an in-depth learning process to get a model for predicting a pair of images, then goes through a deep learning process to obtain a model for predicting an image pair. Incidentally, in this modeling, the researchers selected the goal is to use the area of the explosion from the slate needle, and the prediction through the model uses predictive results in combination with firearm data and firearm owner data stored in the database to identify the gun registration used to shoot, which can be linked to the offender. The tool consists of 50,000 images of the end plate of the shell casing, camera, Compute, Use MATLAB to develop the system by connecting to the database

Suan Sunandha Science and Technology Journal
©2023 Faculty of Science and Technology, Suan Sunandha Rajabhat University

management system. This research was experimental research.

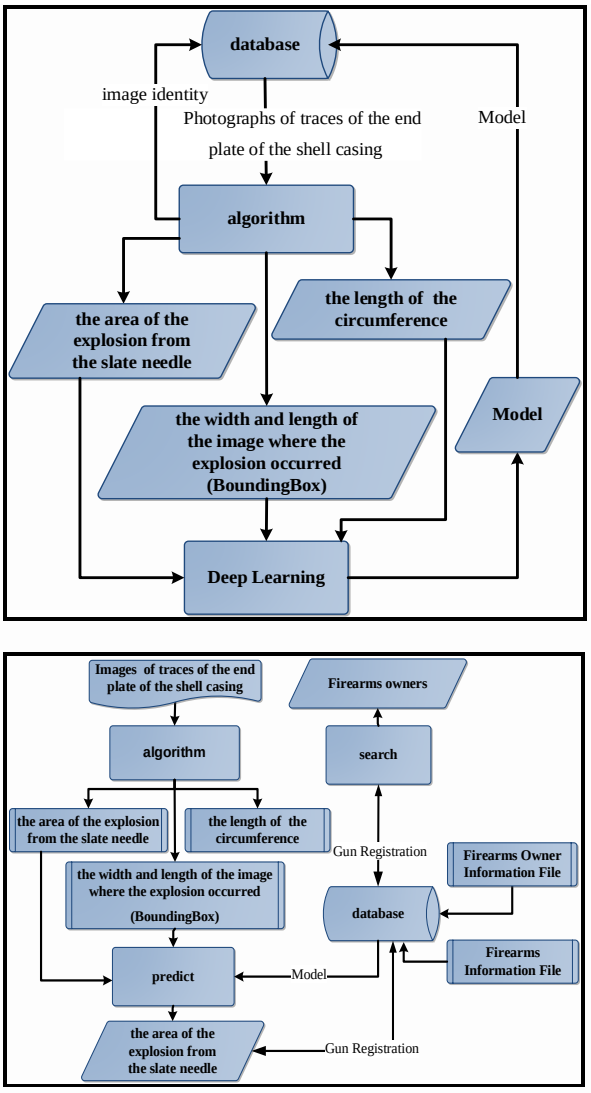

Figure 3. Research framework.

4. Research Result

Development The system recognizes the digital image of pistol shell casings by developing algorithms combined with deep learning. it uses algorithms to identify images in combination with deep learning to predict digital images in a database using database management technology. These operations may be broken down into 4 processes. (1) Image DataSet for Deep Learning (2) Identity from the images (3) Deep Learning and Training (4) Use model to predict pairs of digital images.

4.1 Image DataSet for Deep Learning

The database contains information about firearms, shell casings and gun owners. When capturing firearm information, the system verifies if it is a digital image of the cartridge case. Otherwise, you will be warned that this is not a digital image, and this research will include 400 digital cartridge case images.

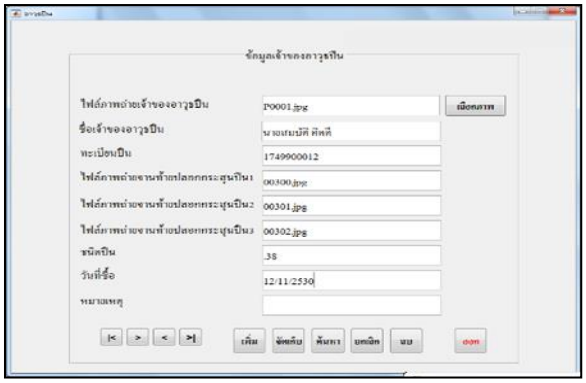

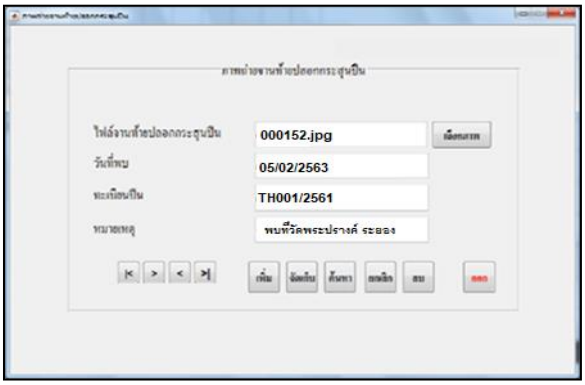

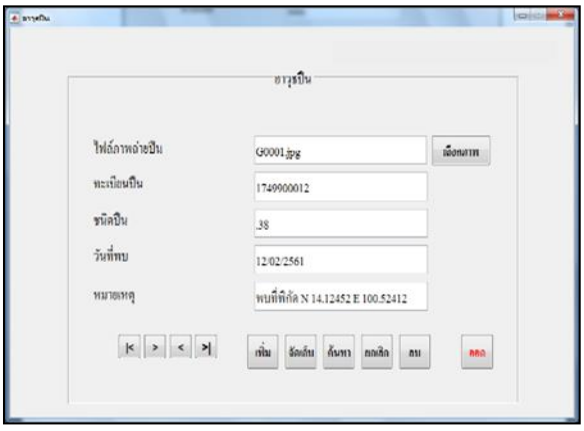

Suan Sunandha Science and Technology Journal
©2023 Faculty of Science and Technology, Suan Sunandha Rajabhat University

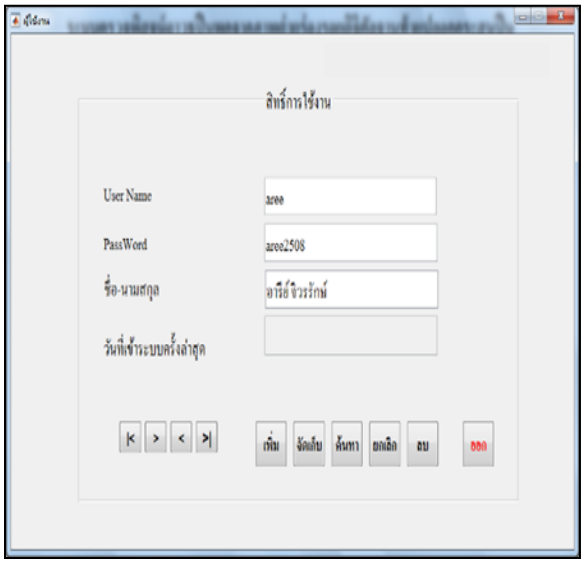

Figure 4. Record form.

Figure 5. Breech Face Digital Image store in database.

4.2 Identity from the image

We can retrieve the images from the Breech Face Digital Image, the casing stored all over the database. To find out the uniqueness of the images through the algorithm that sets it up. With a total of 400 frames, and divide the image density into 5 groups to get a coefficient to equalize the brightness of each image. Composed of 1) fewer than 700 pixels, 2) 701 to 1500 pixels, 3) 1501 to 1900 pixels, 4) 1901 to 2700 pixels, and 5) more than 2701 pixels, then turn at 0, 15, 30, 45 and 60 degrees. Every single degree turn will put types of Gaussians, Salt & Pepper, and Speckle noise. Every noise has a density of 4%, 6%, 8%, 10%, 12%, 14% and 16%. This resulted in a total of 50,000 sample images.

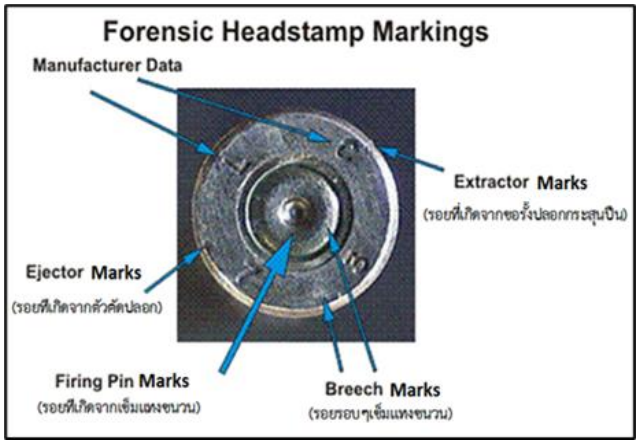

Figure 6. The trace on Breech face (Jivorarak, Meethongjan, & Kunides, 2021).

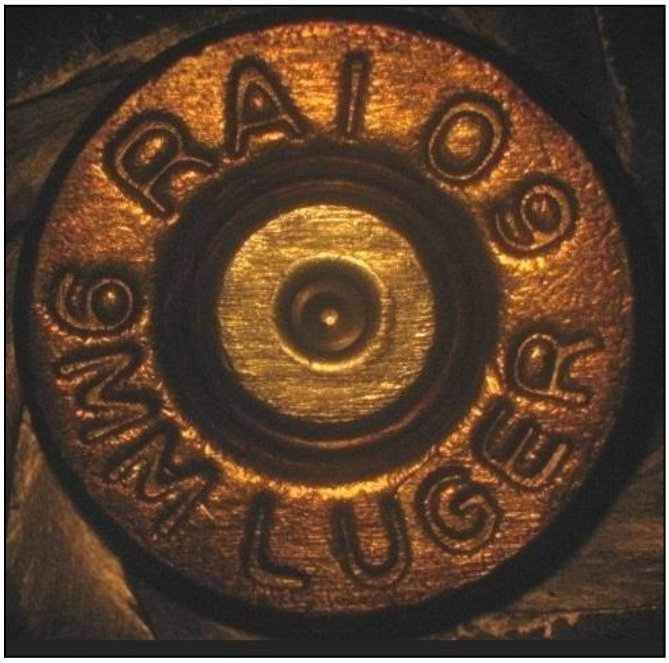

Figure 7. The rows of breech face.

Suan Sunandha Science and Technology Journal
©2023 Faculty of Science and Technology, Suan Sunandha Rajabhat University

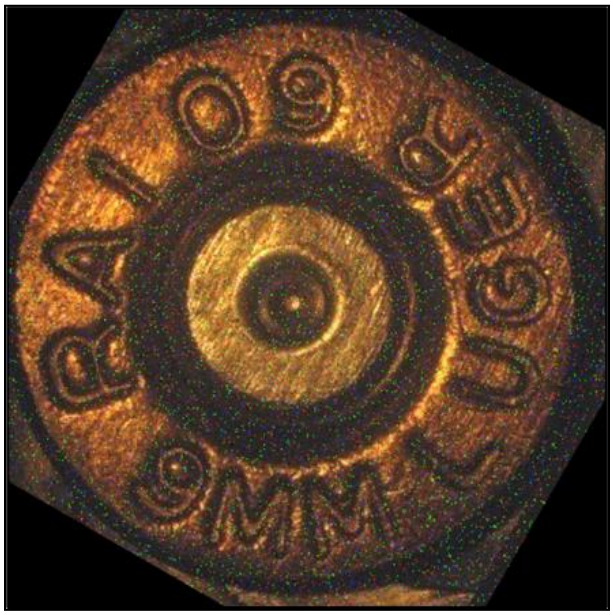

Figure 8. The Breech face after adding noise.

Next, bring 50,000 digital images are processed through algorithms developed with the following processes:

(1) Eliminate noise.
(2) Adjust the images to be parallel with the make from explosion to the line of sight.

Figure 9. Adjust the images parallel to the line of sight.

(3) Adjust the image brightness more accurately.

Figure 10. Adjust the images brightness.

(4) Select the outermost circle and resize the image to 1000*1000.

Figure 11. Resize the image to 1000*1000.

Suan Sunandha Science and Technology Journal
©2023 Faculty of Science and Technology, Suan Sunandha Rajabhat University

(5) Copy the frame of the circle to the bottom of the deepest front.

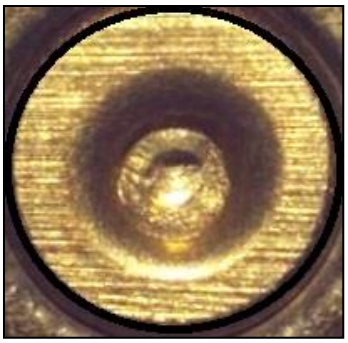

Figure 12: The circle in the breech face part.

(6) Resize image at 600*600 for make horizon line clearer.

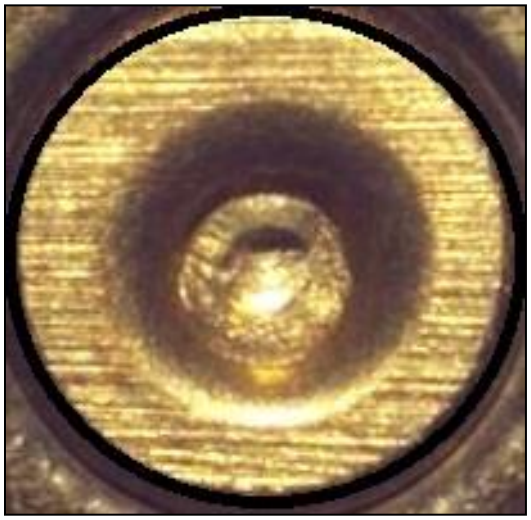

Figure 13. Resize image to 600*600.

(7) Converts the image to grey scale and next to it converts to binary.

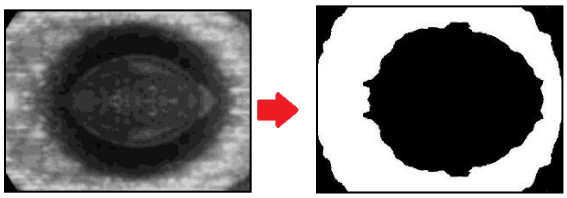

Figure 14. Converts the image to grey scale and binary.

(8) Find the edge and cut the edge. to make a smooth image.

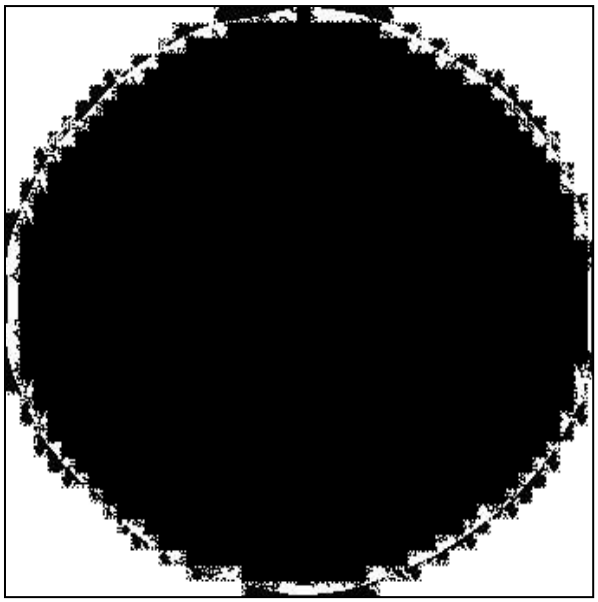

Figure 15. Smooth image.

(9) Select the useful part for Deep learning considers from image at the white area.

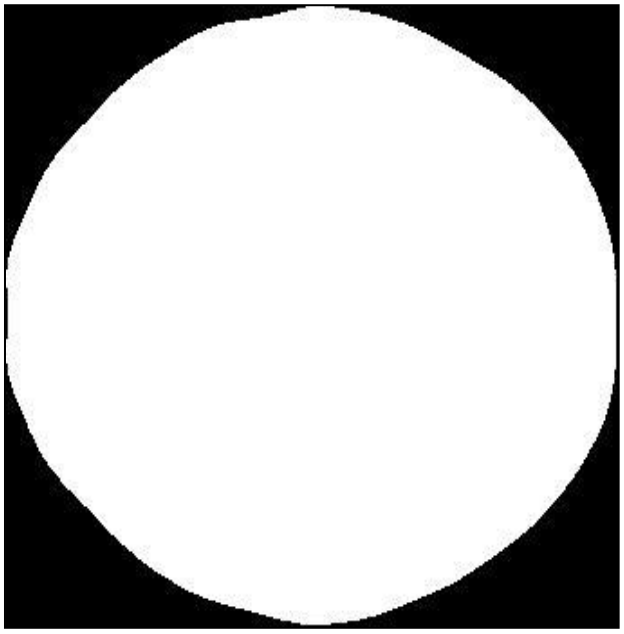

Suan Sunandha Science and Technology Journal
©2023 Faculty of Science and Technology, Suan Sunandha Rajabhat University

Figure 16. White area for use.

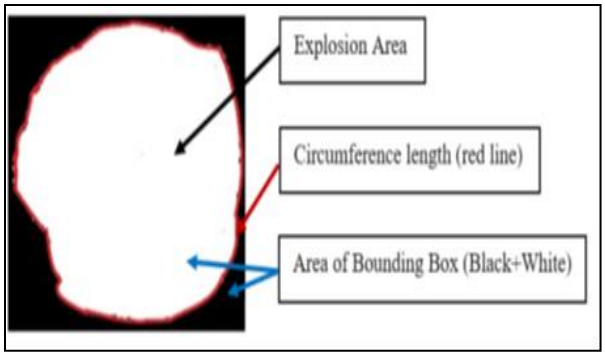

Figure 17. Visual identity applied in deep learning (Jivorarak, Meethongjan, & Kunides, 2021).

The result of identity from the image is the final result according to Figure 17, which is caused by the algorithm for finding the identity of the image. The values are given in Table 2 below.

Table 2. Values brought to training.

No	inputs				target	
	Breech Face Digital Images Files name	Explosion Area x1	Bounding Area Box x2	Circumference length x3	Explosion Area y	Breech Face Digital Images Files name
62552	00100.jpg	63177	79424	126549.433838339	63649.2751510352	00100.jpg
62553	00100-00-1500.jpg	63915	81885	127870.889600899	63984.7254361182	00100.jpg
62554	00100-00-3000.jpg	63965	85995	127959.581371709	63444.5591499887	00100.jpg
62555	00100-00-4500.jpg	69743	91808	139651.56744847	68690.2864799438	00100.jpg
62556	00100-00-6000.jpg	70716	92168	143018.153973714	69662.3672496156	00100.jpg
62557	00100-02-00GS.jpg	63735	82890	127657.887574393	64270.1123138947	00100.jpg
62567	00100-02-00SK.jpg	62182	81204	124520.760406539	63275.096404429	00100.jpg
62562	00100-02-00SP.jpg	63136	79424	126461.106383412	63621.9291345107	00100.jpg
62558	00100-02-15GS.jpg	64225	82415	128479.796339058	64094.8071149126	00100.jpg
62568	00100-02-15SK.jpg	64056	81312	128172.827283629	64111.6034082868	00100.jpg
62563	00100-02-15SP.jpg	64153	82194	128337.944787862	64075.7127226602	00100.jpg
62559	00100-02-30GS.jpg	64073	86858	128188.479152536	63552.961581814	00100.jpg
62569	00100-02-30SK.jpg	80140	104000	160547.555699195	78194.3571414797	00100.jpg
62564	00100-02-30SP.jpg	64368	87216	128782.968111858	63852.000418887	00100.jpg
62560	00100-02-45GS.jpg	69245	90890	138610.417350567	67847.4678855583	00100.jpg
62570	00100-02-45SK.jpg	78749	105168	157882.476211692	78611.1384213362	00100.jpg
62565	00100-02-45SP.jpg	68505	90298	137092.250722377	67225.1622967927	00100.jpg
62561	00100-02-60GS.jpg	71970	94572	145264.135760825	71321.9029902245	00100.jpg
62571	00100-02-60SK.jpg	71698	94004	144407.581257222	70973.5366646101	00100.jpg
62566	00100-02-60SP.jpg	70851	92730	143397.302423617	69957.5869996921	00100.jpg
...	...	...	...	...	...	...
50000	00400-02-60SP.jpg	85410	108360	170871.672547422	74758.7142452141	00400.jpg

4.3 Deep Learning and Training

Deep Learning is an automated learning method with Imitate the function of human neurons by stacking neural networks in layers and learning sample data, which will be used to detect patterns or classify the data (MathWorks, 2022). In this investigation, the data in Table 2 were extracted by choose all three identities (Explosion Area, Bounding Area Box and Circumference Area), including the explosive zone, The selected Explosion Area values are inputs (x1), boundingbox area (x2) and circumference length (x3), while target uses explosive area (y), which is unique to the calculated image, according to Table 2 using MATLAB tools. In this learning, using data for 40,000 training samples, 5,000 validation samples, 5,000 test samples and 100 hidden layers, the learning period is 50.28 minutes. The system switches off at 2000 Epoch. Mean Squares (Training = 10073000.52154, Validation = 0.00000e-0 and Testing = 97223543.32146e-0) Regression (Training = 8.32145e-1, Validation = 0.00000e-0 and Testing = 8.12321e-1) Performance = 1.12e+08 Gradient = 7.51e+06. The resulting recognition accuracy was 95%.

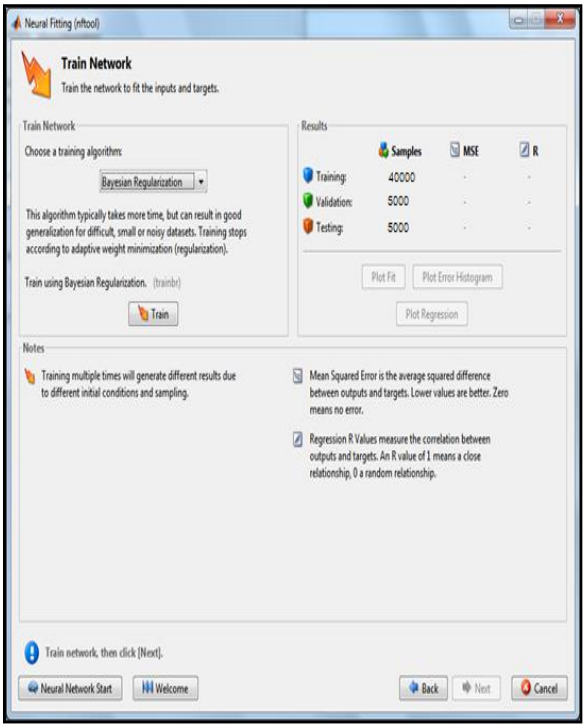

Figure 18. Ratio of data for learning (MATLAB tools).

4.4 Use model to predict pairs of digital images

The formula is as follows:

target = results.net ([inputs1; inputs2; inputs 3])

x1 = inputs1.

x2 = inputs2.

x3 = inputs3.

When input (x 1, x 2, x3) is taken through a model, the target value results are compared in the

Suan Sunandha Science and Technology Journal
©2023 Faculty of Science and Technology, Suan Sunandha Rajabhat University

database. The system will display the results as shown below.

Figure 19. The result of using a model to predict a pair of images.

5. Discussion

This research is an alternative to facilitating experts to gather evidence and prove evidence. The objectives are 1) analyze, design, and develop a Pistol Identification System based on breech face marks of cartridge case digital images, and 2) achieve a guideline or an alternative method for facilitating an expert to investigate firearms linked to the offender. The research hypothesis is that digital trace photographs on the end plate of ammunition casings, firearm data, and data Firearm owners can link/compare gun identities and can link to identify firearm owners. By development the algorithm finds the uniqueness of the bullet casing end plate image, combined with deep learning. It started by developing an algorithm from the MATLAB language to store the end plate of the shell casing, Firearms information, and firearm owner information, along with other parts, are stored in the database. Then take 400 bullet casing end plate data to turn at 0, 15, 30, 45 and 60 degrees. Every single degree turn will put types of Gaussians, Salt & Pepper, and Speckle noise. Every noise has a density of 4%, 6%, 8%, 10%, 12%, 14% and 16%. This resulted in a total of 50,000 sample images. Then take each image to find its identity here, select Explosive Area, boundingbox area and circumference length. The target is compared to the same pair to obtain the gun registration number, which must be related to the gun owner. The results of the research showed that: "The system recognizes the digital image of pistol shell casings by developing algorithms combined with deep learning" developed with high accuracy of more than 95%. This is consistent with the research hypothesis that digital trace images on the surface of the end plate of the shell casing, firearm data, and firearm owner information. It can be related or compared to the identification of firearms and can identify firearms owners. This is because the traces on the end plate of the climbing shell casing can be used to find the uniqueness of each image. Here, deep learning algorithms are used together with database management technology. In fact, the researchers studied and collected firearms, casings and related theories. In addition to the theoretical storage of the data correctly. As for the development of the system researcher developed detailed algorithms such as: while recording the ammunition casing end plate data, the system locks and warns if the data entered into the system is not an image of the end plate of the shell casing. Algorithms in the Identity From the image These include: Eliminate Noise, Adjust the images to be parallel with the make from explosion to the line of sight, Adjust the image brightness more accurately, Select the outermost circle and resize the image to 1000*1000, Copy the frame of the circle to the bottom of the deepest front, Resize image at 600*600 for make horizon line clearer, Converts the image to grey scale and next to it converts to binary, Find the edge and cut the edge, to make a smooth image, and Select the useful part for Deep learning considers from image at the white area. These findings are consistent with the research of Jivorarak, Meethongjan, and Kunides (2021), was found that the traces on the plates at the end of the climbing shell casings can be used to find the uniqueness of each image. This research can be used as an alternative to proof of firearms. Consistent with Boonmatham, Kaewkosol, and Thongthae (2016) mentioned about implementing information systems, Computer networks, and Internet communication to provide the opportunity. As a result, the information system is essential and necessary for the organization's or other units' functioning. Predicting a pair of images was presented with many processes and methods which can be developed by many algorithms of digital images (Hongboonmee & Jantawong, 2020). Deep learning,

Suan Sunandha Science and Technology Journal
©2023 Faculty of Science and Technology, Suan Sunandha Rajabhat University

Wu, Liu, Li, Jin, and Li (2017) is a set of instructions made for computer learning. set of instructions allows the machine to process large amounts of data that it seeks to learn how to replace it efficiently. Beside that Tongkla (1999) says that "sometimes light conditions and natural weather are conducive to the photograph Photography instruction cannot be completely stomped if there are obstacles such as rain, cloudiness, low light and too much light. The location and timing of the shoot are blatantly based on the lighting conditions at different times of the day". Recommendations The relevant sectors should promote and plan. Develop judicial evidence that complies with international standards. Acceptance of technology, lessons learned from successful countries in forensic evidence with state-of-the-art technology, and knowledge. In addition, there is currently a shortage of experts in this field, so it is proposed to develop both research and personnel who will apply this research in parallel by supporting the budget to expand the training and research institute for police forensics. Relevant agencies to cover all areas with the tools and equipment necessary to prove the evidence completely.

Acknowledgement

This study was successful because the researchers were very kind to the Assistant Professor Dr. Kittikhun Meethongjan Chairman of the Thesis Advisory Committee and Head of Department of Applied Sciences, Faculty of Science, Suan Sunandha Rajabhat University and Associate Professor police lieutenant general Dr. Narong Kulnides Member of the Thesis Advisory Committee Chair of The Doctor of Philosophy Program, Department of Forensic Science, Graduate School, Suan Sunandha Rajabhat University, who kindly gives advice, counseling and correcting various defects with great care. In addition, the researchers are aware of the sincerity and dedication of all the faculty members and would like to thank them very much. Also, thank you. police major general Dr. Chuchat Choksathaporn, former commander of Forensic Center 7 and subordinate. Photographs of shell casing end plates, which are data from research studies.

References

Asian Correspondent. (2016). *Baffling statistics fail to hide Thailand's worrying gun crime problem.* Retrieved from https://asiancorrespondent.com/2016/02/thailand-gun-crime/

Boonmatham, S., Kaewkosol, J., & Thongthae, A. (2016). *Development of a management information system of research database of the Faculty of Information Technology at Phetchaburi Rajabhat University*. Retrieved from http://it.rmu.ac.th/itm-journal/downloads/entry/65

Elite+. (2016). *Thailand has a higher rate of gun-related deaths than the us.* Retrieved from https://www.eliteplusmagazine.com/home/content/177/8#gsc.tab=0

Hongboonmee, N., & Jantawong, N. (2020). Apply of deep learning techniques to measure the sweetness level of watermelon via smartphone. *Journal of Information Science and Technology*, *10*(1), 59-69.

Jivorarak, A., Meethongjan, K., & Kunides, N. (2021). Breech face digital images recognition system. *Psychology and Education Journal*, *58*(5), 5422-5430.

MathWorks. (2022). *Deep learning in MATLAB*. Retrieved from https://www.mathworks.com/help/deeplearning/ug/deep-learning-in-matlab.html

National Statistical Office. (2016). *Crime and criminal offenses*. Retrieved from http://statbbi.nso.go.th/staticreport/page/sector/en/09.aspx

NPR. (2016). *The U.S. is a world leader in gun deaths*. Retrieved from http://www.npr.org/sections/goatsandsoda/2015/12/07/458815891/the-u-s-is-a-world-leader-in-gun-deaths

Police Forensic Science Center7. (2015). *Forensic knowledge.* Retrieved from http://scdc7.forensic.police.go.th/index.php/component/k2/itemlist/category/144-2015-11-28-14-41-32

Prasit, C. (2010). *Firearm identification based on FIR system characterizing rotation invariant features of cartridge case image* (Master's thesis). King

Suan Sunandha Science and Technology Journal
©2023 Faculty of Science and Technology, Suan Sunandha Rajabhat University

Mongkut's Institute of Technology Ladkrabang, Thailand.

Thammavarin, P. (2013). *Firearms verification system from a photograph of a gun bullet.* Retrieved from https://www.ryt9.com/s/prg/1651646

Tongkla, J. (1999). *Photography 1*. Phetchaburi, Thailand: Phetchaburi Rajabhat Institute.

Towards Data Science. (2018). *Training deep neural networks*. Retrieved from https://towardsdatascience. com/ training-deep-neural-networks-9fdb1964b964

Wu, Q., Liu Y., Li Q., Jin S., & Li F. (2017). The application of deep learning in computer vision. In *2017 Chinese Automation Congress (CAC)* (pp. 6522-6527). Jinan, China.

Available online at https://li02.tci-thaijo.org/index.php/ssstj

Suan Sunandha Science and Technology Journal
©2023 Faculty of Science and Technology, Suan Sunandha Rajabhat University

Assessment of Fermented Rice Straw as Nutritive Substances for Bio-based Plant Pot

Chadaporn Phrmkhot[1], Somwan Chumphongphan[1,2], Kitiphong Khongphinitbunjong[1,3], Sitthi Duangphet[1,2*]

[1]School of Science, Mae Fah Luang University, Tha Sut, Mueang, Chiang Rai 57100, Thailand.
[2]Center of Innovative Materials for Sustainability (iMatS), Mae Fah Luang University, Tha Sut, Mueang, Chiang Rai 57100, Thailand
[3]Microbial Products and Innovation research group (MP&i), Mae Fah Luang University, Tha Sut, Mueang, Chiang Rai 57100, Thailand
***Corresponding author e-mail: sitthi.dua@mfu.ac.th**

Received: *2 May 2023* / **Revised:** *20 July 2023* / **Accepted:** *27 July 2023*

Abstract

This research aims to develop bio-based nurseries or plant pots that contain soil nourishment from agricultural waste, namely rice straw. Tapioca starch glue as a binder was mixed with rice straw and then pressed by a hydraulic compression machine to form the sheet. To promote soil nourishment, the straw was fermented. The fermentations with and without enzyme assistance were compared as well as the fermentation time. The tensile strength of the specimens was assessed through a tensile test, revealing a surprising increase in strength with fermentation. The key distinction between the specimens with and without enzyme assistance was the time it took to reach the maximum value. Without the presence of enzyme, the specimens reached a maximum tensile strength of 0.67 MPa after 7 days of fermentation. For fermentation with enzyme assistance, this value increased to 0.81 MPa but required 14 days of fermentation to reach its maximum point. Not only the fermentation duration but also the inclusion of enzymes showed a slightly impact on water absorption and water swelling. Spectrophotometry was employed to analyze the value of phosphorus (P) and potassium (K), while the amount of nitrogen (N) was determined by the Kjeldahl method. As expected, soil nourishment can be promoted by fermentation and boosted by enzymes. The sheet from straw fermented with the enzyme at 21 days gives the highest soil nourishment, i.e., 17.90%w/w for total K_2O, 0.40%w/w for total P_2O_5, and 1.89%w/w for total N.

Keywords: Plant pot, Rice straw, Fermentation, Soil nourishment, Enzyme

1. Introduction

In modern agriculture and farming, plastic is the preferred material for plant pots and nursery pots due to its durability, accessibility, and affordability. However, once the seedlings are planted in the ground, these pots become waste that is challenging to decompose. Plastic takes over a century to break down, and it cannot be easily recycled due to its diminished strength and contamination. Consequently, these pots are usually disposed of through incineration or landfills, which contributes to pollution and exacerbates global warming. To address this issue, it is crucial to manufacture plant pots and nursery pots from natural materials instead of relying on plastic.

Biobased plant pots can be made using materials derived from renewable sources or obtained as by-products of productive activities like agriculture, animal husbandry, fishing, tannery, and others (Schettini et al., 2013). The main goal of these alternative pots is their ability to naturally decompose instead of adding to the waste in landfills. Several plant pots made from compressed fibers, which were mentioned earlier among other materials, have been extensively studied and are currently available for purchase in the market such as Cowpots (composted cow manure and natural fibre), Coirpot (coir fibres), and Fertilpots (wood fibre and peat) (Nambuthiri, Fulcher, Koeser, Geneve, & Niu, 2015).

Millions of tons of rice are grown annually in Thailand, with Chiang Rai having high rate of rice cultivation among northern provinces in 2018 (Office of Agricultural Economics, 2022). As a

Suan Sunandha Science and Technology Journal
©2023 Faculty of Science and Technology, Suan Sunandha Rajabhat University

result, utilizing rice straw, a natural byproduct of agriculture waste, to produce pots has emerged as an idea. Rice straw contains fibers that enhance the pot's strength (Sopunna, Pasom, Woradong, & Chaiwangrach, 2015), making it ideal for use. Additionally, these pots can be transferred to the soil without the need for removal, providing an appropriate planting time for seedlings. Furthermore, the pots eventually decompose into fertilizer, making them an environmentally friendly alternative. Some attempts have been made to create containers using rice straw, resulting in patents such as US7681359B2 (Van de Wetering & Athalage, 2010). The market has witnessed the introduction of a commercial product made from rice straw material, known as the StrawPot, developed by Ivy Acres. Numerous researchers have assessed the performance of these StrawPots and have found them to be decomposable, making them suitable substitutes for plastic pots (Conneway et al., 2015; Evans, Taylor, & Kuehny, 2010; Sun et al., 2015). Furthermore, they have demonstrated no adverse effects on plant establishment and the growth of plants after transplantation (Sun et al., 2015).

Rice straw, which is plentiful as an organic waste product, can be transformed into fertilizer via composting. Tiquia and Tam (2002) note that composting is an economical method for treating various organic waste types. The concept of making compost is the first idea for using effective microorganisms (EM) in environmental management. Crop residue and animal waste have been successfully composted to create organic fertilizers. Essentially, this solution containing microorganisms was created for the purpose of being used in natural or organic agricultural practices.

This study aims to develop nursery or plant pots from rice straw to be more useful by adding nutrients from the fermentation process. However, the effect of fermentation on pot quality must be evaluated. To resolve this doubt, a comparison of the effects of EM-assisted and non-EM-assisted fermentation was studied in this work.

2. Materials and Methods

2.1 Materials preparation

All the raw materials were provided from local areas in Phayao, Thailand. Rice straw was harvested and collected from the rice field area in Dok Khamtai subdistrict. It was divided into 3 groups. The first group was used without further fermentation (UF). For the fermented straw, it was soaked in the water and followed by piled up on open air for 7, 14, and 21 days. Then, the water fermented straw (WF) was dry in hot air oven at 90°C for 24 h. The last group is enzyme assisted fermentation straw (EF) where the EM was added during the fermentation. The dried fermented straws were ground until less than 0.5 cm and bound together with tapioca starch glue in various ratios of 1:2, 1:3, 1:4 and 1:5. The mixture was placed in a 300×300×5 mm metal frame sandwiched with metal plates and then pressed at 10.85×104 N/m^2 for 2 min (Sopunna et al., 2015) and baked at 90°C for 24 h. All types of straws were forming as sheets with the same procedure.

2.2 Characterization

2.2.1 Tensile testing

The test specimens were cut from the sheets into the size of 150 mm×25 mm with a gauge length of 100 mm. A universal testing machine (Instron Model 5566) equipped with 1 kN load cell was employed for the test. The test was performed at a constant crosshead speed of 5 mm/min. The average tensile strength, elongation at break and Young's modulus were calculated from at least 5 specimens.

2.2.2 Chemical analysis

The concentrations of total N were analyzed by Kjeldahl technique (Tecator™ 2006 Digestion Block and Kjeltec™ 2100 Distillation Unit) (Kathong & Ruangviriyachai, 2014). Phosphorus contents were measured by Vanadomolybdate method using spectrophotometer at 420 nm absorbance (Kathong & Ruangviriyachai, 2014) (Thermo Scientific™ GENESYS™ 30). The amount of potassium used calcium carbonate in hydrochloric as suppressor (Department of Agriculture, 2016) and determined by spectrophotometer at 722 nm absorbance.

2.2.3 Water absorption and swelling

The sample for water absorption test is done by cutting the test specimen into dimensions of 5×5 cm. The dried sample is weighed (W_1) before being dipped in water. Then, the specimens were immersed in water for 1 h and taken out of the water and weighed after soaking (W_2). The obtained data

Suan Sunandha Science and Technology Journal
©2023 Faculty of Science and Technology, Suan Sunandha Rajabhat University

were used to find the percentage of water absorption as follows (Piyang, Chaichan, & Sagulsawasdipan, 2018):

$$\%\text{Water absorption} = [(W_2-W_1)/W_1] \times 100 \quad (1)$$

For the swelling test, the specimen was cut to a size of 5×5 cm, and the thickness of the specimen was measured while drying (T_1). The specimen was immersed in water at 20±2°C for 1 h, then the specimen was lifted and blotted with a damp cloth on the surface. After that, the test specimen was placed on a non-absorbent material for 1 h and finally the specimen thickness was measured at the same location (T_2). Swelling percentage can be calculated from the equation below (Piyang et al., 2018):

$$\%\text{Swelling} = [(T_2-T_1)/T_1] \times 100 \quad (2)$$

2.2.4 Statistical analysis

The average value difference was analyzed using Two-way analysis of variance (ANOVA) at a significance level of $\alpha = 0.05$ using the statistical analysis program SPSS (Statistical Package for the Social Science version 21). For multiple comparisons, Tukey's test ($p < 0.05$) was performed to check the difference between treatment means.

3. Results and Discussions

3.1 Forming ability

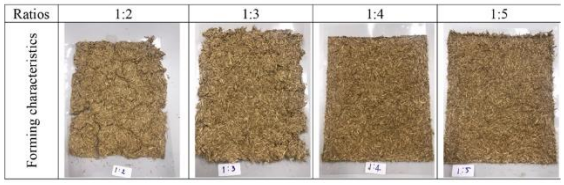

Figure 1. Characteristic of sheets produced from rice straw mixed with tapioca starch glue at various ratios.

The forming ability of straws mixed with tapioca starch glue in various ratios was shown in Figure 1. Sheets produced by 1:2 and 1:3 ratios observed cracks within the sheet and uneven thickness indicating insufficient binder. For the 1:5 ratio, it was found that there was too much binder which was observed from the material overflowing from the edge of the sheet (flash). Therefore, the sheets produced from the ratio of 1:4 are selected for the next step.

3.2 Tensile properties

The mechanical properties of samples were determined via tensile methods in term of tensile strength, elongation at break and Young's modulus. The incorporation of enzyme and fermentation time showed the significant interaction on tensile strength and Young's modulus, but elongation at break. The tensile strength, and Young's modulus of sheets made from fermented straw (whether WF or EF) were observed to be higher overall, except for the sheet made from EF after 7 days and presented in Figure 2. The mechanical properties of EF after 7 days of fermentation were found to be comparable to those of UF, with no significant differences. The initial enzyme activity could potentially explain the fermentation delay. Initially, the biomass entered a lag phase as the microorganisms adjusted to the new conditions, which was then followed by an exponential growth phase according to the growth curve (Glissmann & Conrad, 2000).

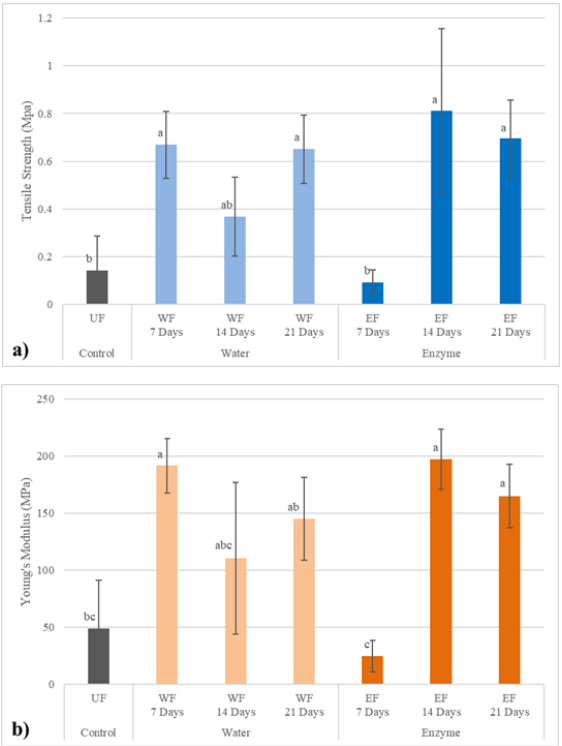

Figure 2. Comparison the mechanical properties of fermented rice straw sheets with and without enzyme assistance (a) Tensile strength, and (b) Young's modulus. Different letters within bars

Suan Sunandha Science and Technology Journal
©2023 Faculty of Science and Technology, Suan Sunandha Rajabhat University

indicate significant difference ($p \leq 0.05$) according to Tukey's multiple comparisons test.

The elongation at break did show significant interaction, only fermentation time effect on this property and show in Figure 3.

However, the analysis conducted using a one-way ANOVA indicated that there were no significant alterations in the elongation at break because of fermentation time until 21 days. Regardless of the effect of enzyme, the result showed a slight increase as a function of time but there were no statistically differences among treatments. Moreover, the elongation at break after 21 days of fermentation was significantly higher when compared to control.

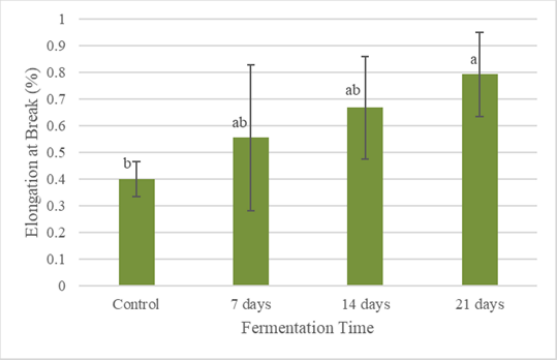

Figure 3. Effect of fermentation time on the elongation at break of sample. Different letters within bars indicate significant difference ($p \leq 0.05$) according to Tukey's multiple comparisons test.

The change in surface morphology might be the reason for mechanical properties development. When a surface is rough, it creates a more favorable environment for wetting, allowing for better mechanical interlocking, which in turn results in improved mechanical properties. The roughness of rice straw is intensified by fermentation (Kumari & Singh, 2022; Liang et al., 2010; Xia et al., 2018), especially when enzymes are added, resulting in a rougher texture than when water is the only medium used (Kumari & Singh, 2022). The increase in surface area of rice straw is due to the degradation of lignin and hemicellulose (Kumari & Singh, 2020).

The main difference between the sheets produced from WF and EF was the duration of fermentation necessary to attain sheets with varying degrees of mechanical properties. In general, the mechanical characteristics of sheets produced via water fermentation alone resulted in the greatest strength after 7 days, with a maximum modulus of 191 MPa, a tensile strength of 0.67 MPa and an elongation at break of 0.69%. The enzyme-assisted fermented sheets achieved their maximum values after 14 days, with the highest modulus, tensile strength, and elongation at break measurements being 197 MPa, 0.81 MPa, and 0.76%, respectively. This difference can be attributed to the previously mentioned delay in the fermentation process.

3.3 Chemical properties

Since the main purpose of using fermented straw is to add nutrients to plant pots, therefore, the changes in N, P and K due to the fermentation process were determined. Table 1 compared the N, P and K values of sheets produced from UF, WF and EF at different fermentation times.

Table 1. Comparison of nitrogen, phosphorus, and potassium content in the samples.

Sample	Total K_2O *(%w/w)*	Total P_2O_5 *(%w/w)*	Total N *(%w/w)*
UF	1.37 ± 0.01^{g}	0.31 ± 0.00^{f}	0.69 ± 0.00^{g}
WF 7 Days	4.57 ± 0.03^{f}	0.32 ± 0.00^{e}	0.76 ± 0.02^{f}
WF 14 Days	11.09 ± 0.07^{d}	0.34 ± 0.00^{c}	1.11 ± 0.02^{d}
WF 21 Days	15.06 ± 0.00^{b}	0.37 ± 0.00^{b}	1.65 ± 0.04^{b}
EF 7 Days	7.79 ± 0.09^{e}	0.33 ± 0.00^{d}	0.91 ± 0.00^{e}
EF 14 Days	13.13 ± 0.12^{c}	0.37 ± 0.00^{b}	1.33 ± 0.02^{c}
EF 21 Days	17.90 ± 0.03^{a}	0.40 ± 0.00^{a}	1.89 ± 0.02^{a}

Mean ± standard deviation. Means in the same column with different letters (a–g) are significantly different ($p < 0.05$).

The results clearly show that the fermentation process greatly affects the N, P and K values as indicated by Tukey's test. The employment of water fermentation only led to a notable rise in all three measurements, which was even more pronounced with an extended fermentation time. The incorporation of enzymes into the fermentation process further intensified these values. At the same fermentation period, the enzyme-assisted fermentation demonstrated a higher value compared to the water fermentation sample. The main function of the EM is to provide microorganisms to the system and to produce useful nutrients (Jusoh, Manaf, & Latiff, 2013). The process of fermentation using only water for 21 days resulted in total N, P_2O_5, and K_2O values of 1.65%, 0.37%, and 15.06% by weight, respectively. However, when EM was added to the mixture for a shorter period of 7 days,

Suan Sunandha Science and Technology Journal
©2023 Faculty of Science and Technology, Suan Sunandha Rajabhat University

the values of N, P, and K increased compared to the fermentation with water alone. Enzymatic fermentation for 21 days resulted in even higher values, with total N increasing to 1.89%w/w, total P_2O_5 to 0.40%w/w, and total K_2O to 17.90%w/w. Furthermore, even after molding and heat treatment, the fermented straw demonstrated substantially greater values of N, P, and K in comparison to non-fermented straw. Hence, it can be deduced that the process of straw fermentation, particularly when combined with EM, can enhance the nutritional properties of plant pots, and this benefit persists even after potting procedures that involve heat treatment. As per the Royal Gazette, non-liquid organic fertilizers are required to contain a minimum of 1.0% total N by weight, 0.5% total P_2O_5 by weight, and 0.5% total K_2O by weight. Alternatively, the total macronutrient content should not be less than 2.0% by weight. Therefore, the N, P, and K values obtained from all specimens in this study meet the criteria for being classified as organic fertilizer.

3.4 Water absorption and swelling

The fermentation process might affect water absorption and swelling. Fermentation not only changes the texture of the straw but also results in increased porosity in the straw (Kumari & Singh, 2022). These pores directly affect the adsorption and swelling values as shown in Table 2. It was expected that the sheets made from longer fermentation time had more water absorption and swelling and were higher than UF. Notably, the sheets produced from EF exhibited higher in number on water absorption and swelling values compared to those obtained from WF at all fermentation durations. The increase in both values may be attributed to a decrease in cellulose crystallinity that occurs during the fermentation process (Xia et al., 2018).

Table 2. Comparison of %water absorption and %swelling in the samples.

Sample	%Water Absorption	%Swelling
UF	58.00	56.25
WF 7 Days	60.00	60.78
WF 14 Days	68.00	61.54
WF 21 Days	70.00	65.45
EF 7 Days	67.00	68.75
EF 14 Days	71.00	70.59
EF 21 Days	78.47	77.59

4. Conclusion

The properties of rice straw nursery plant pots can be altered through the process of fermentation. Over time, fermentation increases the levels of N, P, and K. When combined with an EM enzyme, the fermentation process results in even greater improvements compared to non-enzyme fermentation. The tensile strength and Young's modulus can be improved due to both fermentation time and incorporation of enzyme with reaching the maximum in 14 days for enzyme fermentation and 7 days for non-enzyme fermentation. However, elongation at break was increased to the maximum value at 21 days of fermentation regardless of enzyme assistance. Furthermore, the inclusion of enzymes during fermentation and longer fermentation period leads to an increase in water swelling and water absorption.

In summary, to maximize the nutritional benefits of the material, fermenting rice straw for a duration of 21 days with the aid of enzymes before using it as a material for bio-based plant pots can significantly enhance its nourishing properties, making it suitable as an organic fertilizer.

Acknowledgement

The authors would like to thank the Scientific and Technological Instruments Center (STIC), Mae Fah Luang University, Chiang Rai, Thailand for providing instruments.

Conflict of Interest

The authors do not report any financial or personal connections with other persons or organizations, which might negatively affect the contents of this publication and/or claim authorship rights to this publication.

ORCID

Sitthi Duangphet
https://orcid.org/0000-0003-1189-2078

References

Conneway, R., Verlinden, S., Koeser, A. K., Evans, M., Schnelle, R., Anderson, V., & Stewart, J. R. (2015). Use of alternative containers for long- and short-term greenhouse crop production. *HortTechnology*, *25*(1), 26-34. doi:10.21273/horttech.25.1.26

Suan Sunandha Science and Technology Journal
©2023 Faculty of Science and Technology, Suan Sunandha Rajabhat University

Department of Agriculture. (2016). *Method validation on analysis of water soluble potassium in chemical fertilizers follow the notification of Ministry of Agriculture and Cooperatives Re: Prescribing the method of analysis of chemical fertilizers, B.E. 2559, method 1.12.01 for accreditation to ISO/IEC 17025: 2005*. Retrieved from https://www.doa.go.th/oard8/wp-content/uploads/2019/08/v6102.pdf

Evans, M. R., Taylor, M., & Kuehny, J. (2010). Physical properties of biocontainers for greenhouse crops production. *HortTechnology*, *20*(3), 549-555. doi:10.21273/horttech.20.3.549

Glissmann, K., & Conrad, R. (2000). Fermentation pattern of methanogenic degradation of rice straw in anoxic paddy soil. *FEMS Microbiology Ecology*, *31*(2), 117-126. doi:10.1111/j.1574-6941.2000.tb00677.x

Jusoh, M. L., Manaf, L. A., & Latiff, P. A. (2013). Composting of rice straw with effective microorganisms (EM) and its influence on compost quality. *Iranian Journal of Environmental Health Science and Engineering*, *10*(1), 17. doi:10.1186/1735-2746-10-17

Kathong, S. , & Ruangviriyachai, C. (2014) . Determination of nitrogen, phosphorus and potassium in liquid organic fertilizer. *KKU Research Journal (Graduate Studies)*, *14*(4), 57-68.

Kumari, D., & Singh, R. (2020). Ultrasonic assisted petha waste water pretreatment for rice straw for optimum production of methane and ethanol using mixed microbial culture. *Renewable Energy*, *145*, 682-690. doi:10.1016/j.renene.2019.06.082

Kumari, D., & Singh, R. (2022). Rice straw structure changes following green pretreatment with petha wastewater for economically viable bioethanol production. *Scientific Reports*, *12*, 10443. doi:10.1038/s41598-022-14627-7

Liang, Y. S., Yuan, X. Z., Zeng, G. M., Hu, C. L., Zhong, H., Huang, D. L., ... Zhao, J. J. (2010). Biodelignification of rice straw by *Phanerochaete chrysosporium* in the presence of dirhamnolipid. *Biodegradation*, *21*(4), 615-624. doi:10.1007/s10532-010-9329-0

Nambuthiri, S., Fulcher, A., Koeser, A. K., Geneve, R., & Niu, G. (2015). Moving toward sustainability with alternative containers for greenhouse and nursery crop production: A review and research update. *HortTechnology*, *25*(1), 8-16. doi:10.21273/horttech.25.1.8

Office of Agricultural Economics. (2022). Retrieved from http://www.oae.go.th/assets/portals/1/fileups/prcaidata/files/percent%20rice%20production%2064.pdf

Piyang, T., Chaichan, W., & Sagulsawasdipan, K. (2018). Environment-friendly plant pot production from palm oil sludge and mushroom cultured waste. *RMUTSV Research Journal*, *10*(3), 497-511.

Schettini, E., Santagata, G., Malinconico, M., Immirzi, B., Mugnozza, G. S., & Vox, G. (2013). Recycled wastes of tomato and hemp fibres for biodegradable pots: Physico-chemical characterization and field performance. *Resources, Conservation and Recycling*, *70*, 9-19. doi:10.1016/j.resconrec.2012.11.002

Sopunna, K., Pasom, W., Woradong, K., & Chaiwangrach, A. (2015). Fabrication and properties of biological plant pots. *SNRU Journal of Science and Technology*, *7*(2), 1-7.

Sun, Y., Niu, G., Koeser, A. K., Bi, G., Anderson, V., Jacobsen, K., ... Lovell, S. T. (2015). Impact of biocontainers on plant performance and container decomposition in the landscape. *HortTechnology*, *25*(1), 63-70. doi:10.21273/horttech.25.1.63

Tiquia, S. M., & Tam, N. F. Y. (2002). Characterization and composting of poultry litter in forced-aeration piles. *Process Biochemistry*, *37*(8), 869-880. doi:10.1016/S0032-9592(01)00274-6

Van de Wetering, J., & Athalage, S. (2010). *Biodegradable planters (*U.S. Patent No. 7681359B2). U.S. Patent and Trademark Office.

Xia, T., Sun, E., Tang, W., Huang, H., Wu, G., & Jin, X. (2018). Structural and thermal stability changes of rice straw fibers during anaerobic digestion. *BioResources*, *13*(2), 3447-3461. doi:10.15376/biores.13.2.3447-3461

Available online at https://li02.tci-thaijo.org/index.php/ssstj

Suan Sunandha Science and Technology Journal
©2023 Faculty of Science and Technology, Suan Sunandha Rajabhat University

Analysis and Design of Building's Structural Members (Slabs and Beams) using Microsoft Excel and AUTOCAD Software: A Case Study of MARCGSO' Building

Kilani Abiodun Joseph[1*], Fapohunda Christopher Ajiboye[2], Oladejo Oladipupo Seun[3], Adetayo Oluwaseun[2], Famodimu Babatunde[2]

[1]Department of Civil Engineering, College of Engineering, Science and Technology, Florida Campus, University of South Africa, Johannesburg, South Africa

[2]Department of Civil Engineering, Faculty of Engineering, Federal University, Oye Ekiti, Ekiti State, Nigeria

[3]Department of Civil Engineering, Faculty of Engineering and Technology, Ladoke Akintola University of Technology, Ogbomoso, Oyo State, Nigeria

***Corresponding author e-mail:** abiodun_kilani@yahoo.com

Received: *9 December 2022*/ **Revised:** *31 March 2023*/ **Accepted:***19 June 2023*

Abstract

The frequent collapse of concrete structures (Buildings, Bridges and Culverts) these days in the global construction industries has led to claiming of many innocent lives. From the literature perspective, the observed major causes of this failure are the errors developed from the programmed structural software; the method used in running the software, its usage error during the analysis and design of structural members; and possibly, error committed by unskill personnel while using the structural software. Allowing the continuity of these errors in the construction industries will cause greater damages to lives and properties globally, thus; a more accurate and reliable design software has to be developed to eradicate errors occurrence in structural design. The results of this investigation proved that Microsoft Excel sheet is accurate for structural members' analysis and design; good for accurate calculation in designing, it can be access quick; so reliable, and error free. Its application in construction industries will bring accuracy and stability to designed structures, and more lives will be saved. As a case study, the architectural plans of Maryland Catholic Grammar School, Ogbomoso (MARCGSO)'s principal lodge building was used as a prototype to show how efficient is Microsoft Excel in structural analysis. At MARCGSO, this has been tested and found reliable. During the investigation, the structural details of the designed concrete structural members were carried out using AUTOCAD software. Analysis and design of members were carried out from the basic principle of structural design using BS 8110 part 1:1999. The result shows that, Microsoft Excel and BS 8110 part 1:1999 code are the best design tools needed for analysis and design of structural members. It is very fast, accurate and error free. Also, the output of analysis carried out using Microsoft Excel are traceable, amendable and reliable, thus, its application in designing will prevent sudden structural failure. Likewise, it is very easy for young and structural engineers to operate, thus, its application can be done by: open a fresh Microsoft Excel sheet, get BS 8110 part 1:1999 code of structural design, prepare a general arrangement of architectural plan of structure to design, then follow the step by step of designing stated in this study. It required no application download or software purchase. In conclusion, the use of Microsoft Excel in structural analysis and designing will save many lives and prevent sudden collapse of structures resulting from wrong code or software error.

Keywords: Microsoft Excel, Structural analysis, Design code, Design error, Structural members

1. Introduction

A reinforced concrete is a concrete with series of connected bents jointed by slabs and beams (Mrema, Gumbe, Chepete, & Agullo, 2012). It consists of aggregates like: cement, sand, granite and admixtures together with steel bars (Kilani, Adeleke, & Fapohunda, 2022). Structural design is defined as a process of setting tools or methods in use, to determine the specifications that are safe and economical for a structure in order to develop a sufficient strength to

Suan Sunandha Science and Technology Journal
©2023 Faculty of Science and Technology, Suan Sunandha Rajabhat University

carry its intended load (E-SUB Construction Software, 2018). It also involves the production of structural layout of the proposed structures (like buildings, culverts and bridges), structural dimensioning, production of architectural plans, analysis and design of structural elements, and production of details of design calculations of structural members (Structural Design, 2023). A structural member is a load bearing element of a facility. Examples of structural members are: load bearing walls, columns, slabs and beams (Law-Insider, 2021). Structural members are mainly classified into element, types, structural system, overall shape, form, application and material (Civil Engineering X, 2022). All these seven classes were grouped into two based on their capacities for load bearing, that is, strong and weak members. Strong members are strong stiff load bearing member of a structure while the weak members are non – load bearing members of a structure (Fire Engineering, 2010). Examples of strong members of a structure are: columns, beams and slabs while the weak structural members are: ceilings and non-load supporting walls (Mrema et al., 2012). Columns and beams are the main two members of a structure that bear the building's structural weight and make it stable from slab to foundation of the building. Beams are members of a building's that carries the weights of roof ceilings and floor slabs; transferring them to a perpendicular frame work load bearing member in order to withstand the stacked walls' loads and shear the carried loads heavier for them to carry. Columns are the vertical building's members which were purposely constructed to reinforce (support) some other heavily loaded members of a structure like: beams and slabs (Ram, 2020). Recently, unexpected collapsing of structures like: buildings, culverts and bridges are increasing in our environment. This has claimed many lives of inmates. One of the major sources of these is poor structural designs and errors made by human or by using programmed software for structural analysis. Errors in design are failures made unavoidably when information were applied incorrectly or make the information pertinent inaccessible (Reichart, 1988). Also, errors in design is defined as mistakes made in design, omission of essential data in design and conflicts (Lopez, Love, Edwards, & Davis, 2010). The errors made through the human mistake in design could be from inaccurate mode of designing and insufficient time constraints. This causes inconsistencies in measurement, deviation in actual values and inaccurate in measuring precision (De Quiros, Lopez, Aranda-Mena, & Edwards, 2008). Most of the errors made in structural design are from electrical, mechanical and plumbing (EMP) design systems. To achieve the accurate construction of structures with high safety of inmates, these errors need to be avoided, especially during the structural design (Peansupap & Ly, 2015). Errors in structural design are the sources of many catastrophic accidents that front the injury and death of construction workers, and buildings' inmates as traced by the previous structural scholars (Musa & Obaju, 2016). Harle (2017) designed and analyzed a building structure the use of one language programming software for the analysis and design of its members. Author used STAAD PRO. and MATLAB analysis software to generate and analyzed the loads on building structural members. These two software were used to create accurate design calculations of the concrete reinforcing areas required at a specified area of a structural member like: beam, column and slab, using the maximum bending moment and shear force values gotten from the analyzed members of a building using Staad Pro. Design programming software. Harle (2017) has shifted to the use of Excel sheet (MS) for structural design recently, while the MATLAB software was used for structural programming by the author. These two soft-wares were produced and run in one programming language code, but the programming of these two software in other languages would have contributed to the quick design and analysis performance of the software which is the current limitation of this programming. This could have contributed to the better design output if implemented initially.

Suan Sunandha Science and Technology Journal
©2023 Faculty of Science and Technology, Suan Sunandha Rajabhat University

Time Error 9 Error in Orion CSC Run software is an error that normally occurs as a result of misconfiguration of file codes system in the computer operating windows system. It is a hexadecimal error format that occurs as a result of wrong operating windows used for computer operation together with its other compatible driver and software. This Orion 9 Error usually surface when the system operating windows files are damaged. It was observed that files error come into existence through the incomplete processes of software uninstall, inaccurate deletion of hardware, inadequate installation and recovery of a computer system from being affected by virus. All these might have lead to the corruption of Orion file in the computer operating system (Survey Developer, 2023). In the investigation conducted by Ondrej (2011) on SAP2000 software, the errors developed through the use of SAP 2000 structural design software were categorized into three: codes and windows error; errors of analysis; and other perspective error. Author said, these errors were developed from the use of inadequate virtual and graphic memories, use of no joint memories software, and refilling of formatted database. Navaee (2003) solved the problem of statistical indeterminate and determinate beams using Microsoft Excel. During the process, the analysis and design of a loaded building's beam members were done using Microsoft Excel to generate bending moment and shear force diagrams. The deflections and slopes of the beams were analyzed using Microsoft Excel also. To determine the deflections, slopes, bending moments and shear force of the spanning beams, four standard formulas were developed in B4 to E4 Excel cells. These formulas formed were capable of analyzing the accurate values of beams' deflections, slopes, bending moments and shear forces. The beams analyzed were suggested to the end concentrated loads and were uniformly distributed. Also, author made use of Hardy Cross's method of structural analysis from the theorem of moment distribution method (MDM), to analyze the uniformly distributed loads of the loaded beams, and the moments at the fixed ends were determined from the analysis. Also, the beams factors of loads distribution in the beam members were determined using MDM. At the stages of designing and analyzing the beam with the use of MDM, the ends spans of the beam were clamped while its end moments were fixed to counter balanced moments for the beams' joints perfect equilibrium. At that point, the end spans were unclamped to give room for rotation to distribute the moments that were initially computed. These distributed moments were then carried (over) to the opposite end. The unclamping and clamping processes were repeated until sufficient values of distributed moment were formed. This method of designing and analysis used was prone to error making at the stages of designing. Having considering the design errors developed through the use of existed structural design software that were commonly caused sudden collapsing of the buildings as explained earlier, this paper focuses on cancellation of these design errors resulted from the: installation of design software, use of structural design software, manual design calculations of building structural members (beams, slabs and columns), and building structural details using a simple error free Microsoft Excels calculation sheets for the design and provision of accurate steel bars for accurate member reinforcement.The software (Microsoft Excel spread sheet) is easy to compute and can be operated upon by any structural design engineer. The aim of this study is to develop a simple and standard design platform for structural members' (beams, slabs and columns) analysis and design using Microsoft Excel and AutoCAD. The aim is achieved through the following objectives: (i) to upgrade the level of structural design from manual to that of using Microsoft Excel for designing (ii) to encourage the use of structural design codes such as British Standard (BS 8110:1997)) among engineers for structural designs (iii) to eradicate the problem of building failures normally caused by software and human errors during structural design stages (iv) to develop an accurate and reliable platform for the design of structural members (beams, slabs and columns) using Microsoft Excel sheet. (v) to produce the accurate design details of analysis carried out from Excel platform using AutoCAD software.

Suan Sunandha Science and Technology Journal
©2023 Faculty of Science and Technology, Suan Sunandha Rajabhat University

2. Materials and Methods

2.1 Materials

2.1.1 Architectural plans

In this study, the architectural plans of Maryland Catholic Grammar School, Ogbomoso (MARCGSO)'s principal lodge building was used as case study plans for the design of structural members with the aid of Microsoft Excel. The design of structural members with this type of platform (Microsoft Excel) was first implemented at MARCGSO. The results obtained at MARCGSO were so accurate and reliable. The plans used for the design were grouped into ground and first (upper) floor plans. The ground floor plan is of size 22,600 mm by 16,798 mm in length and breadth. It made up of two guest rooms together with their bath and toilet rooms, a waiting room, a general sitting room, two stair cases, two balconies, a dining room, an office, a kitchen and a store. This ground floor plan was design purposely to serve as guest house (floor) for the visiting priest of MARCGSO (see Figure 1). The first floor plan is of size 22,500 mm by 17,000 mm. Its breath is a little bit longer than the breadth of ground floor plan. The plan consists of a living room, three bedrooms with their bath and toilet rooms, a prayer room, two balconies, a porch, an official store, a dressing room and a study room (Figure 1). The first floor plan was design as a residential floor for the school principal, vice-principal and other school's official staff members. The roof plan, approach view; rear, right and left side elevations, cross – sectional views (Sections C-C and D-D), fences, and septic tank design plans were all projected from the ground and first floor plans as shown in Figure 2.

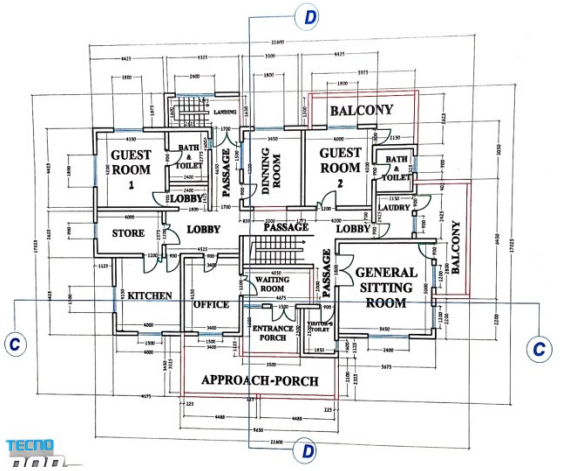

(a)

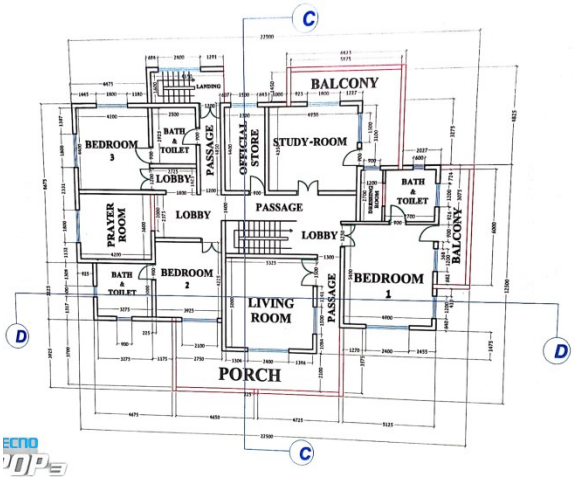

(b)

Figure 1. (a-b) Ground and first floor plans of a proposed principal's lodge.

Suan Sunandha Science and Technology Journal
©2023 Faculty of Science and Technology, Suan Sunandha Rajabhat University

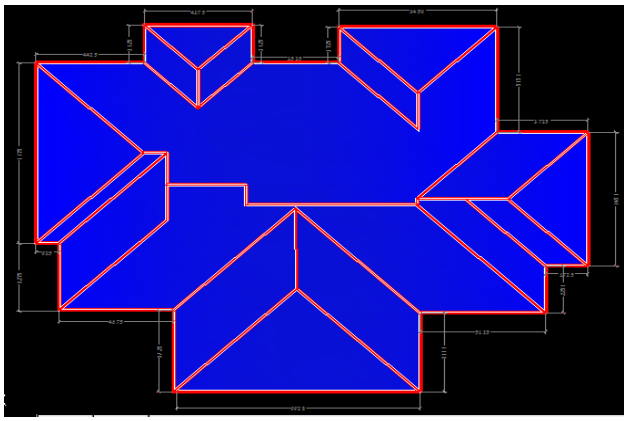

(a)

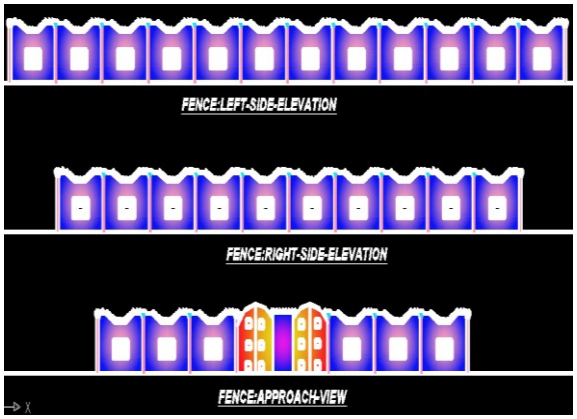

(b)

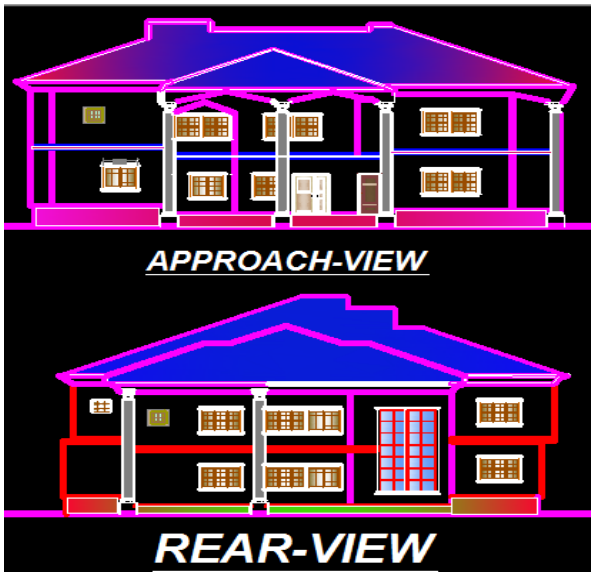

(c)

(d)

Suan Sunandha Science and Technology Journal
©2023 Faculty of Science and Technology, Suan Sunandha Rajabhat University

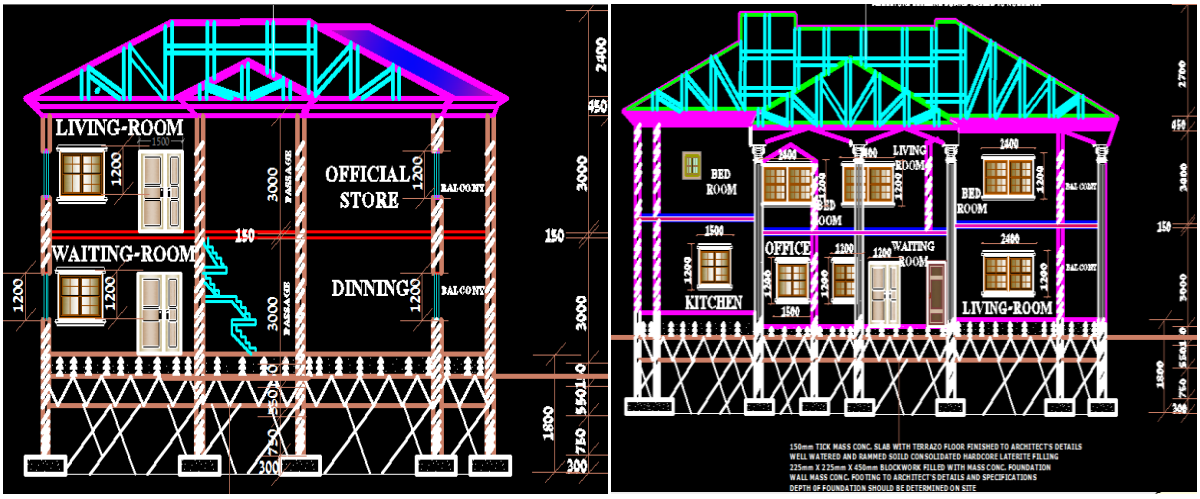

(e) (f)

Figure 2. (a) Building's roof plan (b) fence elevations (c) approach and rear elevations (d) right and left side elevations (e) cross-sectional view of section C - C (f) cross-sectional view of section D – D.

2.1.2 Structural members' arrangement

The structural layouts of the proposed building were generated from ground and first floor plans. The layouts consist of slab panels 1 to 22. All of these panels except that of panel 16, were in two ways spanning while that of panel 16 is one way slab. The slab panels 1 to 22 consist of different types of slab cases as specified by BS 8110 part1:1999 code of structural design (Navaee, 2003). The general arrangements (G.A) of building structural members were labeled from A to L and from 1 to 10 on G.A for easy identification of each structural member as shown in Figure 3. Likewise, the upper floor's G.A consist of 22 slab panels out of which six of them were one –way spanning slabs while others were two – ways spanning slabs. Also, the first floor's G.A shows the arrangement of beams and columns for the support of the building's roof and slabs. It was labeled from A to K and 1 to 8 as shown in Figure 3(a).

2.1.3 Microsoft Excel and AUTOCAD software

The Microsoft Excel programmed spread sheet was used for all the analysis and designs of structural members (beams, slabs) in this studies. While the AutoCAD software of version 2010 classical model was used for the production of architectural plans and structural details.

Suan Sunandha Science and Technology Journal
©2023 Faculty of Science and Technology, Suan Sunandha Rajabhat University

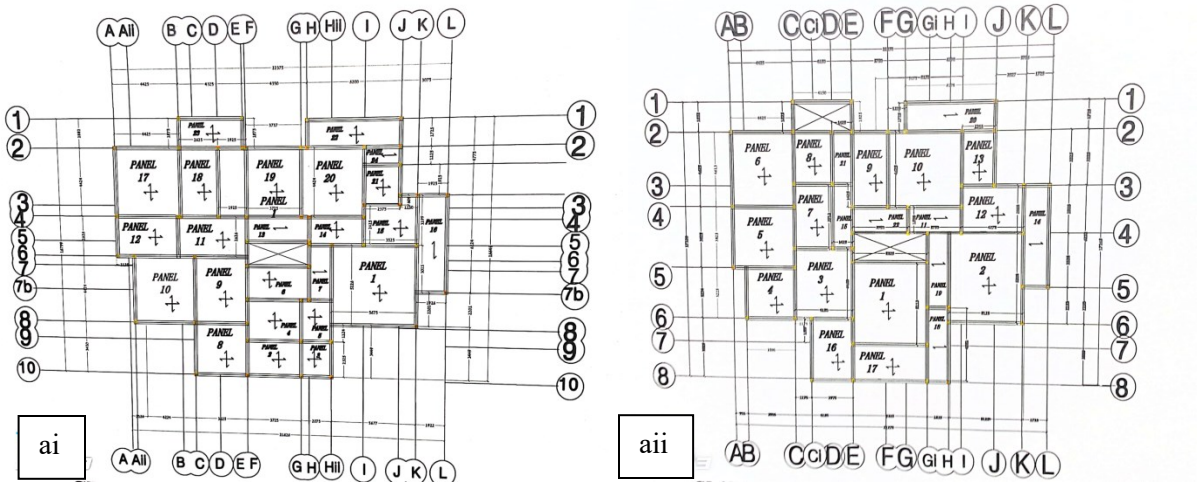

Figure 3(a). (i – ii): General layouts at ground and first floors.

2.2 Methodology

The steps used for the design and analysis of structural members (beams and slabs) in this study are explained as shown in Figure 3(b).

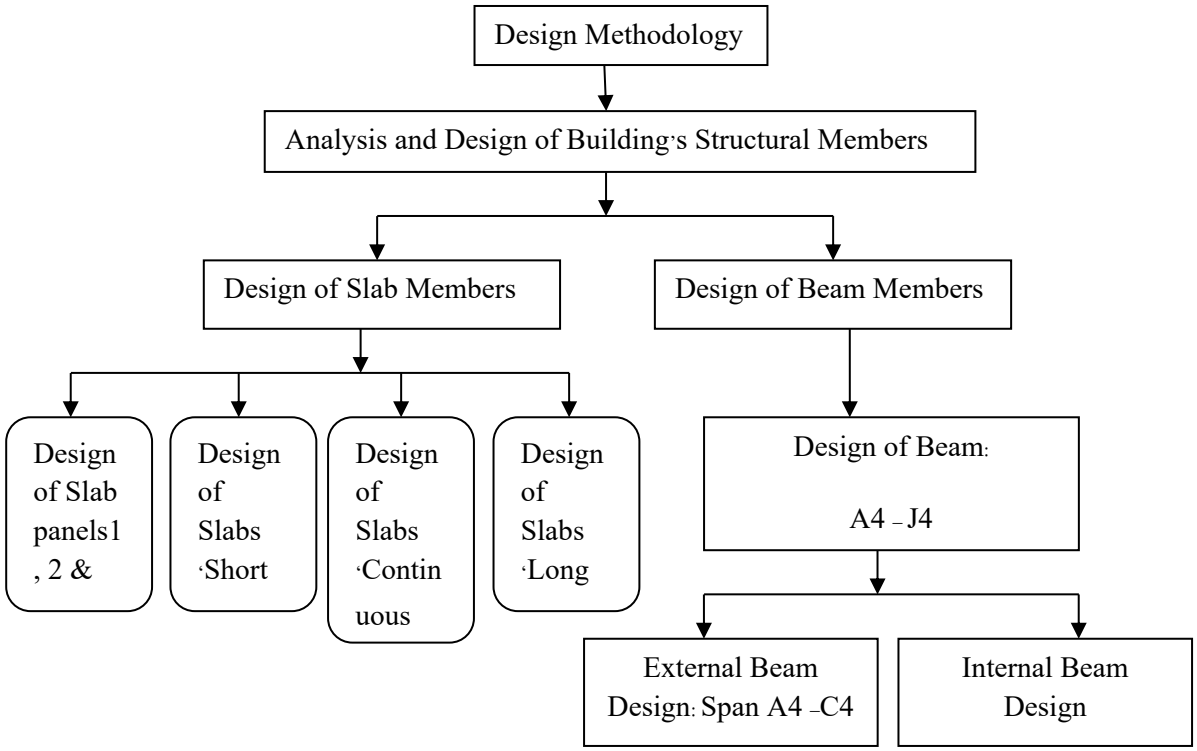

Figure 3(b). Slabs and beams design methodology.

Suan Sunandha Science and Technology Journal
©2023 Faculty of Science and Technology, Suan Sunandha Rajabhat University

2.2.1 Analysis and design of building's structural members using Microsoft Excel

2.2.1.1 Design of slab members

The pre-selection of the building's slab-types to design for was done in order to know if the selected slabs were one – way or two – way spanning slabs. The structural layout plans of the proposed building (both at ground and upper floors) were used for this selection. A selected slab-panel is said to be a one way slab if ly / lx ≥ 2.0 and is two – way slab if ly / lx ≤ 2.0 according to BS 8110 – 1:1997 page 35 for civil and builder engineers. For uniformity in design, the critical slab panels 1, 2 and 10 were selected for design and the details were used to predict the expected reinforcement of the other panels following the specification stated by BS 8110 – 1:1997 code.

(a) Design of Slab Panels 1, 2 and 10

The slab panels 1, 2 and 10 had the same dimensional arrangements; therefore, their designs and analysis were taken to be the same. Among the three panels, panel 1 was selected for reinforcement design which was detailed for the remaining slabs. At the initial stage of slab design, the loads on slab to design were analyzed and determined. In the Excel spread sheet, at cell C7 to F9, the self weight of concrete slab was determined by multiplying the thickness of the slab which is 150mm with the density of concrete which is 24KN/m^3. The computation of their result was done at cell G7 by imputing "=0.15*24 in the cell and press enter. The finishes and partition allowance on the slab was taken as 1KN/m^2 each, which were placed at cell G8 and G9 respectively. The total dead loads of concrete slab (g_k) was determined by adding the values gotten at cells G7, G8 and G9 together at cell G10 as shown in Figure 4 (a). Considering the live purpose of the building, the imposed (live) load (qk) of 1.6KN/m^2 suggested by BS 8110-1:1997 code was used for the design. This load was placed at cell G11. The Uniformly Distributed Load (UDL) on concrete slab was determined from the equation 1

$$UDL = 1.4(gk) + 1.6\,(qk) \qquad (1)$$

Where: 1.4 is the modification factor of concrete slab's dead load; gk is dead load; 1.6 is the modification factor of concrete slab's imposed load. The 1.4 (gk) value was determined at cell G10 and that of 1.6 (qk) at cell G11. Their UDL was calculated for at cell G12 as shown in Figure (4b).

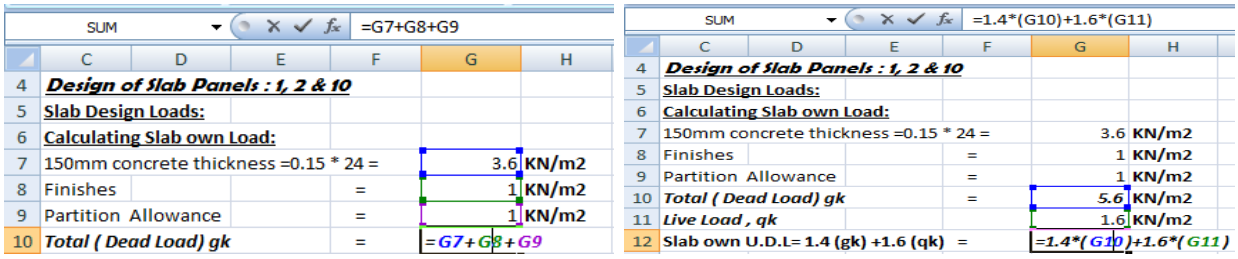

(a) (b)

Figure 4. (a) Calculating the total dead load of slab (gk) (b) analysis of slab own (U.D.L).

The units of all the calculated loads were recorded at H7 to H12 cells. The effective depth of the slab were determined from the formula: Effective Depth (d) = Overall Depth (h) – cover – ½ of bar diameter, that is, d = 150 – 20 – ½ (12) =124 mm. Taking the exposure condition of the concrete slab as Mild and fire resistance as one hour, the concrete cover was given as 20mm and the slab breadth, 1000mm as indicated in Tables 3.3 and 3.4 of BS 8110-1:1997code of structural design page 21.

Considering the slab panel1, the ratio of ly to lx was determined at cell F20 which is 1.1, that is, ly/lx =1.1 ≤ 2.0 as shown in figure 5. It implied that, the slab under design is a two – way spanning slab. Using ly/lx = 1.1 values, the short and long spans coefficients of slab panel1 were determined from Table 3.14 of BS

Suan Sunandha Science and Technology Journal
©2023 Faculty of Science and Technology, Suan Sunandha Rajabhat University

8110-1:1997 at interior panel column as: - 0.037 and 0.028 (for short span coefficients) and -0.032 and 0.024 (for long span coefficients) respectively as indicated in Figure 5.

	A	B	C	D	E	F	G	H	I	J
19			Panel 1	ly	lx	ly/lx	ly/lx <2			
20				5.55	5.225	=D20/E20	1.1 <2	Hence, the Slab is two-way slab		
21				Short Span Coeff.			-0.037		and	0.028
22				Long Span Coeff.			-0.032		and	0.024

Figure 5. First: - Ratio of long span to short span of the slab **(**Ly / Lx**)**; Second:-Long and short span coefficient of slab panel 1.

The additional loads on concrete slab were determined by multiplying the modification factor, wall weight, height of the building, and the addition of both long and short spans. The product was divided by the area (length x breadth) covered by the slabs. The outcome of the division gave the additional uniformly distributed load (UDL) in KN/m^2 on the slab panel 1. This analysis ranged from C14 to J14. The additional UDL was determined at cell K27 and that of Ultimate UDL (concrete own UDL + UDL from Additional partition load) of slab panel 1 was determined at cell L24 as shown in figure 6.

Additional partition Load:							
Mf	wall wt.	Height of buildng	longspan	shortspan	L+S	LOAD	UNIT
1.4	3.47	3.15	5.55	5.225	10.775	=I25*E25*D25*C25	

26		length	breadth	Area =B*L	unit		LOAD(KN)	Area	Load/Area=U.D.L from point load		
27	Area	5.55	5.225	28.99875	m²;	U.d.l =	164.8866	28.99875	5.68599	KN/m²	
28	TOTAL u.d.l = Ultimate U.d.l + u.d.l from point load =						10.4	+	5.68599	=K28+I28	KN/m²

Figure 6. First: - Additional partition load on slab panel 1; Second:- Ultimate uniformly distributed load on slab panel 1.

(b) Design of slab's short span mid span design

The mid span reinforcement design of concrete slab is the main reinforcement design of steel bars needed to bear the weight of dead and imposed loads on the slab. In the analysis, the number of mid span reinforcement bars were calculated for through the area of steel bars gotten using the formulas:

$$As = \frac{M}{0.95fy.la.d^2} \quad (2)$$

Where M is the maximum bending moment of the concrete slab, la is the lever arm, which was calculated from the formula:

$$la = 0.5 + \sqrt{\left(0.25 - \frac{\mathrm{k}}{0.9}\right)} \leq 0.95 \quad (3)$$

And K was determined from:

$$K = \frac{\mathrm{M}}{fcu.bf.d^2} \leq 0.156 \quad (4)$$

Suan Sunandha Science and Technology Journal
©2023 Faculty of Science and Technology, Suan Sunandha Rajabhat University

Where *f*cu is the characteristic strength of concrete which was taking as 20N/mm² and 'd'is the effective depth of the concrete slab for tension reinforcement as shown in BS 8110-1:1997 code of structural design page 25 to 26. In Excel spread sheet, the data were input from cell F30 to J31 to determine the value of M. The ultimate UDL value of the slab calculated early was placed at cell F31 called F (cell F30), then, the θx value was calculated at cell G31, followed by Lx at cell H31 and I31 while the value of M was calculated by multiply the values of F, θx and L²x at cell J31. At cell J31, "= I31*H31*G31*F31" were inputted and 'enter' key of computer keyboard was pressed onceto calculate the value of M in J31 cell (Figure 7). In the calculation of K, the input data in the formula$K = \frac{\mathrm{M}}{fcu.bf.d^2} \leq 0.156$ were placed at cell D33 to H33 while the actual value of K was determined at cell I33. At Cell I33,'= D33/(H33*F33*E33)" was input and pressed 'enter' key to calculate the value of K as shown in Figure 7.

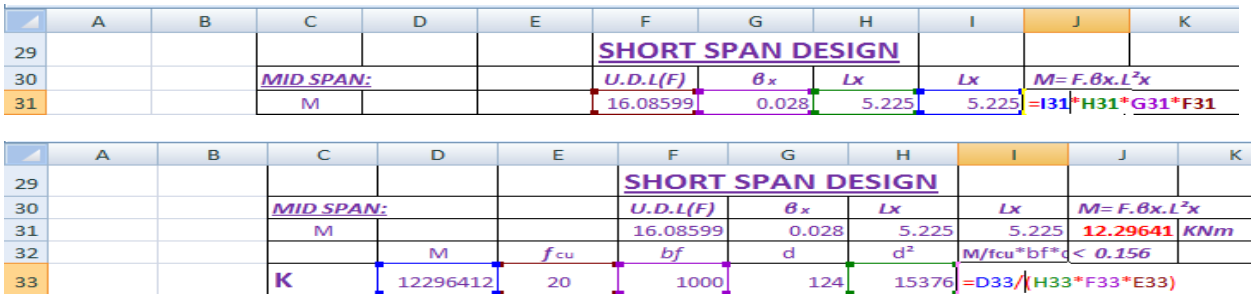

Figure 7. First:- Calculating of maximum bending moment (M) on slab; Second:- Calculating of K value.

The lever arm of the reinforcement design of concrete slab was also calculated from cell D35 to G35. In the calculation, the values of: 0.25 – K / 0.9; √ (0.25 – K / 0.9); and $la = 0.5 + \sqrt{\left(0.25 - \frac{\mathrm{k}}{0.9}\right)}$ were determined at cell D35, E35 and G35 respectively (see figure 8). The areas of the steel required for the concrete slab reinforcement using the formula:$As = \frac{M}{0.95fy.la.d^2}$was calculated at cell I37. This was conducted by input "=D37 / (E37*F37*G37*H37) at cell I37 and press "Enter" button from the keyboard of a computer system in the Excel sheet as a shown in figure 8. The area gotten from the calculation was used to provide the spacing in between the steel bars for concrete slab's reinforcement. Also, structural details of the slab were produced with calculated results.

Suan Sunandha Science and Technology Journal
©2023 Faculty of Science and Technology, Suan Sunandha Rajabhat University

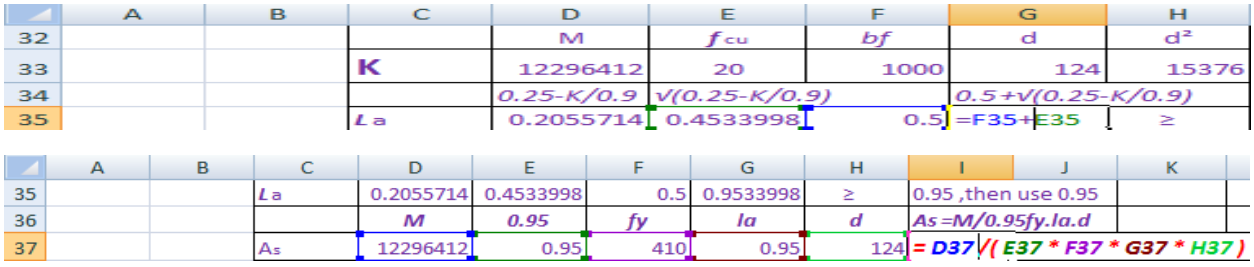

Figure 8. First:- Calculating lever-arm value; Second:- Calculating the area of steel bars (As).

(c) Design of continuous edge of slab panel 1

The negative coefficient of short span of the slab that was gotten earlier was substituted in the formulas used for the design of the mid-span of the slab panel1's short edge for the calculation of the continuous edges. This was done from calculating the Moment at tensile zone of the concrete slab to the calculation of steel bars' areas. The steel bars areas gotten were used to produce the slab reinforcement details

(d) Long span design

The formulas and steps used in the short span design were adopted for the design of slab panel1's long span reinforcement using coefficients of -0.032 and 0.024 for mid-span and continuous edges respectively. The slab's deflection check was done to check the effectiveness of the slab by following the above calculation methods using the formula shown in equation 5.

$$\text{Mf} = 0.55 + \frac{477 - fs}{120\left[0.2 + \frac{M}{(bf * d^2)}\right]} < 2.0 \quad (5)$$

2.2.1.2 Design of beam member

(a) Design of beam A4 – J4

The floor beams were designed based on general arrangement. From BS 8110 -1997 code of structural design, by considering the structural function to be performed by the beams, the size of the beam selected was 450 by 225 mm. The procedure of using Microsoft Excel sheet for the reinforcement design of building's floor beams adopted for floor beam A4 to J4 will be explain while the design of other beam members were done by following the calculating steps of the designed beam A4 -J4. For proper loading and accurate analysis, the beam A4 – J4 design loads were calculated for. During load calculations, the beam own load was calculated from the multiplication of modification factor (1.4), length and breadth of the beam (0.45 m and 0.225 m) with density of concrete (24KN/m^3) plus the finishes of 1.2 KN/m^2 (suggested from BS 8110 – 1997 code) and the results were inputted at cells E163 to I163 respectively as shown in Figure 9.

The Wall / Partition Loads on beam A4 – J4 were calculated by multiplying the modification factor (1.4); wall – weight and height of the building; plus finishes (1.2 KN/m^2). The calculated value was placed at cells F165 to I165 under the load weights (W1 –W4) (Figure 9).

Suan Sunandha Science and Technology Journal
©2023 Faculty of Science and Technology, Suan Sunandha Rajabhat University

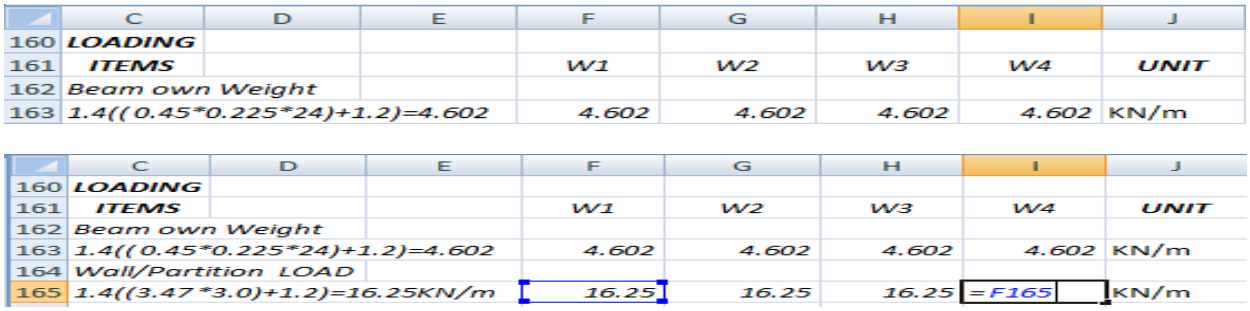

	C	D	E	F	G	H	I	J
160	LOADING							
161	ITEMS			W1	W2	W3	W4	UNIT
162	Beam own Weight							
163	1.4((0.45*0.225*24)+1.2)=4.602			4.602	4.602	4.602	4.602	KN/m
164	Wall/Partition LOAD							
165	1.4((3.47*3.0)+1.2)=16.25KN/m			16.25	16.25	16.25	=F165	KN/m

Figure 9. First:-Beam A4 – J4 own weight calculating method; Second:- Wall / Partition load on beam A4 – J4 calculating method.

The loads from the two slab panels that were attached to each span of the beam A4 – J4 were analyzed and placed at the cells F166 to I167. Addition of all the loads from cells F163 to F167 was determined at cell F168 as W1, that of W2 was determined at cell G168 (from addition of cells G163 to G167), for that of W3, the span load was calculated at cell H168 (from addition of cells H163 to H167) and that of W4 was calculated for at cell I168 (from addition of cells I163 to I167) as shown in Figure 10.

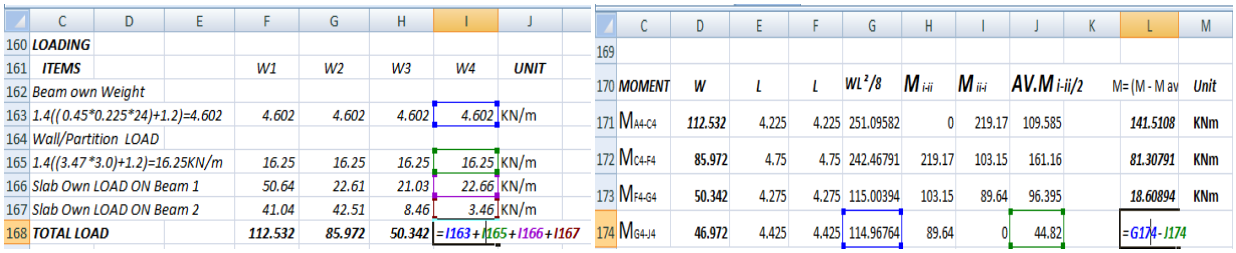

	C	D	E	F	G	H	I	J
160	LOADING							
161	ITEMS			W1	W2	W3	W4	UNIT
162	Beam own Weight							
163	1.4((0.45*0.225*24)+1.2)=4.602			4.602	4.602	4.602	4.602	KN/m
164	Wall/Partition LOAD							
165	1.4((3.47*3.0)+1.2)=16.25KN/m			16.25	16.25	16.25	16.25	KN/m
166	Slab Own LOAD ON Beam 1			50.64	22.61	21.03	22.66	KN/m
167	Slab Own LOAD ON Beam 2			41.04	42.51	8.46	3.46	KN/m
168	TOTAL LOAD			112.532	85.972	50.342	=I163+I165+I166+I167	

	C	D	E	F	G	H	I	J	K	L	M
169											
170	MOMENT	W	L	L	$WL^2/8$	M_{i-ii}	M_{ii-i}	$AV.M_{i-ii/2}$		M=(M - M av	Unit
171	M_{A4-C4}	112.532	4.225	4.225	251.09582	0	219.17	109.585		141.5108	KNm
172	M_{C4-F4}	85.972	4.75	4.75	242.46791	219.17	103.15	161.16		81.30791	KNm
173	M_{F4-G4}	50.342	4.275	4.275	115.00394	103.15	89.64	96.395		18.60894	KNm
174	M_{G4-J4}	46.972	4.425	4.425	114.96764	89.64	0	44.82		=G174-I174	

Figure 10. First:- Calculating total load on beam A4 – J4; Second:- Calculating beam A4 – J4 span moments.

External Beams Design: Span A4 – C4

Here the external span method is showed and procedure is repeated for all other span of Beam A4 – J4. The breadth flange of the external span of the beam was calculated from the formula *bf* = bw+ Lx/10 and that of internal span from *bf* = bw + Lx/5 where b_w is the width of the beam and Lx is the span of the beam. During the Excel calculations, the value of b_w was inputted in the cell D187 and that of Lx/10 was computed at cell G187 while the value of *bf* was calculated at cell H187 as shown in figure 11. Effective depth (d) was calculated from = Total Beam depth (h) – cover – ½Ø – Ø. The value of K was determined for the calculation of the area of steel bars for beam span A4 – CA from cells D191 to I191. The calculated values of M (moment at span A4 – C4 of the beam) was inputted at cell D191, that of f_{cu}, bf and d^2 were placed at cell E191, F191 and H191 respectively. The value of K used was calculated at cell I191. In the cell I191, the value of M at cell D191 was divide by multiplication of fcu, bf and d^2 which were computed as H191*F191*E191 to get the value of K as shown in Figure 11.

Suan Sunandha Science and Technology Journal
©2023 Faculty of Science and Technology, Suan Sunandha Rajabhat University

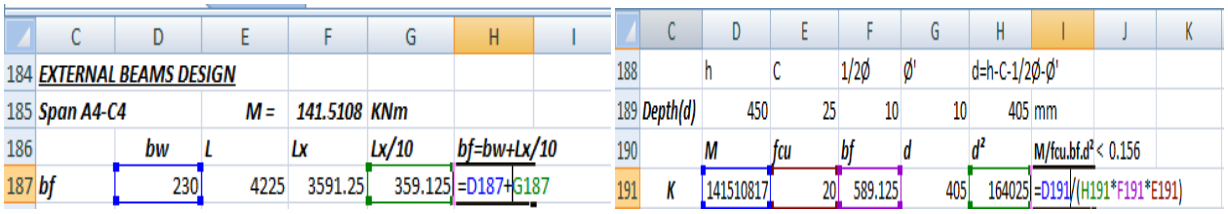

	C	D	E	F	G	H
184	EXTERNAL BEAMS DESIGN					
185	Span A4-C4		M =	141.5108	KNm	
186		bw	L	Lx	Lx/10	bf=bw+Lx/10
187	bf	230	4225	3591.25	359.125	=D187+G187

	C	D	E	F	G	H	I	J	K
188		h	C	1/2Ø	Ø'	d=h-C-1/2Ø-Ø'			
189	Depth(d)	450	25	10	10	405	mm		
190		M	fcu	bf	d	d^2	M/fcu.bf.d^2 < 0.156		
191	K	141510817	20	589.125	405	164025	=D191/(H191*F191*E191)		

Figure 11. First: -Calculating the value of beam's flange breadth; Second:-Calculating the value of K.

Having gotten the value of K, the K value was substituted in equations (3) and (2) to calculate for the area of steel.

3. Results and Discussions

3.1 Result of the design of slab panel 1, (2 and 10)

The value of the uniformly distributed load (UDL) of the slab panel1 owns weight was determined to be 10.4 KN/m^2. Compared with that of manual design, it is more effective than that of the manual (hand calculations). It is error free, and if any error is noticed, the error is traceable and can be fix easily. The ultimate UDL was calculated to be 16.085994 KN/m^2 and displayed in red as shown in Figure 12. The effectiveness of this method is that, all the calculated values were initiated by the designer and the output can be seen as they are being generated. Not like Orion and Staadpro software that were only generating the ultimate UDL with showing how it was calculated.

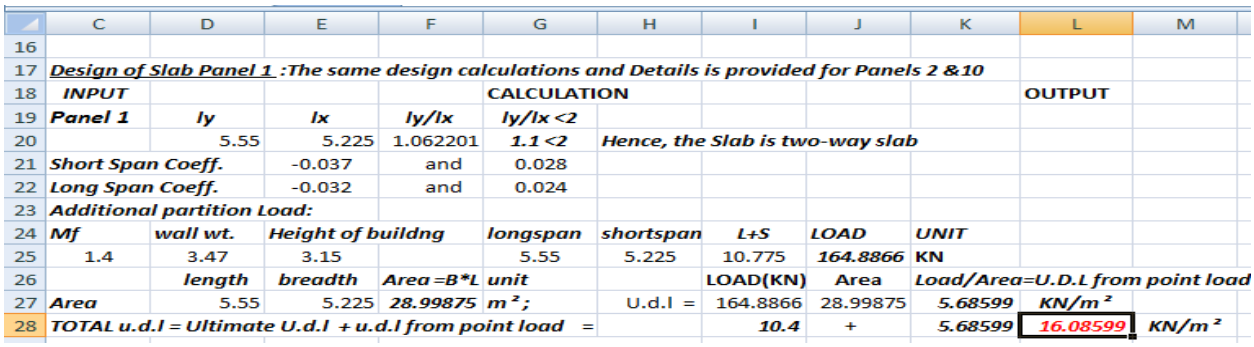

	C	D	E	F	G	H	I	J	K	L	M
16											
17	Design of Slab Panel 1 :The same design calculations and Details is provided for Panels 2 &10										
18	INPUT				CALCULATION					OUTPUT	
19	Panel 1	ly	lx	ly/lx	ly/lx <2						
20		5.55	5.225	1.062201	1.1 <2	Hence, the Slab is two-way slab					
21	Short Span Coeff.		-0.037	and	0.028						
22	Long Span Coeff.		-0.032	and	0.024						
23	Additional partition Load:										
24	Mf	wall wt.	Height of buildng		longspan	shortspan	L+S	LOAD	UNIT		
25	1.4	3.47	3.15		5.55	5.225	10.775	164.8866	KN		
26		length	breadth	Area =B*L	unit		LOAD(KN)	Area	Load/Area=U.D.L from point load		
27	Area	5.55	5.225	28.99875	m^2;	U.d.l =	164.8866	28.99875	5.68599	KN/m^2	
28	TOTAL u.d.l = Ultimate U.d.l + u.d.l from point load =						10.4	+	5.68599	16.08599	KN/m^2

Figure 12. Ultimate uniformly distributed load (U.U.D.L) on slab panel 1.

Considering the results of short span designs of panel1, both at the mid span and continuous edge, the calculated areas of slab steel reinforcement were 267.994 mm^2 and 358.908 mm^2 respectively (see Figure 13). As suggested in the BS 8110-1:1999, the areas of the steel bars provided were Y12@300mm c/c at the bottom with A_s prov. of 377 mm^2; and Y12@250mm c/c at the top with A_s prov. of 452 mm^2 based on the initial areas gotten through calculations. These design outputs are very clear, safe and more economical. Its output calculation can be traceable and fix any error if applicable easily not like that of STAAD Pro and Orion software of which their calculations steps were untraceable (Saha, Ali, Chisanga, & Yasin, 2021). Considering the design of a multistory building, the slab loads analysis and design, as well as their output were generated by STAAD PRO programmed software itself in a vertical sheet (Figure 14) which could developed errors. But, in this study, the computation of design parameters was done one by one in each speculated cell determine each parameter (s) which is far better than the programmed one.

Suan Sunandha Science and Technology Journal
©2023 Faculty of Science and Technology, Suan Sunandha Rajabhat University

	C	D	E	F	G	H	I	J	K
28	TOTAL u.d.l = Ultimate U.d.l + u.d.l from point load =						10.4	+	5.68599
29				SHORT SPAN DESIGN					
30	MID SPAN:			U.D.L(F)	β_x	Lx	Lx	M= F.βx.L²x	
31	M			16.08599	0.028	5.225	5.225	12.29641	KNm
32		M	f_{cu}	bf	d	d²	M/fcu*bf*d²	< 0.156	
33	K	12296412	20	1000	124	15376	0.039986	< 0.156	Okay
34		0.25-K/0.9	√(0.25-K/0.9)		0.5+√(0.25-K/0.9)				
35	La	0.2055714	0.4533998	0.5	0.9533998	≥	0.95 ,then use 0.95		
36		M	0.95	fy	la	d	As =M/0.95fy.la.d		
37	As	12296412	0.95	410	0.95	124	267.994	mm²	
38	PROVIDE Y12mm@300mm c/c (As prov.=377mm²) @ BTM of the Slab								
39	CONTINUOUS EDGES:			U.D.L(F)	βx	Lx	Lx	M= F.βx.L²x	
40	M			16.08599	0.037	5.225	5.225	16.24883	KNm
41		M	f_{cu}	bf	d	d²	M/fcu*bf*d²	< 0.156	
42	K	16248830	20	1000	124	15376	0.052838	< 0.156	Okay
43		0.25-K/0.9	√(0.25-K/0.9)		0.5+√(0.25-K/0.9)				
44	La	0.1912908	0.437368	0.5	0.937368	not ≥	0.95 okay		
45		M	0.95	fy	la	d	As =M/0.95fy.la.d		
46	As	16248830	0.95	410	0.937368	124	358.908	mm²	
47	PROVIDE Y12mm@250mm c/c (As prov.=452mm²) @ TOP of the Slab								

Figure 13. Output of slab panel 1's short span design.

Slabs	Direction		No.of Bars	Spacing mm	Spacing mm	Direction		No.of Bars	Spacing mm c/c	Spacing mm
Slab F1	Short	M con	6φ12	161.3866	150	Long	M con	6 φ12	158.1555	150
		M dis	3 φ12	314	300		M dis	3 φ12	314	300
		M +	5 φ12	215.9392	200		M +	5 φ12	211.7531	200
Slab F2	Short	M con	5 φ12	194.8882	200	Long	M con	5 φ12	195.569	200
		M con	5 φ12	194.8882	200		M dis	3 φ12	314	300
		M +	4 φ12	260.948	250		M +	4 φ12	260.9136	250
Slab F3	Short	M con	4 φ12	252.2731	250	Long	M con	3 φ12	314	300
		M con	4 φ12	252.2731	250		M dis	3 φ12	314	300
		M +	3 φ12	314	300		M +	3 φ12	314	300
Slab F4	Short	M con	5 φ12	215.9775	200	Long	M con	4 φ12	260.5498	250
		M con	5 φ12	215.9775	200		M dis	3 φ12	314	300
		M +	3 φ12	291.448	300		M +	3 φ12	314	300
Slab F5	Short	M con	5 φ12	198.6024	200	Long	M con	5 φ12	209.3954	200
		M con	5 φ12	198.6024	200		M dis	3 φ12	314	300
		M +	4 φ12	266.5324	250		M +	4 φ12	279.191	300
Slab F6	Short	M con	4 φ12	238.1305	250	Long	M con	3 φ12	314	300
		M dis	3 φ12	314	300		M dis	3 φ12	314	300
		M +	3 φ12	314	300		M +	3 φ12	314	300

Figure 14. Outputs of slabs analysis and design using Staad Pro software (Gupta, 2021).

3.1.2 Slab panel 1 deflection check result

The results of deflection check of slab panel 1 show that, the designed slab panel 1 is safe against deflection as shown in Figure 15. The value slab's depth calculated was greater than that of the required depth by 84.49%, this means, the designed slab is safe against deflection. Compare this with that of Gupta (2021) and Harle (2017) output, the safety of their design output could not be evaluated or ascertained, it was only determined by mere STAAD PRO analysis which could contain errors.

Suan Sunandha Science and Technology Journal
©2023 Faculty of Science and Technology, Suan Sunandha Rajabhat University

	C	D	E	F	G	H	I	J	K	L
70										
71	***DEFLECTION CHECK***									
72	M=	***12296412***	**Nmm**	As req.=	***267.99436***	**mm²**	As prov.=	***377***	**mm²**	
73	***fs***	***2fy***	***As req.***	***2fy.As.req***	***3.As prov***	***2fy.As.req/3As prov.***				
74	***fs=***	820	267.99436	219755.4	1131	***194.3018***				
75	Mf	***0.55***	***477-fs***	***120(0.2+(M/(bf. d²)))***		***0.55+ [(477-fs)/ 120(0.2+(M/(bf. d²)))]***				
76	Mf	***0.55***	282.69817	119.9658		2.906491	**> 2,then, use Mf=2.0**			
77		*bf*	*26*Mf*	*bf/26*Mf*						
78	**d req.=**	1000	52	***19.23077***	***≤ d actual=124mm,then,The Slab is saved against deflection***					

Figure 15. Slab panel 1 deflection check.

3.2 Result of design of beam A4 – J4

Beam-Span A4 – C4

The results of Beams analysis and Design were presented as shown in figures 16 to 17. From the results of the loads calculations for Beam A4 – J4, the ultimate load at each span of the beam A4 – J4 were determined to be 112.532 KN/m for W1; 85.972 KN/m for W2; 50.342 KN/m for W3 and 46.972KN/m for W4 respectively as shown in figure 16. Also, in the figure 16, the moments in each span of A4–C4, C4-F4, F4-G4 and G4-J4 of beam A4 – J4 were determined to be 141.5108 KNm, 81.30791 KNm, 18.60894 KNm and 70.14764 KNm respectively.

	C	D	E	F	G	H	I	J	K	L	M
157			***DESIGN OF BEAMS***								
158		**FLOOR-BEAMS DESIGN**									
159	***Reinforcement Design Of Beam A4-J4***										
160	***LOADING***										
161	***ITEMS***			*W1*	*W2*	*W3*	*W4*	***UNIT***			
162	*Beam own Weight*										
163	*1.4((0.45*0.225*24)+1.2)=4.602*			*4.602*	*4.602*	*4.602*	*4.602*	KN/m			
164	*Wall/Partition LOAD*										
165	*1.4((3.47*3.0)+1.2)=16.25KN/m*			*16.25*	*16.25*	*16.25*	*16.25*	KN/m			
166	*Slab Own LOAD ON Beam 1*			*50.64*	*22.61*	*21.03*	*22.66*	KN/m			
167	*Slab Own LOAD ON Beam 2*			*41.04*	*42.51*	*8.46*	*3.46*	KN/m			
168	***TOTAL LOAD***			***112.532***	***85.972***	***50.342***	***46.972***	***KN/m***			
169											
170	***MOMENT***	***W***	***L***	***L***	***WL²/8***	***M i-ii***	***M ii-i***	***AV.M i-ii/2***		M= (M - M av	***Unit***
171	MA4-C4	***112.532***	4.225	4.225	251.09582	0	219.17	109.585		***141.5108***	**KNm**
172	MC4-F4	***85.972***	4.75	4.75	242.46791	219.17	103.15	161.16		***81.30791***	**KNm**
173	MF4-G4	***50.342***	4.275	4.275	115.00394	103.15	89.64	96.395		***18.60894***	**KNm**
174	MG4-J4	***46.972***	4.425	4.425	114.96764	89.64	0	44.82		***70.14764***	**KNm**

Figure 16. Calculating the ultimate load on beam A4 – J4.

In the design of external beam spans A4-C4, the span moment 141.5108KNm was for the design. For A4-C4 span, the flange beam width (b_f) was obtained 589.125 mm and the area of steel (As) calculated for that span was 985.078 mm^2. With 985.078 mm^2 calculated, 4Y20 mm was provided for bottom reinforcement with steel area of 1260 mm^2 using BS8110-1:1997 code (Figure17). Gupta (2021) and Harle (2017), it was the Staad Pro and Orion softwares that predicted this which can be prone to errors.

Suan Sunandha Science and Technology Journal
©2023 Faculty of Science and Technology, Suan Sunandha Rajabhat University

	C	D	E	F	G	H	I	J	K
184	EXTERNAL BEAMS DESIGN								
185	Span A4-C4		M =	141.5108	KNm				
186		bw	L	Lx	Lx/10	bf=bw+Lx/10			
187	bf	230	4225	3591.25	359.125	589.125	mm		
188		h	C	1/2Ø	Ø'	d=h-C-1/2Ø-Ø'			
189	Depth(d)	450	25	10	10	405	mm		
190		M	fcu	bf	d	d^2	M/fcu.bf.d^2	< 0.156	
191	K	141510817	20	589.125	405	164025	0.073222	< 0.156	OKAY
192			0.25-K/0.9	(0.25-K/0.9)^1/2		0.5 + (0.25-K/0.9)^1/2 <= 0.95			
193	La		0.1686421	0.410661		0.910661	<= 0.95	okay	
194			M	0.95	fy	la	d	As=M/0.95fy*la*d	
195	As		141510817	0.95	410	0.910661	405	985.078	mm2
196	USE 4Y20mm BARS@BTM(As pro.=1260mm²)								

Figure 17. Calculating the area of steel for external beam span A4-C4.

4. Details of Designs

4.1 Details of slab and beam designs

The details of slabs design is presented in Figure 18. Considering the design output of Slab panel 1, Y12mm steel bar was suggested for the design details. Also, the spacing among the steel rods of the slab was within 250 – 300 mm. The details of beam A4 – J4 designed is presented at figure 19. In the details, the external span of the beam was detailed with 5Y20mm and 5Y16 mm respectively starting from span A4 – C4 for bottom reinforcement

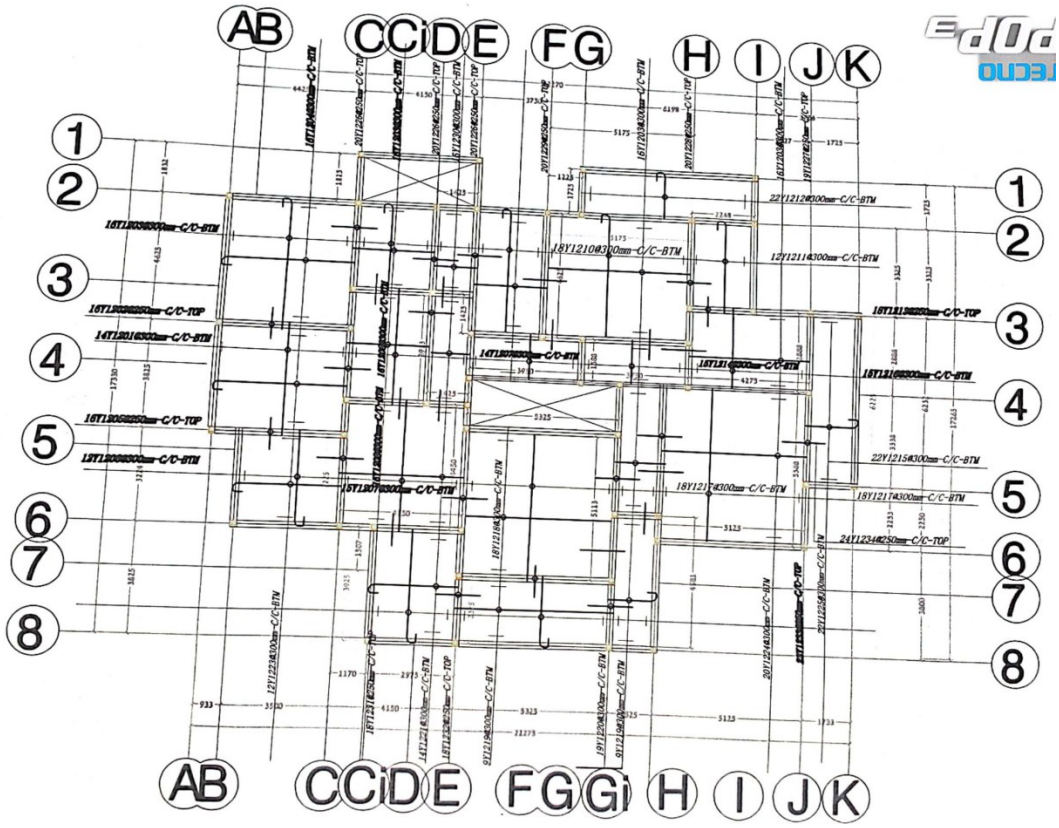

Figure 18. Slab details.

Suan Sunandha Science and Technology Journal
©2023 Faculty of Science and Technology, Suan Sunandha Rajabhat University

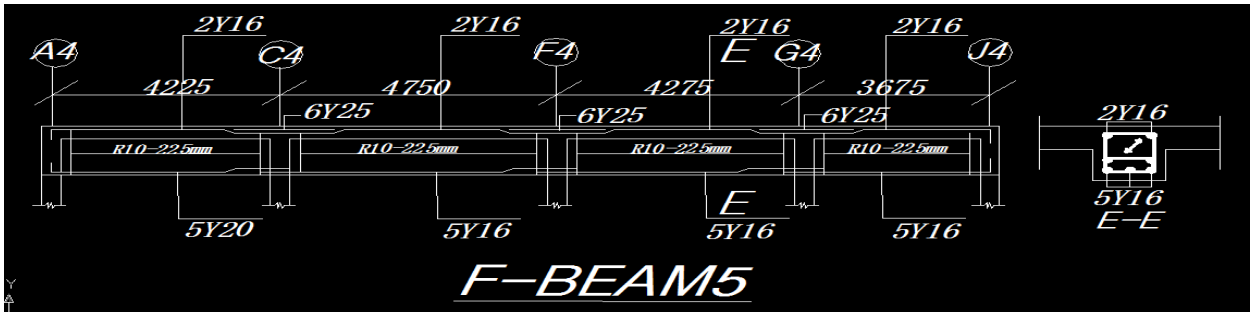

Figure 19. Floor beam A4 – J4 reinforcement details.

5. Significance of Design with Excel

This study has contributed to the knowledge in the sense that, structural member of a building can be design and details with the use of Microsoft Excel and AutoCAD together with BS8110-1:1997 code of structural design, and have a perfect analysis, design and detail results during the analysis. This method is error free and also traceable in case of any error or omission of vita data for quick correction. On like Orion, Staadpro, SAP 2000 software that were programmed with a coded binary algorithm by computer code analyst; the coding, installation, language and human errors using those software were excepted from the use of Excel platform for design. Its application can be done with easy. This program can be operated upon by any structural design engineers without consultation of any binary code programmer once the engineer or designer is a computer literate. Previous software are not reliable and dependable in terms of human, installation and omission errors. It will really assist the site engineers, lecturers and students to design structural members, especially, beams, slabs and columns with easy and error free.

6. Conclusion

As explained earlier in this study, with critical evaluation of design outputs and details of building members analyzed with Microsoft Excel, the following conclusions were made:

Manual analysis and design of structural members is too old for this 21st century. The application of this program as explained in this study (for structural design and analysis) will help in upgrading the existed manual design method. This program is safe, accurate, fast to operate, reliable and encourage the use of BS code for designing. It will help the beginners to make accurate design; also, it will assist engineers, students and lecturers to present clear steps of structural design and analysis together with their details of calculations. Application of this program will increase the rate of British Standard code (BS8110-1:1997) usage for structural design.

Likewise, this method will prevent the formation of design errors caused by software like Orion, StaadPro, SAP 2000 which were the major causes of frequent collapse of buildings in the globe nowadays. With application of this study's method, the quality of structural design and construction in the construction industries will improve. The service life span of structure will also prolong. In a nutshell, the use of structural design code is very important for structural stability and production of standard structures.

Acknowledgement

Authors appreciate the effort of Maryland Catholic Grammar school management staffs, at Otamokun Road, Ogbomoso, Oyo State, Nigeria for their supports during the time of designing the principal lodge (building) of the school.

Fund Acknowledgement

Authors received no fund support from any organization, the project is self sponsored.

Conflict of Interest

There is no conflict of interest.

Suan Sunandha Science and Technology Journal
©2023 Faculty of Science and Technology, Suan Sunandha Rajabhat University

References

British Standard (BS) 8110-1. (1997). *Structural use of concrete. Part 1: Code of practice for design and construction*. London: British Standards Institution.

Civil Engineering X. (2022). *Types of structural members and supports*. Retrieved from https://civilengineeringx.com/structural-analysis/structural-steel/types-of-structural-members-and-supports/

De Quiros, A. C. B., Lopez, R., Aranda-Mena, G., & Edwards, P. (2008). Human reliability as a source of error in research. In A. Dainty (Ed.), *Procs 24th Annual ARCOM Conference* (pp. 687-696). Cardiff, UK.

E-SUB Construction Software. (2018). *What is structural design in civil engineering*? Retrieved from https://esub.com/blog/what-is-structural-design-in-civil-engineering/

Fire Engineering. (2010). *Building Construction: Understanding structural loads and loading*. Retrieved from https://www.fireengineering.com/firefighting/building-construction-understanding-loads-and-loading-2/

Gupta, S. (2021). *Structural analysis and design of multistorey reinforced concrete building using STAAD.Pro*. Retrieved from https://www.researchgate.net/publication/354058835_structural_analysis_and_design_of_multistorey_reinforced_concrete_building_using_staad_pro

Harle, S. M. (2017). Analysis by STAAD-PRO and design of structural elements by MATLAB. *Journal of Asian Scientific Research*, *7*(5), 145-164. doi:10.18488/journal.2.2017.75.145.164

Kilani, A. J., Adeleke, O., & Fapohunda, C. A. (2022). Application of machine learning models to investigate the performance of concrete reinforced with oil palm empty fruit brunch (OPEFB) fibers. *Asian Journal of Civil Engineering*, *23*, 299-320. doi:10.1007/s42107-022-00424-0

Law-Insider. (2021). *Structural member definition*. Retrieved from https://www.lawinsider.com/dictionary/structural-members

Lopez, R., Love, P. E. D., Edwards, D. J., & Davis, P. R. (2010). Design error classification, causation, and prevention in construction engineering. *Journal of Performance of Constructed Facilities*, *24*(4), 399-408. doi:10.1061/(ASCE)cf.1943–5509.0000116

Mrema, G. C., Gumbe, L. O., Chepete, H. J., & Agullo, J. O. (2012). *Rural structures in the tropics: Design and development*. Italy: FAO.

Musa, S., & Obaju, B. (2016). Effects of design error on construction project. *International Journal of Scientific and Engineering Research*, *7*(2), 1099-1114.

Navaee, S. (2003). *Utilization of Excel in solving structural analysis problems*. Paper presented at 2003 Annual Conference, Nashville, Tennessee.

Ondrej. (2011). *Error codes and error descriptions: Technical knowledge base*. Retrieved from https://wiki.csiamerica.com/pages/viewpage.action?pageId=7635149

Peansupap, V., & Ly, R. (2015). Evaluating the impact level of design errors in structural and other building components in building construction projects in Cambodia. *Procedia Engineering*, *123*, 370-378. doi:10.1016/j.proeng.2015.10.049

Ram, J. (2020). *Why beams and columns are important for building construction*? Retrieved from https://www.ramjackokc.com/articles/why-beams-and-columns-are-important-for-building-construction

Reichart, G. (1988). How to reduce design and construction errors. *Nuclear Engineering and Design*, *110*(2), 251-254.

Saha, S., Ali, M. N., Chisanga, W. K., & Yasin, A. (2021). Design and analysis of multistory (G +14) residential building using Staad.Pro & Autocad. *International Journal of Scientific Research in Civil Engineering*, *5*(3), 70-82. doi:10.32628/IJSRCE215311

©2023 Faculty of Science and Technology, Suan Sunandha Rajabhat University

Structural Design. (2023). *Design and development in rural structures*. Retrieved from https://www.fao.org/3/i2433e/i2433e04.pdf

Survey Developer. (2023). *Fiware Orion runtime error*. Retrieved from https://stackoverflow.com/questions/51140211/length-of-dbname-is-max-10

SSSTJ

Suan Sunandha Science and Technology Journal

https://li02.tci-thaijo.org/index.php/ssstj/index